

1 LEVERAGING MULTI-MESSENGER ASTROPHYSICS FOR DARK MATTER SEARCHES

By

Daniel Nicholas Salazar-Gallegos

A DISSERTATION

Submitted to  
Michigan State University  
in partial fulfillment of the requirements  
for the degree of

Physics—Doctor of Philosophy  
Computational Mathematics in Science and Engineering—Dual Major

Today

**ABSTRACT**

3 I did Dark Matter with HAWC and IceCube. I also used Graph Neural Networks

<sup>4</sup> Copyright by

<sup>5</sup> DANIEL NICHOLAS SALAZAR-GALLEGOS

<sup>6</sup> Today

## ACKNOWLEDGMENTS

8 I love my friends. Thanks to everyone that helped me figure this out. Amazing thanks to the people  
9 at LANL who supported me. Eames, etc Dinner Parties Jenny and her child Kaydince Kirsten, Pat,  
10 Andrea Family. You're so far but so critical to my formation. Unconditional love. Roommate

## TABLE OF CONTENTS

12	LIST OF TABLES . . . . .	vii
13	LIST OF FIGURES . . . . .	ix
14	LIST OF ABBREVIATIONS . . . . .	xix
15	CHAPTER 1      INTRODUCTION . . . . .	1
16	CHAPTER 2      DARK MATTER IN THE COSMOS . . . . .	2
17	2.1 Introduction . . . . .	2
18	2.2 Dark Matter Basics . . . . .	3
19	2.3 Evidence for Dark Matter . . . . .	4
20	2.4 Searching for Dark Matter: Particle DM . . . . .	11
21	2.5 Sources for Indirect Dark Matter Searches . . . . .	16
22	2.6 Multi-Messenger Dark Matter . . . . .	18
23	CHAPTER 3      HIGH ALTITUDE WATER CHERENKOV (HAWC) OBSERVATORY . . . . .	21
24	3.1 The Detector . . . . .	21
25	3.2 Construction and Hardware . . . . .	22
26	3.3 Events Reconstruction and Data Acquisition . . . . .	24
27	3.4 Remote Monitoring . . . . .	24
28	CHAPTER 4      ICECUBE NEUTRINO OBSERVATORY . . . . .	25
29	4.1 The Detector . . . . .	25
30	4.2 Events Reconstruction and Data Acquisition . . . . .	25
31	4.3 Northern Test Site . . . . .	25
32	CHAPTER 5      GLORY DUCK: MULTI-WAVELENGTH SEARCH FOR DARK MATTER ANNIHILATION TOWARDS DWARF SPHEROIDAL GALAXIES . . . . .	26
33	5.1 Introduction . . . . .	26
34	5.2 Dataset and Background . . . . .	28
35	5.3 Analysis . . . . .	30
36	5.4 Likelihood Methods . . . . .	34
37	5.5 HAWC Results . . . . .	41
38	5.6 Glory Duck Combined Results . . . . .	43
39	5.7 HAWC Systematics . . . . .	48
40	5.8 <i>J</i> -factor distributions . . . . .	50
41	5.9 Discussion and Conclusions . . . . .	56
44	CHAPTER 6      MULTITHREADING HAWC ANALYSES FOR DARK MATTER SEARCHES . . . . .	60
45	6.1 Introduction . . . . .	60
46	6.2 Dataset and Background . . . . .	60

48	6.3	Analysis . . . . .	62
49	6.4	Likelihood Methods . . . . .	66
50	6.5	Computational Methods: Multithreading . . . . .	66
51	6.6	Analysis Results . . . . .	72
52	6.7	Systematics . . . . .	77
53	6.8	Conclusion and Discussion . . . . .	77
54	<b>CHAPTER 7</b>	<b>HEAVY DARK MATTER ANNIHILATION SEARCH WITH ICE-CUBE'S NORTH SKY TRACK DATA</b>	79
56	7.1	Introduction . . . . .	79
57	7.2	Dataset and Background . . . . .	79
58	7.3	Analysis . . . . .	81
59	7.4	Likelihood Methods . . . . .	90
60	7.5	Background Simulation . . . . .	90
61	7.6	Signal Recovery . . . . .	108
62	7.7	Systematics . . . . .	111
63	7.8	Conclusions . . . . .	114
64	<b>CHAPTER 8</b>	<b>NU DUCK: CONCLUSIONS AND FUTURE DIRECTIONS</b>	116
65	8.1	Conclusions . . . . .	116
66	8.2	Future Directions . . . . .	117
67	<b>APPENDIX A</b>	<b>MULTI-EXPERIMENT SUPPLEMENTARY FIGURES</b>	119
68	<b>APPENDIX B</b>	<b>MULTITHREADING DARK MATTER ANALYSES SUPPLEMENTARY MATERIAL</b>	120
70	B.1	Remaining Spectral Models . . . . .	120
71	B.2	<code>mpu_analysis.py</code> . . . . .	121
72	B.3	Comparison with Glory Duck . . . . .	130
73	<b>APPENDIX C</b>	<b>ICECUBE HEAVY DARK MATTER ANALYSIS SUPPLEMENTARY MATERIAL</b>	133
75	C.1	Docker Image for Oscillating Neutrino Spectra . . . . .	133
76	C.2	Spline Fitting Statuses . . . . .	136
77	C.3	Neutrino Composite Spectra . . . . .	137
78	C.4	Segue 1 And Ursa Major II Signal Recovery . . . . .	138
79	C.5	$n_s$ Sensitivities . . . . .	144
80	<b>BIBLIOGRAPHY</b>		146

## LIST OF TABLES

82    Table 5.1    Summary of the relevant properties of the dSphs used in the present work. 83    Column 1 lists the dSphs. Columns 2 and 3 present their heliocentric distance 84    and galactic coordinates, respectively. Columns 4 and 5 report the $J$ -factors of 85    each source given from the $\mathcal{GS}$ and $\mathcal{B}$ independent studies and their estimated 86 $\pm 1\sigma$ uncertainties. The values $\log_{10} J$ ( $\mathcal{GS}$ set) [47] correspond to the mean 87 $J$ -factor values for a source extension truncated at the outermost observed star. 88    The values $\log_{10} J$ ( $\mathcal{B}$ set) [51] are provided for a source extension at the tidal 89    radius of each dSph. <b>Bolded sources are within HAWC's field of view and</b> 90 <b>provided to the Glory Duck analysis.</b>	35
91    Table 5.2    Summary of dSph observations by each experiment used in this work. A 92    ‘-’ indicates the experiment did not observe the dSph for this study. For 93    Fermi-LAT, the exposure at 1 GeV is given. For HAWC, $ \Delta\theta $ is the absolute 94    difference between the source declination and HAWC latitude. HAWC is more 95    sensitive to sources with smaller $ \Delta\theta $ . For IACTs, we show the zenith angle 96    range, the total exposure, the energy range, the angular radius $\theta$ of the signal or 97    ON region, the ratio of exposures between the background-control (OFF) and 98    signal (ON) regions ( $\tau$ ), and the significance of gamma-ray excess in standard 99    deviations, $\sigma$ .	36
100    Table 6.1    Summary of the relevant properties of the dSphs used in the present work. 101    Column 1 lists the dSphs. Columns 2 and 3 present their heliocentric distance 102    and galactic coordinates, respectively. Column 4 reports the $J$ -factors of each 103    source given from the $\mathcal{LS}$ studies and estimated $\pm 1\sigma$ uncertainties. The 104    values $\log_{10} J$ ( $\mathcal{LS}$ set) [68] correspond to the mean $J$ -factor values for a 105    source extension truncated at $0.5^\circ$ .	66
106    Table 6.2    Timing summaries for analyses for serial and multithreaded processes. $M$ 107    tasks is the number of functional-parallel tasks ran for the computation. $T_{p,c}$ 108    is a single run time in hours:minutes:seconds for runs utilizing $p$ nodes and 109 $c$ threads. Runs are run interactively on the same computer to maximize 110    consistency. Empty entries are indicated with ‘-’. (.) entries are estimated 111    entries extrapolated from data earlier in the column.	70
112    Table 6.3    Speed up summaries for analyses for serial and multithreaded processes. $M$ 113    tasks is the number of functional-parallel tasks ran for the computation. $S_{p,c}$ 114    is a single speedup comparison for runs utilizing $p$ nodes and $c$ threads. $[\cdot]$ 115    are the estimated speedups calculated from Tab. 6.2, Eq. (6.7), and Eq. (6.4). 116    Empty entries are indicated with ‘-’.	72

117	Table 7.1	Spline err tolerances used for input in particle physics component to Eq. (5.1).	
118		Column 1 is the DM annihilation channel being fit. Columns 2, 3, and 4	
119		are the tolerances for "GOOD" (pass), "OK" requires inspection, and "FAIL"	
120		(tune and refit) respectively. Column 5 has the X ranges over which the error	
121		is evaluated. MAX/MIN $[ \cdot, \cdot ]$ takes the maximum or minimum of the two	
122		enclosed values. . . . .	87
123	Proof I know how to include		

## LIST OF FIGURES

125	Figure 2.1	Rotation curve fit to NGC 6503 from [7]. Dashed line is the contribution 126 from visible matter. Dotted curves are from gas. Dash-dot curves are from 127 dark matter (DM). Solid line is the composite contribution from all matter 128 and DM sources. Data are indicated with bold dots with error bars. Data 129 agree strongly with a matter + DM composite prediction. . . . .	5
130	Figure 2.2	Light from distant galaxy is bent in unique ways depending on the distribution 131 of mass between the galaxy and Earth. Yellow dashed lines indicate where 132 the light would have gone if the matter were not present [8]. . . . .	7
133	Figure 2.3	(left) Optical image of galactic cluster 1E0657-558. (right) X-ray image of the 134 cluster with redder meaning hotter and higher baryon density. (both) Green 135 contours are reconstruction of gravity contours from weak lensing. White 136 rings are the best fit mass maxima at 68.3%, 95.5%, and 99.7% confidence. 137 The matter maxima of the clusters are clearly separated from x-ray maxima. [9]	8
138	Figure 2.4	Plank CMB sky. Sky map features small variations in temperature in primor- 139 dial light. These anisotropies are used to make inferences about the universe's 140 energy budget and developmental history. [10] . . . . .	9
141	Figure 2.5	Observed Cosmic Microwave Background power spectrum as a function of 142 multipole moment from Plank [10]. Blue line is best fit model from $\Lambda$ CDM. 143 Red points and lines are data and error, respectively. . . . .	10
144	Figure 2.6	Predicted power spectra of CMB for different $\Omega_m h^2$ values for fixed baryon 145 density from [11]. (left) Low $\Omega_m h^2$ increases the prominence of first and 146 second peaks. (middle) $\Omega_m h^2$ is most similar to the observed power spectrum. 147 The second and third peaks are similar in height. (right) $\Omega_m h^2$ is large which 148 suppresses the first peak and raises the prominence of the third peak. . . . .	10
149	Figure 2.7	The Standard Model (SM) of particle physics. Figure taken from <a href="http://www.quantumdiaries.org/2014/03/14/the-standard-model-a-beautiful-but-flawed-theory/">http://www.quantumdiaries.org/2014/03/14/the-standard-model-a-beautiful-but-flawed-theory/</a> . . . . .	12
152	Figure 2.8	Simplified Feynman diagram demonstrating with different ways DM can 153 interact with SM particles. The 'X's refer to the DM particles whereas the 154 SM refer to fundamental particles in the SM. The large circle in the center 155 indicates the vertex of interaction and is purposely left vague. The colored 156 arrows refer to different directions of time as well as their respective labels. 157 The arrows indicate the initial and final state of the DM -SM interaction in time.	13

158	Figure 2.9 A single jet event in ATLAS detector from 2017 [16]. Jet momentum was 159 observed to be 1.9 TeV. Missing transverse momentum was observed to be 160 1.9 TeV compared to the initial transverse momentum of the event was 0. 161 Implied MET is traced by a red dashed line in event display. . . . .	14
162	Figure 2.10 More detailed pseudo-Feynman diagram of particle cascade from dark matter 163 annihilation into 2 quarks. The quarks hadronize and down to stable particles 164 like $\gamma$ or the anti-proton ( $p^-$ ). Diagram pulled from ICRC 2021 presentation 165 on DM annihilation search [17]. . . . .	15
166	Figure 2.11 Dark Matter (DM) decay spectrum for $b\bar{b}$ initial state and $\gamma$ final state. Redder 167 spectra are for larger DM masses. Bluer spectra are light DM masses. $x$ is a 168 unitless factor defined as the ratio of the mass of DM, $m_\chi$ , and the final state 169 particle energy $E_\gamma$ . Figure from [19]. . . . .	17
170	Figure 2.12 Different dark matter density profiles compared. Some models produce ex- 171 ceptionally large densities at small r [20]. . . . .	18
172	Figure 2.13 The Milky Way Galaxy in photons ( $\gamma$ ) and neutrinos ( $\nu$ ) [22]. The Galactic 173 center is at $l=0^\circ$ and is the brightest region in all panels. (top) An Optical 174 color image of the Milky Way galaxy seen from Earth. Clouds of gas and dust 175 obscure some light from stars. (2nd down) Integrated flux of $\gamma$ -rays observed 176 by the Fermi-LAT telescope [23]. (middle) Expected neutrino emission 177 that corresponds with Fermi-LAT observations. (2nd up) Expected neutrino 178 emission profile after considering detector systematics of IceCube. (bottom) 179 Observed neutrino emission from region of the galactic plane. Substantial 180 neutrino emission was detected. . . . .	19
181	Figure 2.14 Dark Matter annihilation spectra for different final state particle and standard 182 model annihilation channels [24]. Photons (red), $e^\pm$ (green), $\bar{p}$ (blue), $\nu$ (black). . . . .	20
183	Figure 3.1 Photo of the HAWC detector that I took on May 17, 2023. Main array is 184 centered in the photo and comprised of the larger tanks. Outriggers are the 185 smaller tanks around the main array. . . . .	21
186	Figure 3.2 A particle physics illustration of high energy particle showers. Left shower is 187 an electromagnetic shower from a high energy gamma-ray. Most particles in 188 the shower will be a combination of photons and charged leptons, in this case 189 electrons (e). Right figure shows a cosmic ray particle shower. The cosmic 190 ray will produce many more types of particles including pions ( $\pi$ ), neutrinos, 191 and charged leptons. Figured pulled from [26]. . . . .	22
192	Figure 3.3 The WCDs. Left image features several WCDs looking from within the main 193 array of HAWC. Right image shows a schematic of a WCD pulled from [25]. . . . .	23

194	Figure 5.1	Sensitivities of five gamma-ray experiments compared to percentages of the Crab nebula's emission and dark matter annihilation. Solid lines present estimated sensitivities to power law spectra [FACT CHECK THIS]for each experiment. Green lines are Fermi-LAT sensitivities where lighter green is the sensitivity to the galactic center and dark green is its sensitivity to higher declinations. Orange, red, and purple solid lines represent the MAGIC, HESS, and VERITAS 50 hour sensitivities respectively. The maroon and brown lines are the HAWC 1 year and 5 year sensitivities. Across four decades of gamma-ray energy, these experiments have similar sensitivities on the order $10^{-12}$ erg cm $^{-2}$ s $^{-1}$ . The dotted lines are estimated dark matter fluxes assuming $m_\chi = 5$ TeV DM annihilating to bottom quarks (red), tau leptons (blue), and W bosons (green). Faded gray lines outline percentage flux of the Crab nebula. Figure is an augmented version of [27] . . . . .	27
207	Figure 5.2	Effect of Electroweak (EW) corrections on expected DM annihilation spectrum for $\chi\chi \rightarrow W^-W^+$ . Solid lines are spectral models that consider EW corrections. Dash-dot lines are spectral models without EW corrections. Red lines are models for $M_\chi = 1$ TeV. Blue lines represent models for $M_\chi = 100$ TeV. All models are sourced from the PPPC4DMID [46]. . . . .	31
212	Figure 5.3	$\frac{dJ}{d\Omega}$ maps for Segue1 (top) and Coma Berenices (bottom). Origin is centered on the specific dwarf spheroidal galaxies (dSph). X and Y axes are the angular separation from the center of the dwarf. Profile is truncated at the scale radius. Plots of the remaining 11 dSph HAWC studied are linked in Fig. A.1. . . . .	33
216	Figure 5.4	Illustration of the combination technique showing a comparison between $-2 \ln \lambda$ provided by four instruments (colored lines) from the observation of the same dSph without any $J$ nuisance and their sum, <i>i.e.</i> the resulting combined likelihood (thin black line). According to the test statistics of Equation (5.7), the intersection of the likelihood profiles with the line $-2 \ln \lambda = 2.71$ indicates the 95% C.L. upper limit on $\langle \sigma v \rangle$ . The combined likelihood (thin black line) shows a smaller value of upper limit on $\langle \sigma v \rangle$ than those derived by individual instruments. We also show how the uncertainties on the $J$ factor effects the combined likelihood and degrade the upper limit on $\langle \sigma v \rangle$ (thick black line). All likelihood profiles are normalized so that the global minimum $\widehat{\langle \sigma v \rangle}$ is 0. We note that each profile depends on the observational conditions in which a target object was observed. The sensitivity of a given instrument can be degraded and the upper limits less constraining if the observations are performed in non-optimal conditions such as a high zenith angle or a short exposure time. . . . .	39
231	Figure 5.5	. . . . .	42

232	Figure 5.6 HAWC TS values for best fit $\langle\sigma v\rangle$ versus $m_\chi$ for seven SM annihilation channels with $J$ factors from $\mathcal{GS}$ . The solid black line shows the combined best fit TS values. The colored, dashed lines are the TS values for each of the 13 sources HAWC studied.	43
236	Figure 5.7 HAWC Brazil bands at 95% confidence level on $\langle\sigma v\rangle$ versus DM mass for seven annihilation channels with $J$ -factors from $\mathcal{GS}$ [57]. The solid line represents the combined limit from 13 dSphs. The dashed line is the expected limit. The green band is the 68% containment. The yellow band is the 95% containment.	44
241	Figure 5.8 Upper limits at 95% confidence level on $\langle\sigma v\rangle$ in function of the DM mass for eight annihilation channels, using the set of $J$ factors from Ref. [57] ( $\mathcal{GS}$ set in Table 5.1). The black solid line represents the observed combined limit, the black dashed line is the median of the null hypothesis corresponding to the expected limit, while the green and yellow bands show the 68% and 95% containment bands. Combined upper limits for each individual detector are also indicated as solid, colored lines. The value of the thermal relic cross-section in function of the DM mass is given as the red dotted-dashed line [58].	45
250	Figure 5.9 Same as Fig. 5.8, using the set of $J$ factors from Ref. [51, 59] ( $\mathcal{B}$ set in Table 5.1).	46
251	Figure 5.10 Comparisons of the combined limits at 95% confidence level for each of the eight annihilation channels when using the $J$ factors from Ref. [57] ( $\mathcal{GS}$ set in Table 5.1), plain lines, and the $J$ factor from Ref. [51, 59] ( $\mathcal{B}$ set in Table 5.1), dashed lines. The cross-section given by the thermal relic is also indicated [58].	48
255	Figure 5.11 Comparisons of the combined limits at 95% confidence level for a point source analysis and extended source using [57] $\mathcal{GS}$ J-factor distributions and PPPC [46] annihilation spectra. Shown are the limits for Segue1 which will have the most significant impact on the combined limit. 6 of the 7 DM annihilation channels are shown. Solid lines are extended source studies. Dashed lines are point source studies. Overall, the extended source analysis improves the limit by a factor of 2.	50
262	Figure 5.12 Same as Fig. 5.11 on Coma Berenices. This dSph also contributes significantly to the limit. The limits are identical in this case.	51
264	Figure 5.13 Comparison of combined limits when correcting for HAWC's pointing systematic. All DM annihilation channels are shown. The solid black line is the ratio between published limit to the declination corrected limit. The blue solid line or "Combined_og" represented the limits computed for Glory Duck. The solid orange line or "Combined_ad" represented the limits computed after correcting for the pointing systematic.	52

270	Figure 5.14 Differential map of $dJ/\Omega$ from model built in Section 5.8.1 and profiles provided directly from authors. (Top) Differential from Segue1. (bottom) Differential from Coma Berenices. Note that their scales are not the same. Segue1 shows the deepest discrepancies which is congruent with its large uncertainties. Both models show anuli where unique models become apparent.	53
275	Figure 5.15 HAWC limits for Coma Berenices (top) and Segue1 (bottom) for two different map sets. Blue lines are limits calculated on maps with poor model representation. Orange lines are limits calculated on spatial profiles provided by the authors of [47]. Black line is the ratio of the poor spatial model limits to the corrected spatial models. The left y-axis measures $\langle\sigma v\rangle$ for the blue and orange lines. The right y-axis measures the ratio and is unitless.	54
281	Figure 5.16 Comparisons between the $J$ -factors versus the angular radius for the computation of $J$ factors from Ref. [57] ( $\mathcal{GS}$ set in Table 5.1) in blue and for the computation from Ref. [51, 59] ( $\mathcal{B}$ set in Tab. 5.1) in orange. The solid lines represent the central value of the $J$ -factors while the shaded regions correspond to the $1\sigma$ standard deviation.	56
286	Figure 5.17 Comparisons between the $J$ -factors versus the angular radius for the computation of $J$ factors from Ref. [57] ( $\mathcal{GS}$ set in Tab. 5.1) in blue and for the computation from Ref. [51, 59] ( $\mathcal{B}$ set in Tab. 5.1) in orange. The solid lines represent the central value of the $J$ -factors while the shaded regions correspond to the $1\sigma$ standard deviation.	57
291	Figure 6.1 Spectral hypotheses from PPPC [46] and HDM [67] for DM annihilation: $\chi\chi \rightarrow W^-W^+$ . Solid lines are spectral models with EW corrections from the PPPC. Dash-dot lines are spectral models from HDM. Red lines are models for $M_\chi = 1$ TeV. Blue lines represent models for $M_\chi = 100$ TeV.	62
295	Figure 6.2 Photon spectra for $\chi\chi \rightarrow \gamma\gamma$ (left) and $\chi\chi \rightarrow ZZ$ (right) after Gaussian convolution of line features. Both spectra have $\delta$ -features at photon energies equal to the DM mass. Bluer lines are annihilation spectra with lower DM mass. Redder lines are spectra from larger DM mass. All spectral models are sourced from the Heavy Dark Matter models [67]. Axes are drawn roughly according to the energy sensitivity of HAWC.	63
301	Figure 6.3 $\frac{dJ}{d\Omega}$ maps for Coma Berenices, Draco, Segue1, and Sextans. Columns are divided for the $\pm 1\sigma$ uncertainties in $dJ/d\Omega$ around the mean value from $\mathcal{LS}$ [68]. Origin is centered on the specific dwarf spheroidal galaxies (dSph). $\theta$ and $\phi$ axes are the angular separation from the center of the dwarf. Profiles are truncated at $1^\circ$ and flattened beyond.	65

306	Figure 6.4	Infographic on how jobs and DM computation was organized in Section 5.3. Jobs were built for each permutation of CHANS and SOURCES shown by the left block in the figure. Each job, which took on the order 2 hrs to compute, had the following work flow: 1. Import HAWC analysis software, 2 min to run. 2. Load HAWC count maps, 5 min to run. 3. Load HAWC energy and spatial resolutions, 4 min. 5. Load DM spatial source templates and spectral models, less than 1 s. 6. Perform likelihood fit on data and model, about 8 min per DM mass. 7. Write results to file, less than 1s. . . . .	67
314	Figure 6.5	Graphic of Gustafson parallel coding pattern. $f_s$ is the fraction of a program, in time, spent on serial computation. $f_p$ is the fraction of computing time that is parallelizable. $T_p$ is the total time for a parallel program to run. $T_1$ is the total time for a parallel program to run if only 1 processor is allocated. $P_N$ is the $N$ -th processor where it's row is the computation the processor performs. The Gustafson pattern is most similar to what is implemented for this analysis. Figure is pulled from [70]. . . . .	68
321	Figure 6.6	Task chart for one multithreaded job developed for this project. Green blocks indicate a shared resource across the threads AND computation performed serially. Red blocks indicate functional parallel processing within each thread. 3 threads are represented here, yet many more can be employed during the full analysis. Jobs are defined by the SOURCE as these require unique maps to be loaded into the likelihood estimator. The $m_\chi$ , CHAN, and $\langle\sigma v\rangle$ variables are entered into the thread pool and allocated as evenly as possible across the threads. . . . .	70
329	Figure 6.7	HAWC upper limits at 95% confidence level on $\langle\sigma v\rangle$ versus $m_\chi$ for $\chi\chi \rightarrow b\bar{b}$ , $t\bar{t}$ , $u\bar{u}$ , $d\bar{d}$ , $s\bar{s}$ , $c\bar{c}$ , $gg$ , $W^+W^-$ , and $hh$ . Limits are with $\mathcal{LS}$ $J$ -factors [68]. The solid line represents the observed combined limit. Dashed lines represent limits from individual dSphs. . . . .	73
333	Figure 6.8	HAWC upper limits at 95% confidence level on $\langle\sigma v\rangle$ versus $m_\chi$ for $\chi\chi \rightarrow \nu_e\bar{\nu}_e$ , $\nu_\mu\bar{\nu}_\mu$ , $\nu_\tau\bar{\nu}_\tau$ , $e\bar{e}$ , $\mu\bar{\mu}$ , $\tau\bar{\tau}$ , $\gamma\gamma$ and $ZZ$ . Limits use $\mathcal{LS}$ $J$ -factors [68]. The solid line represents the observed combined limit. Dashed lines represent limits from individual dSphs. . . . .	74
337	Figure 6.9	HAWC TS values for best fit $\langle\sigma v\rangle$ versus $m_\chi$ for SM annihilation channels: $\chi\chi \rightarrow b\bar{b}$ , $t\bar{t}$ , $u\bar{u}$ , $d\bar{d}$ , $s\bar{s}$ , $c\bar{c}$ , $gg$ , $W^+W^-$ , and $hh$ . Limits use $\mathcal{LS}$ $J$ -factors. The solid black line shows the combined best fit TS values. The colored, dashed lines are the TS values from each dSph. . . . .	75
341	Figure 6.10	HAWC TS values for best fit $\langle\sigma v\rangle$ versus $m_\chi$ for SM annihilation channels: $\chi\chi \rightarrow \nu_e\bar{\nu}_e$ , $\nu_\mu\bar{\nu}_\mu$ , $\nu_\tau\bar{\nu}_\tau$ , $e\bar{e}$ , $\mu\bar{\mu}$ , $\tau\bar{\tau}$ , $\gamma\gamma$ and $ZZ$ . Limits use $\mathcal{LS}$ $J$ -factors. The solid black line shows the combined best fit TS values. The colored, dashed lines are the TS values from each dSph. . . . .	76

345	Figure 6.11 Comparison of HAWC limits from this analysis to Glory Duck (Fig. 5.5) for 3 dSphs and 3 DM annihilation channels: $b\bar{b}$ , $\tau\bar{\tau}$ , and $e\bar{e}$ . Each sector shows the 95% confidence limit from Glory Duck (blue line) and this analysis (orange line) in the top plot. The lower plot features the ratio in log scale of Glory Duck to this analysis in a red solid line. Horizontal dashed lines are for ratios of 1.0 (black) and $\sqrt{2}$ (blue). Ratios larger than 1.0 are for limits smaller, or stricter, than Glory Duck. Ratios larger than $\sqrt{2}$ indicates limits are stricter than a simple doubling of the Glory Duck data. . . . .	78
353	Figure 7.1 Neutrino spectra at production (left panels) and after oscillation at Earth (right panels). Blue, orange, and green lines are the $\nu_e$ , $\nu_\mu$ , and $\nu_\tau$ spectra respectively. Top panels show the spectra in $\frac{dN}{dE}$ . Lower panels plot the flavor ratio to $\nu_e + \nu_\mu + \nu_\tau$ . SM annihilation channels $b\bar{b}$ , $\tau\bar{\tau}$ , and $\nu_\mu\bar{\nu}_\mu$ are shown for $M_\chi = 1$ PeV, TeV, and EeV. . . . .	83
358	Figure 7.2 Signal recovery for 100 TeV DM annihilation into $\nu_\mu\bar{\nu}_\mu$ for a source at Dec = $16.06^\circ$ . $n_{\text{inj}}$ is the number of injected signal events in simulation. $n_s$ is the number of reconstructed signal events from the simulation data. Although the uncertainties are small and tight, the reconstructed $n_s$ are systematically underestimated. . . . .	84
363	Figure 7.3 Left panel shows the two kernels overlaying the original spectrum from $\chi$ arony after propagation to Earth [73]. The vertical red line indicates where the original neutrino line is maximized. Blue line is the output from $\chi$ aroy. Green line is the spectrum after convolution with a flat kernel. Orange line is the spectrum after Gaussian convolution. Right panel shows the signal recovery of the spectral model using the Gaussian kernel with parameters enumerated above. . . . .	85
370	Figure 7.4 Example spline that failed the fit. Failed splined are corrected on a case by case basis unless the SM channel has a systematic problem fitting the splines. In this case, I made a bookkeeping error and loaded the incorrect spectral model	87
373	Figure 7.5 Summary of input spectral models that were smoothed with Gaussian kernels. Spectral models are for $\chi\chi \rightarrow e\bar{e}, \mu\bar{\mu}, \tau\bar{\tau}, \nu_e\bar{\nu}_e, \nu_\mu\bar{\nu}_\mu$ , and $\nu_\tau\bar{\nu}_\tau$ . These spectra are the composite ( $\nu_\mu + \nu_\tau$ ) of neutrino flavors. Every spectral model used for this analysis is featured as a colored solid line. Bluer lines are for low $m_\chi$ models. $m_\chi$ ranges from 681 GeV to 100 PeV. HDM [67], $\chi$ aroy [73], and Photospline [77] are used to generate these spectra. Energy (x-axis) was chosen to roughly represent the energy sensitivity of NST. . . . .	88

380	Figure 7.6 Test statistic (TS) distributions for Segue 1 and $\chi\chi \rightarrow b\bar{b}$ . Each subplot, 381 except the final, is the TS distribution for a specific DM mass listed in the 382 subplot. Orange dashed lines are the traces for a $\chi^2$ distribution with 1 degree 383 of freedom. $\epsilon[\cdot]$ is the fraction of trials smaller than the bracketed value. The 384 final subplot features the all DM spectral models, similar to Fig. 7.5, used as 385 input for the TS distributions. . . . .	91
386	Figure 7.7 Same as Fig. 7.6 for Segue 1 $\chi\chi \rightarrow \tau\bar{\tau}$ . . . . .	92
387	Figure 7.8 Same as Fig. 7.6 for Segue 1 $\chi\chi \rightarrow \nu_\mu\bar{\nu}_\mu$ . . . . .	93
388	Figure 7.9 Same as Fig. 7.6 for Ursa Major II 1 $\chi\chi \rightarrow b\bar{b}$ . . . . .	94
389	Figure 7.10 Same as Fig. 7.6 for Ursa Major II 1 $\chi\chi \rightarrow \tau\bar{\tau}$ . . . . .	95
390	Figure 7.11 Same as Fig. 7.6 for Ursa Major II 1 $\chi\chi \rightarrow \nu_\mu\bar{\nu}_\mu$ . . . . .	96
391	Figure 7.12 Same as Fig. 7.6 for 15, GS $J$ -factor, stacked sources and $\chi\chi \rightarrow b\bar{b}$ . . . . .	97
392	Figure 7.13 Same as Fig. 7.6 for 15, GS $J$ -factor, stacked sources and $\chi\chi \rightarrow t\bar{t}$ . . . . .	98
393	Figure 7.14 Same as Fig. 7.6 for 15, GS $J$ -factor, stacked sources and $\chi\chi \rightarrow u\bar{u}$ . . . . .	99
394	Figure 7.15 Same as Fig. 7.6 for 15, GS $J$ -factor, stacked sources and $\chi\chi \rightarrow d\bar{d}$ . . . . .	100
395	Figure 7.16 Same as Fig. 7.6 for 15, GS $J$ -factor, stacked sources and $\chi\chi \rightarrow e\bar{e}$ . . . . .	101
396	Figure 7.17 Same as Fig. 7.6 for 15, GS $J$ -factor, stacked sources and $\chi\chi \rightarrow \mu\bar{\mu}$ . . . . .	102
397	Figure 7.18 Same as Fig. 7.6 for 15, GS $J$ -factor, stacked sources and $\chi\chi \rightarrow \tau\bar{\tau}$ . . . . .	103
398	Figure 7.19 Same as Fig. 7.6 for 15, GS $J$ -factor, stacked sources and $\chi\chi \rightarrow W^+W^-$ . . . . .	104
399	Figure 7.20 Same as Fig. 7.6 for 15, GS $J$ -factor, stacked sources and $\chi\chi \rightarrow ZZ$ . . . . .	105
400	Figure 7.21 Same as Fig. 7.6 for 15, GS $J$ -factor, stacked sources and $\chi\chi \rightarrow \nu_e\bar{\nu}_e$ . . . . .	106
401	Figure 7.22 Same as Fig. 7.6 for 15, GS $J$ -factor, stacked sources and $\chi\chi \rightarrow \nu_\mu\bar{\nu}_\mu$ . . . . .	107

402	Figure 7.23 Signal Recovery study for an analysis with 15 stacked sources using the $\mathcal{GS}$	109
403	$J$ -factors [47]. Above shows 14 studies for DM mass ranging between 1	
404	TeV and 20 PeV for $\chi\chi \rightarrow \mu_\mu\overline{\mu_\mu}$ . The bottom right subplot features every	
405	spectral model used as input for the remaining subplots. The remaining	
406	subplots show $n_{\text{inj}}$ as the number of signal events injected into background	
407	simulation. Whereas, $n_s$ is the number of signal events recovered from	
408	analyzing the injected simulation. Blue line represents the median values of	
409	100 simulations. Light blue bands show the $1\sigma$ statistical uncertainty around	
410	the median. . . . .	
411	Figure 7.24 Same as Fig. 7.23 but for $\chi\chi \rightarrow t\bar{t}$ (top) and $b\bar{b}$ (bottom). . . . .	110
412	Figure 7.25 IceCube North Sky Track Sensitivities. Each panel shows sensitivity curves	
413	for various DM annihilation channels. Sensitivities are for the velocity-	
414	weighted cross-section $\langle\sigma v\rangle$ versus $m_\chi$ . Doted, colored lines are sensitivities	
415	for individual sources. Solid white lines are for the combined sensitivity of	
416	all 15 $\mathcal{GS}$ sources used in this study. . . . .	112
417	Figure 7.26 Same as Fig. 7.25 for three additional DM annihilation channels. . . . .	113
418	Figure 7.27 Panel A: Neutrino's from the Northern sky and incident on the IceCube	
419	detector will travel through the Earth. How much of the Earth these neutrinos	
420	travels is a function of zenith from the vertical axis. Panel B: SM prediction of	
421	neutrino transmission probabilities for neutrinos arriving at $90^\circ - 180^\circ$ zenith	
422	and with 100 GeV to 100 PeV energies. High-energy neutrinos traversing	
423	the whole Earth are completely absorbed, whereas low-energy neutrinos pass	
424	through unimpeded. Neutrinos coming from above the horizon will arrive	
425	unimpeded for all neutrino energies. Figure pulled from [80]. . . . .	114
426	Figure 7.28 $\langle\sigma v\rangle$ sensitivities for 5 imaginary sources with $\log_{10} J = 19.42 \log_{10}(\text{GeV}^2\text{cm}^{-5})$ .	
427	Each imaginary source shares a declination with a source in Tab. 5.1 . . . . .	115
428	Figure 8.1 The prompt electron neutrino and photon spectrum resulting from the decay	
429	of a 2EeV DM particle to $\nu_e\overline{\nu}_e$ , as currently being searched for at IceCube	
430	[5]. Solid curves represent the results of this work, and predict orders of	
431	magnitude more flux at certain energies than the dashed results of Pythia 8.2,	
432	one of the only existing methods to generate spectra at these masses. In both	
433	cases energy conservation is satisfied: there is a considerable contribution to	
434	a $\delta$ -function at $x = 1$ , associated with events where an initial W or Z was never	
435	emitted and thus no subsequent shower developed. Large disagreements are	
436	generically observed at these masses for electroweak dominated channels,	
437	while the agreement is better for colored initial SM states. . . . .	117
438	Figure 8.2 TODO: neutrino and bb plot with nu Sensitivities[NEEDS A SOURCE][FACT	
439	CHECK THIS] . . . . .	118

440	Figure A.1 Sister figure to Figure 5.3. Sources in the first row from left to right: Bootes I, Canes Venatici I, II. In second row: Draco, Hercules, Leo I. In the first row: Leo II, Leo IV, Sextans. In the final row: Ursa Major I, Ursa Major II. . . . .	119
443	Figure B.1 Sister figure to Figure 6.2 for remaining SM primary annihilation channels studied for this thesis. These did not require any post generation smoothing and so are directly pulled from [67] with a binning scheme most helpful for a HAWC analysis. . . . .	120
447	Figure B.2 Comparison of HAWC limits from this analysis to Glory Duck (Fig. 5.5) for Coma Berenices and 7 DM annihilation channels. . . . .	130
449	Figure B.3 Same as Fig. B.2 but for Segue 1. . . . .	131
450	Figure B.4 Same as Fig. B.2 but for Sextans. . . . .	132
451	Figure C.1 Current status of spline tables according to constraints defined by Tab. 7.1. Green splines are splines that passed under the GOOD tolerance. Yellow are splines that are OK. Red are splines that FAIL. All yellow splines were inspected individually before running the analysis. Splines were made for the $\mu$ (PID 14; top panel) flavor and $\tau$ (PID 16; bottom panel) neutrino flavors. . . . .	136
456	Figure C.2 Sister figure to Fig. 7.5 for annihilation channels that did not require kernel smoothing. These spectra are the composite ( $\nu_\mu + \nu_\tau$ ) of neutrino flavors. Every spectral model used for this analysis is featured as a colored solid line. Bluer lines are for lower DM mass spectral models. DM masses range from 681 GeV to 100 PeV. . . . .	137
461	Figure C.3 Same as Fig. 7.23 but for Segue 1 and $\chi\chi \rightarrow b\bar{b}$ . . . . .	138
462	Figure C.4 Same as Fig. 7.23 but for Segue 1 and $\chi\chi \rightarrow t\bar{t}$ . . . . .	139
463	Figure C.5 Same as Fig. 7.23 but for Segue 1 and $\chi\chi \rightarrow \nu_\mu\bar{\nu}_\mu$ . . . . .	140
464	Figure C.6 Same as Fig. 7.23 but for Ursa Major II and $\chi\chi \rightarrow b\bar{b}$ . . . . .	141
465	Figure C.7 Same as Fig. 7.23 but for Ursa Major II and $\chi\chi \rightarrow t\bar{t}$ . . . . .	142
466	Figure C.8 Same as Fig. 7.23 but for Ursa Major II and $\chi\chi \rightarrow \nu_\mu\bar{\nu}_\mu$ . . . . .	143
467	Figure C.9 IceCube North Sky Track Sensitivities for $n_s/\langle N \rangle$ . $n_s$ values are the counts fed into Eq. (7.8) to produce Fig. 7.26 and Fig. 7.25. . . . .	144
469	Figure C.10 Same as Fig. C.9 for three additional DM annihilation channels. . . . .	145

**LIST OF ABBREVIATIONS**

- 471 **MSU** Michigan State University  
472 **LANL** Los Alamos National Laboratory  
473 **DM** Dark Matter  
474 **SM** Standard Model  
475 **HAWC** High Altitude Water Cherenkov Observatory  
476 **dSph** Dwarf Spheroidal Galaxy

## CHAPTER 1

### INTRODUCTION

478 Is the text not rendering right? Ah ok it knows im basically drafting the doc still

## CHAPTER 2

479

### DARK MATTER IN THE COSMOS

480 **2.1 Introduction**

481 The dark matter problem can be summarized in part by the following thought experiment.

482 Let us say you are the teacher for an elementary school classroom. You take them on a field  
483 trip to your local science museum and among the exhibits is one for mass and weight. The exhibit  
484 has a gigantic scale, and you come up with a fun problem for your class.

485 You ask your class, "What is the total weight of the classroom? Give your best estimation to  
486 me in 30 minutes, and then we'll check your guess on the scale. If your guess is within 10% of the  
487 right answer, we will stop for ice cream on the way back."

488 The students are ecstatic to hear this, and they get to work. The solution is some variation of  
489 the following strategy. The students should give each other their weight or best guess if they do  
490 not know. Then, all they must do is add each student's weight and get a grand total for the class.

491 The measurement on the giant scale should show the true weight of the class. When comparing  
492 the measured weight to your estimation, multiply the measurement by  $1.0 \pm 0.1$  to get the  $\pm 10\%$   
493 tolerances for your estimation.

494 Two of your students, Sandra and Mario, return to you with a solution.

495 They say, "We weren't sure of everyone's weight. We used 65 lbs. for the people we didn't  
496 know and added everyone who does know. There are 30 of us, and we got 2,000 lbs.! That's a ton!"

497 You estimated 1,900 lbs. assuming the average weight of a student in your class was 60 lbs.  
498 So, you are pleased with Sandra's and Mario's answer. You instruct your students to all gather on  
499 the giant scale and read off the weight together. To all your surprise, the scale reads *10,000 lbs.*!  
500 10,000 is significantly more than a 10% error from 2,000. In fact, it is approximately 5 times more  
501 massive than either your or your students' estimates. You think to yourself and conclude there  
502 must be something wrong with the scale. You ask an employee to check the scale and verify it is  
503 well calibrated. They confirm that the scale is in working order. You weigh a couple of students  
504 individually to assess that the scale is well calibrated. Sandra weighs 59 lbs., and Mario weighs

505 62 lbs., typical weights for their age. You then weigh each student individually and see that their  
506 weights individually do not deviate greatly from 60 lbs. So, where does all the extra weight come  
507 from?

508 This thought experiment serves as an analogy to the Dark Matter problem. The important  
509 substitution to make however is to replace the students with stars and the classroom with a galaxy,  
510 say the Milky Way. Individually the mass of stars is well measured and defined with the Sun as our  
511 nearest test case. However, when we set out to measure the mass of a collection of stars as large as  
512 galaxies, our well-motivated estimation is wildly incorrect. There simply is no way to account for  
513 this discrepancy except without some unseen, or dark, contribution to mass and matter in galaxies.  
514 I set out in my thesis to narrow the possibilities of what this Dark Matter could be.

515 This chapter is organized like the following... **TODO: Text should look like ... Chapter x has**  
516 **blah blah blah.**

## 517 2.2 Dark Matter Basics

518 Presently, a more compelling theory of cosmology that includes Dark Matter (DM) in order  
519 to explain a variety of observations is  $\Lambda$  Cold Dark Matter, or  $\Lambda$ CDM. I present the evidence  
520 supporting  $\Lambda$ CDM in Section 2.3 yet discuss the conclusions of the  $\Lambda$ CDM model here. According  
521 to  $\Lambda$ CDM fit to observations on the Cosmic Microwave Background (CMB), DM is 26.8% of the  
522 universe's current energy budget. Baryonic matter, stuff like atoms, gas, and stars, contributes to  
523 4.9% of the universe's current energy budget [1, 2, 3].

524 DM is dark; it does not interact readily with light at any wavelength. DM also does not interact  
525 noticeably with the other standard model forces (Strong and Weak) at a rate that is readily observed  
526 [3]. DM is cold, which is to say that the average velocity of DM is below relativistic speeds [1].  
527 'Hot' DM would not likely manifest the dense structures we observe like galaxies, and instead  
528 would produce much more diffuse galaxies than what is observed [3, 1]. DM is old; it played a  
529 critical role in the formation of the universe and the structures within it [1, 2].

530 Observations of DM have so far been only gravitational. The parameter space available to what  
531 DM could be therefore is extremely broad. The broad DM parameter space is iteratively tested in

532 DM searches by supposing a hypothesis that has not yet been ruled out and performing observations  
533 to test them. When the observations yield a null result, the parameter space is constrained further.  
534 I present some approaches for DM searches in Section 2.4.

535 **2.3 Evidence for Dark Matter**

536 Dark Matter (DM) has been a looming problem in physics for almost 100 years. Anomalies  
537 have been observed by astrophysicists in galactic dynamics as early as 1933 when Fritz Zwicky  
538 noticed unusually large velocity dispersion in the Coma cluster. Zwicky's measurement was the  
539 first recorded to use the Virial theorem to measure the mass fraction of visible and invisible matter  
540 in celestial bodies [4]. From Zwicky in [5], "*If this would be confirmed, we would get the surprising*  
541 *result that dark matter is present in much greater amount than luminous matter.*" Zwicky's and  
542 others' observation did not instigate a crisis in astrophysics because the measurements did not  
543 entirely conflict with their understanding of galaxies [4]. In 1978, Rubin, Ford, and Norbert  
544 measured rotation curves for ten spiral galaxies [6]. Rubin et al.'s 1978 publication presented a  
545 major challenge to the conventional understanding of galaxies that could no longer be dismissed by  
546 measurement uncertainties. Evidence has been mounting ever since for this exotic form of matter.  
547 The following subsections provide three compelling pieces of evidence in support of the existence  
548 of DM.

549 **2.3.1 First Clues: Stellar Velocities**

550 Zwicky, and later Rubin, measured the stellar velocities of various galaxies to estimate their  
551 virial mass. The Virial Theorem upon which these observations are interpreted is written as

$$2T + V = 0. \quad (2.1)$$

552 Where  $T$  is the kinetic energy and  $V$  is the potential energy in a self-gravitating system. The  
553 classical Newton's law of gravity from stars and gas was used for gravitational potential modeled in  
554 the observed galaxies:

$$V = -\frac{1}{2} \sum_i \sum_{j \neq i} \frac{m_i m_j}{r_{ij}}. \quad (2.2)$$

555 Zwicky et al. measured just the velocities of stars apparent in optical wavelengths [5]. Rubin et al.  
 556 added by measuring the velocity of the hydrogen gas via the 21 cm emission line of Hydrogen [6].  
 557 The velocities of the stars and gas are used to infer the total mass of galaxies and galaxy clusters  
 558 via Equation (2.1). An inferred mass is obtained from the luminosity of the selected sources. The  
 559 two inferences are compared to each other as a luminosity to mass ratio which typically yielded [1]

$$\frac{M}{L} \sim 400 \frac{M_{\odot}}{L_{\odot}} \quad (2.3)$$

560  $M_{\odot}$  and  $L_{\odot}$  referring to stellar mass and stellar luminosity, respectively. These ratios clearly indicate  
 561 a discrepancy in apparent light and mass from stars and gas and their velocities.

562 Rubin et al. [6] demonstrated that the discrepancy was unlikely to be an underestimation of  
 563 the mass of the stars and gas. The inferred "dark" mass was up to 5 times more than the luminous  
 564 mass. This dark mass also needed to extend well beyond the extent of the luminous matter.

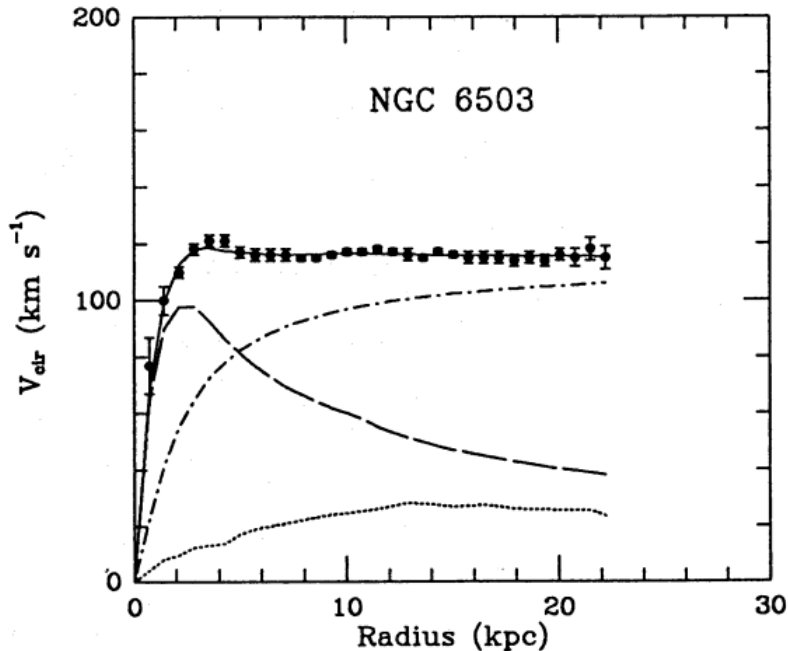


Figure 2.1 Rotation curve fit to NGC 6503 from [7]. Dashed line is the contribution from visible matter. Dotted curves are from gas. Dash-dot curves are from dark matter (DM). Solid line is the composite contribution from all matter and DM sources. Data are indicated with bold dots with error bars. Data agree strongly with a matter + DM composite prediction.

565 Figure 2.1 features one of many rotation curves plotted from the stellar velocities within galaxies.

566 The measured rotation curves mostly feature a flattening of velocities at higher radius which is not  
567 expected if the gravity was only coming from gas and luminous matter. The extension of the  
568 flat velocity region also indicates that the DM is distributed far from the center of the galaxy.  
569 Modern velocity measurements include significantly larger objects, galactic clusters, and smaller  
570 objects, dwarf galaxies. Yet, measurements along this regime are leveraging the Virial theorem  
571 with Newtonian potential energies. We know Newtonian gravity is not a comprehensive description  
572 of gravity. New observational techniques have been developed since 1978, and those are discussed  
573 in the following sections.

574 **2.3.2 Evidence for Dark Matter: Gravitational Lensing**

575 Modern evidence for dark matter comes from new avenues beyond stellar velocities. Grav-  
576 itational lensing from DM is a new channel from general relativity. General relativity predicts  
577 aberrations in light caused by massive objects. In recent decades we have been able to measure the  
578 lensing effects from compact objects and DM halos. Figure 2.2 shows how different massive ob-  
579 jects change the final image of a faraway galaxy resulting from gravitational lensing. Gravitational  
580 lensing developed our understanding of dark matter in two important ways.

581 Gravitational lensing provides additional compelling evidence for DM. The observation of two  
582 merging galactic clusters in 2006, shown in Figure 2.3, provided a compelling argument for DM  
583 outside the Standard Model. These clusters merged recently in astrophysical time scales. Galaxies  
584 and star cluster have mostly passed by each other as the likelihood of their collision is low. Therefore,  
585 these massive objects will mostly track the highest mass, dark and/or baryonic, density. Yet, the  
586 intergalactic gas is responsible for the majority of the baryonic mass in the systems [4]. These gas  
587 bodies will not phase through and will heat up as they collide together. The hot gas is located via  
588 x-ray emission from the cluster. Two observations of the clusters were performed independently of  
589 each other.

590 The first was the lensing of light around the galaxies due to their gravitational influences.  
591 When celestial bodies are large enough, the gravity they exert bends space and time itself. The  
592 warped space-time lenses light and will deflect in an analogous way to how glass lenses will bend

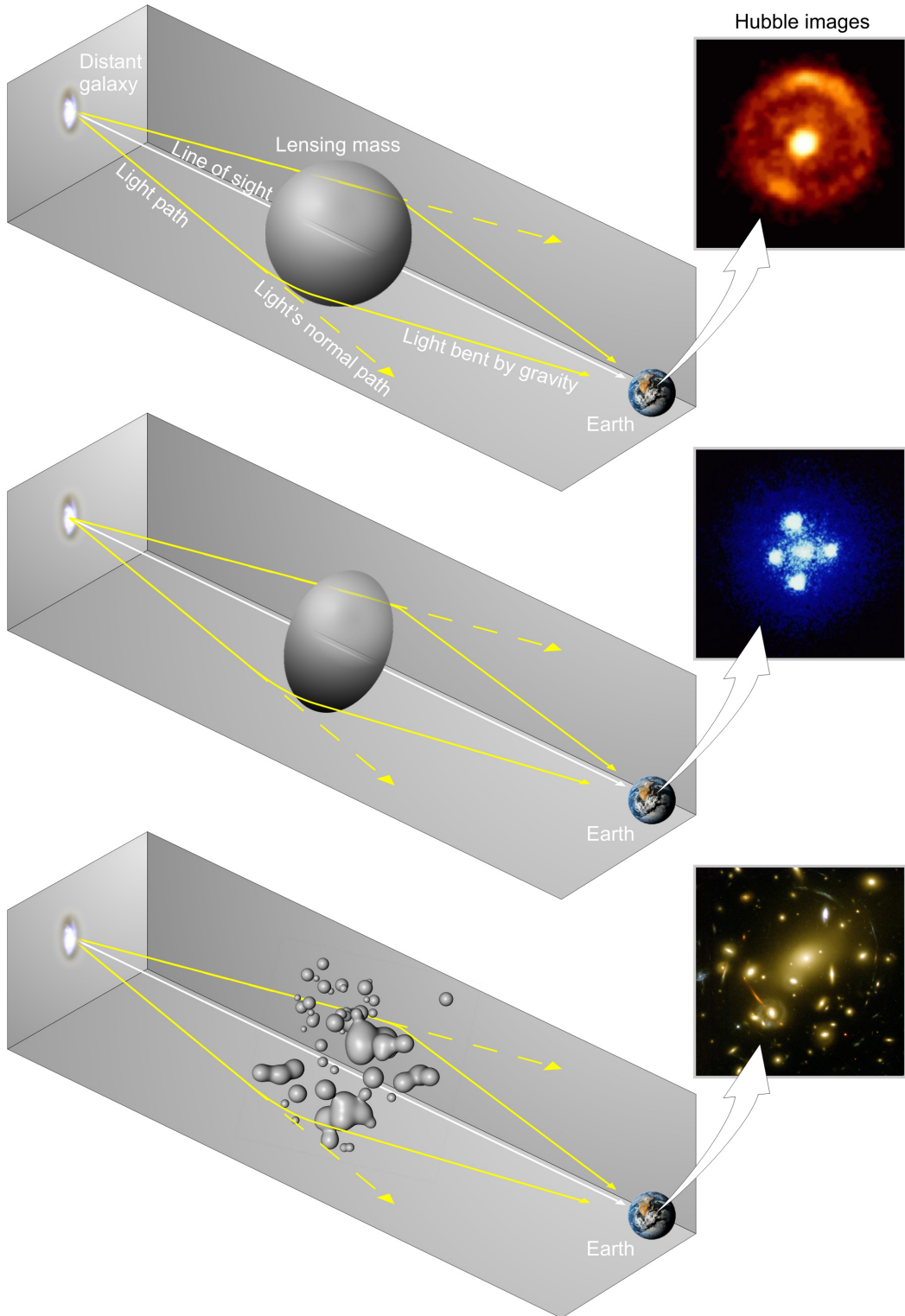


Figure 2.2 Light from distant galaxy is bent in unique ways depending on the distribution of mass between the galaxy and Earth. Yellow dashed lines indicate where the light would have gone if the matter were not present [8].

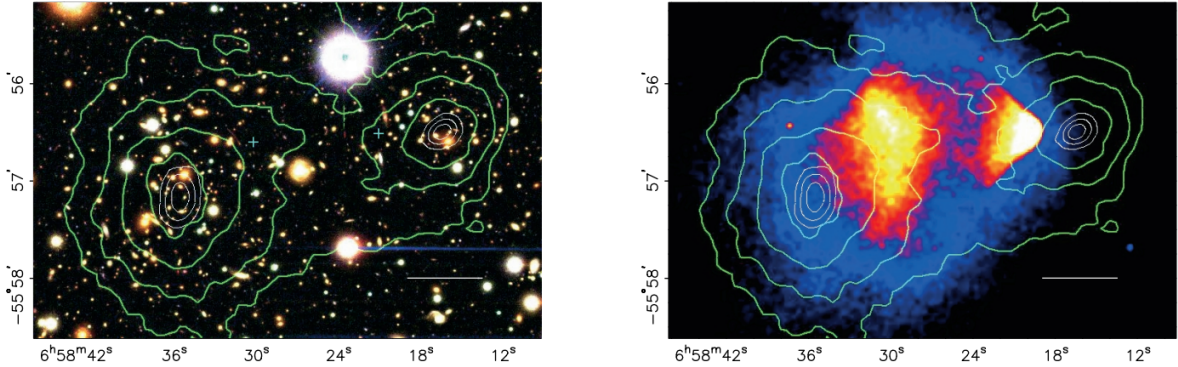


Figure 2.3 (left) Optical image of galactic cluster 1E0657-558. (right) X-ray image of the cluster with redder meaning hotter and higher baryon density. (both) Green contours are reconstruction of gravity contours from weak lensing. White rings are the best fit mass maxima at 68.3%, 95.5%, and 99.7% confidence. The matter maxima of the clusters are clearly separated from x-ray maxima. [9]

593 light, see Figure 2.2. With a sufficient understanding of light sources behind a massive object, we  
 594 can reconstruct the contours of the gravitational lenses. The gradient of the contours shown in  
 595 Figure 2.3 then indicates how dense the matter is and where it is.

596 The x-ray emission can then be observed from the clusters. Since these galaxies are mostly gas  
 597 and are merging, then the gas should be getting hotter. If they are merging, the x-ray emissions  
 598 should be the strongest where the gas is mostly moving through each other. Hence, X-ray emission  
 599 maps out where the gas is in the merging galaxy cluster.

600 The lensing and x-ray observations were done on the Bullet cluster featured on Figure 2.3.  
 601 The x-ray emissions do not align with the gravitational contours from lensing. The incongruence  
 602 in mass density and baryon density suggests that there is a lot of matter somewhere that does  
 603 not interact with light. Moreover, this dark matter cannot be baryonic [9]. The Bullet Cluster  
 604 measurement did not really tell us what DM is exactly, but it did give the clue that DM also does  
 605 not interact with itself very strongly. If DM did interact strongly with itself, then it would have been  
 606 more aligned with the x-ray emission [9]. There have been follow-up studies of galaxy clusters with  
 607 similar results. The Bullet Cluster and others like it provide a persuasive case against something  
 608 possibly amiss in our gravitational theories.

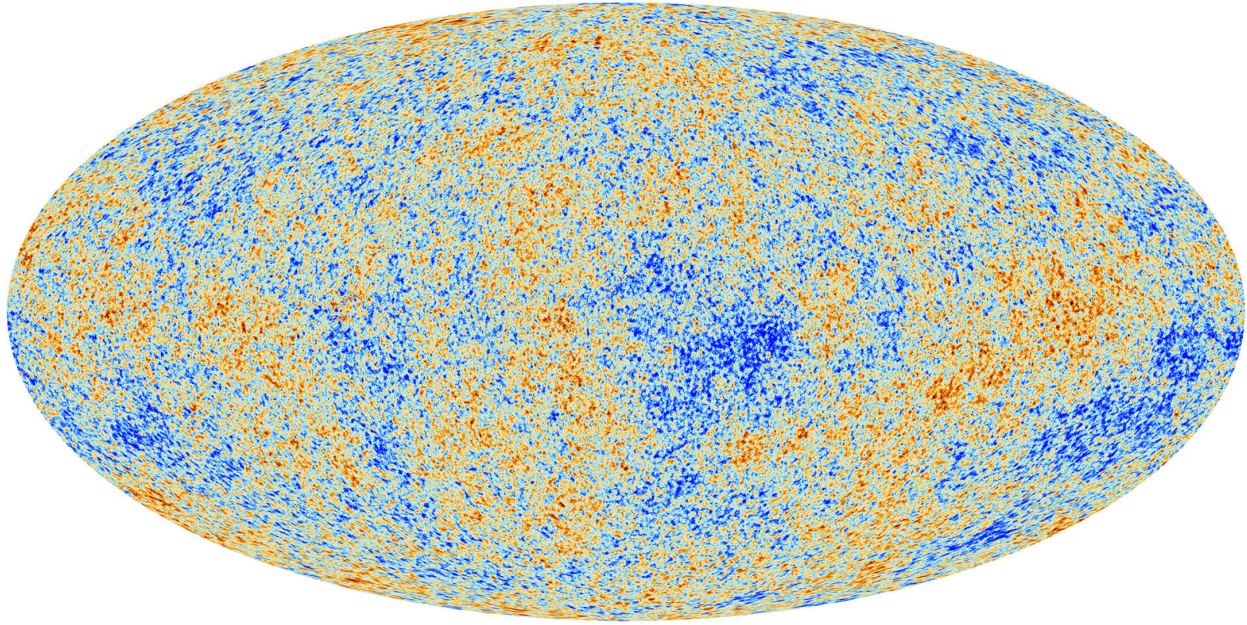


Figure 2.4 Plank CMB sky. Sky map features small variations in temperature in primordial light. These anisotropies are used to make inferences about the universe's energy budget and developmental history. [10]

### 609 2.3.3 Evidence for Dark Matter: Cosmic Microwave Background

610 The Cosmic Microwave Background (CMB) is the primordial light from the early universe

611 when Hydrogen atoms formed from the free electron and proton soup in the early universe. The

612 CMB is the earliest light we can observe; released when the universe was about 380,000 years old.

613 Then we look at how the simulated universes look like compared to what we see. Figure 2.4 is the

614 most recent CMB image from the Plank satellite after subtracting the average value and masking the

615 galactic plane [10]. Redder regions indicate a slightly hotter region in the CMB, and blue indicates

616 colder. The intensity variations are on the order of 1 in 1000 with respect to the average value.

617 The Cosmic Microwave Background shows that the universe had DM in it from an incredibly

618 early stage. To measure the DM, Dark Energy, and matter fractions of the universe from the CMB,

619 the image is analyzed into a power spectrum, which shows the amplitude of the fluctuations as

620 a function of spherical multipole moments.  $\Lambda$ CDM provides the best fit to the power spectra of

621 the CMB as shown in Figure 2.5. The CMB power spectrum is quite sensitive to the fraction

622 of each energy contribution in the early universe. Low  $l$  modes are dominated by variations

623 in gravitational potential. Intermediate  $l$  emerge from oscillations in photon-baryon fluid from

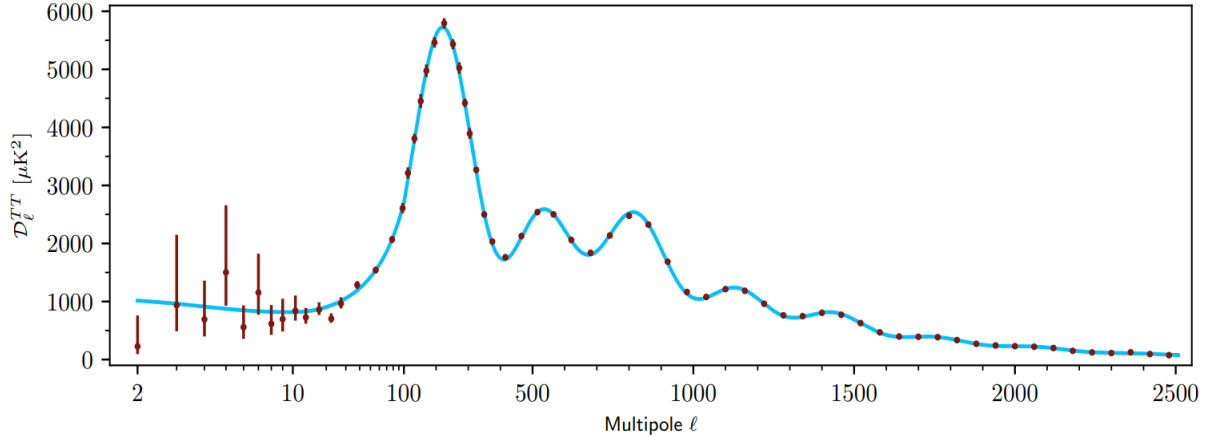


Figure 2.5 Observed Cosmic Microwave Background power spectrum as a function of multipole moment from Plank [10]. Blue line is best fit model from  $\Lambda$ CDM. Red points and lines are data and error, respectively.

624 competing baryon pressures and gravity. High  $l$  is a damped region from the diffusion of photons  
 625 during electron-proton recombination. [1]

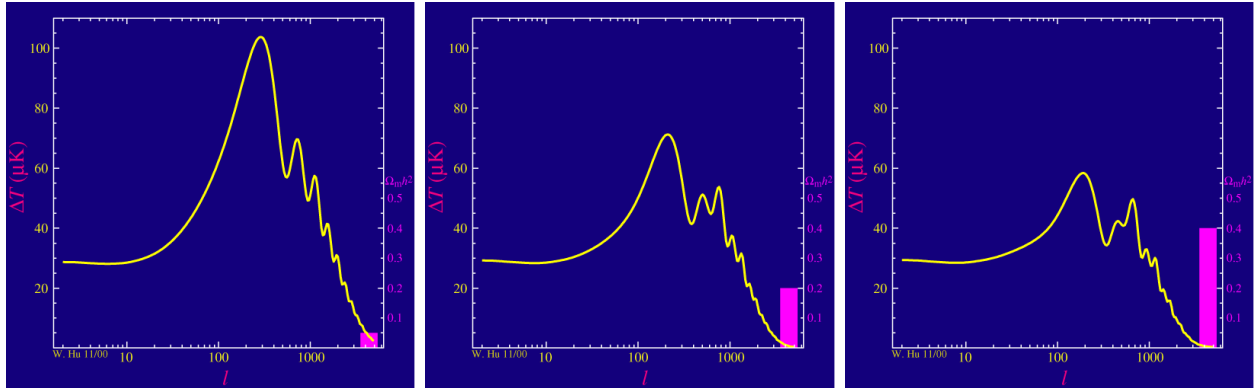


Figure 2.6 Predicted power spectra of CMB for different  $\Omega_m h^2$  values for fixed baryon density from [11]. (left) Low  $\Omega_m h^2$  increases the prominence of first and second peaks. (middle)  $\Omega_m h^2$  is most similar to the observed power spectrum. The second and third peaks are similar in height. (right)  $\Omega_m h^2$  is large which suppresses the first peak and raises the prominence of the third peak.

626 The harmonics would look quite different for a universe with less DM. Figure 2.6 demonstrates  
 627 the effect  $\Omega_m h^2$  has on the expected power spectrum for fixed baryon matter density. [11] Sweeping  
 628  $\Omega_m h^2$  in this way clearly shows the effect dark matter has on the CMB power spectrum. The  
 629 observations fit well with the  $\Lambda$ CDM model, and the derived fractions are as follows. The matter  
 630 fraction:  $\Omega_m = 0.3153$ ; and the baryon fraction:  $\Omega_b = 0.04936$  [10]. Plank's observations also  
 631 provide a measure of the Hubble constant,  $H_0$ .  $H_0$  especially has seen a growing tension in the

632 past decade that continues to deepened with observations from instruments like the James Webb  
633 Telescope [12, 13]. As Hubble tensions deepen, we may find that perhaps  $\Lambda$ **CDM**, despite its  
634 successes, is missing some critical physics.

635 Overall, the Newtonian motion of stars in galaxies, weak lensing from galactic clusters, and  
636 power spectra from primordial light form a compelling body of research in favor of dark matter.  
637 It takes another leap of theory and experimentation to make observations of DM that are non-  
638 gravitational in nature. In Section 2.3, the evidence for DM implies strongly that the DM is matter  
639 and not a lost parameter in the gravitational fields between massive objects. Finally, if we take one  
640 axiom: that this matter has quantum behavior, such as being described by some Bohr wavelength  
641 and abiding by some fermion or boson statistics; then we arrive at particle dark matter. One particle  
642 DM hypothesis is the Weakly Interacting Massive Particle (WIMP). This DM candidate theory is  
643 discussed further in the next section and is the focus of this thesis.

644 **2.4 Searching for Dark Matter: Particle DM**

645 Section 2.4 shows the Standard Model of particle physics and is currently the most accurate  
646 model for the dynamics of fundamental particles like electrons and photons. The current status  
647 of the SM does not have a viable DM candidate. When looking at the standard model, we can  
648 immediately exclude any charged particle because charged particles interact strongly with light.  
649 Specifically, this will rule out the following charged, fundamental particles:  $e, \mu, \tau, W, u, d, s, c, t, b$   
650 and their corresponding antiparticles. Recalling from Section 2.2 that DM must be long-lived and  
651 stable over the age of the universe which excludes all SM particles with decay half-lives at or shorter  
652 than the age of the universe. The lifetime constraint additionally eliminates the  $Z$  and  $H$  bosons.  
653 Finally, the candidate DM needs to be somewhat massive. Recall from Section 2.2 that DM is cold  
654 or not relativistic through the universe. This eliminates the remaining SM particles:  $\nu_{e,\mu,\tau}, g, \gamma$  as  
655 DM candidates. Because there are no DM candidates within the SM, the DM problem strongly  
656 hints to physics beyond the SM (BSM).

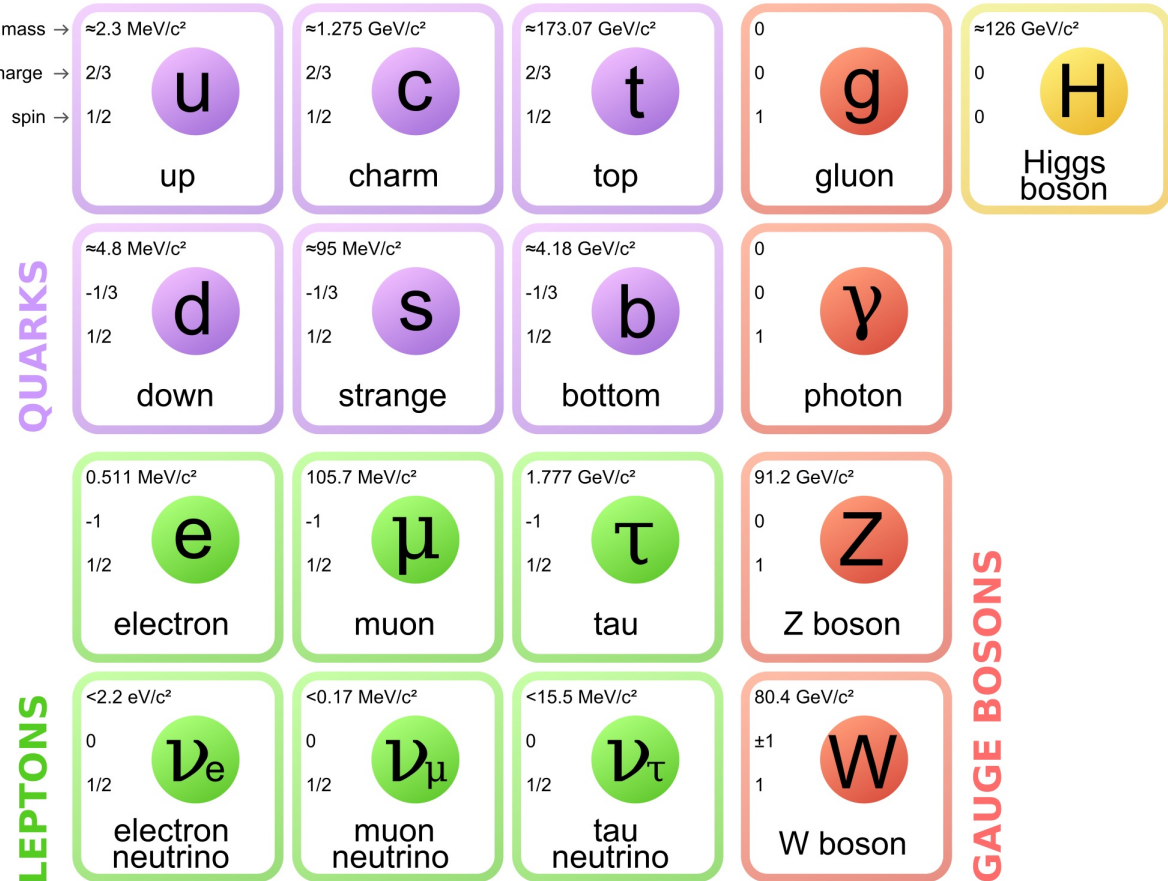


Figure 2.7 The Standard Model (SM) of particle physics. Figure taken from <http://www.quantumdiaries.org/2014/03/14/the-standard-model-a-beautiful-but-flawed-theory/>

### 657 2.4.1 Shake it, Break it, Make it

658 When considering DM that couples in some way with the SM, the interactions are roughly  
 659 demonstrated by interaction demonstrated in Figure 2.8. The figure is a simplified Feynman  
 660 diagram where the arrow of time represents the interaction modes of: **Shake it, Break it, Make it.**

661 **Shake it** refers to the direct detection of dark matter. Direct detection interactions start with  
 662 a free DM particle and an SM particle. The DM and SM interact via elastic or inelastic collision  
 663 and recoil away from each other. The DM remains in the dark sector and imparts some momentum  
 664 onto the SM particle. The hope is that the momentum imparted onto the SM particle is sufficiently  
 665 high enough to pick up with extremely sensitive instruments. Because we cannot create the DM in  
 666 the lab, a direct detection experiment must wait until DM is incident on the detector. Most direct  
 667 detection experiments are therefore placed in low-background environments with inert detection

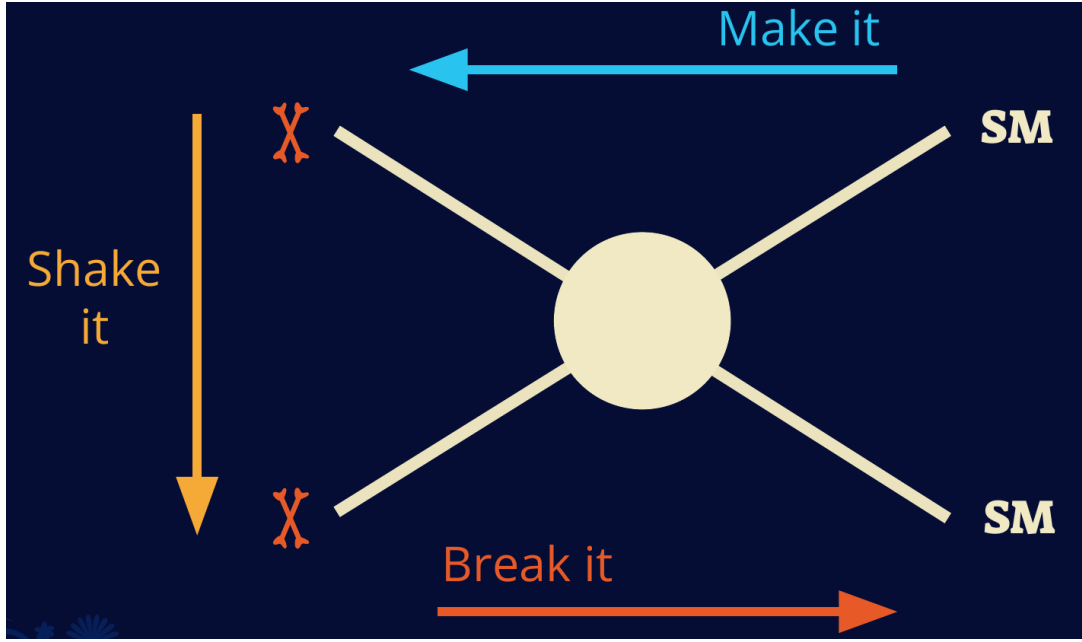


Figure 2.8 Simplified Feynman diagram demonstrating different ways DM can interact with SM particles. The 'X's refer to the DM particles whereas the SM refer to fundamental particles in the SM. The large circle in the center indicates the vertex of interaction and is purposely left vague. The colored arrows refer to different directions of time as well as their respective labels. The arrows indicate the initial and final state of the DM -SM interaction in time.

668 media like the noble gas Xenon. [14]

669 **Make it** refers to the production of DM from SM initial states. The experiment starts with  
 670 particles in the SM. These SM particles are accelerated to incredibly high energies and then collide  
 671 with each other. In the confluence of energy, DM hopefully emerges as a byproduct of the SM  
 672 annihilation. Often it is the collider experiments that are energetic enough to hypothetically produce  
 673 DM. These experiments include the world-wide collaborations ATLAS and CMS at CERN where  
 674 proton collide together at extreme energies. The DM searches, however, are complex. DM likely  
 675 does not interact with the detectors and lives long enough to escape the detection apparatus of  
 676 CERN's colliders. This means any DM production experiment searches for an excess of events  
 677 with missing momentum or energy in the events. An example event with missing transverse  
 678 momentum is shown in Figure 2.9. The missing momentum with no particle tracks implies a  
 679 neutral particle carried the energy out of the detector. However, there are other neutral particles  
 680 in the SM, like neutrons or neutrinos, so any analysis has to account for SM signatures of missing

681 momentum. [15]

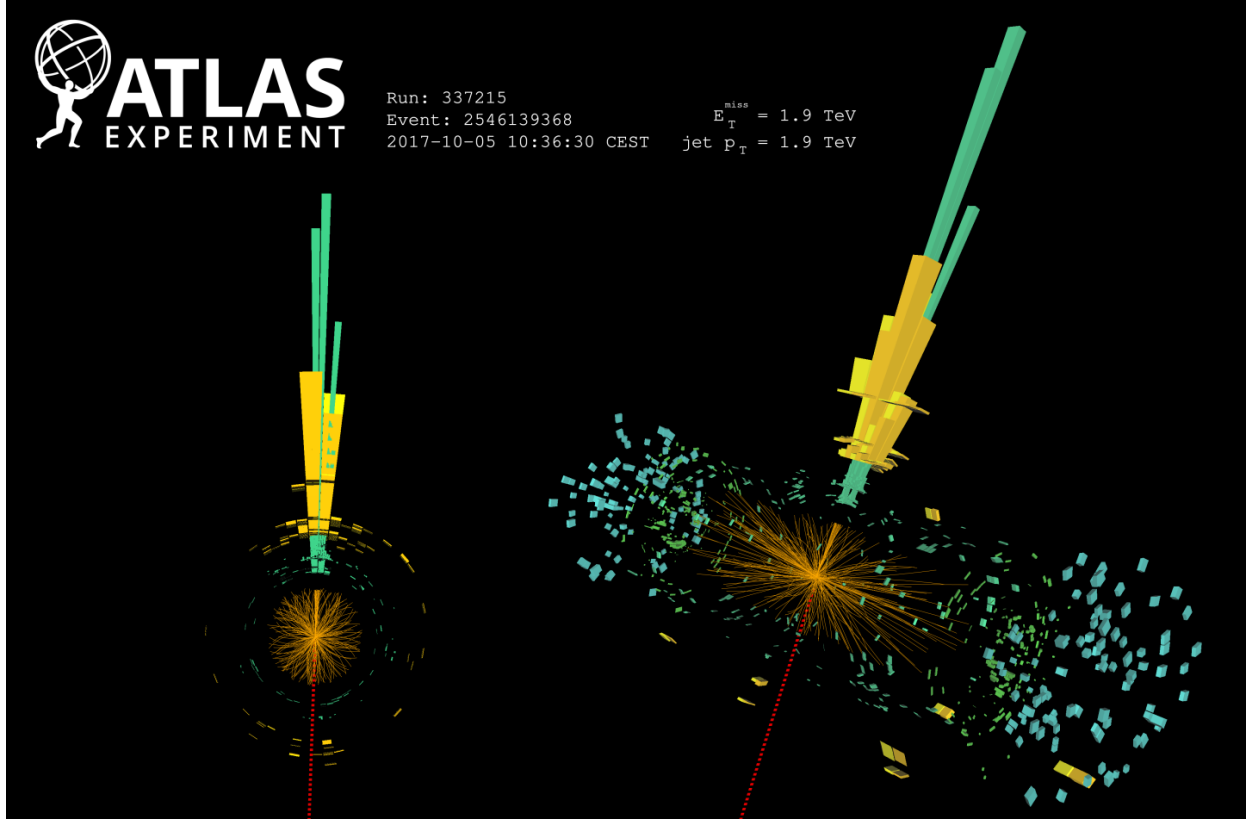


Figure 2.9 A single jet event in ATLAS detector from 2017 [16]. Jet momentum was observed to be 1.9 TeV. Missing transverse momentum was observed to be 1.9 TeV compared to the initial transverse momentum of the event was 0. Implied MET is traced by a red dashed line in event display.

#### 682 2.4.2 Break it: Standard Model Signatures of Dark Matter through Indirect Searches

683 **Break it** refers to the creation of SM particles from the dark sector, and it is the primary focus  
684 of this thesis. The interaction begins with DM or in the dark sector. The hypothesis is that this  
685 DM will either annihilate with itself or decay and produce an SM byproduct. This method is  
686 often referred to as the Indirect Detection of DM because we have no lab to directly control or  
687 manipulate the DM. Therefore, most indirect DM searches are performed using observations of  
688 known DM densities among the astrophysical sources. The strength is that we have the whole of the  
689 universe and its 13.6-billion-year lifespan to use as a detector and particle accelerator. Additionally,  
690 locations of dark matter are well cataloged since it was astrophysical observations that presented

691 the problem of DM in the first place.

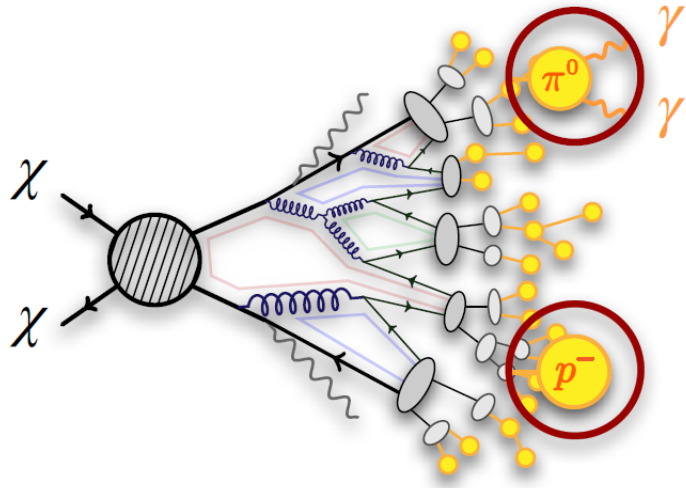


Figure 2.10 More detailed pseudo-Feynman diagram of particle cascade from dark matter annihilation into 2 quarks. The quarks hadronize and down to stable particles like  $\gamma$  or the anti-proton ( $p^-$ ). Diagram pulled from ICRC 2021 presentation on DM annihilation search [17].

692 However, anything can happen in the universe. There are many difficult to deconvolve back-  
693 grounds when searching for DM. One prominent example is the galactic center. We know the  
694 galactic center has a large DM content because of stellar kinematics in our Milky Way and DM halo  
695 simulations. Yet, any signal from the galactic center is challenging to parse apart from the extreme  
696 environment of our supermassive black hole, unresolved sources, and diffuse emission from the  
697 interstellar medium [18]. Despite the challenges, any DM model that yields evidence in the other  
698 two observation methods, **Shake it or Make it** must be corroborated with indirect observations of  
699 the known DM sources. Without corroborating evidence, DM observation in the lab is hard-pressed  
700 to demonstrate that it is the model contributing to the DM seen at the universal scale.

701 In the case of WIMP DM, signals are described in terms of primary SM particles produced  
702 from DM decay or annihilation. The SM initial state particles are then simulated down to stable  
703 final states such as the  $\gamma$ ,  $\nu$ ,  $p$ , or  $e$  which can traverse galactic lengths to reach Earth.

704 Figure 2.10 shows the quagmire of SM particles that emerges from SM initial states that are not  
705 stable [17]. There are many SM particles with varying energies that can be produced in such an

706 interaction. For any arbitrary DM source and stable SM particle, the SM flux from DM annihilating  
 707 to a neutral particle in the SM,  $\phi$ , from a region in the sky is described by the following.

$$\frac{d\Phi_\gamma}{dE_\gamma} = \frac{\langle\sigma v\rangle}{8\pi m_\chi^2} \frac{dN_\gamma}{dE_\gamma} \times \int_{\text{source}} d\Omega \int_{l.o.s} \rho_\chi^2 dl(r, \theta') \quad (2.4)$$

708 In Equation (5.1),  $\langle\sigma v\rangle$  is the velocity-weighted annihilation cross-section of DM to the SM.  $m_\chi$   
 709 refers to the mass of DM, noted with Greek letter  $\chi$ .  $\frac{dN_\phi}{dE_\phi}$  is the N particle flux weighted by the  
 710 particle energy. An example is provided in Figure 2.11 for the  $\gamma$  final state. The integrated terms  
 711 are performed over the solid angle,  $d\Omega$ , and line of sight, l.o.s.  $\rho$  is the density of DM for a  
 712 location  $(r, \theta')$  in the sky. The terms left of the '×' are often referred to as the particle physics  
 713 component. The terms on the right are referred to as the astrophysical component. For decaying  
 714 DM, the equation changes to...

$$\frac{d\Phi_\phi}{dE_\phi} = \frac{1}{4\pi\tau m_\chi} \frac{dN_\phi}{dE_\phi} \times \int_{\text{source}} d\Omega \int_{l.o.s} \rho_\chi dl(r, \theta') \quad (2.5)$$

715 In Equation (2.5),  $\tau$  is the decay lifetime of the DM. Just as in Equation (5.1), the left and right  
 716 terms are the particle physics and the astrophysical components respectively. The integrated  
 717 astrophysical component of Equation (5.1) is often called the J-Factor. Whereas the integrated  
 718 astrophysical component of Equation (2.5) is often called the D-Factor.

719     Exact DM  $\text{DM} \rightarrow \text{SM SM}$  branching ratios are not known, so it is usually assumed to go 100%  
 720 into an SM particle/anti-particle. Additionally, when a DM annihilation or decay produces one of  
 721 the neutral, long-lived SM particles ( $\nu$  or  $\gamma$ ), the particle is traced back to a DM source. For DM  
 722 above GeV energies, there are very few SM processes that can produce particles with such a high  
 723 energy. Seeing such a signal would almost certainly be an indication of the presence of dark matter.  
 724 Fortunately, the universe provides us with the largest volume and lifetime ever for a particle physics  
 725 experiment.

## 726 2.5 Sources for Indirect Dark Matter Searches

727     The first detection of DM relied on optical observations. Since then, we have developed new  
 728 techniques to find DM dense regions. As described in Section 2.3.1, many DM dense regions were  
 729 through observing galactic rotation curves. Our Milky Way galaxy is among DM dense regions

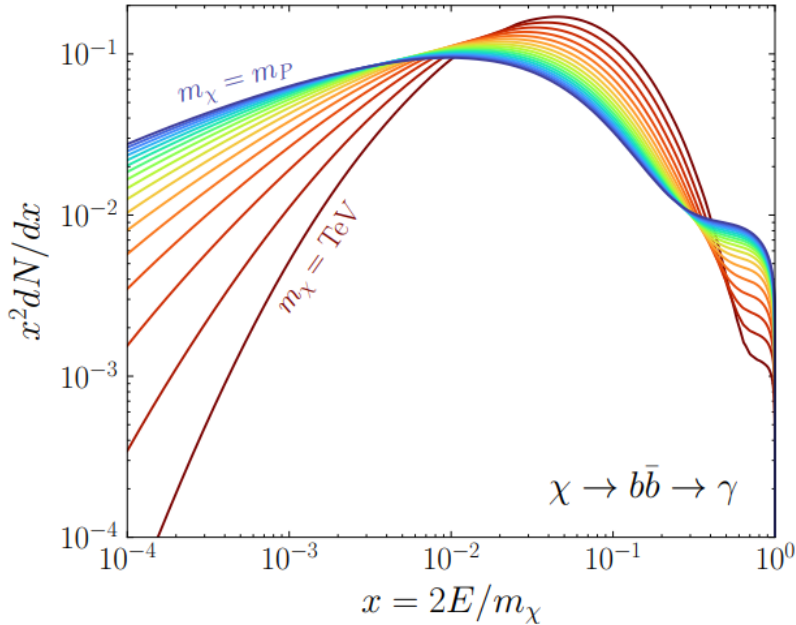


Figure 2.11 Dark Matter (DM) decay spectrum for  $b\bar{b}$  initial state and  $\gamma$  final state. Redder spectra are for larger DM masses. Bluer spectra are light DM masses.  $x$  is a unitless factor defined as the ratio of the mass of DM,  $m_\chi$ , and the final state particle energy  $E_\gamma$ . Figure from [19].

discovered, and it is the largest nearby DM dense region to look at. Additionally, the DM halo surrounding the Milky Way is clumpy [18]. There are regions in the DM halo of the Milky Way that have more DM than others that have captured gas over time. These sub-halos were dense enough to collapse gas and form stars. These apparent sub galaxies are known as dwarf spheroidal galaxies and are the main sources studied in this thesis. Each source type comes with different trade-offs. Galactic Center studies will be very sensitive to the assumed distribution of DM. The central DM density can vary substantially as demonstrated in Figure 2.12. At distances close to the center of the galaxy, or small  $r$ , the differences in DM densities can be 3-4 orders of magnitude. Searches toward the galactic center will therefore be quite sensitive to the assumed DM distribution.

Searches toward Dwarf Spheroidal Galaxies (dSph's) suffer from uncertainties in the DM density less than the galactic center studies. This is mostly from their diminutive size being smaller than the angular resolution of most  $\gamma$ -ray observatories [18]. The DM content dSph's are typically determined with the Virial theorem, Equation (2.1), and are usually majority DM [18] in mass. DSph's tend to be ideal sources to look at for DM searches. Their environments are quiet with little

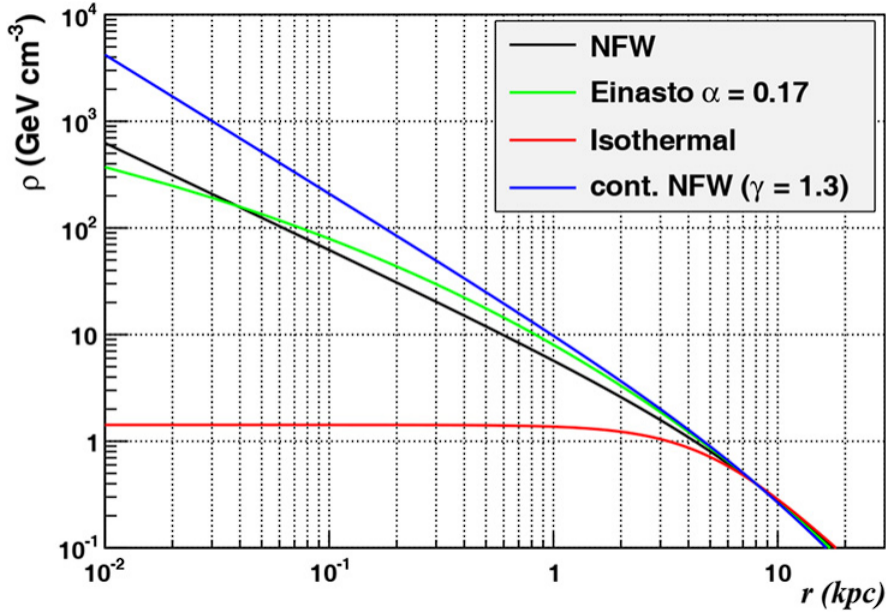


Figure 2.12 Different dark matter density profiles compared. Some models produce exceptionally large densities at small  $r$  [20].

744 astrophysical background. Unlike the galactic center, the most active components of dSph's are the  
 745 stars within them versus a violent accretion disc around a black hole. All this together means that  
 746 dSph's are among the best sources to look at for indirect DM searches. dSph's are the targets of  
 747 focus for this thesis.

## 748 2.6 Multi-Messenger Dark Matter

749 Astrophysics entered a new phase in the past few decades that leverages our increasing sensitivity  
 750 to SM channels and general relativity (GR). Up until the 21st century, astrophysical observations  
 751 were performed with photons ( $\gamma$ ) only. Astrophysics with this 'messenger' is fairly mature now.  
 752 Novel observations of the universe have since only adjusted the sensitivity of the wavelength of  
 753 light that is observed except at MeV energies. Gems like the CMB [10], and more have ultimately  
 754 been observations of different wavelengths of light. Multi-messenger astrophysics proposes using  
 755 other SM particles such the  $p^{+-}$ , or  $\nu$  or gravitation waves predicted by general relativity.

756 The experiment LIGO had a revolutionary discovery in 2016 with the first detection of a binary  
 757 black hole merger [21]. This opened the collective imagination to observing the universe through  
 758 gravitational waves. There has also been a surge of interest in the neutrino ( $\nu$ ) sector. IceCube

759 demonstrated that we are sensitive to neutrinos in regions that correlate with significant photon  
 760 emission like the galactic plane [22]. Neutrinos, like gravitational waves and light, travel mostly  
 761 unimpeded from their source to our observatories. This makes pointing to the originating source  
 762 of these messengers much easier than it is for cosmic rays which are deflected from their source by  
 763 magnetic fields.

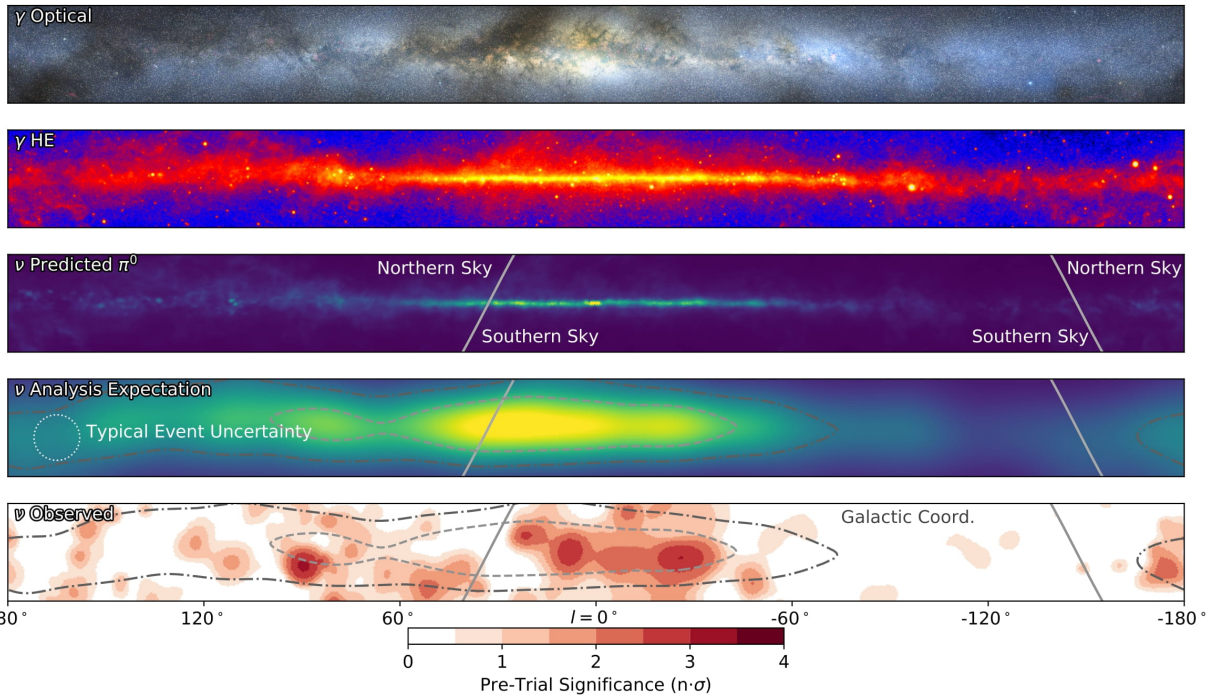


Figure 2.13 The Milky Way Galaxy in photons ( $\gamma$ ) and neutrinos ( $\nu$ ) [22]. The Galactic center is at  $l=0^\circ$  and is the brightest region in all panels. (top) An Optical color image of the Milky Way galaxy seen from Earth. Clouds of gas and dust obscure some light from stars. (2nd down) Integrated flux of  $\gamma$ -rays observed by the Fermi-LAT telescope [23]. (middle) Expected neutrino emission that corresponds with Fermi-LAT observations. (2nd up) Expected neutrino emission profile after considering detector systematics of IceCube. (bottom) Observed neutrino emission from region of the galactic plane. Substantial neutrino emission was detected.

764 The IceCube collaboration recently published a groundbreaking result of the Milky Way in  
 765 neutrinos. The recent result from IceCube, shown in Figure 2.13, proves that we can make  
 766 observations under different messenger regimes. The top two panels show the appearance of the  
 767 galactic plane to different wavelengths of light. Some sources are more apparent in some panels,  
 768 while others are not. This new channel is powerful because neutrinos are readily able to penetrate  
 769 through gas and dust in the Milky Way. This new image also refines our understanding of how high

770 energy particles are produced. For example, the fit to IceCube data prefers neutrino production  
 771 from the decay of  $\pi^0$  [22].

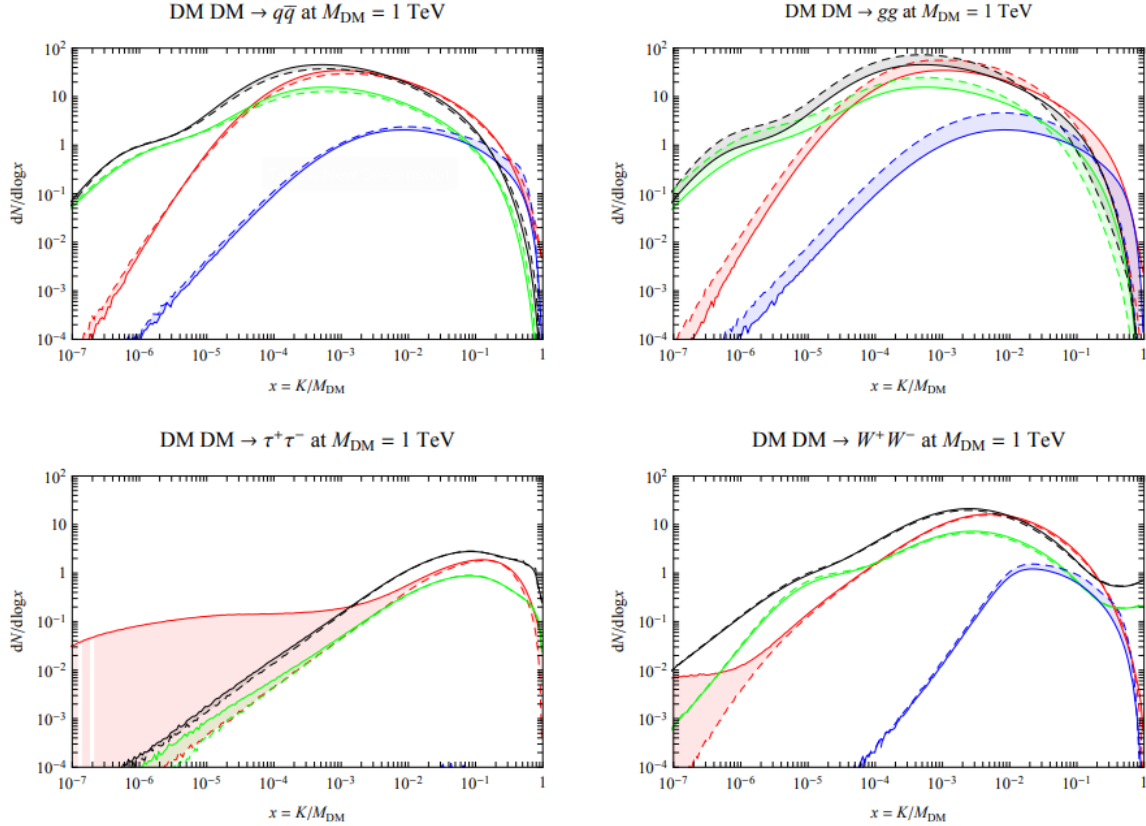


Figure 2.14 Dark Matter annihilation spectra for different final state particle and standard model annihilation channels [24]. Photons (red),  $e^\pm$  (green),  $\bar{p}$  (blue),  $\nu$  (black).

772 Exposing our observations to more cosmic messengers greatly increases our sensitivity to  
 773 rare processes. In the case of DM, Figure 2.14, there are many SM particles produced in DM  
 774 annihilation. Among the final state fluxes are gammas and neutrinos. Charged particles are also  
 775 produced however they would not likely make it to Earth since they will be deflected by magnetic  
 776 fields between the source and Earth. This means observatories that can see the neutral messengers  
 777 are especially good for DM searches and for combining data for a multi-messenger DM search.

## CHAPTER 3

778

### HIGH ALTITUDE WATER CHERENKOV (HAWC) OBSERVATORY

779 **3.1 The Detector**



Figure 3.1 Photo of the HAWC detector that I took on May 17, 2023. Main array is centered in the photo and comprised of the larger tanks. Outriggers are the smaller tanks around the main array.

780 The High Altitude Water Cherenkov (HAWC) Observatory is a specialized instrument designed  
781 for the observation of high energy gamma-rays and cosmic rays [25]. Located on the Sierra  
782 Negra volcano in Mexico, HAWC observes gamma rays and cosmic rays in the energy range of  
783 approximately 100 GeV to 100's of TeV. HAWC is strategically situated to maximize observational  
784 efficiency due to its high altitude. At an elevation of 4,100 meters, it monitors about two-thirds of  
785 the sky every day with an uptime above 90%. This capability is essential for studying high-energy  
786 astronomical phenomena.

787 HAWC comprises of 300 water Cherenkov detectors (WCDs) spread over 22,000 square meters.  
788 Each main array detector is filled with purified water and equipped with four, upward-facing  
789 photomultiplier tubes (PMTs). These PMTs detect Cherenkov radiation from charged particles  
790 passing through the tanks. These charged particles are generated when a high energy gamma or

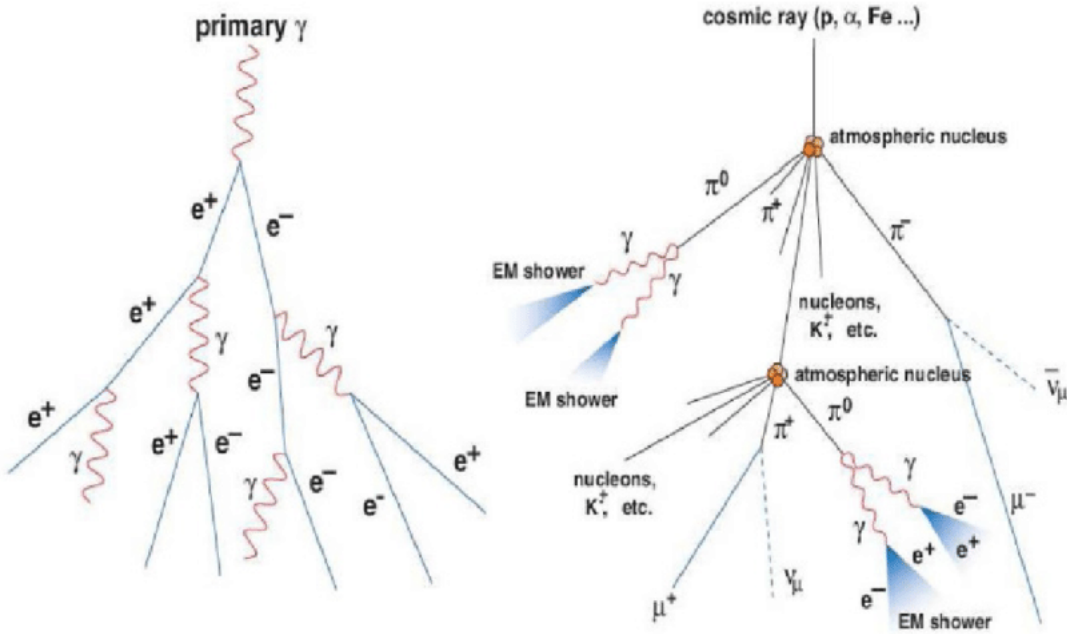


Figure 3.2 A particle physics illustration of high energy particle showers. Left shower is an electromagnetic shower from a high energy gamma-ray. Most particles in the shower will be a combination of photons and charged leptons, in this case electrons ( $e$ ). Right figure shows a cosmic ray particle shower. The cosmic ray will produce many more types of particles including pions ( $\pi$ ), neutrinos, and charged leptons. Figured pulled from [26].

791 cosmic ray collides with gas in the atmosphere to create a charged particle shower, see Fig. 3.2.  
 792 The observatory includes a separate tank configuration which are referred to as the outriggers. They  
 793 are a secondary array of 345 smaller WCD's. Surrounding the main array, each outrigger tank  
 794 measures 1.55 meters in diameter and height and contain a single upward-facing eight-inch PMT.  
 795 This expansion increases the instrumented footprint fourfold. It improves the reconstruction of  
 796 showers extending beyond the main array, especially for events above 10 TeV. However, at the time  
 797 of writing this thesis, the outriggers have not been fully integrated into HAWC's reconstruction  
 798 software.

### 799 3.2 Construction and Hardware

800 **TODO: fact check the content below. GPT may have hallucinated** Each main array WCD is a  
 801 cylindrical tank with dimensions of 7.3 m in diameter and 5 m in height [25]. The metal shell  
 802 of these tanks is made from bolted together, corrugated, galvanized steel panels. This assembly

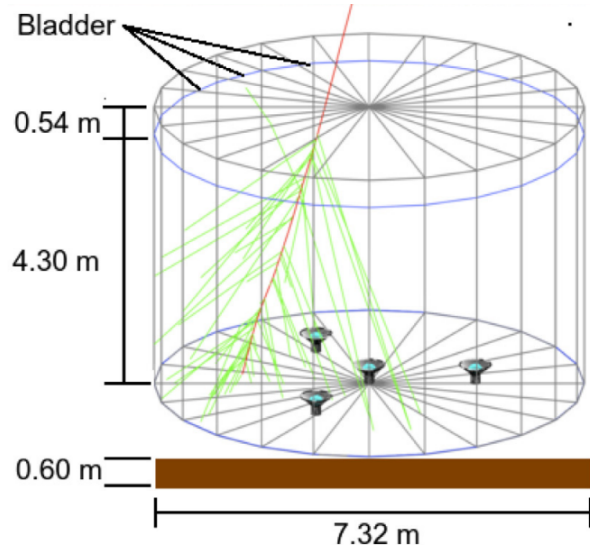


Figure 3.3 The WCDs. Left image features several WCDs looking from within the main array of HAWC. Right image shows a schematic of a WCD pulled from [25].

803 process involves constructing the top ring of panels at ground level, subsequently raising it to add  
 804 additional rings below until the structure is complete. The finished tank is placed into a 0.6 m deep  
 805 trench filled with rammed earth to secure it against seismic activity. The interior of each tank is  
 806 lined with a black, low-density polyethylene bladder, designed to be impermeable to external light  
 807 and to prevent reflection of Cherenkov light within the tank. This bladder is approximately 0.4  
 808 mm thick, composed of two layers of three-substrate film bonded during a co-extrusion process.  
 809 To further minimize light penetration, a black agricultural foil covers the bladder, and the ground  
 810 and walls inside the tank are protected with geo-textile felt and a layer of sand to safeguard against  
 811 punctures. The tanks are filled 4.5 m deep of purified water, achieving a photon attenuation length  
 812 for Cherenkov photons that exceeds the tank's dimensions. This purification level ensures the  
 813 optimal detection environment for the photons generated by traversing charged particles.

814 **3.3 Events Reconstruction and Data Acquisition**

815 **3.3.1 G/H Discrimination**

816 **3.3.2 Angle**

817 **3.3.3 Energy**

818 **3.4 Remote Monitoring**

819 **3.4.1 ATHENA Database**

820 **3.4.2 HOMER**

821

## CHAPTER 4

### ICECUBE NEUTRINO OBSERVATORY

822 **4.1 The Detector**

823 **4.2 Events Reconstruction and Data Acquisition**

824 **4.2.1 Angle**

825 **4.2.2 Energy**

826 **4.3 Northern Test Site**

827 **4.3.1 PIgeon remote dark rate testing**

828 **4.3.2 Bulkhead Construction**

## CHAPTER 5

### 829      **GLORY DUCK: MULTI-WAVELENGTH SEARCH FOR DARK MATTTER** 830      **ANNIHILATION TOWARDS DWARF SPHEROIDAL GALAXIES**

#### 831    **5.1 Introduction**

832       The field of astrophysics now has several instruments and observatories sensitive to high energy  
833       gamma-rays. The energy sensitivity for the modern gamma-ray program spans many orders of  
834       magnitude. Figure 5.1 demonstrates these comparable sensitivities across energies for the five  
835       experiments: Fermi-LAT, HAWC, HESS, MAGIC, and VERITAS.

836       Each of the five experiments featured in Figure 5.1 have independently searched for DM  
837       annihilation from dwarf spheroidal galaxies (dSph) and set limits on annihilation cross-section of  
838       WIMPs. Intriguingly, there are regions of substantial overlap in their energy sensitivities. This  
839       clearly motivates an analysis that combines data from these five. Each experiment has unique  
840       gamma-ray detection methods and their weaknesses and strengths can be leveraged with each other.  
841       The HAWC gamma-ray observatory is extensively introduced in chapter 3, so it is not introduced  
842       here. A brief description of the remaining experiments are in the following paragraphs.

843       The Large Area Telescope (LAT) is a pair conversion telescope mounted on the NASA Fermi  
844       satellite in orbit  $\sim$ 550 km above the Earth [28]. LAT's field of view covers about 20% of the  
845       whole sky, and it sweeps the whole sky approximately every 3 hours. LAT's gamma-ray energy  
846       sensitivity ranges from 20 MeV up to 1 TeV. Previous DM searches towards dSphs using Fermi-LAT  
847       are published in [29] and [30].

848       The High Energy Spectroscopic System (HESS), Major Atmospheric Gamma Imaging  
849       Cherenkov (MAGIC), and Very Energetic Radiation Imaging Telescope Array System (VERI-  
850       TAS) are arrays of Imaging Atmospheric Cherenkov Telescopes (IACT). These telescopes observe  
851       the Cherenkov light emitted from gamma-ray showers in the Earth's atmosphere. The field of  
852       view for these telescopes is no larger than  $5^\circ$  with energy sensitivities ranging from 30 GeV up  
853       to 100 TeV [31, 32, 33]. IACTs are able to make precise observations in selected regions of the  
854       sky, however can only be operated in ideal dark conditions. HESS's observations of the dwarves

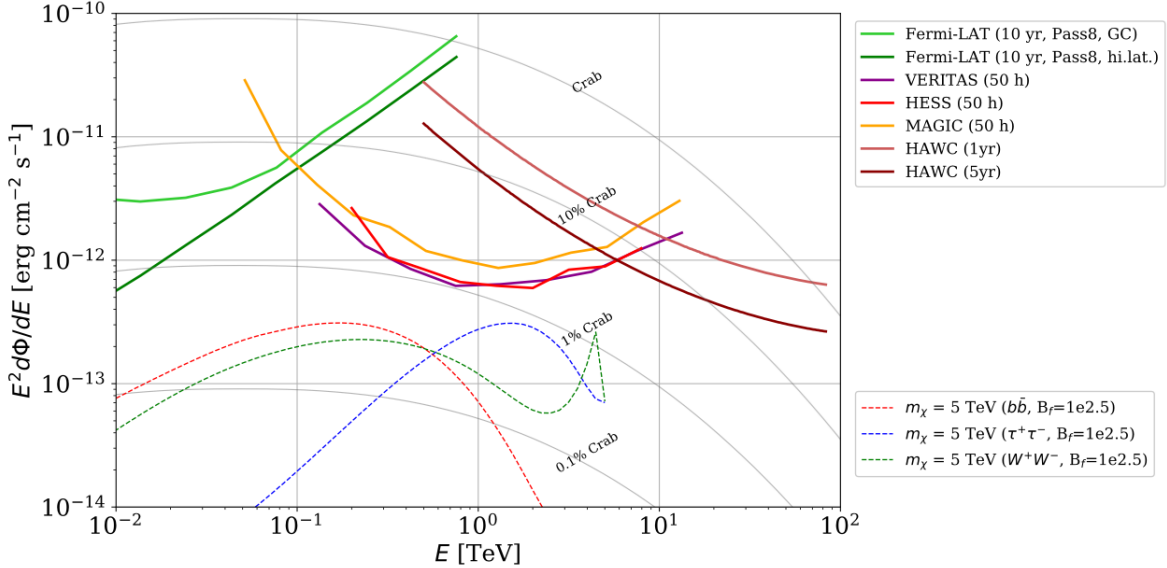


Figure 5.1 Sensitivities of five gamma-ray experiments compared to percentages of the Crab nebula’s emission and dark matter annihilation. Solid lines present estimated sensitivities to power law spectra [FACT CHECK THIS] for each experiment. Green lines are Fermi-LAT sensitivities where lighter green is the sensitivity to the galactic center and dark green is its sensitivity to higher declinations. Orange, red, and purple solid lines represent the MAGIC, HESS, and VERITAS 50 hour sensitivities respectively. The maroon and brown lines are the HAWC 1 year and 5 year sensitivities. Across four decades of gamma-ray energy, these experiments have similar sensitivities on the order  $10^{-12}$  erg  $\text{cm}^{-2}\text{s}^{-1}$ . The dotted lines are estimated dark matter fluxes assuming  $m_\chi = 5$  TeV DM annihilating to bottom quarks (red), tau leptons (blue), and W bosons (green). Faded gray lines outline percentage flux of the Crab nebula. Figure is an augmented version of [27]

855 Sculptor and Carina were between January 2008 and December 2009. HESS’s observations of  
 856 Coma Berenices were taken from 2010 to 2013, and Fornax was observed in 2010 [34, 35, 36].  
 857 MAGIC provided deep observations of Segue1 between 2011 and 2013 [37]. MAGIC also provides  
 858 data for three additional dwarves: Coma Berenices, Draco, and Ursa Major II where observations  
 859 were made in: January - June 2019 [38], March - September 2018 [38], and 2014 - 2016 [39]  
 860 respectively. VERITAS provided data for Boötes I, Draco, Segue 1, and Ursa Minor from 2009 to  
 861 2016 [40].

862 This chapter presents the Glory Duck analysis, the name given for the search for dark matter  
 863 annihilation from dSph by combining data from the five gamma-ray observatories: Fermi-LAT,  
 864 HAWC, HESS, MAGIC, and VERITAS. Specifically, the methods in analysis and modeling are  
 865 presented for the HAWC gamma-ray observatory. This work will be published in the Journal of

866 Cosmology and Astroparticle Physics and presented at the International Cosmic Ray Conference  
867 in 2019, 2021, and 2023 [41, 42, 43] and others.

868 **5.2 Dataset and Background**

869 This section enumerates the data analysis and background estimation methods used for HAWC's  
870 study of dSphs. Section 5.2.1 and Section 5.2.2 are most useful for fellow HAWC collaborators  
871 looking to replicate the Glory Duck analysis.

872 **5.2.1 Itemized HAWC files**

873 These files are only available withing HAWC's internal documentation and collaborators. They  
874 are not meant for public access, and are presented here so that HAWC collaborators can reproduce  
875 results accurately.

- 876 • Detector Response: `response_aerie_svn_27754_systematics_best_mc_test_noBr`  
877     `oadpulse\10pctlogchargesmearing_0.63qe_25kHzNoise_run5481_curvature`  
878     `0_index3.root`
- 879 • Data Map: `maps-20180119/liff/maptree_1024.root`
- 880 • Spectral Dictionary: `DM_CirrelliSpectrum_dict_gammas.npy`
- 881 • Analysis wiki: [https://private.hawc-observatory.org/wiki/index.php/Glory\\_Duck\\_Multi-Experiment\\_Dark\\_Matter\\_Search](https://private.hawc-observatory.org/wiki/index.php/Glory_Duck_Multi-Experiment_Dark_Matter_Search)

883 **5.2.2 Software Tools and Development**

884 This analysis was performed using HAL and 3ML [44, 45] in Python version 2. I built software  
885 to implement the *A Poor Particle Physicist Cookbook for Dark Matter Indirect Detection* (PPPC)  
886 [46] DM spectral model and dSphs spatial model from [47] for HAWC analysis. A NumPy version  
887 of this dictionary was made for both Py2 and Py3. The code base for creating this dictionary is  
888 linked on my GitLab sandbox:

- 889 • Py2: [Dictionary Generator \(Deprecated\)](#)

- 890     • Py3: [PPPC2Dict](#)

891     The analysis was performed using the  $f_{hit}$  framework as used and described in the HAWC Crab  
892 paper [44]. The Python2 NumPy dictionary file for gamma-ray final states is `dmCirSpecDict.npy`.  
893 The corresponding Python3 file is `DM_CirrelliSpectrum_dict_gammas.npy`. These files can  
894 also be used for decay channels and the PPPC describes how [46]. All other software used for data  
895 analysis, DM profile generation, and job submission to SLURM are also kept in my sandbox for  
896 [the Glory Duck](#) project.

897 **5.2.3 Data Set and Background Description**

898     The HAWC data maps used for this analysis contain 1017 days of data between runs 2104  
899 (2014-11-26) and 7476 (2017-12-20). They were generated from pass 4.0 reconstruction. The  
900 analysis is performed using the  $f_{hit}$  energy binning scheme with bins (1-9) similar to what was done  
901 for the Crab and previous HAWC dSph analysis [44, 48]. Bin 0 was excluded as it has substantial  
902 hadronic contamination and poor angular resolution.

903     This analysis was done on dSphs because of their large DM mass content relative to baryonic  
904 mass. We consider the following to estimate the background to this study.

- 905     • The dSphs' angular extent are small relative to HAWC's spatial resolution, so the analysis is  
906 not sensitive to large or small scale anisotropies.
- 907     • The dSphs used in this analysis are off the galactic plane and therefore not contaminated by  
908 diffuse emission from the galaxy.
- 909     • The dSphs are baryonically faint relative to their expected dark matter content and are not  
910 expected to contain high energy gamma-ray sources.

911     Therefor we make no additional assumptions on the background from our sources and use  
912 HAWC's standard direct integration method for background estimation [44]. The largest background  
913 under this consideration is from an isotropic flux of cosmic rays. The contamination of this hadronic  
914 flux is worse at lower energies where HAWC's gamma/hadron discrimination worse. It is possible

915 for gamma rays from DM annihilation to scatter in transit to HAWC via Inverse Compton Scattering  
 916 (ICS). This was investigated and its impact on the flux is negligible. Supporting information on  
 917 this is in Section 5.7.1

918 **5.3 Analysis**

919 The expected differential photon flux from DM-DM annihilation to standard model particles,  
 920  $d\Phi_\gamma/dE_\gamma$ , over solid angle,  $\Omega$ , is described by the familiar equation.

$$\frac{d\Phi_\gamma}{dE_\gamma} = \frac{\langle\sigma v\rangle}{8\pi m_\chi^2} \frac{dN_\gamma}{dE_\gamma} \times \int_{\text{source}} d\Omega \int_{l.o.s} dl \rho_\chi^2 J(r, \theta') \quad (5.1)$$

921 Where  $\langle\sigma v\rangle$  is the velocity weighted annihilation cross-section.  $\frac{dN}{dE}$  is the expected differential  
 922 number of photons produced at each energy per annihilation.  $m_\chi$  is the rest mass of the supposed  
 923 DM particle.  $\rho_\chi$  is the DM density.  $J$  is the astrophysical J-factor and is defined as

$$J = \int d\Omega \int_{l.o.s} dl \rho_\chi^2(r, \theta') \quad (5.2)$$

924  $l$  is the distance to the source from Earth.  $r$  is the radial distance from the center of the source.  $\theta'$  is  
 925 the half angle defining a cone containing the DM source. How each component is synthesized and  
 926 considered for HAWC's analysis is presented in the following sections. Section 5.3.1 presents the  
 927 particle physics model for DM annihilation. Section 5.3.2 presents the spatial distributions built  
 928 for each dSph.

929 **5.3.1  $\frac{dN_\gamma}{dE_\gamma}$  - Particle Physics Component**

930 For these spectra, we import the PPPC with Electroweak (EW) corrections [46]. Public versions  
 931 of the imported tables are provided by the [authors online](#). The spectrum is implemented as a model  
 932 script in astromodels for 3ML. The EW corrections were previously not considered for HAWC and  
 933 are significant for DM annihilating to EW coupled SM particles such as all leptons, and the  $\gamma$ ,  
 934  $Z$ , and  $W$  bosons [48]. Figure 5.2 demonstrates the significance of EW corrections for W boson  
 935 annihilation. Across EW SM channels, the gamma-ray spectra become harder than spectra without  
 936 EW corrections. Tables from the PPPC were reformatted into Python NumPy dictionaries for  
 937 collaboration-wide use. A class in astromodels was developed to include the EW correction from  
 938 the PPPC and is aptly named `PPPCSpectra` within `DM_models.py`.

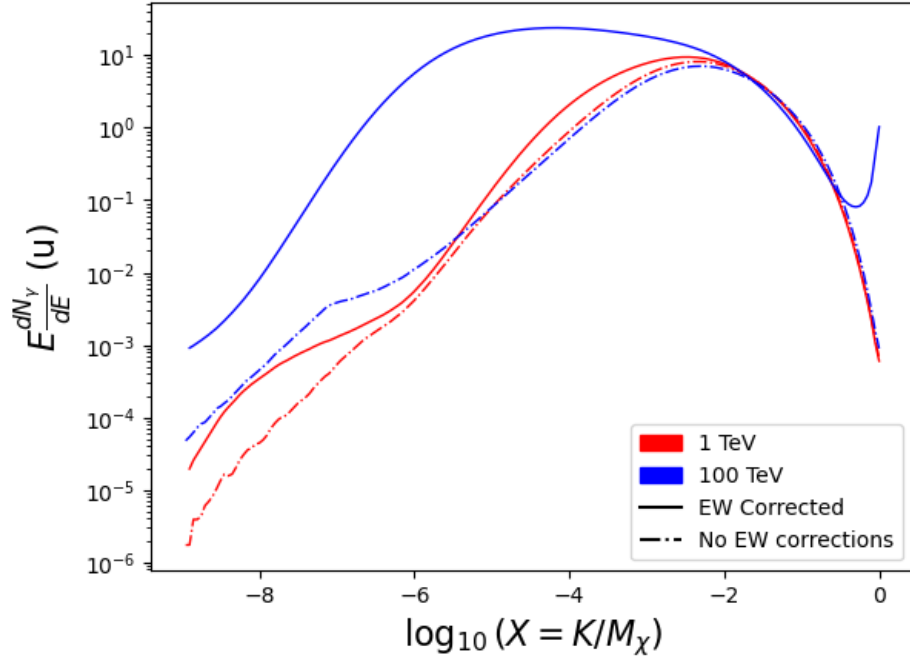


Figure 5.2 Effect of Electroweak (EW) corrections on expected DM annihilation spectrum for  $\chi\chi \rightarrow W^-W^+$ . Solid lines are spectral models that consider EW corrections. Dash-dot lines are spectral models without EW corrections. Red lines are models for  $M_\chi = 1$  TeV. Blue lines represent models for  $M_\chi = 100$  TeV. All models are sourced from the PPPC4DMID [46].

### 939 5.3.2 J- Astrophysical Component

940 The J-factor profiles for each source are imported from Geringer-Sameth (referred to with  $\mathcal{GS}$ )  
 941 [47].  $\mathcal{GS}$  fits the Zhao DM profile to the dSphs which has a DM density described as [49]

$$\rho(r) = \frac{\rho_0}{(r/R_s)^\gamma (1 + (r/R_s)^\alpha)^{(\beta-\gamma)}}. \quad (5.3)$$

942  $R_s$  is the scale radius and free parameter in the model.  $\gamma$  is the logarithmic slope in the region  
 943  $r \ll R_s$ .  $\beta$  is the logarithmic slope in the region  $r \gg R_s$ .  $\alpha$  is known as the sharpness of transition  
 944 where  $r \approx R_s$ . The classic Navarro-Frenk-White [50] (NFW) can be retrieved from Zhao by fixing  
 945  $(\alpha, \beta, \gamma) = (1, 3, 1)$ .

946  $\mathcal{GS}$  best fits were pulled from the publication as  $J(\theta)$ , where  $\theta$  is the angular separation from  
 947 the center of the source. HAWC requires maps in terms of  $\frac{dJ}{d\Omega}$ , so the conversion from the maps  
 948 was done in the following way...

949 First, convert the angular distances to solid angles

$$\Omega = 2 \cdot \pi(1 - \cos(\theta)) \quad (5.4)$$

950 which reduces with a small angle approximation to  $\pi\theta^2$ . Next, the central difference for both the  
951  $\Delta J$  and  $\Delta\Omega$  value were calculated from the discretized  $J(\theta)$  with the central difference stencil:

$$\Delta\phi_i = \phi_{i+1} - \phi_{i-1} \quad (5.5)$$

952 Where  $\phi$  is either  $\Omega$  or  $J$ . These were done separately in case the grid spacing in  $\theta$  was not uniform.  
953 Finally, these lists are divided so that we are left with an approximation of the  $dJ/d\Omega$  profile that  
954 is a function of  $\theta$ . Admittedly, this is an approximation method for the map which introduces small  
955 errors compared to the true profile estimate. This was checked as a systematic against the author's  
956 profiling of the spatial distribution and is documented in Section 5.8.1.

957 With  $\frac{dJ}{d\Omega}(\theta)$ , a map is generated, first by filling in the north-east quadrant of the map. This  
958 quadrant is then reflected twice, vertically then horizontally, to fill the full map. Maps are then  
959 normalized by dividing the discrete 2D integral of the map. The 2D integral was a simple height  
960 of bins, Newton's integral:

$$p^2 \cdot \sum_{i,j=0}^{N,M} \frac{dJ}{d\Omega}(\theta_{i,j}, \phi_{i,j}) \quad (5.6)$$

961 These maps are HEALpix maps with NSIDE 16384 and saved in the .fits format. The hyper fine  
962 resolution was selected to better preserve the total expected counts after integrating Eq. (5.1) with  
963 the detector response.

964 Another DM spatial distribution model from Bonnivard ( $\mathcal{B}$ ) [51] was used for the Glory Duck  
965 study. However, to save computational time, limits from  $\mathcal{GS}$  were scaled to  $\mathcal{B}$  instead of each  
966 experiment performing a full study a second time. How these models compare is demonstrated  
967 for each dSph in Figure 5.16 and Figure 5.17 Plots of these maps are provided for each source  
968 in chapter A Examples of the two most impactful dSphs derived from  $\mathcal{GS}$ , Segue1 and Coma  
969 Berenices are featured in Figure 5.3

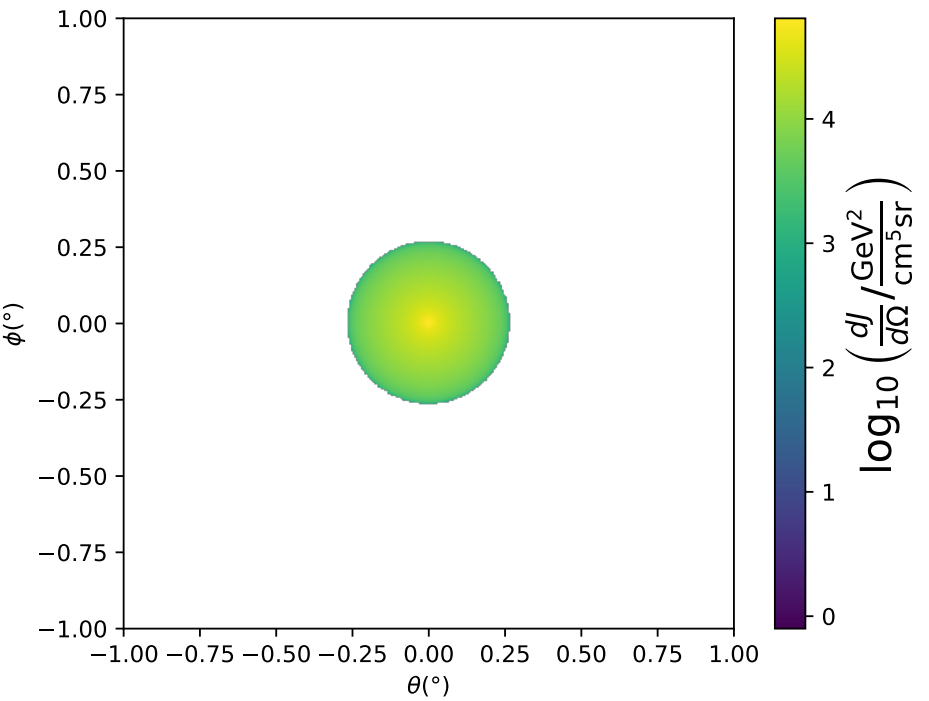
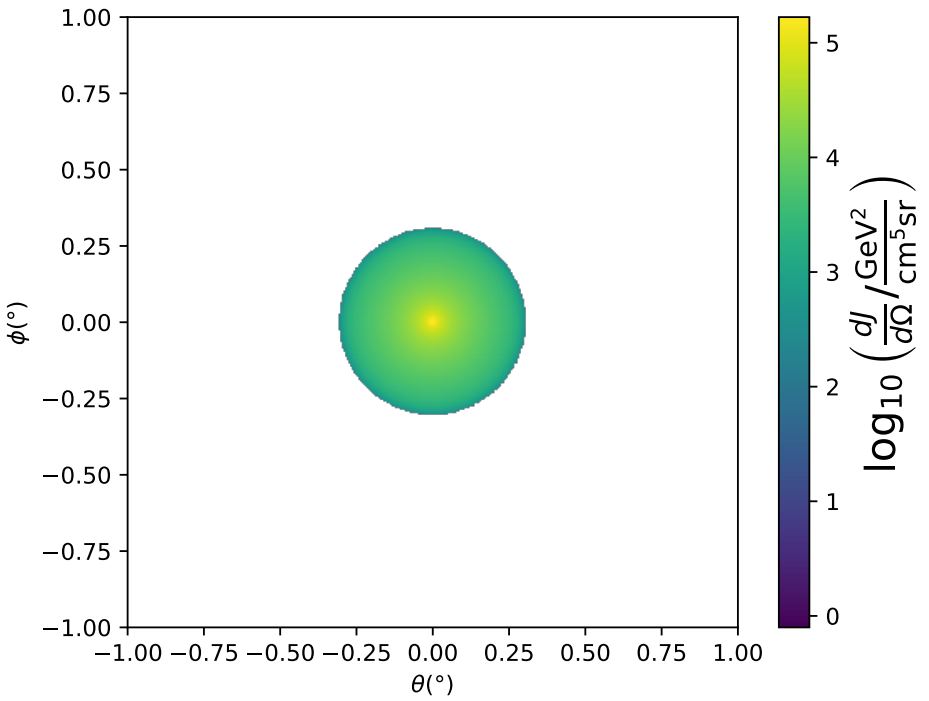


Figure 5.3  $\frac{dJ}{d\Omega}$  maps for Segue1 (top) and Coma Berenices (bottom). Origin is centered on the specific dwarf spheroidal galaxies (dSph). X and Y axes are the angular separation from the center of the dwarf. Profile is truncated at the scale radius. Plots of the remaining 11 dSph HAWC studied are linked in Fig. A.1.

970 **5.3.3 Source Selection and Annihilation Channels**

971 We use many of the dSphs presented in HAWC’s previous dSph DM search [48]. HAWC’s  
972 sources for Glory Duck include Boötes I, Coma Berenices, Canes Venatici I + II, Draco, Hercules,  
973 Leo I, II, + IV, Segue 1, Sextans, and Ursa Major I + II. A full description of all sources used  
974 in Glory Duck is found in Table 5.1. Triangulum II was excluded from the Glory Duck analysis  
975 because of large uncertainties in its  $J$  factor. Ursa Minor was excluded from HAWC’s contribution  
976 to the combination because the source extension model extended Ursa Minor beyond HAWC’s field  
977 of view. Ursa Minor was not expected to contribute significantly to the combined limit, so work  
978 was not invested in a solution to include Ursa Minor.

979 This analysis improves on the previous HAWC dSph paper [48] in the following ways. Pre-  
980 viously, the dSphs were treated and implemented as point sources. For this analysis, dSphs are  
981 modeled and treated as extended source. The impact of this change with respect to the upper limit  
982 is source dependent and is explored in Section 5.7.2. Previously, the particle physics model used for  
983 gamma-ray spectra from DM annihilation did not have EW corrections where the PPPC includes  
984 them. Finally, the gamma-ray ray dataset is much larger. The study performed here analyzes over  
985 1000 days of data compared to 507.

986 The SM annihilation channels probed for the Glory Duck combination include  $b\bar{b}$ ,  $e\bar{e}$ ,  $\mu\bar{\mu}$ ,  $\tau\bar{\tau}$ ,  
987  $t\bar{t}$ ,  $W^+W^-$ , and  $ZZ$ . A summary of all sources, with a description of each experiments’ sensitivity  
988 to the source, is provided in Table 5.2.

989 **5.4 Likelihood Methods**

990 **5.4.1 HAWC Likelihood**

991 For every analysis bin in energy,  $f_{hit}$  bins (1-9), and location, we can expect  $N$  signal events and  
992  $B$  background events. The expected number of excess signal events from dark matter annihilation,  
993  $S$ , is estimated by convolving Equation (5.1) with HAWC’s energy response and pixel point spread  
994 functions. I then compute the test statistic (TS) with the log-likelihood ratio test,

$$TS_{\max} = -2 \ln \left( \frac{\mathcal{L}_0}{\mathcal{L}^{\max}} \right) \quad (5.7)$$

Table 5.1 Summary of the relevant properties of the dSphs used in the present work. Column 1 lists the dSphs. Columns 2 and 3 present their heliocentric distance and galactic coordinates, respectively. Columns 4 and 5 report the  $J$ -factors of each source given from the  $\mathcal{GS}$  and  $\mathcal{B}$  independent studies and their estimated  $\pm 1\sigma$  uncertainties. The values  $\log_{10} J$  ( $\mathcal{GS}$  set) [47] correspond to the mean  $J$ -factor values for a source extension truncated at the outermost observed star. The values  $\log_{10} J$  ( $\mathcal{B}$  set) [51] are provided for a source extension at the tidal radius of each dSph. **Bolded sources are within HAWC's field of view and provided to the Glory Duck analysis.**

Name	Distance (kpc)	$l, b$ ( $^{\circ}$ )	$\log_{10} J$ ( $\mathcal{GS}$ set) $\log_{10}(\text{GeV}^2\text{cm}^{-5}\text{sr})$	$\log_{10} J$ ( $\mathcal{B}$ set) $\log_{10}(\text{GeV}^2\text{cm}^{-5}\text{sr})$
<b>Boötes I</b>	66	358.08, 69.62	$18.24^{+0.40}_{-0.37}$	$18.85^{+1.10}_{-0.61}$
<b>Canes Venatici I</b>	218	74.31, 79.82	$17.44^{+0.37}_{-0.28}$	$17.63^{+0.50}_{-0.20}$
<b>Canes Venatici II</b>	160	113.58, 82.70	$17.65^{+0.45}_{-0.43}$	$18.67^{+1.54}_{-0.97}$
Carina	105	260.11, -22.22	$17.92^{+0.19}_{-0.11}$	$18.02^{+0.36}_{-0.15}$
<b>Coma Berenices</b>	44	241.89, 83.61	$19.02^{+0.37}_{-0.41}$	$20.13^{+1.56}_{-1.08}$
<b>Draco</b>	76	86.37, 34.72	$19.05^{+0.22}_{-0.21}$	$19.42^{+0.92}_{-0.47}$
Fornax	147	237.10, -65.65	$17.84^{+0.11}_{-0.06}$	$17.85^{+0.11}_{-0.08}$
<b>Hercules</b>	132	28.73, 36.87	$16.86^{+0.74}_{-0.68}$	$17.70^{+1.08}_{-0.73}$
<b>Leo I</b>	254	225.99, 49.11	$17.84^{+0.20}_{-0.16}$	$17.93^{+0.65}_{-0.25}$
<b>Leo II</b>	233	220.17, 67.23	$17.97^{+0.20}_{-0.18}$	$18.11^{+0.71}_{-0.25}$
<b>Leo IV</b>	154	265.44, 56.51	$16.32^{+1.06}_{-1.70}$	$16.36^{+1.44}_{-1.65}$
Leo V	178	261.86, 58.54	$16.37^{+0.94}_{-0.87}$	$16.30^{+1.33}_{-1.16}$
Leo T	417	214.85, 43.66	$17.11^{+0.44}_{-0.39}$	$17.67^{+1.01}_{-0.56}$
Sculptor	86	287.53, -83.16	$18.57^{+0.07}_{-0.05}$	$18.63^{+0.14}_{-0.08}$
<b>Segue I</b>	23	220.48, 50.43	$19.36^{+0.32}_{-0.35}$	$17.52^{+2.54}_{-2.65}$
Segue II	35	149.43, -38.14	$16.21^{+1.06}_{-0.98}$	$19.50^{+1.82}_{-1.48}$
<b>Sextans</b>	86	243.50, 42.27	$17.92^{+0.35}_{-0.29}$	$18.04^{+0.50}_{-0.28}$
<b>Ursa Major I</b>	97	159.43, 54.41	$17.87^{+0.56}_{-0.33}$	$18.84^{+0.97}_{-0.43}$
<b>Ursa Major II</b>	32	152.46, 37.44	$19.42^{+0.44}_{-0.42}$	$20.60^{+1.46}_{-0.95}$
Ursa Minor	76	104.97, 44.80	$18.95^{+0.26}_{-0.18}$	$19.08^{+0.21}_{-0.13}$

Table 5.2 Summary of dSph observations by each experiment used in this work. A ‘-’ indicates the experiment did not observe the dSph for this study. For Fermi-LAT, the exposure at 1 GeV is given. For HAWC,  $|\Delta\theta|$  is the absolute difference between the source declination and HAWC latitude. HAWC is more sensitive to sources with smaller  $|\Delta\theta|$ . For IACTs, we show the zenith angle range, the total exposure, the energy range, the angular radius  $\theta$  of the signal or ON region, the ratio of exposures between the background-control (OFF) and signal (ON) regions ( $\tau$ ), and the significance of gamma-ray excess in standard deviations,  $\sigma$ .

Source name	Fermi-LAT	HAWC	H.E.S.S, MAGIC, VERITAS						
	Exposure ( $10^{11}$ s m $^2$ )	$ \Delta\theta $ ( $^\circ$ )	IACT	Zenith ( $^\circ$ )	Exposure (h)	Energy range (GeV)	$\theta$ ( $^\circ$ )	$\tau$	$S$ ( $\sigma$ )
Boötes I	2.6	4.5	VERITAS	15 – 30	14.0	100–41000	0.10	8.6	-1.0
Canes Venatici I	2.9	14.6	–	–	–	–	–	–	–
Canes Venatici II	2.9	15.3	–	–	–	–	–	–	–
Carina	3.1	–	H.E.S.S.	27 – 46	23.7	310 – 70000	0.10	18.0	-0.3
Coma Berenices	2.7	4.9	H.E.S.S.	47 – 49	11.4	550 – 70000	0.10	14.4	-0.4
			MAGIC	5 – 37	49.5	60 – 10000	0.17	1.0	–
			MAGIC	29 – 45	52.1	70 – 10000	0.22	1.0	–
Draco	3.8	38.1	VERITAS	25 – 40	49.8	120 – 70000	0.10	9.0	-1.0
Fornax	2.7	–	H.E.S.S.	11 – 25	6.8	230 – 70000	0.10	45.5	-1.5
Hercules	2.8	6.3	–	–	–	–	–	–	–
Leo I	2.5	6.7	–	–	–	–	–	–	–
Leo II	2.6	3.1	–	–	–	–	–	–	–
Leo IV	2.4	19.5	–	–	–	–	–	–	–
Leo V	2.4	–	–	–	–	–	–	–	–
Leo T	2.6	–	–	–	–	–	–	–	–
Sculptor	2.7	–	H.E.S.S.	10 – 46	11.8	200 – 70000	0.10	19.8	-2.2
Segue I	2.5	2.9	MAGIC	13 – 37	158.0	60 – 10000	0.12	1.0	-0.5
			VERITAS	15 – 35	92.0	80 – 50000	0.10	7.6	0.7
Segue II	2.7	–	–	–	–	–	–	–	–
Sextans	2.4	20.6	–	–	–	–	–	–	–
Ursa Major I	3.4	32.9	–	–	–	–	–	–	–
Ursa Major II	4.0	44.1	MAGIC	35 – 45	94.8	120 – 10000	0.30	1.0	-2.1
Ursa Minor	4.1	–	VERITAS	35 – 45	60.4	160 – 93000	0.10	8.4	-0.1

995 where  $\mathcal{L}_0$  is the null hypothesis, or no DM emission, likelihood.  $\mathcal{L}^{\max}$  is the best fit signal  
 996 hypothesis where  $\langle\sigma v\rangle$  maximizes the likelihood. We calculate the likelihood of each source and  
 998 model, assuming events are Poisson distributed, with

$$\mathcal{L} = \prod_i \frac{(B_i + S_i)^{N_i} e^{-(B_i + S_i)}}{N_i!} \quad (5.8)$$

999 where  $S_i$  is the sum of expected number of signal counts.  $B_i$  is the number of background counts  
 1000 observed.  $N_i$  is the total number of counts.

1001 I also calculate an upper limit on  $\langle\sigma v\rangle$  by calculating the 95% confidence level (CL). For the  
 1002 CL, we define a parameter,  $TS_{95}$ , as

$$TS_{95} \equiv \sum_{\text{bins}} \left[ 2N \ln \left( 1 + \frac{\epsilon S_{\text{ref}}}{B} \right) - 2\epsilon S_{\text{ref}} \right] \quad (5.9)$$

1003 where the expected signal counts from a dSph is scaled by  $\epsilon$ .  $S_{\text{ref}}$  is the expected number of excess  
 1004 counts in a bin from DM emission from a dSph with a corresponding annihilation cross-section,  
 1005  $\langle\sigma v\rangle$ . We scan  $\epsilon$  such that

$$2.71 = TS_{\max} - TS_{95} \quad (5.10)$$

1006 HAWC's exclusive results are provided in Section 5.5.

#### 1007 5.4.2 Glory Duck Joint Likelihood

1008 The joint likelihood for the 5-experiment combination was done similarly as Section 5.4.1. We  
 1009 calculate upper limits on  $\langle\sigma v\rangle$  from the TS, Eq. (5.7), and define the likelihood ratio more generally

$$\lambda(\langle\sigma v\rangle | \mathcal{D}_{\text{dSphs}}) = \frac{\mathcal{L}(\langle\sigma v\rangle; \hat{\nu} | \mathcal{D}_{\text{dSphs}})}{\mathcal{L}(\widehat{\langle\sigma v\rangle}; \hat{\nu} | \mathcal{D}_{\text{dSphs}})} \quad (5.11)$$

1010  $\mathcal{D}_{\text{dSphs}}$  is the totality of observations across experiments and dSphs.  $\nu$  are the nuisance parameters  
 1011 which are the  $J$  factors in this study.  $\widehat{\langle\sigma v\rangle}$  and  $\hat{\nu}$  are the respective estimate that maximize  $\mathcal{L}$   
 1012 globally. Finally,  $\hat{\nu}$  is the set of nuisance parameters that maximize  $\mathcal{L}$  for a fixed value of  $\langle\sigma v\rangle$ .

1013 The *complete* joint likelihood,  $\mathcal{L}$  that encompasses all observations from all instruments and  
 1014 dSphs can be factorized into *partial* functions for each dSph  $l$  (with  $\mathcal{L}_{\text{dSph},l}$ ) and its  $J$  factor ( $\mathcal{J}_l$ ):

$$\mathcal{L}(\langle\sigma v\rangle; \nu | \mathcal{D}_{\text{dSphs}}) = \prod_{l=1}^{N_{\text{dSphs}}} \mathcal{L}_{\text{dSph},l}(\langle\sigma v\rangle; J_l, \nu_l | \mathcal{D}_l) \times \mathcal{J}_l(J_l | J_{l,\text{obs}}, \sigma_{\log J_l}). \quad (5.12)$$

1015 For this study,  $N_{\text{dSphs}} = 20$  is the number of dSphs studied.  $\mathcal{D}_l$  are the gamma-ray observations  
 1016 of dSph,  $l$ .  $\nu_l$  are the nuisance parameters modifying the gamma-ray observations of dSph,  $l$ ,  
 1017 but excludes  $\mathcal{J}_l$ .  $\mathcal{J}_l$  is the  $J$  factor for dSph,  $l$ , as defined in Equation (5.2), and it is a nuisance  
 1018 parameter whose value is unknown.  $\log_{10} J_{l,\text{obs}}$  and  $\sigma_{\log J_l}$  are obtained by fitting a log-normal  
 1019 function of  $J_{l,\text{obs}}$  to the posterior distribution of  $J_l$  [52].  $\log_{10} J_{l,\text{obs}}$  and  $\sigma_{\log J_l}$  values are provided  
 1020 in Table 5.1. The term  $\mathcal{J}_l$  constraining  $J_l$  is written as:

$$\mathcal{J}_l(J_l | J_{l,\text{obs}}, \sigma_{\log J_l}) = \frac{1}{\ln(10)J_{l,\text{obs}}\sqrt{2\pi}\sigma_{\log J_l}} \exp\left(-\frac{(\log_{10} J_l - \log_{10} J_{l,\text{obs}})^2}{2\sigma_{\log J_l}^2}\right). \quad (5.13)$$

1021 Both the  $\mathcal{GS}$  and  $\mathcal{B}$ , displayed in Table 5.1, sets of  $J$  factors are used in this analysis. Equation (5.13)  
 1022 is also normalized, so it can also be interpreted as a probability density function (PDF) for  $J_{l,\text{obs}}$ .  
 1023 From Equation (5.1), we can also see that  $\langle\sigma v\rangle$  and  $J_l$  are degenerate when computing  $\mathcal{L}_{\text{dSph},l}$ .  
 1024 Therefore, as noted in [53], it is sufficient to compute  $\mathcal{L}_{\text{dSph},l}$  versus  $\langle\sigma v\rangle$  for a fixed value of  $J_l$ .  
 1025 We used  $J_{l,\text{obs}}(\mathcal{GS})$  reported in Tab. 5.1, in order to perform the profile of  $\mathcal{L}$  with respect to  $J_l$ .  
 1026 The degeneracy implies that for any  $J'_l \neq J_{l,\text{obs}}$  (in practice in our case we used  $J'_l = J_{l,\text{obs}}(\mathcal{B})$  to  
 1027 compute results from a different set of  $J$  factors):

$$\mathcal{L}_{\text{dSph},l}(\langle\sigma v\rangle; J'_l, \nu_l | \mathcal{D}_l) = \mathcal{L}_{\text{dSph},l}\left(\frac{J'_l}{J_{l,\text{obs}}} \langle\sigma v\rangle; J_{l,\text{obs}}, \nu_l | \mathcal{D}_l\right), \quad (5.14)$$

1028 which is a straightforward rescaling operation that reduces the computational needs of the profiling  
 1029 operation since:

$$\mathcal{L}(\langle\sigma v\rangle; \hat{\nu} | \mathcal{D}_{\text{dSphs}}) = \prod_{l=1}^{N_{\text{dSphs}}} \max_{J_l} \left[ \mathcal{L}_{\text{dSph},l}(\langle\sigma v\rangle; J_l, \hat{\nu}_l | \mathcal{D}_l) \times \mathcal{J}_l(J_l | J_{l,\text{obs}}, \sigma_{\log J_l}) \right]. \quad (5.15)$$

1030 In addition, Eq. (5.14) enables the combination of data from different gamma-ray instruments and  
 1031 observed dSphs via tabulated values of  $\mathcal{L}_{\text{dSph},l}$ , or equivalently of  $\lambda$  from Eq. (5.11) as was done in  
 1032 this work, versus  $\langle\sigma v\rangle$ .  $\mathcal{L}_{\text{dSph},l}$  is computed for a fixed value of  $J_l$  and profiled with respect to all  
 1033 instrumental nuisance parameters  $\nu_l$ , these nuisance parameters are discussed in more detail below.  
 1034 These values are produced by each detector independently and therefore there is no need to share  
 1035 sensitive low-level information used to produce them, such as event lists. Figure 5.4 illustrates the  
 1036 multi-instrument combination technique used in this study with a comparison of the upper limit

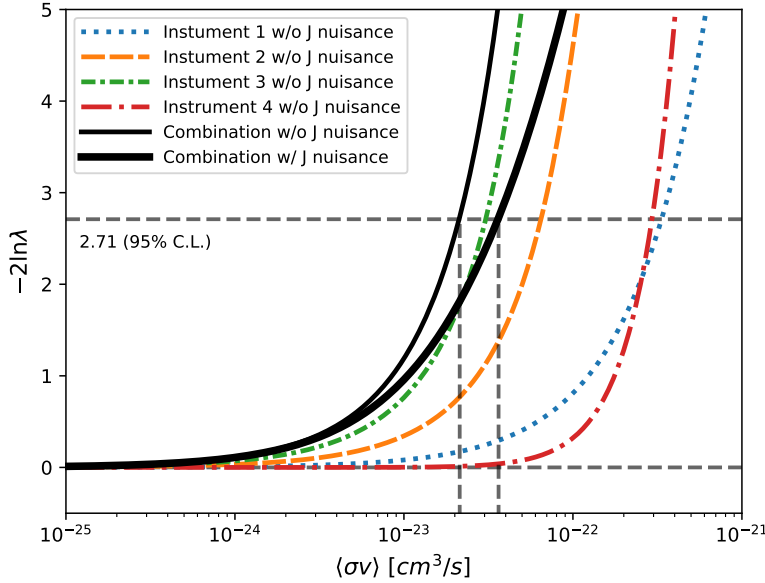


Figure 5.4 Illustration of the combination technique showing a comparison between  $-2 \ln \lambda$  provided by four instruments (colored lines) from the observation of the same dSph without any  $J$  nuisance and their sum, *i.e.* the resulting combined likelihood (thin black line). According to the test statistics of Equation (5.7), the intersection of the likelihood profiles with the line  $-2 \ln \lambda = 2.71$  indicates the 95% C.L. upper limit on  $\langle\sigma v\rangle$ . The combined likelihood (thin black line) shows a smaller value of upper limit on  $\langle\sigma v\rangle$  than those derived by individual instruments. We also show how the uncertainties on the  $J$  factor effects the combined likelihood and degrade the upper limit on  $\langle\sigma v\rangle$  (thick black line). All likelihood profiles are normalized so that the global minimum  $\widehat{\langle\sigma v\rangle}$  is 0. We note that each profile depends on the observational conditions in which a target object was observed. The sensitivity of a given instrument can be degraded and the upper limits less constraining if the observations are performed in non-optimal conditions such as a high zenith angle or a short exposure time.

1037 on  $\langle\sigma v\rangle$  obtained from the combination of the observations of four experiments towards one dSph  
 1038 versus the upper limit from individual instruments. It also shows graphically the effect of the  
 1039  $J$ -factor uncertainty on the combined observations.

1040 The *partial* joint likelihood function for gamma-ray observations of each dSph ( $\mathcal{L}_{\text{dSph},l}$ ) is  
 1041 written as the product of the likelihood terms describing the  $N_{\text{exp},l}$  observations performed with  
 1042 any of our observatories:

$$\mathcal{L}_{\text{dSph},l} (\langle\sigma v\rangle; J_l, \nu_l | \mathcal{D}_l) = \prod_{k=1}^{N_{\text{exp},l}} \mathcal{L}_{lk} (\langle\sigma v\rangle; J_l, \nu_{lk} | \mathcal{D}_{lk}), \quad (5.16)$$

1043 where each  $\mathcal{L}_{lk}$  term refers to an observation of the  $l$ -th dSph with associated  $k$ -th instrument

1044 responses.  $N_{\text{exp},l}$  varies from dSph to dSph and can be inferred from Table 5.2.

1045     Each collaboration separately analyzes their data for  $\mathcal{D}_{lk}$  corresponding to dSph  $l$  and gamma-  
1046     ray detector  $k$ , using as many common assumptions as possible in the analysis. HAWC's treatment  
1047     was described earlier in Section 5.4.1 whereas the specifics of the remaining experiments is left to  
1048     the publication. We compute the values for the likelihood functions  $\mathcal{L}_{lk}$  (see Eq. (5.16)) for a fixed  
1049     value of  $J_l$  and profile over the rest of the nuisance parameters  $\nu_{lk}$ . Then, values of  $\lambda$  from Eq. (5.11)  
1050     are computed as a function of  $\langle\sigma v\rangle$ , and shared using a common format. Results are computed for  
1051     seven annihilation channels,  $W^+W^-$ ,  $ZZ$ ,  $b\bar{b}$ ,  $t\bar{t}$ ,  $e^+e^-$ ,  $\mu^+\mu^-$ , and  $\tau^+\tau^-$  over 62  $m_\chi$  values between  
1052     5 GeV and 100 TeV provided in [46]. The  $\langle\sigma v\rangle$  range is defined between  $10^{-28}$  and  $10^{-18}\text{cm}^3 \cdot \text{s}^{-1}$ ,  
1053     with 1001 logarithmically spaced values. The likelihood combination, i.e. Equation (5.12), and  
1054     profile over the  $J$ -factor to compute the profile likelihood ratio  $\lambda$ , Equation (5.11), are carried out  
1055     with two different public analysis software packages, namely gLike [54] and LklCom [55], that  
1056     provide the same results [56].

1057     As mentioned previously, each experiment computes the  $\mathcal{L}_{lk}$  from Equation (5.11) differently.  
1058     The remainder of this section highlights the differences in this calculation across the experiments.  
1059     Four experiments, namely *Fermi*-LAT, H.E.S.S., HAWC and MAGIC, use a binned likelihood to  
1060     compute the  $\mathcal{L}_{lk}$ . For these experiments, for each observation  $\mathcal{D}_{lk}$  of a given dSph  $l$  carried out  
1061     using a given gamma-ray detector  $k$ , the binned likelihood function is:

$$\mathcal{L}_{lk} (\langle\sigma v\rangle; J_l, \nu_{lk} | \mathcal{D}_{lk}) = \prod_{i=1}^{N_E} \prod_{j=1}^{N_P} \left[ \mathcal{P}(s_{lk,ij}(\langle\sigma v\rangle, J_l, \nu_{lk}) + b_{lk,ij}(\nu_{lk}) | N_{lk,ij}) \right] \times \mathcal{L}_{lk,\nu} (\nu_{lk} | \mathcal{D}_{\nu_{lk}}) \quad (5.17)$$

1062     where  $N_E$  and  $N_P$  are the number of considered bins in reconstructed energy and arrival direction,  
1063     respectively;  $\mathcal{P}$  represents a Poisson PDF for the number of gamma-ray candidate events  $N_{lk,ij}$   
1064     observed in the  $i$ -th bin in energy and  $j$ -th bin in arrival direction, when the expected number is  
1065     the sum of the expected mean number of signal events  $s_{ij}$  (produced by DM annihilation) and of  
1066     background events  $b_{ij}$ ;  $\mathcal{L}_{lk,\nu}$  is the likelihood term for the extra  $\nu_{lk}$  nuisance parameters that vary  
1067     from one instrument  $k$  to another. The expected counts for signal events  $s_{ij}$  for a given dSph  $l$  and

1068 detector  $k$  is given by:

$$s_{ij}(\langle\sigma\nu\rangle, J) = \int_{E'_{\min,i}}^{E'_{\max,i}} dE' \int_{P'_{\min,j}}^{P'_{\max,j}} d\Omega' \int_0^\infty dE \int_{\Delta\Omega_{tot}} d\Omega \int_0^{T_{\text{obs}}} dt \frac{d^2\Phi(\langle\sigma\nu\rangle, J)}{dEd\Omega} \text{IRF}(E', P' | E, P, t) \quad (5.18)$$

1069 where  $E'$  and  $E$  are the reconstructed and true energies,  $P'$  and  $P$  the reconstructed and true  
1070 arrival directions;  $E'_{\min,i}$ ,  $P'_{\min,j}$ ,  $E'_{\max,i}$ , and  $P'_{\max,j}$  are their lower and upper limits of the  $i$ -th  
1071 energy bin and the  $j$ -th arrival direction bin;  $T_{\text{obs}}$  is the (dead-time corrected) total observation  
1072 time;  $t$  is the time along the observations;  $d^2\Phi/dEd\Omega$  is the DM flux in the source region (see  
1073 Equation (5.1)); and  $\text{IRF}(E', P' | E, P, t)$  is the IRF, which can be factorized as the product of the  
1074 effective collection area of the detector  $A_{\text{eff}}(E, P, t)$ , the PDFs for the energy estimator  $f_E(E' | E, t)$ ,  
1075 and arrival direction  $f_P(P' | E, P, t)$  estimators. Note that for Fermi-LAT, HAWC, MAGIC, and  
1076 VERITAS the effect of the finite angular resolution is taken into account through the convolution  
1077 of  $d\Phi/dEd\Omega$  with  $f_P$  in Equation (5.18), whereas in the cases of H.E.S.S.  $f_P$  is approximated by a  
1078 delta function. This approximation has been made in order to maintain compatibility of the result  
1079 with what has been previously published. The difference introduced by this approximation is  $< 5\%$   
1080 for all considered dSphs. A more comprehensive review of the differences between the analyses of  
1081 different instruments can be found in [27].

## 1082 5.5 HAWC Results

1083 13 of the 20 dSphs considered for the Glory Duck analysis are within HAWC's field of view.  
1084 These dSph are analyzed for emission from DM annihilation according to the likelihood method  
1085 described in Section 5.4. The 13 likelihood profiles are then stacked to synthesize a combined  
1086 limit on the dark matter cross-section,  $\langle\sigma\nu\rangle$ . This combination is done for the 7 SM annihilation  
1087 channels used in the Glory Duck analysis. Figure 5.5 shows the combined limit for all annihilation  
1088 channels with HAWC only observations. We also perform 300 studies of Poisson trials on the  
1089 background. These trials are used to produce HAWC sensitivities with  $\pm 1\sigma$  and  $\pm 2\sigma$  uncertainty  
1090 bands which were shared with the other collaborators for combination. The results on fitting to  
1091 HAWC's Poisson trials of the DM hypothesis is shown in Figure 5.7 for all the DM annihilation  
1092 channels studied for Glory Duck.

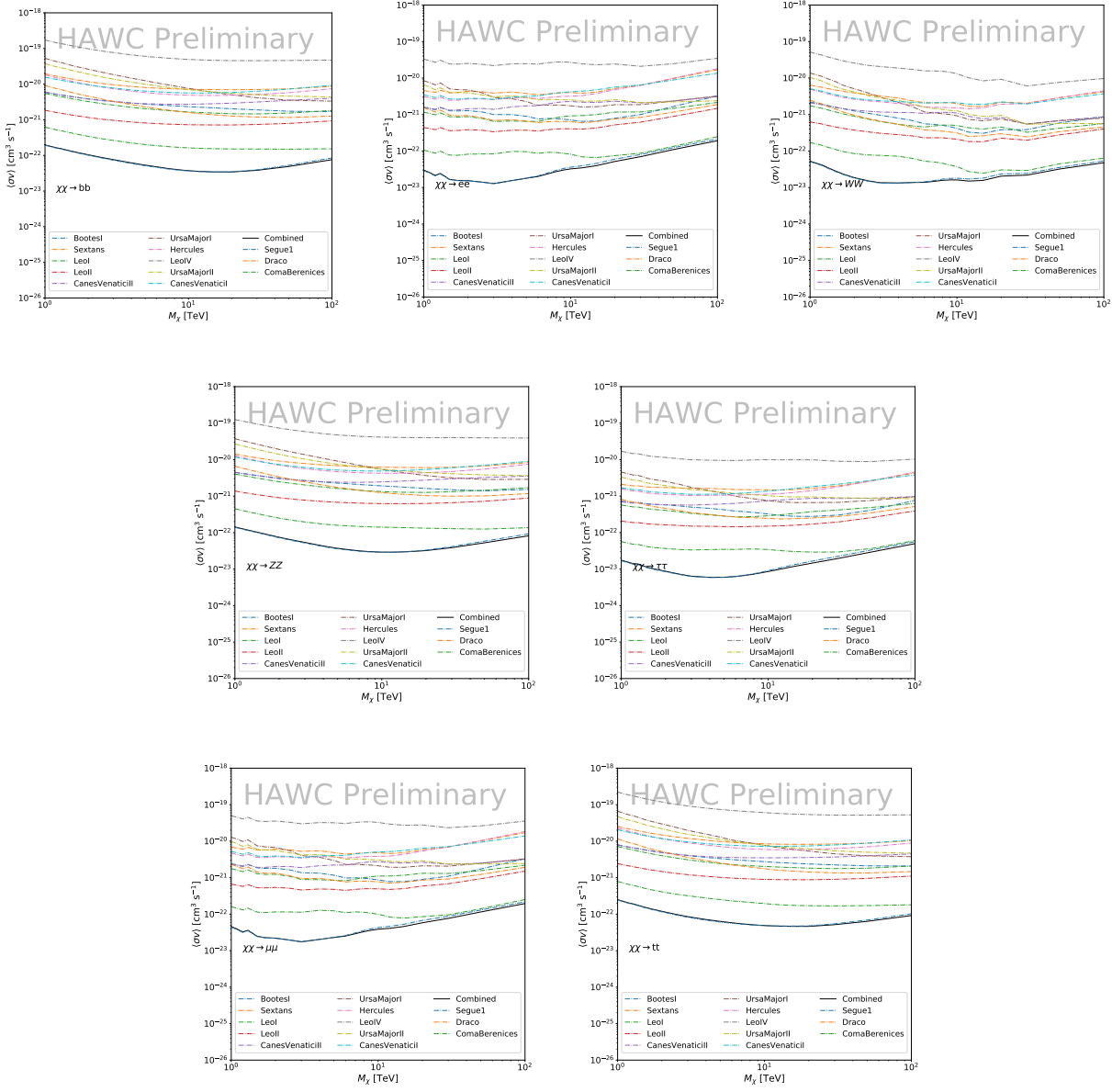


Figure 5.5

1093 No DM was found in HAWC observations. HAWC's limits are dominated by the dSphs Segue1  
 1094 and Coma Berenices. The remaining 11 dSphs do not contribute significantly to the limit because  
 1095 they are at high zenith and/or have much smaller  $J$  factors. Even though some remaining dSphs  
 1096 have large  $J$  factors, they are towards the edge of HAWC's field of view where HAWC analysis is  
 1097 less sensitive.

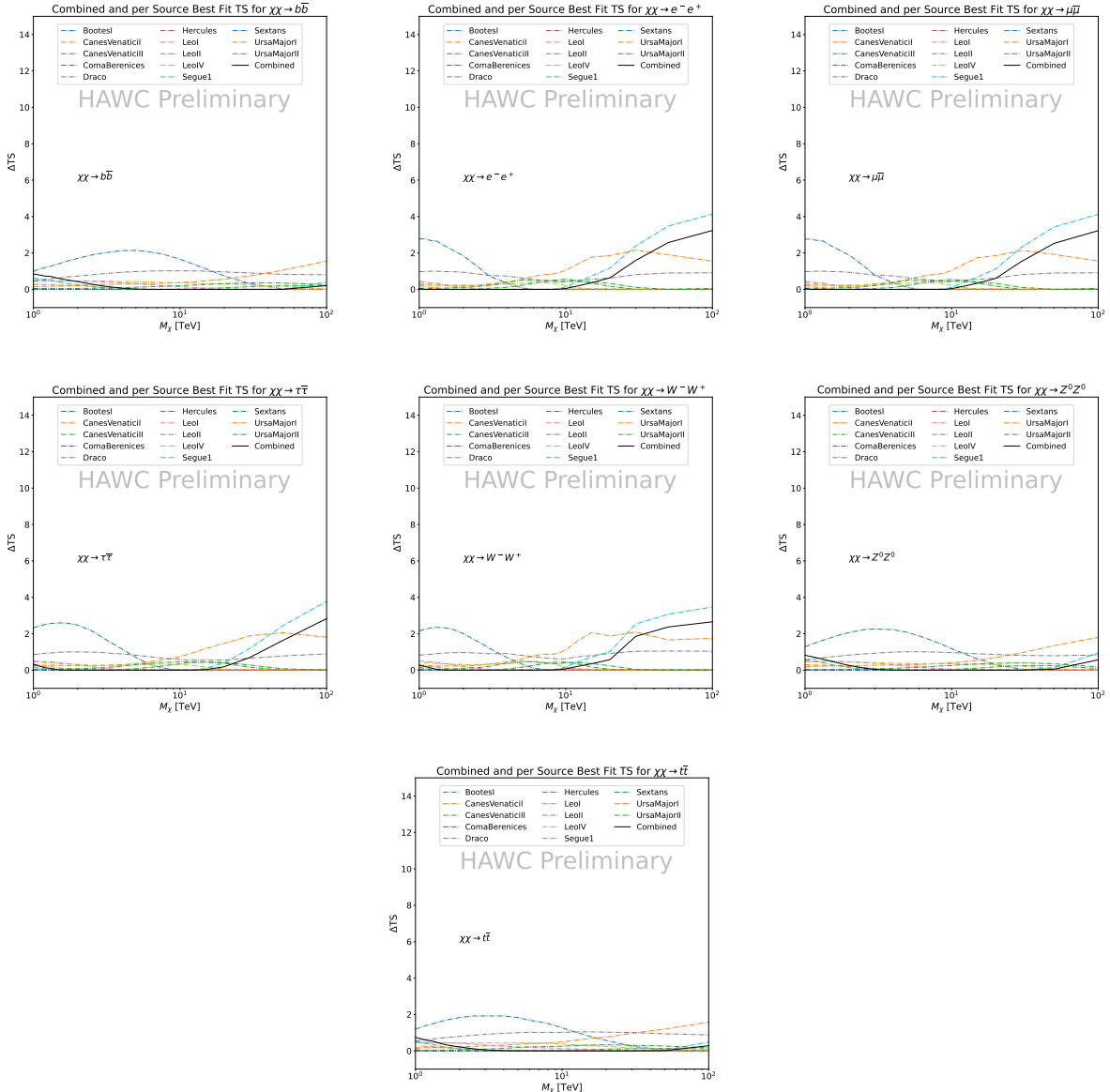


Figure 5.6 HAWC TS values for best fit  $\langle\sigma v\rangle$  versus  $m_\chi$  for seven SM annihilation channels with  $J$  factors from  $\mathcal{GS}$ . The solid black line shows the combined best fit TS values. The colored, dashed lines are the TS values for each of the 13 sources HAWC studied.

## 1098 5.6 Glory Duck Combined Results

1099 The crux of this analysis is that HAWC's results are combined with 4 other gamma-ray observa-  
 1100 tories: Fermi-LAT, H.E.S.S., MAGIC, and VERITAS. No significant DM emission was observed  
 1101 by any of the five instruments. We present the upper limits on  $\langle\sigma v\rangle$  assuming seven independent  
 1102 DM self annihilation channels, namely  $W^+W^-$ ,  $Z^+Z^-$ ,  $b\bar{b}$ ,  $t\bar{t}$ ,  $e^+e^-$ ,  $\mu^+\mu^-$ , and  $\tau^+\tau^-$ . The 68%

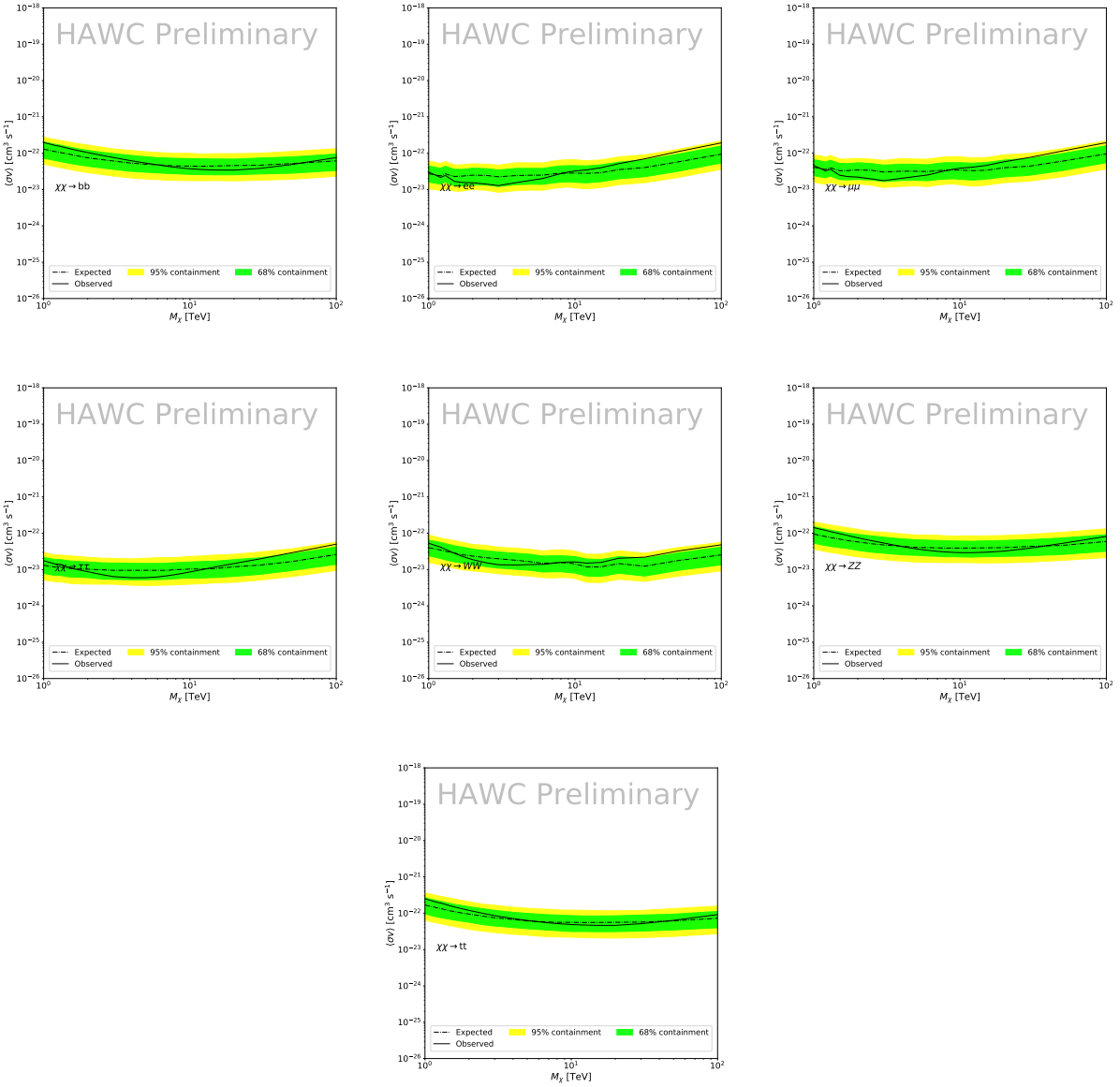


Figure 5.7 HAWC Brazil bands at 95% confidence level on  $\langle\sigma v\rangle$  versus DM mass for seven annihilation channels with  $J$ -factors from  $\mathcal{GS}$  [57]. The solid line represents the combined limit from 13 dSphs. The dashed line is the expected limit. The green band is the 68% containment. The yellow band is the 95% containment.

and 95% containment bands are produced from 300 Poisson realizations of the null hypothesis corresponding to each of the combined datasets. These 300 realizations are combined identically to dSph observations. The containment bands and the median are extracted from the distribution of resulting limits on the null hypothesis. These 300 realizations are obtained either by fast simulations of the OFF observations, for H.E.S.S., MAGIC, VERITAS, and HAWC, or taken from real

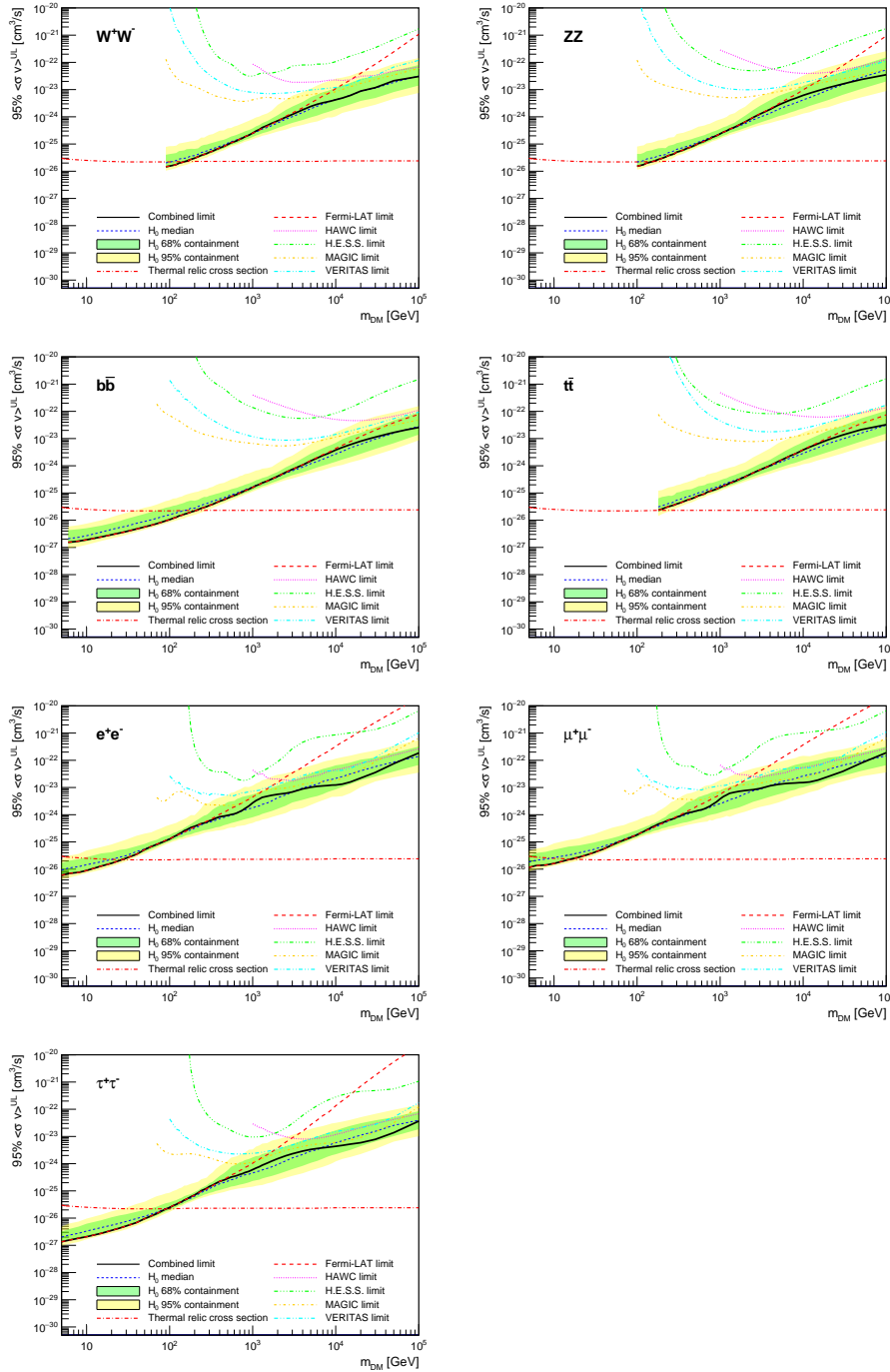


Figure 5.8 Upper limits at 95% confidence level on  $\langle\sigma v\rangle$  in function of the DM mass for eight annihilation channels, using the set of  $J$  factors from Ref. [57] ( $\mathcal{GS}$  set in Table 5.1). The black solid line represents the observed combined limit, the black dashed line is the median of the null hypothesis corresponding to the expected limit, while the green and yellow bands show the 68% and 95% containment bands. Combined upper limits for each individual detector are also indicated as solid, colored lines. The value of the thermal relic cross-section in function of the DM mass is given as the red dotted-dashed line [58].

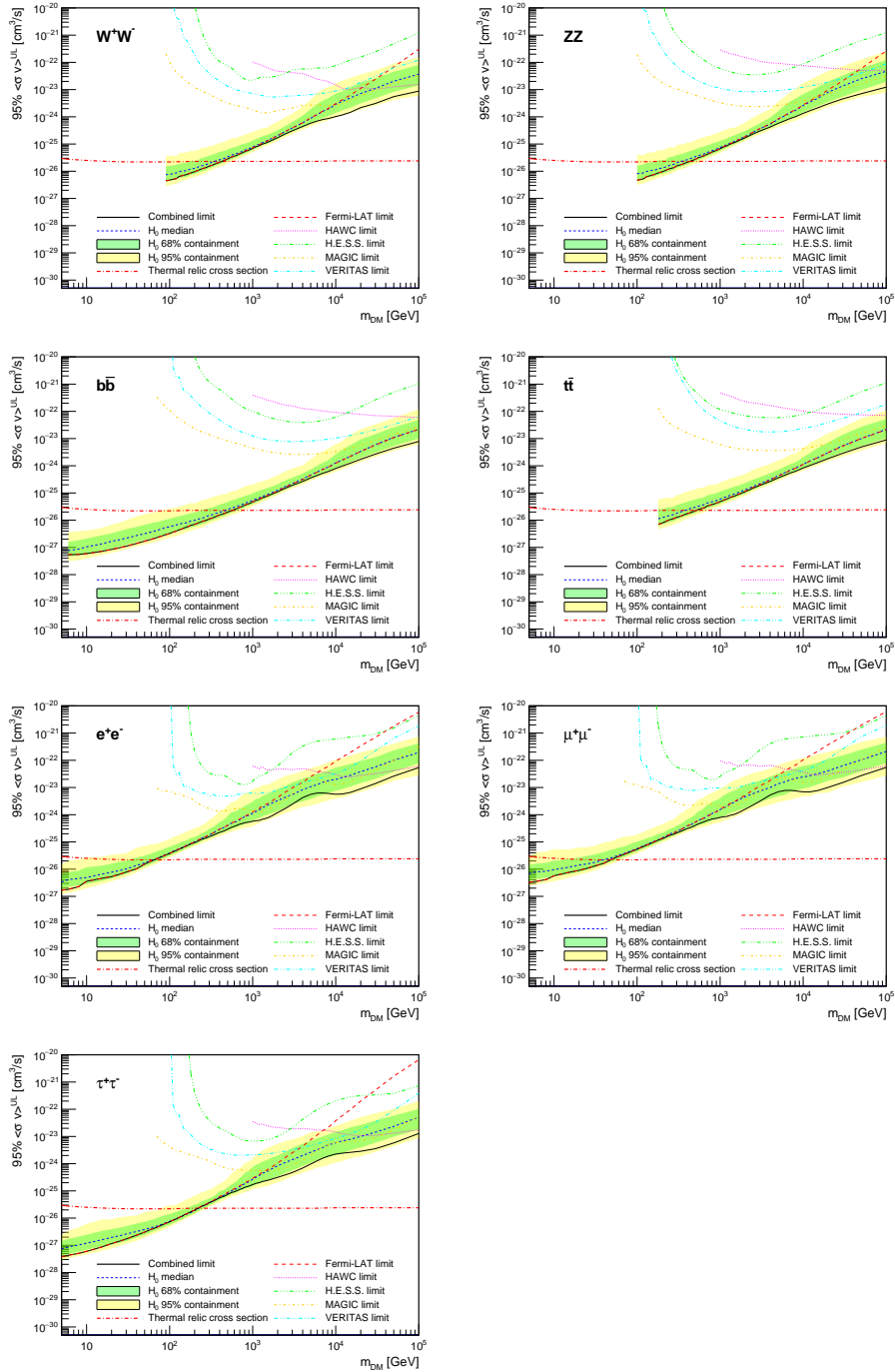


Figure 5.9 Same as Fig. 5.8, using the set of  $J$  factors from Ref. [51, 59] ( $\mathcal{B}$  set in Table 5.1).

1108 observations of empty fields of view in the case of Fermi-LAT [52, 60, 61].

1109 The obtained limits are shown in Figure 5.8 for the  $\mathcal{GS}$  set of  $J$ -factors [57] and in Figure 5.9  
1110 for the  $\mathcal{B}$  set of  $J$ -factors [51, 59]. The combined limits are presented with their 68% and 95%  
1111 containment bands, and are expected to be close to the median limit when no signal is present.

1112 We observe agreement with the null hypothesis for all channels, within  $2\sigma$  standard deviations,  
1113 between the observed limits and the expectations given by the median limits. Limits obtained from  
1114 each detector are also indicated in the figures, where limits for all dSphs observed by the specific  
1115 instrument have been combined.

1116 Below  $\sim 300$  GeV, the *Fermi*-LAT dominates the DM limits for all annihilation channels. From  
1117  $\sim 300$  GeV to  $\sim 2$  TeV, *Fermi*-LAT continues to dominate for the hadronic and bosonic DM channels,  
1118 yet the IACTs (H.E.S.S., MAGIC, and VERITAS) and *Fermi*-LAT all contribute to the limit for  
1119 leptonic DM channels. For DM masses between  $\sim 2$  TeV to  $\sim 10$  TeV, the IACTs dominate leptonic  
1120 DM annihilation channels, whereas both the *Fermi*-LAT and the IACTs dominate bosonic and  
1121 hadronic DM annihilation channels. From  $\sim 10$  TeV to  $\sim 100$  TeV, both the IACTs and HAWC  
1122 contribute significantly to the leptonic DM limit. For hadronic and bosonic DM, the IACTs and  
1123 *Fermi*-LAT both contribute strongly.

1124 We notice that the limits computed using the  $\mathcal{B}$  set of  $J$ -factor are always better compared to the  
1125 ones calculated with the  $\mathcal{GS}$  set. For the  $W^+W^-$ ,  $Z^+Z^-$ ,  $b\bar{b}$ , and  $t\bar{t}$  channels, the ratio between the  
1126 limits computed with the two sets of  $J$ -factor is varying between a factor of  $\sim 3$  and  $\sim 5$  depending  
1127 on the energy, with the largest ratio around 10 TeV. For the channels  $e^+e^-$ ,  $\mu^+\mu^-$ , and  $\tau^+\tau^-$ , the  
1128 ratio lies between  $\sim 2$  to  $\sim 6$ , being maximum around 1 TeV. Examining Figure 5.16 and Figure 5.17  
1129 in Section 5.8, these differences are explained by the fact that the  $\mathcal{B}$  set provides higher  $J$ -factors  
1130 for the majority of the studied dSphs, with the notable exception of Segue I. The variation on the  
1131 ratio of the limits for the two sets is due to different dSph dominating the limits depending on the  
1132 energy. One set,  $\mathcal{B}$ , pushes the range of which thermal cross-section which can be excluded to  
1133 higher mass. This comparison demonstrates the magnitude of systematic uncertainties associated  
1134 with the choice of the  $J$ -factor calculation. The  $\mathcal{GS}$  and  $\mathcal{B}$  sets present a difference in the limits for  
1135 all channels of about This difference is explained, see Figure 5.16 and Figure 5.17, by the fact that  
1136 the  $\mathcal{B}$  set provides higher  $J$ -factors for all dSph except for Segue I.

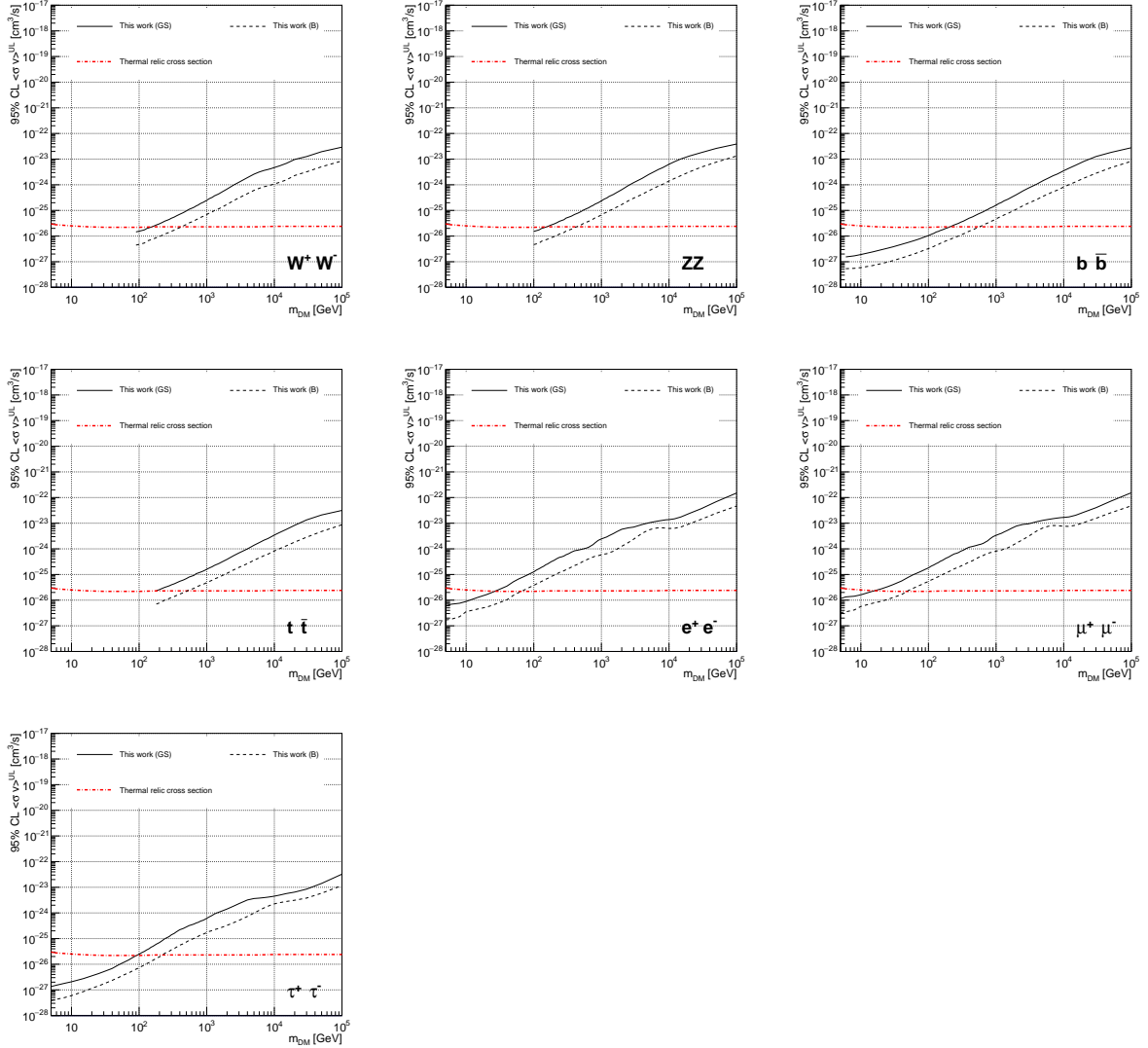


Figure 5.10 Comparisons of the combined limits at 95% confidence level for each of the eight annihilation channels when using the  $J$  factors from Ref. [57] ( $\mathcal{GS}$  set in Table 5.1), plain lines, and the  $J$  factor from Ref. [51, 59] ( $\mathcal{B}$  set in Table 5.1), dashed lines. The cross-section given by the thermal relic is also indicated [58].

## 1137 5.7 HAWC Systematics

### 1138 5.7.1 Inverse Compton Scattering

1139 The DM-DM annihilation channels produce many high energy electrons regardless of the  
 1140 primary annihilation channel. These high energy electrons can produce high energy gamma-rays  
 1141 through Inverse Compton Scattering (ICS). If this effect is strong, it would change the morphology  
 1142 of the source and increase the total expected gamma-ray counts from any source. The PPPC [46]

1143 provides tools in Mathematica for calculating the impact of ICS for an arbitrary location in the  
1144 sky for a specified annihilation channel. We calculated the change in gamma-ray counts for DM  
1145 annihilation to primary  $e\bar{e}$  for RA and Dec corresponding to Segue1 and Coma Berenices. These  
1146 dSphs were chosen because they are the strongest contributors to the limit.  $e\bar{e}$  was selected because  
1147 it would have the largest number of high energy electrons. The effect was found to be on the order  
1148 of  $10^{-7}$  on the gamma-ray spectrum. As a result, this systematic is not considered in our analysis.

1149 **5.7.2 Point Source Versus Extended Source Limits**

1150 The previous DM search toward dSph approximated the dSphs as point sources [48]. In  
1151 this analysis, the dSphs are implemented as extended with J-factor distributions following those  
1152 produced by [57]. The resolution of the cited map is much finer than HAWC's angular resolution.  
1153 The vast majority of the J-factor distribution is represented on the central HAWC pixel of the dSph  
1154 spatial map. However, the neighboring 8 pixels are not negligible and contribute to our limit.

1155 Figure 5.11 shows a substantial improvement to the limit for Segue1. Fig. 5.12 however showed  
1156 identical limits. These disparities are best explained by the relative difference in their J-Factors.  
1157 Both dSphs pass almost overhead the HAWC detector, however Segue1 has the larger J-Factor  
1158 between the two. Adjacent pixels to the central pixel will therefore contribute to the limits. This is  
1159 the case for other dSph that are closer to the zenith of the HAWC detector.

1160 Comparison plots for all sources and the combined limit can be found in the sandbox for the  
1161 Glory Duck project.

1162 **5.7.3 Impact of Pointing Systematic**

1163 During the analysis it was discovered that directional reconstruction of gamma-rays had a  
1164 systematic bias at large zenith angles. Slides describing this systematic can be found [here](#). Shown  
1165 on the presentation is dependence on the pointing systematic on declination. New spatial profiles  
1166 were generated for every dSph and limits were computed for the adjusted declination.

1167 Section 5.7.3 demonstrates the impact of this systematic for all DM annihilation channels  
1168 studied by HAWC. The impact is a tiny improvement, yet mostly identical, to the combined limits.

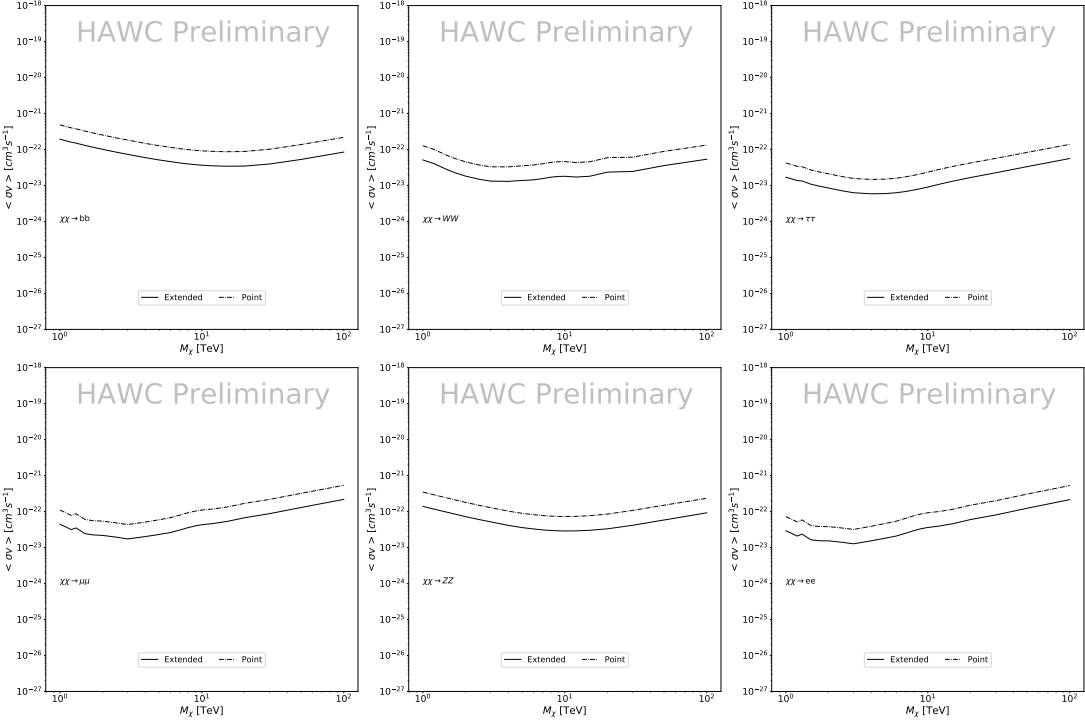


Figure 5.11 Comparisons of the combined limits at 95% confidence level for a point source analysis and extended source using [57] *GS* J-factor distributions and PPPC [46] annihilation spectra. Shown are the limits for Segue1 which will have the most significant impact on the combined limit. 6 of the 7 DM annihilation channels are shown. Solid lines are extended source studies. Dashed lines are point source studies. Overall, the extended source analysis improves the limit by a factor of 2.

## 1169 5.8 *J*-factor distributions

### 1170 5.8.1 Numerical integration of *GS* maps

1171 It was discovered well after the HAWC analysis was completed that the published tables from  
 1172 *GS* [47] quoted median *J*-factors were computed in a non-trivial manner. The assumption myself  
 1173 and collaborators had been that the published tables represented the *J*-factor as a function of  $\theta$  for  
 1174 the best global fit model on a per-source basis. However, this is not the case. Instead, what is  
 1175 published are the best fit model for each dwarf that only considers stars up to the angular separation  
 1176  $\theta$ . Therefore, the model is changing for each value of  $\theta$  for each dwarf. Yet, the introduced features  
 1177 from unique models at each  $\theta$  are much smaller than the angular resolution of HAWC. It is not  
 1178 expected for these effects to impact the limits and TS greatly as a result.

1179 Median *J*-factor model profiles were provided by the authors. New maps were generated

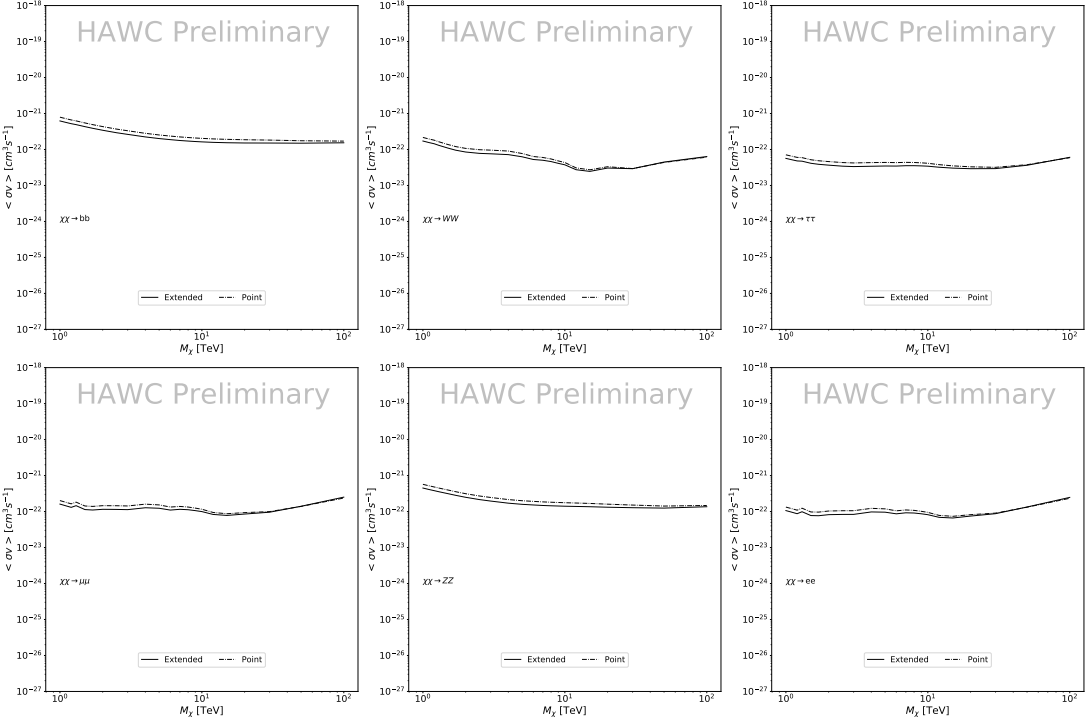


Figure 5.12 Same as Fig. 5.11 on Coma Berenices. This dSph also contributes significantly to the limit. The limits are identical in this case.

and analyzed for Segue1 and Coma Berenices. Figure 5.14 shows the differential between maps generated with the method from Section 5.8.1 and from the authors of [47]. These maps were reanalyzed for all SM DM annihilation channels. Upper limits for these channels are shown in Figure 5.15

From Figure 5.15, we can see that the impact of these model difference was no substantial. The observed impact was a fractional effect which is much smaller than the impact from selecting another DM spatial distribution model as was shown in Figure 5.10.

### 5.8.2 $\mathcal{GS}$ Versus $\mathcal{B}$ spatial models

We show in this appendix a comparison between the  $J$ -factors computed by Geringer-Sameth *et al.* [57] (the  $\mathcal{GS}$  set) and the ones computed by Bonnivard *et al.* [51, 59] (the  $\mathcal{B}$  set). The  $\mathcal{GS}$   $J$ -factors are computed through a Jeans analysis of the kinematic stellar data of the selected dSphs, assuming a dynamic equilibrium and a spherical symmetry for the dSphs. They adopted the generalized DM density distribution, known as Zhao-Hernquist, introduced by [49], carrying

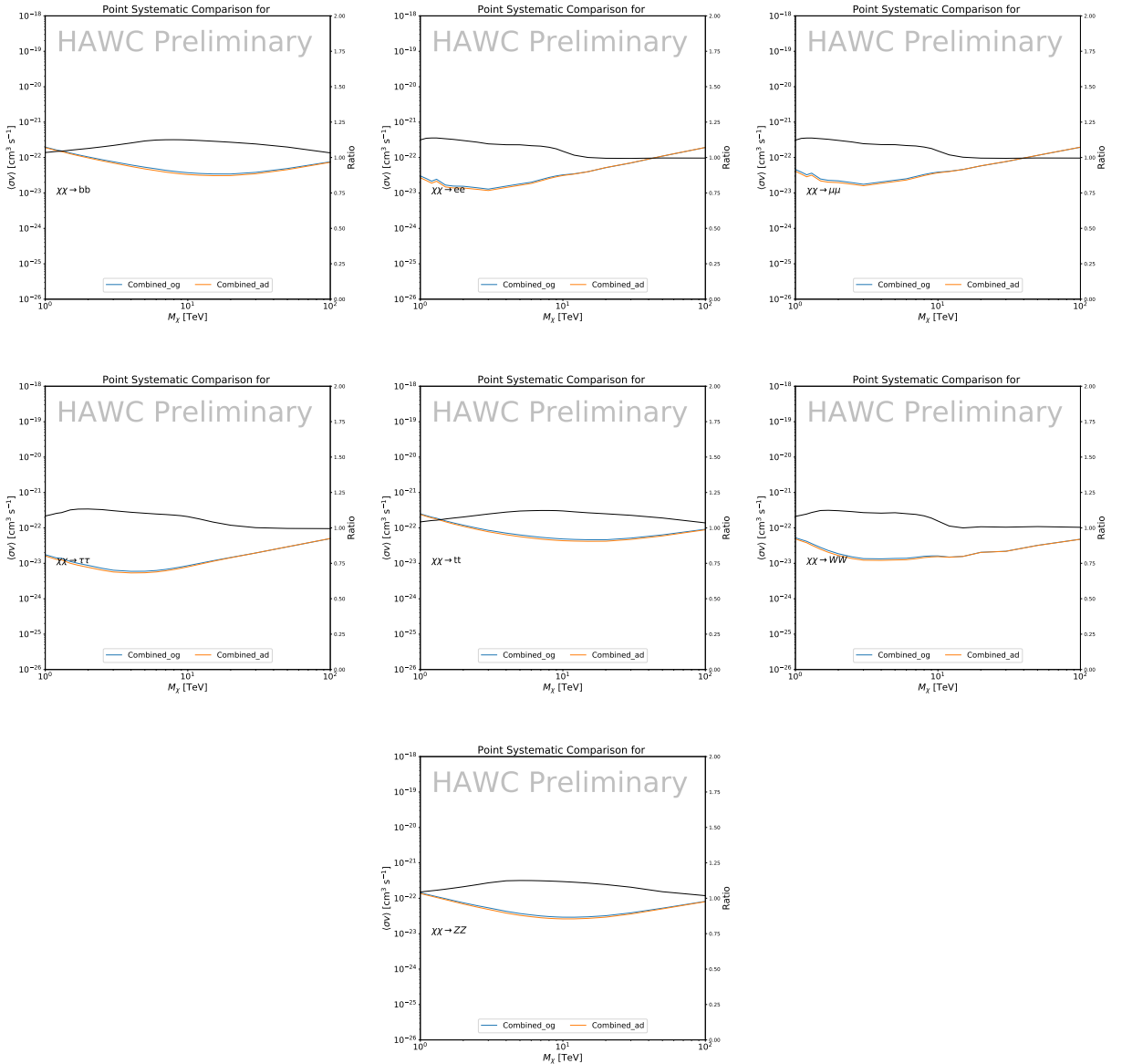


Figure 5.13 Comparison of combined limits when correcting for HAWC's pointing systematic. All DM annihilation channels are shown. The solid black line is the ratio between published limit to the declination corrected limit. The blue solid line or "Combined\_og" represented the limits computed for Glory Duck. The solid orange line or "Combined\_ad" represented the limits computed after correcting for the pointing systematic.

1193 three additional index parameters to describe the inner and outer slopes, and the break of the  
 1194 density profile. Such a profile parametrization allows the reduction of the theoretical bias from  
 1195 the choice of a specific radial dependency on the kinematic data. In other words, the increase of  
 1196 free parameters with the use of the Zhao-Hernquist profile allows a better description of the mass

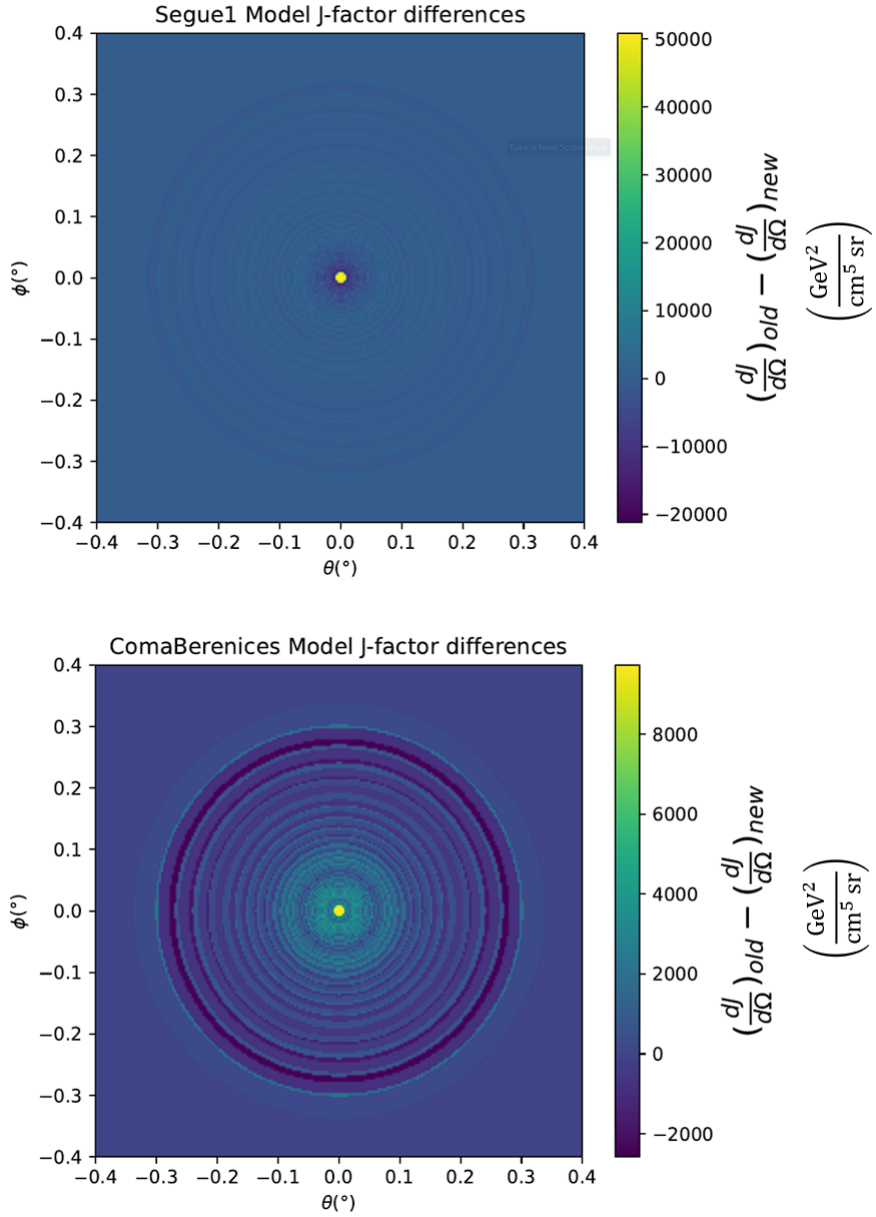


Figure 5.14 Differential map of  $dJ/\Omega$  from model built in Section 5.8.1 and profiles provided directly from authors. (Top) Differential from Segue1. (bottom) Differential from Coma Berenices. Note that their scales are not the same. Segue1 shows the deepest discrepancies which is congruent with its large uncertainties. Both models show anuli where unique models become apparent.

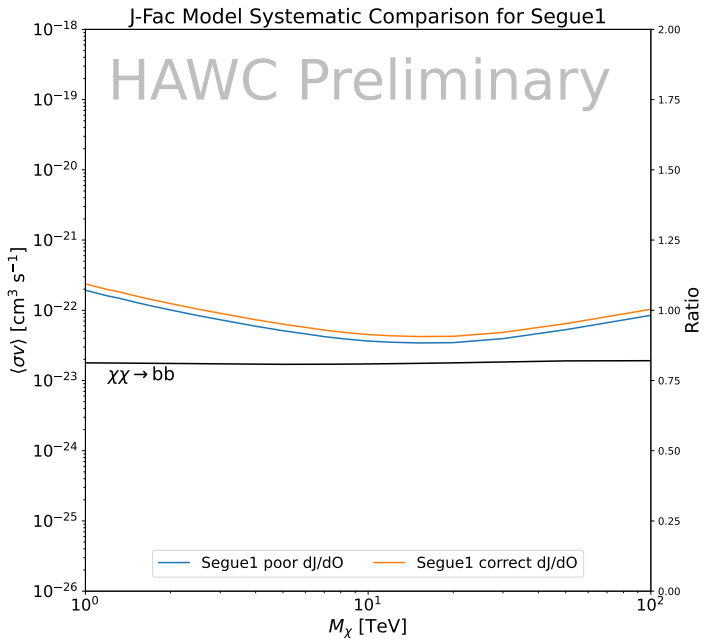
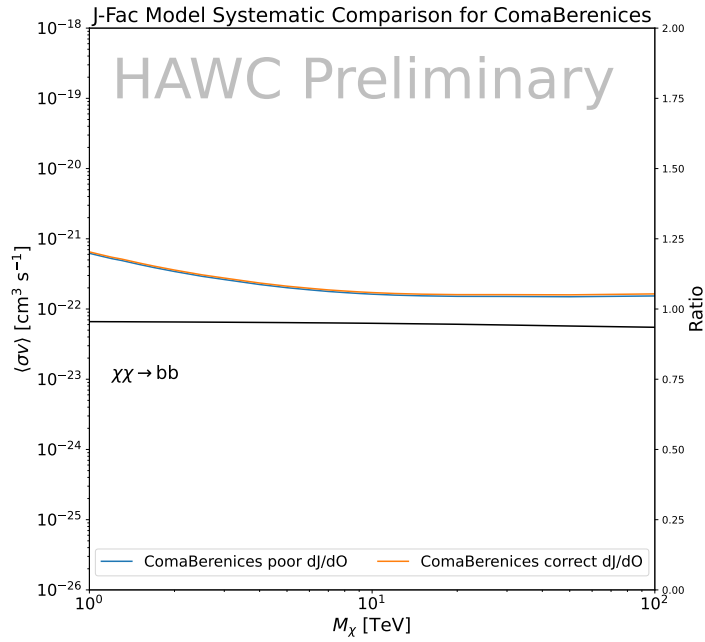


Figure 5.15 HAWC limits for Coma Berenices (top) and Segue1 (bottom) for two different map sets. Blue lines are limits calculated on maps with poor model representation. Orange lines are limits calculated on spatial profiles provided by the authors of [47]. Black line is the ratio of the poor spatial model limits to the corrected spatial models. The left y-axis measures  $\langle \sigma v \rangle$  for the blue and orange lines. The right y-axis measures the ratio and is unitless.

1197 density distribution of dark matter.

1198 In addition, a constant velocity anisotropy profile and a Plummer light profile [62] for the stellar  
1199 distribution were assumed. The velocity anisotropy profile depends on the radial and tangential  
1200 velocity dispersion. However, its determination remains challenging since only the line-of-sight  
1201 velocity dispersion can be derived from velocity measurements. Therefore, the parametrization of  
1202 the anisotropy profile is obtained from simulated halos (see [63] for more details). They provide the  
1203 values of the  $J$ -factors of regions extending to various angular radius up to the outermost member  
1204 star.

1205 The  $\mathcal{B}$   $J$ -factors were computed through a Jeans analysis taking into account the systematic  
1206 uncertainties induced by the DM profile parametrization, the radial velocity anisotropy profile, and  
1207 the triaxiality of the halo of the dwarf galaxies. They performed a more complete study of the dSph  
1208 kinematics and dynamics than  $\mathcal{GS}$  for the determination of the  $J$ -factor. Conservative values of the  
1209  $J$ -factors where obtained using an Einasto DM density profile [64], a realistic anisotropy profile  
1210 known as the Baes & Van Hese profile [65] which takes into account that the inner regions can be  
1211 significantly non-isotropic, and a Zhao-Hernquist light profile [49].

1212 For both sets,  $J$ -factor values are provided for all dSphs as a function of the radius of the  
1213 integration region [57, 51, 59]. Table 5.1 shows the heliocentric distance and Galactic coordinates  
1214 of the twenty dSphs, together with the two sets of  $J$ -factor values integrated up to the outermost  
1215 observed star for  $\mathcal{GS}$  and the tidal radius for  $\mathcal{B}$ . Both  $J$ -factor sets were derived through a Jeans  
1216 analysis based on the same kinematic data, except for Draco where the measurements of [66] have  
1217 been adopted in the computation of the  $\mathcal{B}$  value. The computations for producing the  $\mathcal{GS}$  and  $\mathcal{B}$   
1218 samples differ in the choice of the DM density, velocity anisotropy, and light profiles, for which the  
1219 set  $\mathcal{B}$  takes into account some sources of systematic uncertainties.

1220 Figure 5.16 and Figure 5.17 show the comparisons for the  $J$ -factor versus the angular radius  
1221 for each of the 20 dSphs used in this study. The uncertainties provided by the authors are also  
1222 indicated in the figures. For the  $\mathcal{GS}$  set, the computation stops at the angular radius corresponding  
1223 to the outermost observed star, while for the  $\mathcal{B}$  set, the computation stops at the angular radius

1224 corresponding to the tidal radius.

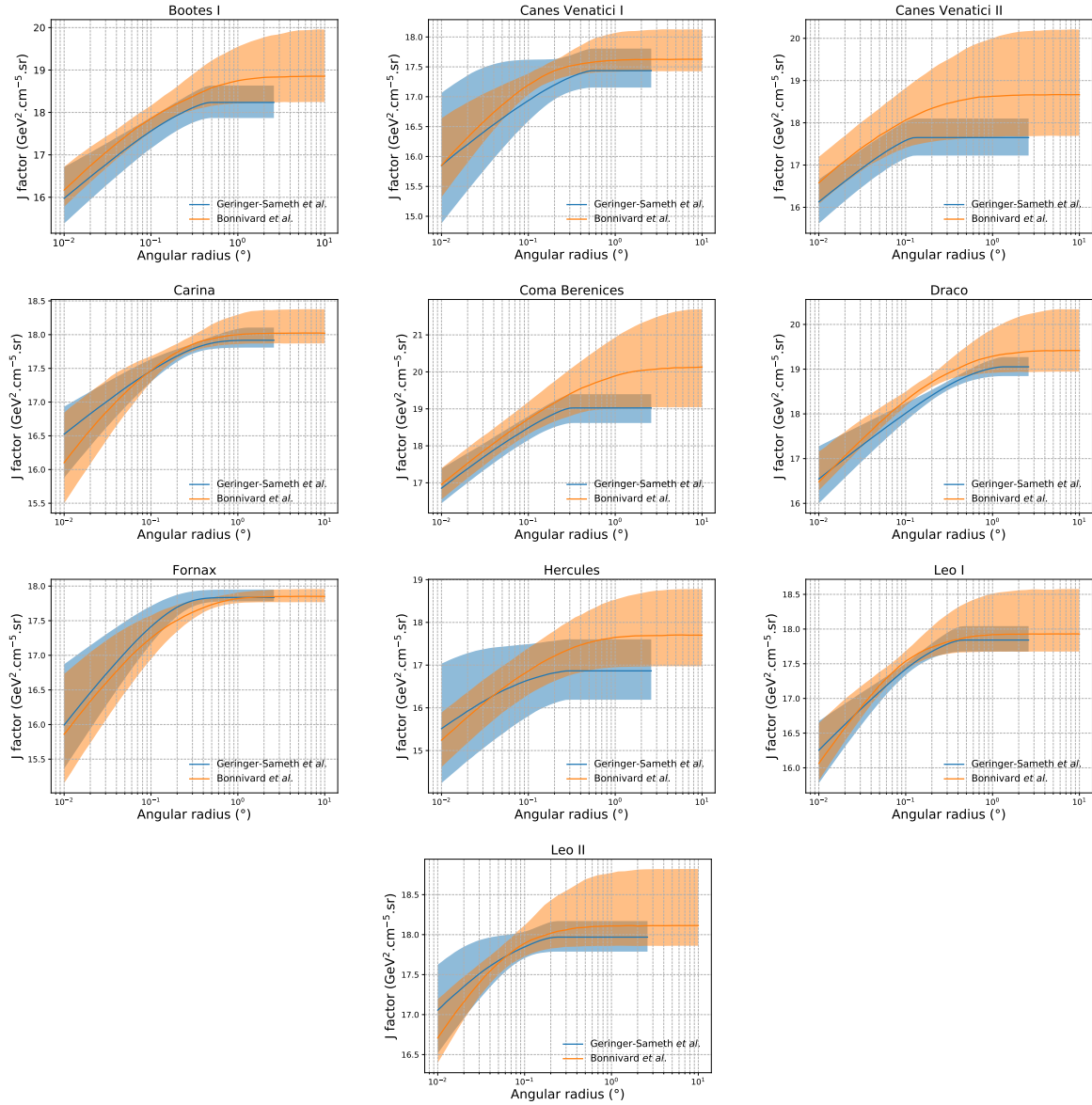


Figure 5.16 Comparisons between the  $J$ -factors versus the angular radius for the computation of  $J$  factors from Ref. [57] ( $\mathcal{GS}$  set in Table 5.1) in blue and for the computation from Ref. [51, 59] ( $\mathcal{B}$  set in Tab. 5.1) in orange. The solid lines represent the central value of the  $J$ -factors while the shaded regions correspond to the  $1\sigma$  standard deviation.

## 1225 5.9 Discussion and Conclusions

1226 In this multi-instrument analysis, we have used observations of 20 dSphs from the gamma-ray  
 1227 telescopes Fermi-LAT, H.E.S.S., MAGIC, VERITAS, and HAWC to perform a collective DM  
 1228 search annihilation signals. The data were combined across sources and detectors to significantly

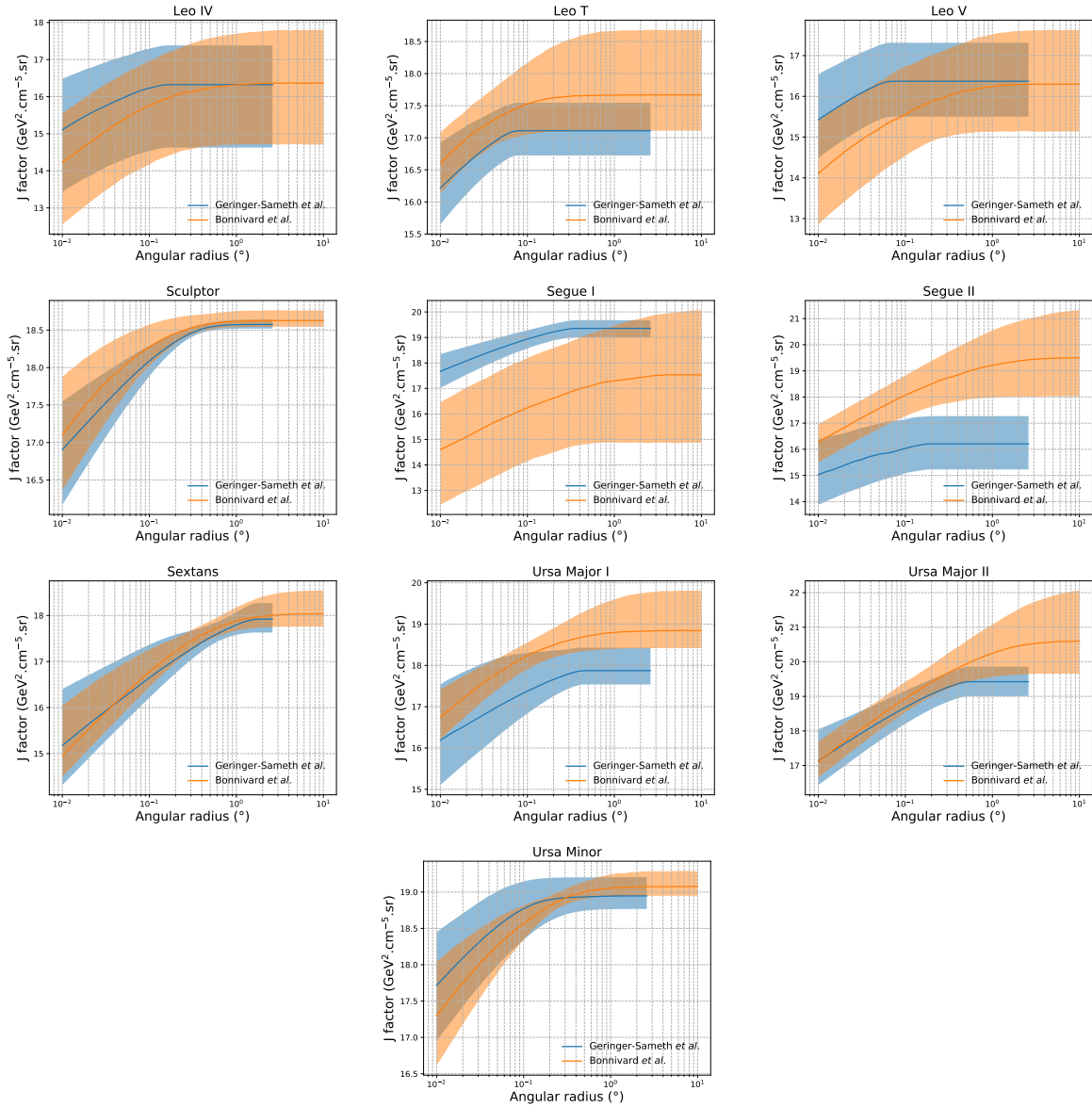


Figure 5.17 Comparisons between the  $J$ -factors versus the angular radius for the computation of  $J$  factors from Ref. [57] ( $\mathcal{GS}$  set in Tab. 5.1) in blue and for the computation from Ref. [51, 59] ( $\mathcal{B}$  set in Tab. 5.1) in orange. The solid lines represent the central value of the  $J$ -factors while the shaded regions correspond to the  $1\sigma$  standard deviation.

increase the sensitivity of the search. We have observed no significant deviation from the null, no DM hypothesis, and so present our results in terms of upper limits on the annihilation cross-section for seven potential DM annihilation channels.

Fermi-LAT brings the most stringent constraints for continuum channels below approximately 1 TeV. The remaining detectors dominate at higher energies. Overall, for multi-TeV DM mass,

1234 the combined DM constraints from all five telescopes are 2-3 times stronger than any individual  
1235 telescope for multi-TeV DM.

1236     Derived from observations of many dSphs, our results produce robust limits given the DM  
1237 content of the dSphs is relatively well constrained. The obtained limits span the largest mass  
1238 range of any WIMP DM search. Our combined analysis improves the sensitivity over previously  
1239 published results from each detector which produces the most stringent limits on DM annihilation  
1240 from dSphs. These results are based on deep exposures of the most promising known dSphs with  
1241 the currently most sensitive gamma-ray instruments. Therefore, our results constitute a legacy of  
1242 a generation of gamma-ray instruments on WIMP DM searches towards dSphs. Our results will  
1243 remain the reference in the field until a new generation of more sensitive gamma-ray instruments  
1244 begin operations, or until new dSphs with higher  $J$ -factors are discovered.

1245     This analysis serves as a proof of concept for future multi-instrument and multi-messenger  
1246 combination analyses. With this collaborative effort, we have managed to sample over four orders  
1247 in magnitude in gamma-ray energies with distinct observational techniques. Determining the nature  
1248 of DM continues to be an elusive and difficult problem. Larger datasets with diverse measurement  
1249 techniques could be essential to tackling the DM problem. A future collaboration using similar  
1250 techniques as the ones described in this paper could grow even beyond gamma rays. The models we  
1251 used for this study include annihilation channels with neutrinos in the final state. Advanced studies  
1252 could aim to merge our results with those from neutrino observatories with large data sets. Efforts  
1253 are already underway to add data from the IceCube, ANTARES, and KM3NeT observatories to  
1254 these gamma-ray results.

1255     From this work, a selection of the best candidates for observations, according to the latest  
1256 knowledge on stellar dynamics and modelling techniques for the derivation of the  $J$ -factors on  
1257 the potential dSphs targets, is highly desirable at the time that new experiments are starting their  
1258 dark matter programs using dSphs. Given the systematic uncertainty inherent to the derivation of  
1259 the  $J$ -factors, an informed observational strategy would be to select both objects with the highest  
1260  $J$ -factors that could lead to DM signal detection, and objects with robust  $J$ -factor predictions, i.e.

1261 with kinematic measurements on many bright stars, which would strengthen the DM interpretation  
1262 reliability of the observation outcome.

1263 This analysis combines data from multiple telescopes to produce strong constraints on astro-  
1264 physical objects. From this perspective, these methods can be applied beyond just DM searches.  
1265 Almost every astrophysical study can benefit from multi-telescope, multi-wavelength gamma-ray  
1266 studies. We have enabled these telescopes to study the cosmos with greater precision and detail.  
1267 Many astrophysical searches can benefit from multi-instrument gamma-ray studies, for which our  
1268 analysis lays the foundation.

## CHAPTER 6

### MULTITHREADING HAWC ANALYSES FOR DARK MATTER SEARCHES

#### 6.1 Introduction

HAWC's current software suite, plugins to 3ML and HAL [56, 44], do not fully utilize computational advancements of recent decades. Said advancements include the proliferation of Graphical Processing Units (GPUs), and multithreading on multicore processors. The analysis described in chapter 5 took up to 3 months of wall time waiting for the full gambit of data analysis and simulation of background to compute. Additionally, with the updated 2D energy binning scheme,  $f_{\text{hit}}$  and Neural Network (NN), the time needed to compute expected to grow. Although excessive computing time was, in part, from an intense use of a shared computing cluster, it was evident that there was room for improvement. In HAWC's next generation dSph DM search, I decided to develop codes that would utilize the multicore processors on modern high performance computing clusters. The results of this work are featured in this chapter and brought a human timing improvement to computation that scales approximately as  $1/N$  where  $N$  is the number of threads.

#### 6.2 Dataset and Background

This section enumerates the data and background methods used for HAWC's multithreaded study of dSphs. Section 6.2.1 and Section 6.2.2 are most useful for fellow HAWC collaborators looking to replicate a multithreaded dSph DM search.

##### 6.2.1 Itemized HAWC files

These files are only available within HAWC's internal documentation and collaborators. They are not meant for public access, and are presented here so that HAWC collaborators can reproduce results accurately.

- Detector Resolution: `refit-Pass5-Final-NN-detRes-zenith-dependent.root`
- Data Map: `Pass5-Final-NN-maptree-ch103-ch1349-zenith-dependent.root`
- Spectral Dictionary: `HDMspectra_dict_gamma.npy`

1293 **6.2.2 Software Tools and Development**

1294 This analysis was performed using HAL and 3ML [44, 45] in Python3. I built software  
1295 in collaboration with Michael Martin and Letrell Harris to implement the *Dark Matter Spectra*  
1296 *from the Electroweak to the Planck Scale* (HDM) [67] and dSphs spatial model from [68] for  
1297 HAWC analysis. A NumPy dictionary of HDM, `HDMspectra_dict_gamma.npy`, was made for  
1298 portability within the collaboration. These dictionaries were generated from the [git repository](#) [67].  
1299 The analysis was performed using the Neural Network energy estimator for Pass 5.F. A description  
1300 of this estimator was provided in chapter 3. [TODO: Define a subsection when it's written](#), and its  
1301 key, relevant improvements are an improved energy estimation and improved sensitivities at higher  
1302 zenith angles. All other software used for data analysis, DM profile generation, and job submission  
1303 to SLURM are also kept in my sandbox in the [Dark Matter HAWC](#) project. The above repository  
1304 also incorporates the model inputs used previously in Glory Duck, described in chapter 5, so Glory  
1305 Duck remains compatible with modern software.

1306 **6.2.3 Data Set and Background Description**

1307 The HAWC data maps used for this analysis contain 2565 days of data between runs 2104 and  
1308 7476. They were generated from pass 5.f reconstruction. The analysis is performed using the NN  
1309 energy estimator with bin list:

1310 `B1C0Ea, B1C0Eb, B1C0Ec, B1C0Ed, B1C0Ee, B2C0Ea, B2C0Eb, B2C0Ec, B2C0Ed, B2C0Ee,`  
1311 `B3C0Ea, B3C0Eb, B3C0Ec, B3C0Ed, B3C0Ee, B3C0Ef, B4C0Eb, B4C0Ec, B4C0Ed, B4C0Ee,`  
1312 `B4C0Ef, B5C0Ec, B5C0Ed, B5C0Ee, B5C0Ef, B5C0Eg, B6C0Ed, B6C0Ee, B6C0Ef, B6C0Eg,`  
1313 `B6C0Eh, B7C0Ee, B7C0Ef, B7C0Eg, B7C0Eh, B7C0Ei, B8C0Ee, B8C0Ef, B8C0Eg, B8C0Eh,`  
1314 `B8C0Ei, B8C0Ej, B9C0Ef, B9C0Eg, B9C0Eh, B9C0Ei, B9C0Ej, B10C0Eg, B10C0Eh,`  
1315 `B10C0Ei, B10C0Ej, B10C0Ek, B10C0El`

1316 Bin 0 was excluded as it has substantial hadronic contamination and poor angular resolution.

1317 Background considerations and source selection was identical to Section 5.2.3, and no additional  
1318 arguments are provided here. Many of the HAWC systematics explored in Section 5.7 also apply

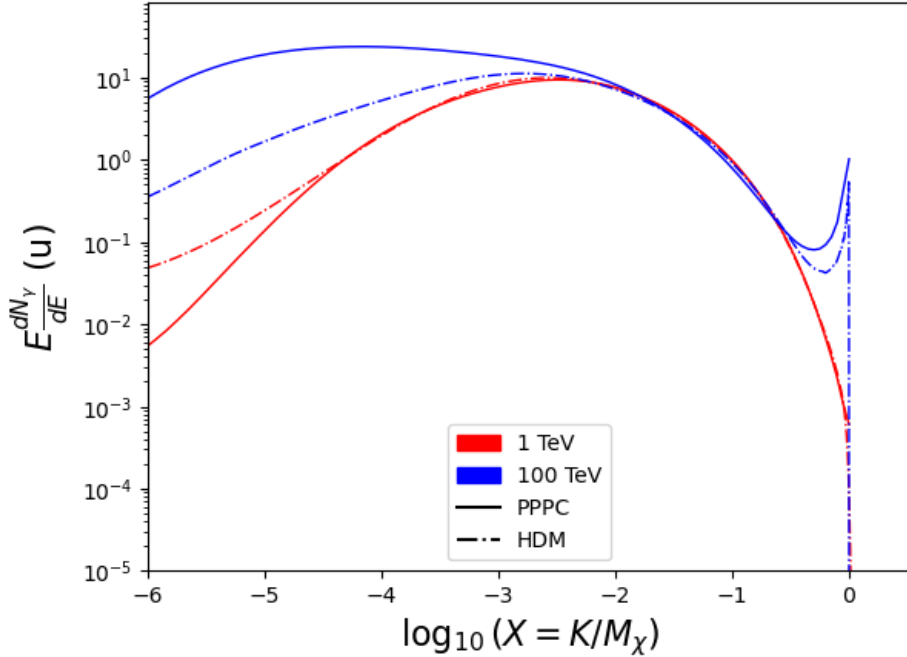


Figure 6.1 Spectral hypotheses from PPPC [46] and HDM [67] for DM annihilation:  $\chi\chi \rightarrow W^-W^+$ . Solid lines are spectral models with EW corrections from the PPPC. Dash-dot lines are spectral models from HDM. Red lines are models for  $M_\chi = 1$  TeV. Blue lines represent models for  $M_\chi = 100$  TeV.

1319 for this DM search and are not added upon here.

### 1320 6.3 Analysis

1321 The analysis and its systematics are almost identical to Section 5.3. Importantly, we use the  
 1322 same [TODO: fix this ref](#) Equation (5.1) and Equation (5.2) for estimating the gamma-ray flux at  
 1323 HAWC from our sources.

#### 1324 6.3.1 $\frac{dN_\gamma}{dE_\gamma}$ - Particle Physics Component

1325 For these spectra, we import HDM with Electroweak (EW) corrections and additional correc-  
 1326 tions for neutrinos above the EW scale [67]. The spectra are implemented as a model script in  
 1327 astromodels for 3ML. A comprehensive description of EW corrections and neutrino considerations  
 1328 are provided later in Sec. 8.

1329 Figure 6.1 demonstrates the impact of changes implemented in HDM on DM annihilation to W  
 1330 bosons. A class in astromodels was developed to include HDM and is aptly named `HDMspectra`  
 1331 within `DM_models.py`. The SM DM annihilation channels studied here are  $\chi\chi \rightarrow$ :

1332       $e^+e^-$ ,  $\mu^+\mu^-$ ,  $\tau^+\tau^-$ ,  $b\bar{b}$ ,  $t\bar{t}$ ,  $gg$ ,  $W^+W^-$ ,  $ZZ$ ,  $c\bar{c}$ ,  $u\bar{u}$ ,  $d\bar{d}$ ,  $s\bar{s}$ ,  $\nu_e\bar{\nu}_e$ ,  $\nu_\mu\bar{\nu}_\mu$ ,  $\nu_\tau\bar{\nu}_\tau$ ,  $\gamma\gamma$ ,  $hh$ .

1333 For  $\gamma\gamma$  and  $ZZ$ , a substantial fraction of the signal photons are expected to have  $E_\gamma = m_\chi$  [67].  
 1334 This introduces  $\delta$ -function that is much narrower than the energy resolution of the HAWC detector.  
 1335 To ensure that this feature is not lost in the likelihood fits, the 'line' feature is convolved with a  
 1336 Gaussian kernel with a  $1\sigma$  width of  $0.05 \cdot m_\chi$  and total kernel window of  $\pm 4\sigma$ . This differs from  
 1337 HAWC's previous line study where 30% of HAWC's energy resolution was used for the kernel [69].  
 1338 The NN energy estimator's strength compared to  $f_{\text{hit}}$  at low gamma-ray energy enables narrower  
 1339 kernels [67].  $\chi\chi \rightarrow \gamma\gamma$  and  $ZZ$  spectral hypotheses are shown in Figure 6.2. We did not explore  
 1340 how well we reconstruct injected signal events for various kernels widths. This is a systematic  
 1341 that should be tested before publication to journal. Spectral models for the remaining annihilation  
 1342 channels are plotted for each  $m_\chi$  in Figure B.1.

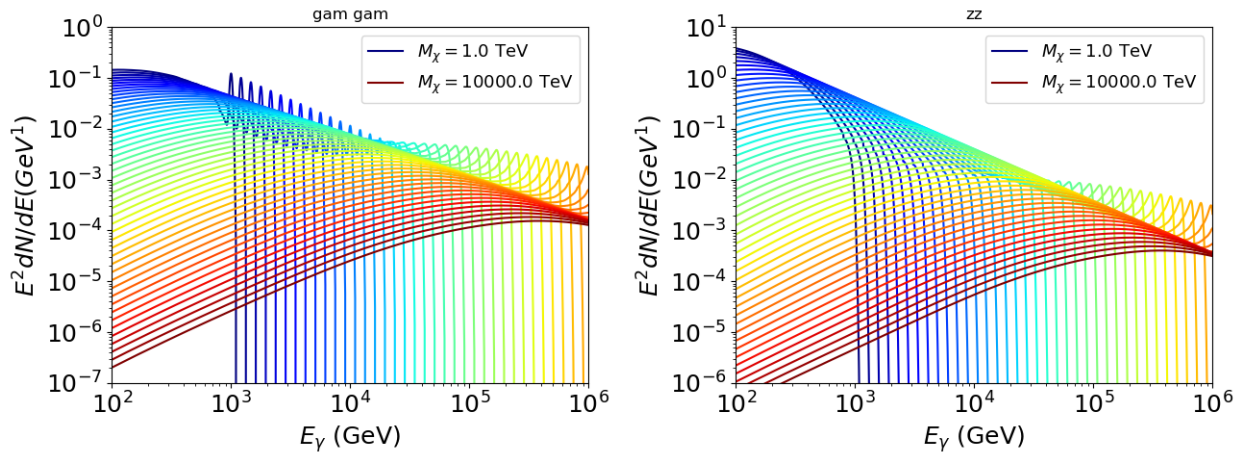


Figure 6.2 Photon spectra for  $\chi\chi \rightarrow \gamma\gamma$  (left) and  $\chi\chi \rightarrow ZZ$  (right) after Gaussian convolution of line features. Both spectra have  $\delta$ -features at photon energies equal to the DM mass. Bluer lines are annihilation spectra with lower DM mass. Redder lines are spectra from larger DM mass. All spectral models are sourced from the Heavy Dark Matter models [67]. Axes are drawn roughly according to the energy sensitivity of HAWC.

1343 **6.3.2 J Astrophysical Components**

1344 The J-factor profiles for each source are imported from Louis Strigari et al. (referred to with  
 1345  $\mathcal{LS}$ ) [68]. The  $\mathcal{LS}$  catalog fits a Navarro–Frenk–White (NFW) [50] spatial DM distributions to

1346 the dSphs which has a DM density of

$$\rho(r) = \frac{\rho_0}{\frac{r}{R_s} \left(1 + \frac{r}{R_s}\right)^2}. \quad (6.1)$$

1347  $\rho_0$  and the scale radius,  $R_s$  are free parameters fit for each dSph.  $r$  is the distance from the center  
1348 of the dSph.

1349 Profiles in  $\frac{dJ}{d\Omega}(\theta)$  up to an angular separation  $\theta = 0.5^\circ$  were provided directly from the authors.

1350 Map generation from these profiles were almost identical to Section 5.3.2 except that a higher order  
1351 trapezoidal integral was used for the normalization of the square, uniformly-spaced map:

$$p^2 \cdot \sum_{i=0}^N \sum_{j=0}^M w_{i,j} \frac{dJ}{d\Omega}(\theta_{i,j}, \phi_{i,j}) \quad (6.2)$$

1352  $p$  is the angular side of one pixel in the map.  $w_{i,j}$  is a weight assigned the following ways:

1353  $w_{i,j} = 1$  if  $(\theta_{i,j}, \phi_{i,j})$  is fully within the region of integration

1354  $w_{i,j} = 1/2$  if  $(\theta_{i,j}, \phi_{i,j})$  is on an edge of the region of integration

1355  $w_{i,j} = 1/4$  if  $(\theta_{i,j}, \phi_{i,j})$  is on a corner of the region of integration

1356 Figure 6.3 shows the median and  $\pm 1\sigma$  maps used as input for this DM annihilation study.

### 1357 6.3.3 Source Selection and Annihilation Channels

1358 HAWC's sources for this multithreaded analysis include Coma Berenices, Draco, Segue 1, and  
1359 Sextans.  $\mathcal{LS}$  observed up to 43 sources in its publication, however only 4 of the best fit profiles  
1360 were provided at the time this thesis was written. A full description of each source used in this  
1361 analysis is found in Table 6.1.

1362 This analysis improves on chapter 5 in the following ways. Previously, the particle physics  
1363 model used for gamma-ray spectra from DM annihilation was from the PPPC [46] which missed  
1364 important considerations relevant for the neutrino sector. HDM is used to account for this shortfall  
1365 [67]. HDM also models DM to the Planck scale which permits HAWC to probe PeV scale DM. For  
1366 this study, we sample DM masses: 1 TeV - 10 PeV with 6 mass bins per decade in DM mass. In

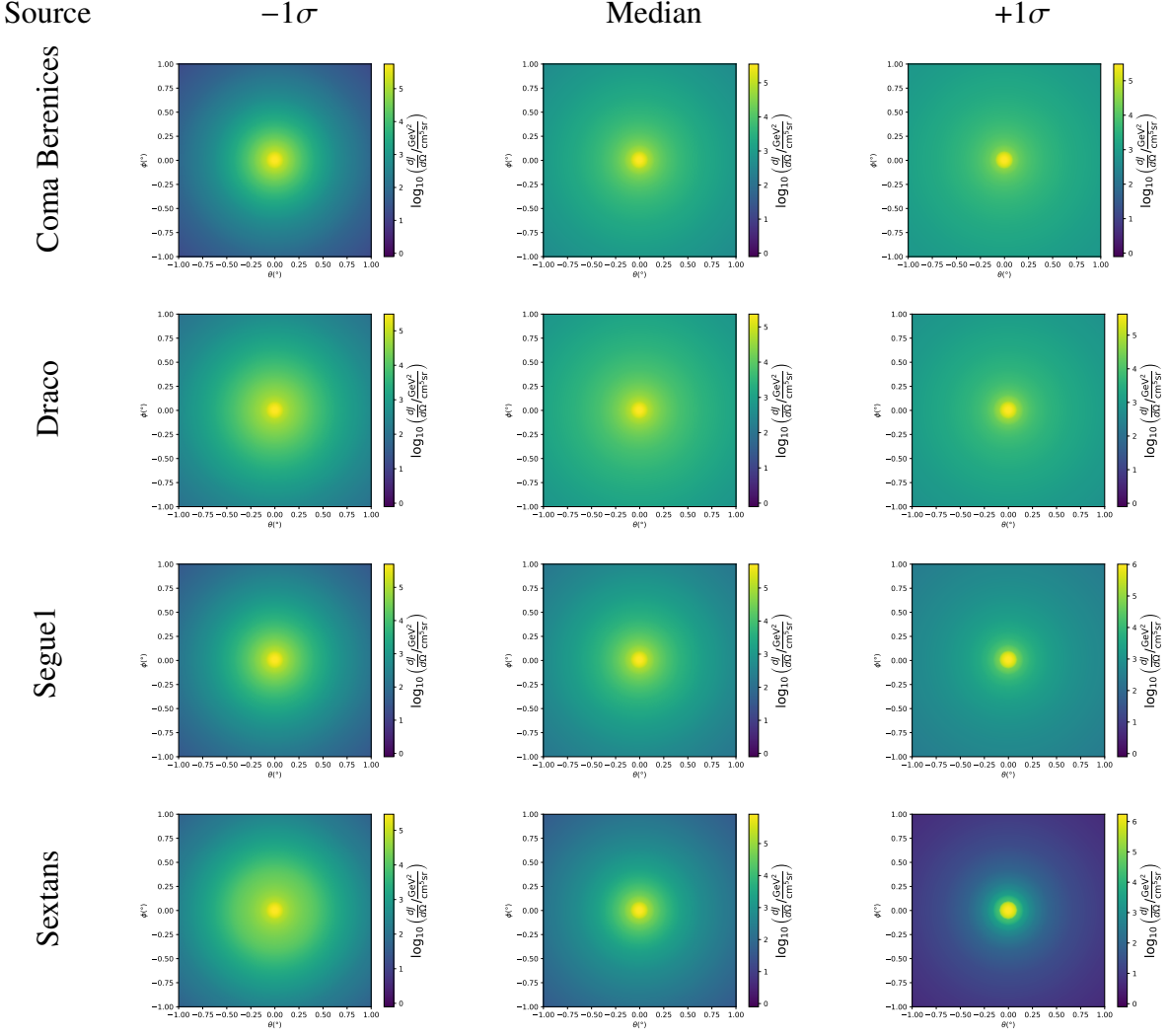


Figure 6.3  $\frac{dJ}{d\Omega}$  maps for Coma Berenices, Draco, Segue1, and Sextans. Columns are divided for the  $\pm 1\sigma$  uncertainties in  $dJ/d\Omega$  around the mean value from  $\mathcal{LS}$  [68]. Origin is centered on the specific dwarf spheroidal galaxies (dSph).  $\theta$  and  $\phi$  axes are the angular separation from the center of the dwarf. Profiles are truncated at  $1^\circ$  and flattened beyond.

the case of line spectra ( $\chi\chi \rightarrow \gamma\gamma$ , or  $ZZ$ ), we double the mass binning to 12 DM mass bins per decade in DM mass.

$\mathcal{LS}$  provides 25 sources within HAWC's field of view. Additionally, NFW [50] DM distributions have fewer parameters than Zhao [49], so  $\mathcal{LS}$  fits ultra-faint dwarves which expands the number of sources. However, all sources were not provided by the authors in time for the completion of this dissertation. Finally, the gamma-ray ray dataset is much larger. The study performed here analyzes 2565 days of data compared to 1017 days analyzed in chapter 5.

1374 **6.4 Likelihood Methods**

1375 These are identical to Section 5.4.1 and no additional changes are made to the likelihood. Bins  
 1376 in this analysis are expanded to include HAWC’s NN energy estimator.

1377 **6.5 Computational Methods: Multithreading**

1378 Previously, as in Section 5.3, the likelihood was minimized for one model at a time. One model  
 1379 in this case representing a DM annihilation channel (CHAN), DM mass ( $m_\chi$ ), and dSph ((SOURCE)).  
 1380 In an effort to conserve human and CPU time, jobs submitted for high performance computing  
 1381 contained a list of  $m_\chi$  to iterate over for likelihood fitting. Jobs were then trivially parallelized  
 1382 for each permutation of the two lists: CHANS and SOURCES. The lists for CHANS and SOURCES are  
 1383 found in Section 6.3.1 and Table 6.1, respectively. Initially, 11  $m_\chi$  were serially sampled for one  
 1384 job defined by a [CHAN, SOURCE] tuple. Computing the likelihoods would take between 1.5 to 2 hrs,  
 1385 stochastically, for a job. We expect to compute likelihoods for data and 300 Poisson background  
 1386 trials. The estimated CPU time based on the above for all CHAN (N = 17) and SOURCE (M = 25)  
 1387 was estimated to 127,925 jobs. In total, 1,407,175 likelihood fits and profiles would be computed  
 1388 for the 11 mass bins we wished to study. The estimated CPU time ranged between 8k CPU days  
 1389 to 10k CPU days. Human time is more challenging to estimate as job allocation is stochastic and  
 1390 highly dependent on what other users are submitting. Yet, it is unlikely that all jobs would run  
 1391 simultaneously. Therefore, we can expect human time to be about as long as was seen in chapter 5

Name	Distance (kpc)	$l, b$ ( $^\circ$ )	$\log_{10} J$ ( $\mathcal{LS}$ set) $\log_{10}(\text{GeV}^2\text{cm}^{-5}\text{sr})$
Coma Berenices	44	241.89, 83.61	$19.00^{+0.36}_{-0.35}$
Draco	76	86.37, 34.72	$18.83^{+0.12}_{-0.12}$
Segue I	23	220.48, 50.43	$19.12^{+0.49}_{-0.58}$
Sextans	86	243.50, 42.27	$17.73^{+0.13}_{-0.12}$

Table 6.1 Summary of the relevant properties of the dSphs used in the present work. Column 1 lists the dSphs. Columns 2 and 3 present their heliocentric distance and galactic coordinates, respectively. Column 4 reports the  $J$ -factors of each source given from the  $\mathcal{LS}$  studies and estimated  $\pm 1\sigma$  uncertainties. The values  $\log_{10} J$  ( $\mathcal{LS}$  set) [68] correspond to the mean  $J$ -factor values for a source extension truncated at  $0.5^\circ$ .

1392 which was on the order of months to fully compute on a smaller analysis. A visual aid to describe  
 1393 how jobs were organized is provided in Figure 6.4.

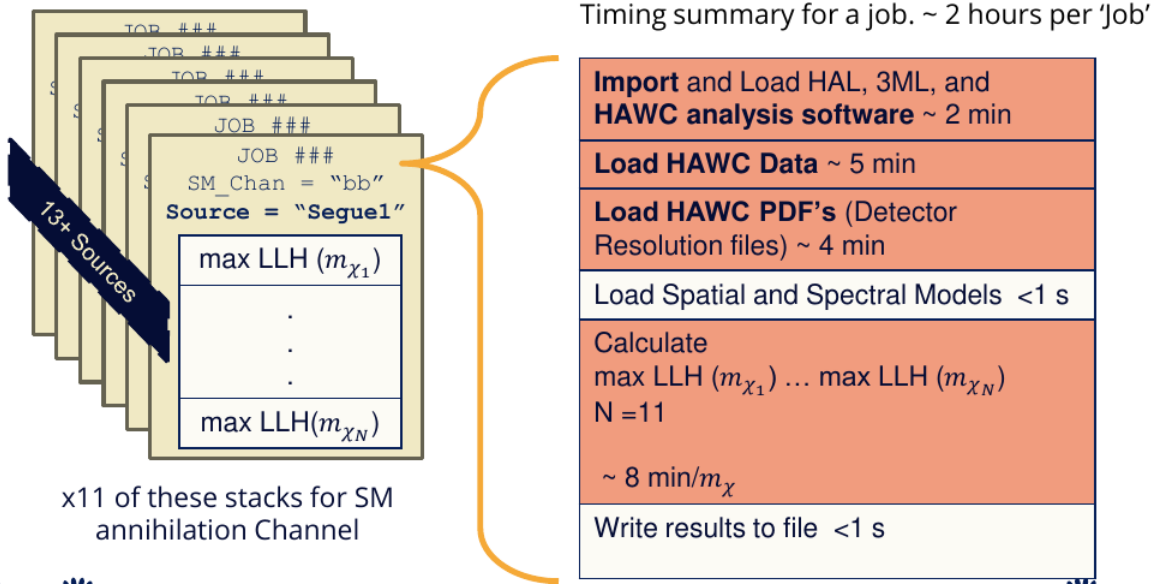


Figure 6.4 Infographic on how jobs and DM computation was organized in Section 5.3. Jobs were built for each permutation of CHANS and SOURCES shown by the left block in the figure. Each job, which took on the order 2 hrs to compute, had the following work flow: 1. Import HAWC analysis software, 2 min to run. 2. Load HAWC count maps, 5 min to run. 3. Load HAWC energy and spatial resolutions, 4 min. 5. Load DM spatial source templates and spectral models, less than 1 s. 6. Perform likelihood fit on data and model, about 8 min per DM mass. 7. Write results to file, less than 1s.

1394 The computational needs for this next generation DM analysis are extreme and is unlike other  
 1395 analyses performed on HAWC. It became clear that there was a lot to gain from optimizing how  
 1396 the likelihoods are computed. This section discusses how multi-threading was applied to solve and  
 1397 reduce HAWC's computing of likelihoods for large parameter spaces like in DM searches.

### 1398 6.5.1 Relevant Foundational Information

1399 The profiling of the likelihood for HAWC is done via gradient descent where the normalization  
 1400 of Equation (5.1) (linearly correlated with  $\langle \sigma v \rangle$ ) is rescaled in the descent. Additionally, we sample  
 1401 the likelihood space for a defined list of  $\langle \sigma v \rangle$ 's described in Section 5.4.2. The time to compute  
 1402 these values is not predictable or consistent because many variables can change across the full  
 1403 model-space. Comprehensively, these variables are:

1404     •  $m_\chi$  : DM rest mass  
 1405     • CHAN : DM annihilation channel in SM.  
 1406     • SOURCE : dSph. Involves a spatial template AND coordinate in HAWC data.  
 1407     •  $\langle\sigma v\rangle$ : Effectively the flux normalization and free parameter in the likelihood fit.  
 1408   Therefore, we develop an asynchronous, functional-parallel coding pattern. Asynchronous meaning  
 1409   the instructions within a function are independent and permitted to be out of sync with sibling  
 1410   computations. Functional-parallel meaning that instructions are the subject of parallelization  
 1411   rather than threading the likelihood computation. This is close to trivial parallelization seen in  
 1412   Figure 6.4 except that we seek to consolidate the loading stages (software, data, and detector  
 1413   resolution loading). Multiple asynchronous threads are expected to reduce total serial processing  
 1414   time and total overhead across the entire project in addition to saving human time.

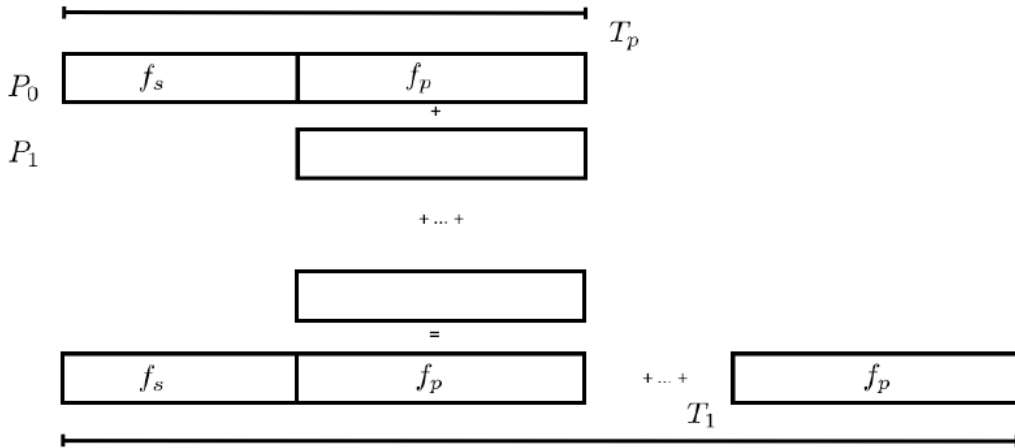


Figure 6.5 Graphic of Gustafson parallel coding pattern.  $f_s$  is the fraction of a program, in time, spent on serial computation.  $f_p$  is the fraction of computing time that is parallelizable.  $T_p$  is the total time for a parallel program to run.  $T_1$  is the total time for a parallel program to run if only 1 processor is allocated.  $P_N$  is the  $N$ -th processor where it's row is the computation the processor performs. The Gustafson pattern is most similar to what is implemented for this analysis. Figure is pulled from [70].

1415   We need a way to measure and compare the expected speedup and efficiency gain for this  
 1416   asynchronous coding pattern. I pull inspiration for timing measurement from [70] and use *Amdahl's*

1417 law with hybrid programming. Hybrid programming meaning that the computation is a mix of  
 1418 distributed and shared memory programming. If we assume the code is fully parallelizable over  $p$   
 1419 processors and  $c$  threads, the ideal speedup is simply  $pc$ , and ideal run-time is  $T_1/(pc)$ .  $T_1$  is the  
 1420 total time for a parallel program to run if only 1 processor is allocated. However, the coding pattern  
 1421 contains some amount of unavoidable serial computation, as shown in Figure 6.5. In our case, the  
 1422 run time,  $T_{p,c}$ , is estimated to be

$$T_{p,c} = \frac{T_1}{pc} (1 + F_s(c - 1)). \quad (6.3)$$

1423  $F_s$  is the fraction of CPU time dedicated to serial computation. The expected speedup,  $S_{p,c}$ , is

$$S_{p,c} \equiv \frac{T_1}{T_{p,c}} = \frac{pc}{1 + F_s(c - 1)}. \quad (6.4)$$

1424 From Equation (6.4), we can see that the speed-up scales with  $p/F_s$ . We are free to minimize  $F_s$   
 1425 asymptotically by enlarging the total models that are submitted to the thread pool, thereby shrinking  
 1426 the CPU fraction dedicated to serial operation. We are also free to define exactly how many threads  
 1427 and processors we utilize, yet eventually hit a hard cap at the hardware available on our computing  
 1428 cluster. HAWC uses Intel Xeon™processors with 48 cores and 96 threads. We see that a successful  
 1429 code will scale well as the expected speedup is inversely correlated with  $F_s$ . As the total number  
 1430 of models sampled grows, the speedup will also.

### 1431 6.5.2 Implementation

1432 The multithreaded code was written in Python3 and is documented in the `dark_matter_hawc`  
 1433 [repository](#) within the script named `mpu_analysis.py`. A version of the script as of April 25  
 1434 **TODO: make sure to update on this date** is also provided in Section B.2. It has many dependencies  
 1435 including the HAWC analysis software. Figure 6.6 displays the workflow of a job with 3 threads.  
 1436 Within a job, SOURCE is kept fixed and CHANS remains 17 elements long. More  $m_\chi$  are sampled  
 1437 from 11 bins up to 49 (for  $\gamma\gamma$  and ZZ) and 25 (for remaining CHANS) which amounts to 12 or 6  
 1438 mass bins per decade.  $m_\chi$  and CHANS are permuted into a 473 element list which is split evenly  
 1439 across N threads where N is [2, 8, 16]. For each  $m_\chi$ -CHAN tuple, 1001  $\langle\sigma v\rangle$  values are sampled in

Timing summary for a multi-threaded job.

Import and Load HAL, 3ML, and <b>HAWC analysis software</b> ~ 2 min		
Load HAWC Data ~ 5 min		
Load HAWC PDF's (Detector Resolution files) ~ 4 min		
Load Spatial Model < 1s		
Load Spectra Models <1 s	Load Spectra Models <1 s	Load Spectra Models <1 s
Calculate max LLH (Chan_0, $m_{\chi_1}$ ) ... max LLH (Chan_?, $m_{\chi_N}$ ) N = TOTAL/N_THREADS  ~ 8 min/Spec_model	Calculate max LLH (Chan_?, $m_{\chi_1}$ ) ... max LLH (Chan_?, $m_{\chi_N}$ ) N = TOTAL/N_THREADS  ~ 8 min/Spec_model	Calculate max LLH (Chan_?, $m_{\chi_1}$ ) ... max LLH (Chan_?, $m_{\chi_N}$ ) N = TOTAL/N_THREADS  ~ 8 min/Spec_model
Write results to file <1 s	Write results to file <1 s	Write results to file <1 s
Join Threads and terminate < 1s		

Figure 6.6 Task chart for one multithreaded job developed for this project. Green blocks indicate a shared resource across the threads AND computation performed serially. Red blocks indicate functional parallel processing within each thread. 3 threads are represented here, yet many more can be employed during the full analysis. Jobs are defined by the SOURCE as these require unique maps to be loaded into the likelihood estimator. The  $m_{\chi}$ , CHAN, and  $\langle \sigma v \rangle$  variables are entered into the thread pool and allocated as evenly as possible across the threads.

- 1440 the likelihood, and the value of  $\langle \sigma v \rangle$  that maximizes the likelihood is found. Although rare, fits  
 1441 that failed are handled on a case by case basis.

### 1442 6.5.3 Performance

M Tasks	$T_{p,c}$ (hr:min:s)			
	$T_{1,1}$	$T_{1,2}$	$T_{1,8}$	$T_{1,16}$
50	1:40:37.5	0:52:43.7	0:19:13.8	0:13:44.0
74	2:22:30.0	1:15:00.6	0:25:21.3	0:15:49.8
100	(3:07:51.9)	1:40:10.5	0:30:44.4	0:20:01.4
200	(6:02:20.6)	-	1:00:32.0	0:30:35.0
473	(13:58:40.3)	-	2:01:41.4	1:07:53.2

Table 6.2 Timing summaries for analyses for serial and multithreaded processes. M tasks is the number of functional-parallel tasks ran for the computation.  $T_{p,c}$  is a single run time in hours:minutes:seconds for runs utilizing  $p$  nodes and  $c$  threads. Runs are run interactively on the same computer to maximize consistency. Empty entries are indicated with '-'. (·) entries are estimated entries extrapolated from data earlier in the column.

- 1443 We see a significant reduction to wall time needed for our dSph analyses to run. Table 6.2

1444 shows the timing summaries for analyses of different sizes and thread counts. Additionally, the  
 1445 efficiency gained when consolidating the serial loading of data is also apparent in our ability to  
 1446 study many more tasks in about the same amount of wall time as a smaller serial computation. Trials  
 1447 represented in the table were run on an AMD Opteron® processor 6344 with 48 cores, 2 threads per  
 1448 core; 2.6 GHz clock. This is not the same architecture used for analysis on the HAWC computing  
 1449 cluster however they are similar enough that results shown here are reasonably representative of  
 1450 computing on the HAWC computing cluster. I use Tab. 6.2 for the inferences and conclusions in  
 1451 the following paragraphs.

1452 First, we want to find  $T_s$ , the time of serial computation. From Fig. 6.5, the timing for our  
 1453 coding pattern can be written as

$$T_s + Mt_p = T_{1,1}^M. \quad (6.5)$$

1454  $M$  is the number of functional-parallel tasks (represented as column 1 of Tab. 6.2), and  $t_p$  is the  
 1455 average time to complete a single parallel task.  $T_{1,1}^M$  is the total time for a parallel program to run if  
 1456 only 1 processor is allocated for  $M$  parallel task. With two runs of different  $M$  ( $M_1$  and  $M_2$ ), we  
 1457 can use a system of equations to compute

$$T_s = 803.1\text{s} \text{ and } t_p = 104.6\text{s} \quad (6.6)$$

1458 Now, we have specific estimation for the fraction of serial computing time,  $F_s$ :

$$F_s = \frac{803.1}{803.1 + 104.6 \cdot M}. \quad (6.7)$$

1459 The maximum  $M$  for this study is 473 which evaluates to:  $F_s = 0.016$  or 1.6% of computing time.  
 1460 Table 6.3 shows the resulting speedups.

1461 We see a speedup that generally exceeds expectations from Eq. (6.4) for real trail runs. We also  
 1462 see that there are diminishing returns as the number of threads increases. For small jobs with large  $c$ ,  
 1463 both the expected and observed speedup are significantly smaller than  $c$ . One thing not considered  
 1464 in Eq. (6.4) is the time incurred via communication latency. Communication latency increases  
 1465 with the number of threads and contributes to diminishing returns. Additionally, these values are

M Tasks	$F_s$	$S_{1,2}$	$S_{1,8}$	$S_{1,16}$
50	1.33 E-1	1.90 [1.76]	5.23 [4.14]	6.35 [5.34]
74	9.40 E-2	1.90 [1.83]	5.62 [4.82]	9.00 [6.64]
100	7.13 E-2	1.88 [1.87]	6.11 [5.34]	9.38 [7.73]
200	3.70 E-2	- [1.93]	5.98 [6.36]	11.85 [10.29]
473	1.60 E-2	- [1.97]	6.89 [7.20]	12.35 [12.91]

Table 6.3 Speed up summaries for analyses for serial and multithreaded processes. M tasks is the number of functional-parallel tasks ran for the computation.  $S_{p,c}$  is a single speedup comparison for runs utilizing  $p$  nodes and  $c$  threads. [·] are the estimated speedups calculated from Tab. 6.2, Eq. (6.7), and Eq. (6.4). Empty entries are indicated with '-'.

1466 for single runs and do not consider the stochastic variation expected in a shared high performance  
 1467 computing resource. Therefor, these results are not strictly conclusive, yet demonstrate the merits  
 1468 of multi-threading. We see very clearly that there is a lot to gain, and this new coding pattern will  
 1469 expand HAWC's analysis capabilities.

## 1470 6.6 Analysis Results

1471 3 of the 43  $\mathcal{L}\mathcal{S}$  dSphs considered for the multithreaded analysis. These dSph are analyzed  
 1472 for emission from DM annihilation according to the likelihood method described in Section 5.4.  
 1473 The three likelihood profiles are then stacked to synthesize a combined limit on the dark matter  
 1474 annihilation cross-section,  $\langle\sigma v\rangle$ . This combination is done each of the 17 SM annihilation channels.  
 1475 Figure 6.7 and Fig. 6.8 show the combined limits for all annihilation channels with HAWC's  
 1476 observations. Test statistics of the best fit  $\langle\sigma v\rangle$  values for each  $m_\chi$  and CHAN are shown in Fig. 6.9  
 1477 and Fig. 6.10. We also compare these limits to HAWC's Glory Duck limits shown in Section 5.5.  
 1478 The comparison to Glory Duck are featured in Fig. 6.11 for all the DM annihilation channels studied  
 1479 for Glory Duck. A full comparison is provided in the appendix in Fig. B.2, Fig. B.3, and Fig. B.4.  
 1480 Here, we show updated limits for  $\chi\chi \rightarrow b\bar{b}, e\bar{e}, \mu\bar{\mu}, \tau\bar{\tau}, t\bar{t}, W^+W^-$ ,  $\gamma\gamma$  and  $ZZ$ . For the first time  
 1481 ever, we show limits for  $\chi\chi \rightarrow c\bar{c}, s\bar{s}, u\bar{u}, d\bar{d}, \nu_e\bar{\nu}_e, \nu_\mu\bar{\nu}_\mu, \nu_\tau\bar{\nu}_\tau, gg$ , and  $hh$ .

1482 No DM was found in HAWC observations. The largest excess found in HAWC data was for DM  
 1483 annihilating to  $W$ -bosons or  $\nu_e\bar{\nu}_e$  for  $m_\chi = 10$  TeV at significance  $2.11\sigma$  and  $2.14\sigma$  respectively.  
 1484 HAWC's limits and excesses are dominated by Segue1. Coma Berenices shows excesses at higher  
 1485 DM mass, yet no similar excesses were observed in Segue1 or Sextans. Sextans did not contribute

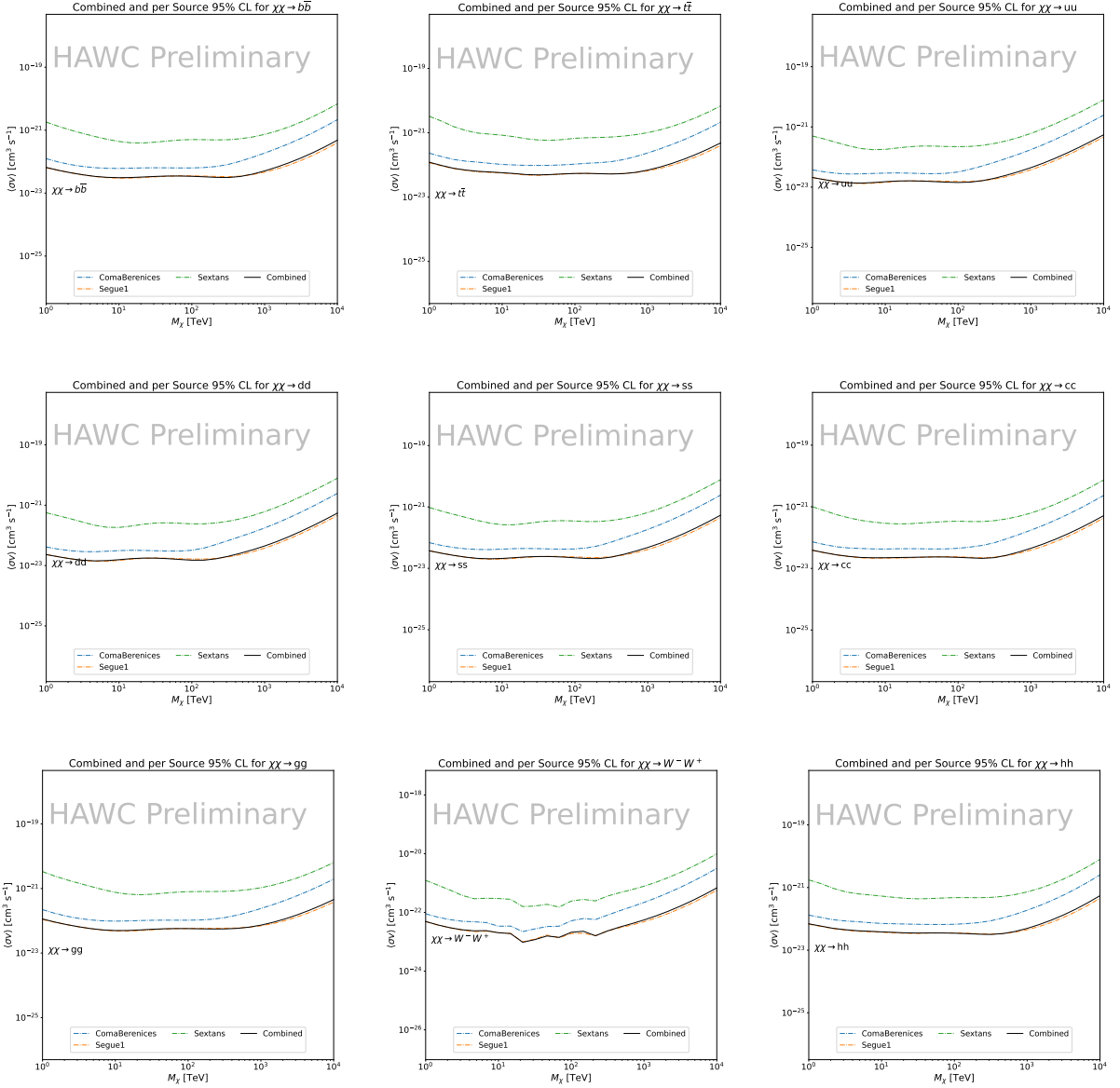


Figure 6.7 HAWC upper limits at 95% confidence level on  $\langle\sigma v\rangle$  versus  $m_\chi$  for  $\chi\chi \rightarrow b\bar{b}$ ,  $t\bar{t}$ ,  $u\bar{u}$ ,  $d\bar{d}$ ,  $s\bar{s}$ ,  $c\bar{c}$ ,  $gg$ ,  $W^+W^-$ , and  $hh$ . Limits are with  $\mathcal{L}\mathcal{S}$   $J$ -factors [68]. The solid line represents the observed combined limit. Dashed lines represent limits from individual dSphs.

1486 significantly to signal excesses or the combined limit as it is at high zenith. Draco was not included  
 1487 as the PDF of some of our analysis bins were wider than what is reasonable for a point source  
 1488 analysis. Draco is at a high zenith for HAWC, so the effort required to include it was not justified  
 1489 by the benefits.

1490 We did not generate background trials in time of writing this thesis. These are not shown and

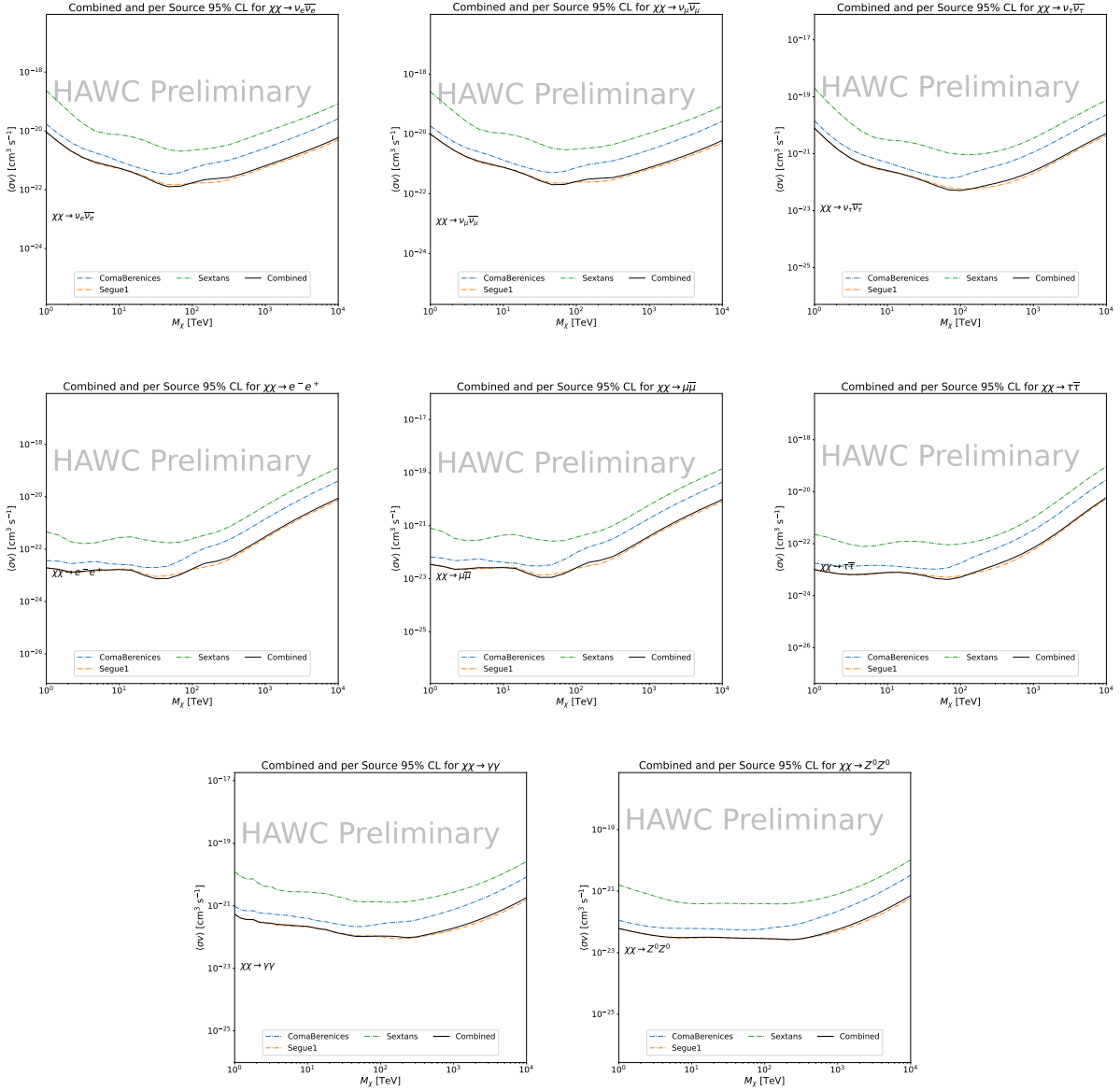


Figure 6.8 HAWC upper limits at 95% confidence level on  $\langle\sigma v\rangle$  versus  $m_\chi$  for  $\chi\chi \rightarrow \nu_e \bar{\nu}_e$ ,  $\nu_\mu \bar{\nu}_\mu$ ,  $\nu_\tau \bar{\nu}_\tau$ ,  $e \bar{e}$ ,  $\mu \bar{\mu}$ ,  $\tau \bar{\tau}$ ,  $\gamma\gamma$  and  $ZZ$ . Limits use  $\mathcal{L}S$   $J$ -factors [68]. The solid line represents the observed combined limit. Dashed lines represent limits from individual dSphs.

1491 are an immediate next step for this analysis before publication.

1492 When comparing these results to Section 5.5, we see an overall decrease to the confidence limit  
 1493 therefore improvement to HAWC's expected sensitivity. This improvement is generally stronger  
 1494 than a doubling of data, or a factor  $\sqrt{2}$  decrease. The comparison is somewhat complex and  
 1495 dependent on the dSph and SM annihilation channel. Figure 6.11 shows the comparisons of limits

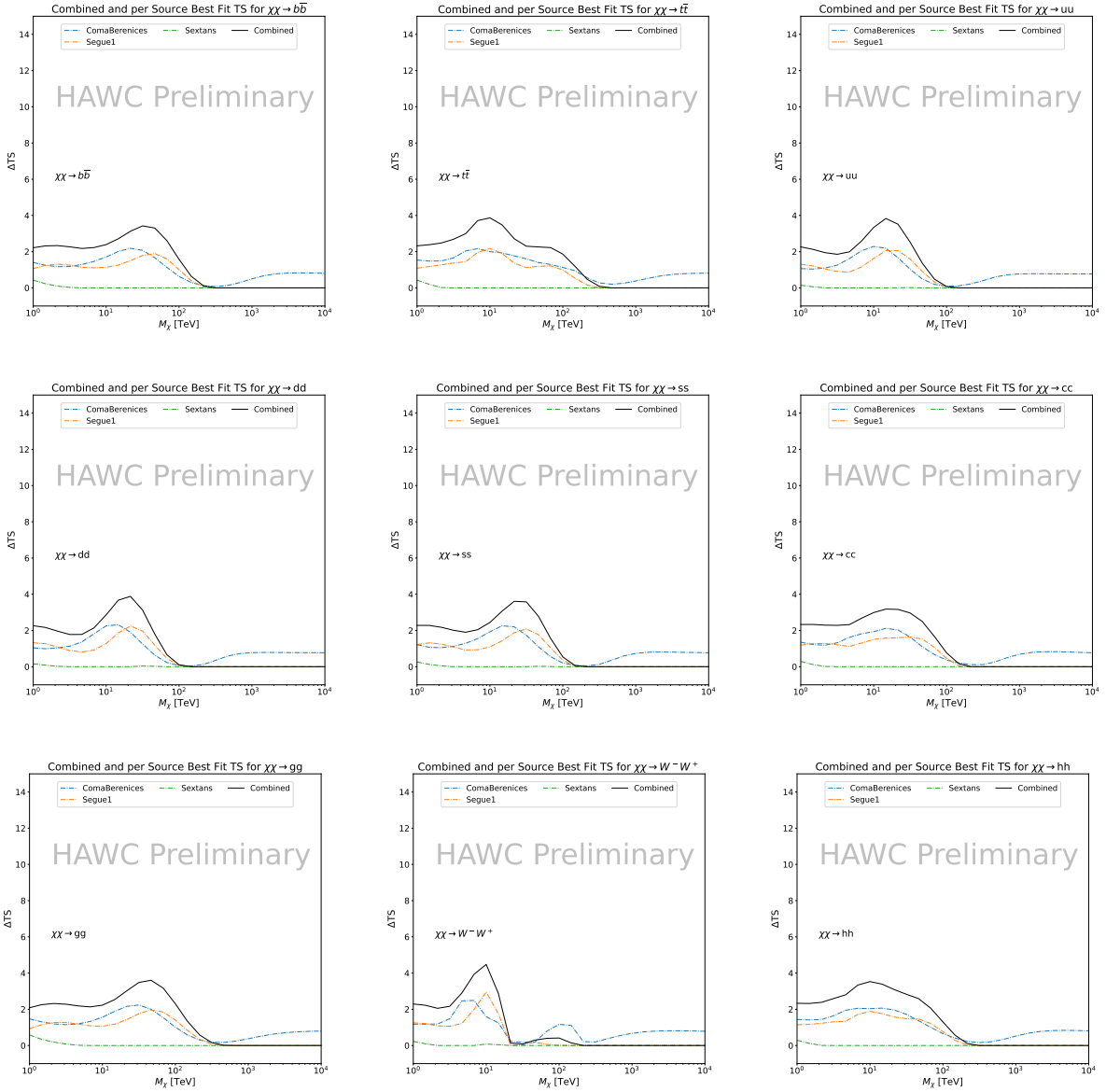


Figure 6.9 HAWC TS values for best fit  $\langle\sigma v\rangle$  versus  $m_\chi$  for SM annihilation channels:  $\chi\chi \rightarrow b\bar{b}$ ,  $t\bar{t}$ ,  $u\bar{u}$ ,  $d\bar{d}$ ,  $s\bar{s}$ ,  $c\bar{c}$ ,  $gg$ ,  $W^-W^+$ , and  $hh$ . Limits use  $\mathcal{LS}$   $J$ -factors. The solid black line shows the combined best fit TS values. The colored, dashed lines are the TS values from each dSph.

1496 calculated for this analysis and Glory Duck (Section 5.5). Segue 1 and Coma Berenices are low  
 1497 zenith where improvements to HAWC's analysis come only from energy estimation. Differences  
 1498 between these two are dominantly from their differences in  $J$ -factor, half-light radii of the dSphs,  
 1499 and the particle physics inputs. Substantial gains in HAWC's analysis methods (pass 5.F) were  
 1500 made at high zenith which is important for sources like Sextans. The HDM particle physics model

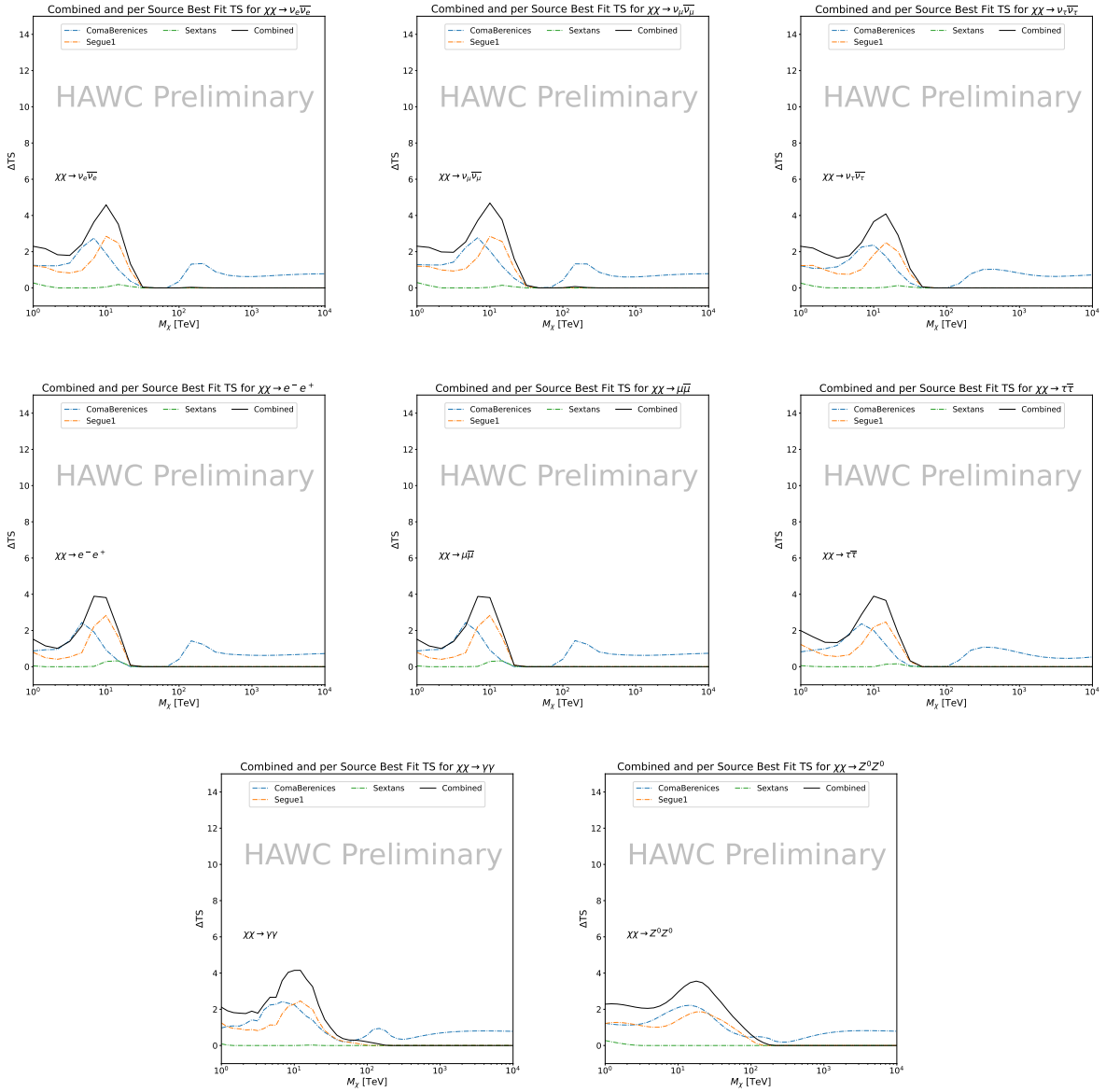


Figure 6.10 HAWC TS values for best fit  $\langle\sigma v\rangle$  versus  $m_\chi$  for SM annihilation channels:  $\chi\chi \rightarrow \nu_e \bar{\nu}_e$ ,  $\nu_\mu \bar{\nu}_\mu$ ,  $\nu_\tau \bar{\nu}_\tau$ ,  $e^- e^+$ ,  $\mu \bar{\mu}$ ,  $\tau \bar{\tau}$ ,  $\gamma\gamma$  and  $ZZ$ . Limits use  $\mathcal{LS}$   $J$ -factors. The solid black line shows the combined best fit TS values. The colored, dashed lines are the TS values from each dSph.

1501 produces almost identical spectra to the PPPC for  $\chi\chi \rightarrow e^- e^+$ . This channel can be used to  
 1502 compare limits between dSph spatial models. Overhead sources see minimal improvement to the  
 1503 limits, while high zenith sources see an order of magnitude improvement for all DM masses. Softer  
 1504 SM annihilation channels see broad improvements to the limit compared to harder channels.

1505 **6.7 Systematics**

1506     Systematics to this analysis are identical to what was performed earlier in Glory Duck, Sec-  
1507     tion 5.7. We are also sensitive to the choice in spatial template, and this was explored in Section 5.7.2  
1508     and Section 5.8.2.

1509 **6.8 Conclusion and Discussion**

1510     In this multithreaded analysis, we have used observations of 3 dSphs from HAWC to perform  
1511     a collective DM annihilation search towards dSphs. The data were combined across sources  
1512     to significantly increase the sensitivity of the search. Advanced computational techniques were  
1513     deployed to accelerate wall-time spent analyzing by an order of magnitude. We have observed  
1514     no significant deviation from the null, no DM hypothesis, and so present our results in terms of  
1515     upper limits on the velocity-weighted cross-section,  $\langle\sigma v\rangle$ , for seventeen potential DM annihilation  
1516     channels across four decades of DM mass.

1517     This analysis serves as a proof of concept for multithreaded HAWC analyses with large parameter  
1518     spaces. Larger datasets with fast techniques will be essential to tackling the DM problem. The  
1519     models we used for this study include annihilation channels with neutrinos in the final state.  
1520     Advanced studies could aim to merge our results with those from neutrino observatories with large  
1521     data sets.

1522     A full HAWC analysis will include systematic studies of the  $J$ -factor distributions. Additionally,  
1523     because of the timing reduction, the study can be doubled in size to include DM decay. We have not  
1524     yet received the remaining spatial profiles to the  $\mathcal{LS}$  catalog, and limits can be quickly computed  
1525     once these are received. Finally, statistical studies with Poisson variation of HAWC's background  
1526     are essential to a comprehensive understanding of our observed excesses.

Segue1

Coma Berenices

Sextans

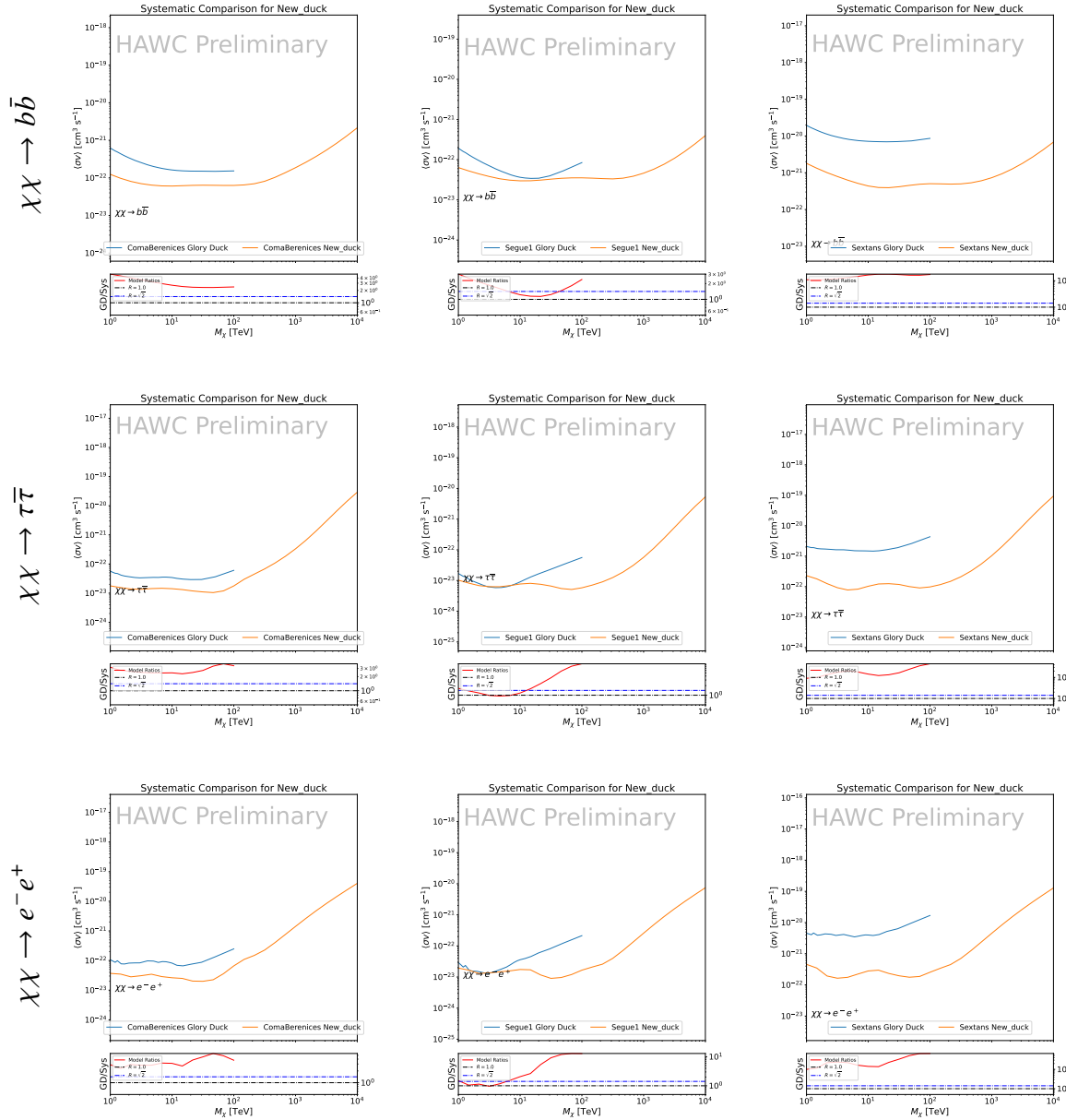


Figure 6.11 Comparison of HAWC limits from this analysis to Glory Duck (Fig. 5.5) for 3 dSphs and 3 DM annihilation channels:  $b\bar{b}$ ,  $\tau\bar{\tau}$ , and  $e^-e^+$ . Each sector shows the 95% confidence limit from Glory Duck (blue line) and this analysis (orange line) in the top plot. The lower plot features the ratio in log scale of Glory Duck to this analysis in a red solid line. Horizontal dashed lines are for ratios of 1.0 (black) and  $\sqrt{2}$  (blue). Ratios larger than 1.0 are for limits smaller, or stricter, than Glory Duck. Ratios larger than  $\sqrt{2}$  indicates limits are stricter than a simple doubling of the Glory Duck data.

## CHAPTER 7

### HEAVY DARK MATTER ANNIHILATION SEARCH WITH ICECUBE'S NORTH SKY TRACK DATA

#### 7.1 Introduction

Neutrinos are another astrophysical messenger than can travel long distances without significant attenuation or deflection. Additionally, Neutrinos come in three flavors which triples the multiplicity of the particles we are searching for. Uniquely, they interact less readily than photons especially above PeV energies. Neutrinos therefore provide another window through which we can perform dark matter searches.

The previous IceCube DM annihilation analysis towards dwarf galaxies was performed in 2013 [71] which, in technical terms, is more than a minute ago. This is in spite of IceCube's crucial sensitivity afforded from neutrino spectral lines [72]. A lot has changed in IceCube since its previous DM annihilation search such as, additional strings, more sophisticated analysis methods, and more accurate theory modeling. It has come time for IceCube to make a DM dSph contribution.

IceCube is sensitive to annihilating DM for DM masses above 1 TeV. Additionally, IceCube's sensitivity is comparable gamma-ray observatories in spectral models that produce hard neutrino features. The goal of this analysis is to perform a DM annihilation search using the Northern Sky Tracks datasets. The search will only be towards dwarf spheroidal galaxies (dSph) for the strengths mentioned in Section 5.3.3. These sources are treated as point sources for IceCube with little loss to sensitivity or model dependence on how the DM is distributed. DM masses from 500 GeV to 100 PeV are considered for this analysis. Several DM annihilation channels available from the HDMspectra [67] are studied in this analysis. This chapter presents the analysis work for IceCube to update our DM searches toward dSphs.

#### 7.2 Dataset and Background

This section enumerates the data and background methods used for IceCube's study of dSphs. Section 7.2.1 and Section 7.2.2 are most useful for fellow IceCube collaborators looking to replicate this analysis.

1553 **7.2.1 Itemized IceCube files**

1554 These files are only available within IceCube’s internal documentation and wikis. They are not  
1555 meant for public access, and are presented here so that IceCube collaborators can reproduce results  
1556 accurately.

1557 • Software Environment: CVMFS Py3-v4.1.1

1558 • Data Sample: Northern Tracks NY86v5p1

1559 • Analysis Software: csky ([nu\\_dark\\_matter](#))

1560 • Analysis wiki: [https://wiki.icecube.wisc.edu/index.php/Dark\\_Matter\\_Annihilation\\_Search\\_towards\\_dwarf\\_spheroidals\\_with\\_NST\\_and\\_DNN\\_Cascades](https://wiki.icecube.wisc.edu/index.php/Dark_Matter_Annihilation_Search_towards_dwarf_spheroidals_with_NST_and_DNN_Cascades)

1562 • Project repository

1563 **7.2.2 Software Tools and Development**

1564 This analysis was performed inside IceCube’s CVMFS (3.4.1.1) software environment using  
1565 csky for likelihood calculations. Csky at first did not come with dark matter spectral models nor  
1566 could accommodate custom flux models. We developed these capacities for single source and  
1567 stacked source studies for this analysis. The analysis code is held in a separate repository from  
1568 csky. The [nu\\_dark\\_matter branch of csky](#) manages the input of custom dark matter spectra and  
1569 accompanied DM astrophysical source. Csky also enables the use of multithreading which was  
1570 shown to be crucial for DM searches (see Sec. 6). Csky then calculates likelihoods with a selected  
1571 data sample. The [IceCube Dark Matter dSph repository](#) manages the generation of spectral models  
1572 for neutrinos, physics parameter extraction from  $n_{\text{sig}}$ ,  $J$ -factor per source inputs, and bookkeeping  
1573 for the large parameter space. The project repository required a secondary software environment  
1574 for neutrino oscillations. How to launch and run those calculations are documented in the project  
1575 repository and the Docker image is additionally saved in Section C.1.

1576 **7.2.3 Data Set and Background Description**

1577 For this analysis, I use the Northern Sky Tracks (NST) Sample (Version V005-P01). The sample  
1578 contains up-going track-like events, usually from  $\nu_\mu$  and  $\nu_\tau$ , with a superior angular resolution  
1579 compared to the cascade dataset. This sample covers 10.4 years of data (IC86\_2011-2021). The  
1580 accepted neutrino energy range used for the analysis is unique from most other IceCube searches  
1581 because DM spectra are hard with large contributions close to  $E_\nu = m_\chi$ . Therefore, the sampled  
1582 energy range is  $1 < \log(E_\nu/\text{GeV}) < 9.51$  with step size 0.125.

1583 The strengths of a dwarf analysis is that there are no additional background considerations  
1584 beyond nominal, baseline background estimations (see Section 5.2.3). For NST, the nominal  
1585 contributions come from atmospheric neutrinos and isotropic astrophysical neutrinos. We estimate  
1586 the background by scrambling NST data along Right Ascension.

1587 **7.3 Analysis**

1588 The expected differential neutrino flux from DM-DM annihilation to standard model particles,  
1589  $d\Phi_\nu/dE_\nu$ , over solid angle,  $\Omega$  is described by the familiar equation.

$$\frac{d\Phi_\nu}{dE_\nu} = \frac{\langle\sigma\nu\rangle}{8\pi m_\chi^2} \frac{dN_\nu}{dE_\nu} \times \int_{\text{source}} d\Omega \int_{l.o.s} \rho_\chi^2 dl(r, \theta') \quad (7.1)$$

1590 This is identical to Eq. (5.1) except that there are 3 neutrino flavors, so there are a corresponding  
1591 3 flux equations. Section 5.3 has a complete description of each term in Eq. (7.1). Additionally,  
1592 neutrinos oscillate between flavors which needs to be considered for the expected neutrino flux  
1593 at Earth. Section 7.3.1 presents the particle physics model and processing for DM annihilation.  
1594 Section 7.3.2 presents the spatial distributions built for each dSph.

1595 **7.3.1  $\frac{dN_\nu}{dE_\nu}$  - Particle Physics Component**

1596 Neutrino spectra from heavy DM annihilation were generated using HDMspectra [67] and  
1597  $\chi$ arov [73]. HDMspectra has tables for the decay and annihilation of heavy DM for different  
1598 dark DM and SM primary annihilation channels. The simulation includes electroweak or gluon  
1599 radiative corrections and higher order loop corrections from the  $W$  and  $Z$  bosons ( $WWZ$  and  $WW\gamma$ ).  
1600 These corrections are especially important for accurately estimating the prompt neutrino flux. This

1601 publication also pushes the simulated DM mass to the Plank scale (1 EeV), however this study will  
1602 not explore that high.

1603 An important feature in the spectra is that neutrino line channels will be accompanied by a low  
1604 energy tail [67], see Fig. 7.1. Thus, the Earth will not fully attenuate a heavy neutrino line-like  
1605 signal from high declination sources where the neutrino flux must first traverse through the Earth.  
1606 The DM annihilation channels that feature lines include all leptonic channels:  $\nu_{e,\mu,\tau}$ ,  $e$ ,  $\mu$ , and  $\tau$ . We  
1607 use the `xarov` software to propagate and oscillate the neutrinos from the source to Earth. Because  
1608 these sources are quite large in absolute terms, and also far (order 10 kpc or more), the resulting  
1609 flavor spectra are the averages of the transition probabilities [73]:

$$P(\nu_\alpha \rightarrow \nu_\beta) \approx \begin{bmatrix} 0.55 & 0.18 & 0.27 \\ 0.18 & 0.44 & 0.38 \\ 0.27 & 0.38 & 0.35 \end{bmatrix} \quad (7.2)$$

1610 Examples of the spectra before and after propagation are shown in Fig. 7.1.

1611 When calculating the expected contribution to  $n_s$ , only  $\nu_\mu$  and  $\nu_\tau$  are considered as NST's  
1612 effective area to  $\nu_e$  is negligible [74]. Therefore, the expected composite neutrino spectrum is the  
1613 sum of the two flavors:  $\frac{dN\nu_\mu}{dE\nu_\mu} + \frac{dN\nu_\tau}{dE\nu_\tau}$ . The spectral tables are then converted to splines to condense  
1614 information, enable random sampling of the spectra, and reduce computing times. The spectral  
1615 splines are finally implemented as a DM class in csky.

### 1616 7.3.1.1 Treatment of Neutrino Line Features

1617 All DM annihilation channels into leptons  $\chi\chi \rightarrow [\nu_{e,\mu,\tau}, e, \mu, \tau]$  develop a prominent and  
1618 narrow spectral line feature. For all neutrino flavors, this line is visible and prominent in all  $m_\chi$   
1619 studied in this analysis. For charged leptons, the feature typically manifests at  $m_{ch} > 10$  TeV, yet  
1620 its prominence varies slightly between the flavors. Examples for lines in the annihilation spectra  
1621 with neutrinos or charged leptons are provided in Fig. 7.1.

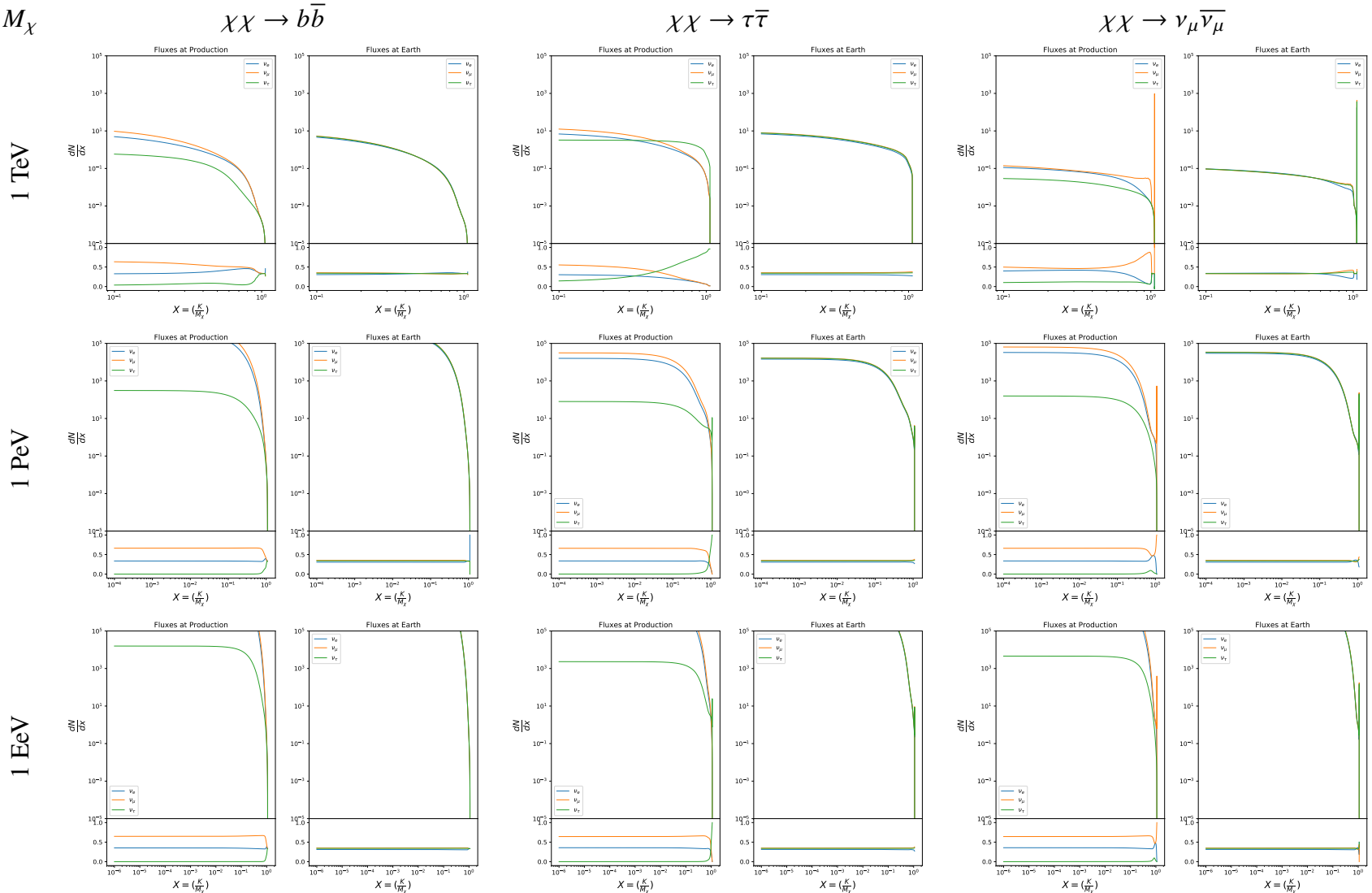


Figure 7.1 Neutrino spectra at production (left panels) and after oscillation at Earth (right panels). Blue, orange, and green lines are the  $\nu_e$ ,  $\nu_\mu$ , and  $\nu_\tau$  spectra respectively. Top panels show the spectra in  $\frac{dN}{dE}$ . Lower panels plot the flavor ratio to  $\nu_e + \nu_\mu + \nu_\tau$ . SM annihilation channels  $b\bar{b}$ ,  $\tau\bar{\tau}$ , and  $\nu_\mu \bar{\nu}_\mu$  are shown for  $M_\chi = 1 \text{ PeV}$ ,  $\text{TeV}$ , and  $\text{EeV}$ .

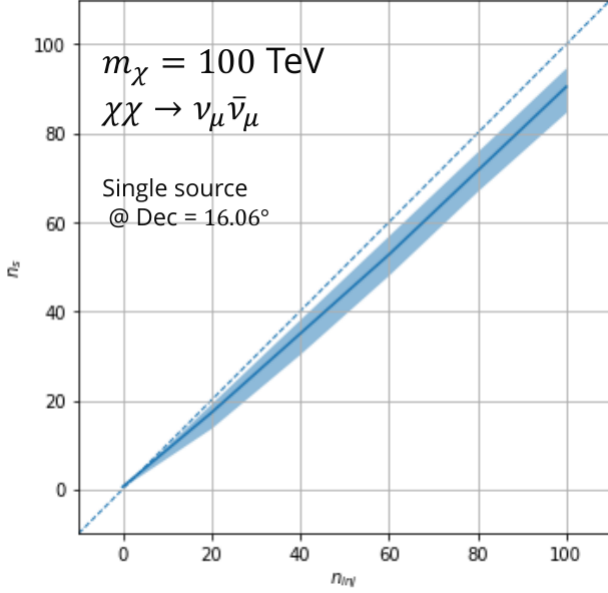


Figure 7.2 Signal recovery for 100 TeV DM annihilation into  $\nu_\mu \bar{\nu}_\mu$  for a source at Dec = 16.06°.  $n_{\text{inj}}$  is the number of injected signal events in simulation.  $n_s$  is the number of reconstructed signal events from the simulation data. Although the uncertainties are small and tight, the reconstructed  $n_s$  are systematically underestimated.

1622     The neutrino line feature is so narrow relative the sampled energy range that the random  
 1623     sampling of the spectra and likelihood fitting rarely capture the line in computation. As a result,  
 1624     often the best fit to simulation of background will always floor to TS = 0 and the signal recovery  
 1625     systematically underestimates the signal (see Fig. 7.2).

1626     To remedy this, we take a similar approach to the IceCube’s decay analysis [75] and the previous  
 1627     gamma-ray study in Section 6.3.1. Two smoothing kernels were tested (Gaussian and uniform)  
 1628     to widen the line feature. The widths were tuned such that the signal recovery approached unity  
 1629     for DM mass 100 TeV to 1 PeV for a source at Segue 1’s declination, 16.06°. Near horizon  
 1630     was chosen in order to isolate loss in signal recovery away from Earth’s attenuation of very high  
 1631     energy neutrinos and atmospheric backgrounds. The kernel convolution needed closely preserve  
 1632     the integrated counts of neutrinos. The optimized kernel parameters for all lines are summarized  
 1633     as:

- 1634     • Gaussian kernel with  $1\sigma$  width =  $1.75\text{E-}3 \cdot m_\chi$   
 1635     • Minimum energy included in convolution =  $\text{MIN}[0.995 \cdot m_\chi, E(\nu_{\text{line}}) - 4\sigma]$

- 1636 • Maximum energy included in convolution =  $\text{MAX}[1.005 \cdot m_\chi, E(\nu_{\text{line}}) + 4\sigma]$

1637 where  $E(\nu_{\text{line}})$  is the neutrino energy where the neutrino line is at the maximum.

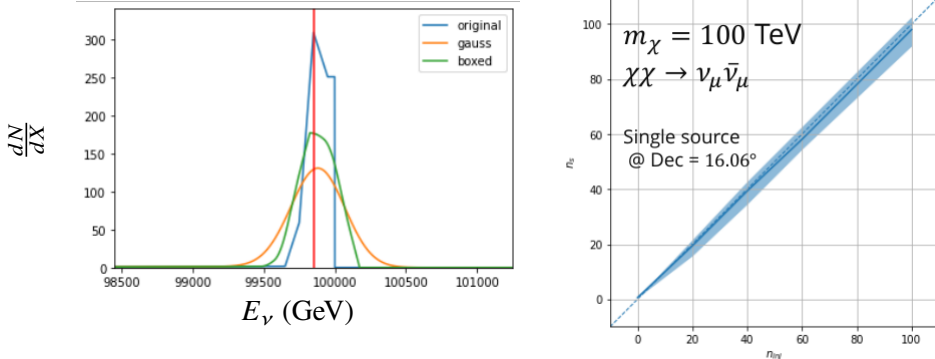


Figure 7.3 Left panel shows the two kernels overlaying the original spectrum from  $\chi\text{aron}\nu$  after propagation to Earth [73]. The vertical red line indicates where the original neutrino line is maximized. Blue line is the output from  $\chi\text{aron}\nu$ . Green line is the spectrum after convolution with a flat kernel. Orange line is the spectrum after Gaussian convolution. Right panel shows the signal recovery of the spectral model using the Gaussian kernel with parameters enumerated above.

1638 These parameters broadly improved the signal recovery of the line spectra. An example is in  
1639 Fig. 7.3. Analysis level signal recovery studies are expanded upon in Section 7.6.

### 1640 7.3.1.2 Spline Fitting

1641 In an effort to reduce computational work, memory burden, and align with point source methods  
1642 used for NGC1068 [76], spectral splines were created and adopted for estimating the neutrino flux  
1643 for the different spectral models. Software was written to generate, book keep, and calculate values  
1644 on the splines.

1645 When using splines, one has to be careful of the goodness to fit. The spline software used  
1646 here, Photospline [77], uses the penalized spline technique [78]. Through the penalized technique,  
1647 poor fits are penalized according to the accuracy of the nominal value, and the smoothness of the  
1648 first and second derivatives. However, this construction does not penalize on the integral of the  
1649 fit distribution which is critical in low signal studies, such as DM searches. There are additional  
1650 caveats when testing the goodness to fit to the MC generated above for all DM annihilation channels.

- 1651     • The splines must be Log10(\*) in Energy and dN/dX to account for the exponential nature of  
 1652       the flux.
- 1653     • The fidelity of the fit matters more at  $E_\nu \approx m_\chi$  where the model uncertainties are minimal  
 1654       and physical considerations (like the cut-off) are most important.
- 1655     • The fidelity of the fit matters less at low  $E_\nu$  as the model uncertainties are large AND  
 1656       IceCube's sensitivity diminishes significantly below 500 GeV.
- 1657     • Total integrated counts should be well-preserved.

1658   The resulting cost function was built to evaluate the goodness of spline fits to account for the above  
 1659   considerations.

$$e_i = x_i \cdot \left( \frac{dN_i}{dX_i} - 10^{\hat{e}_i} \right) \quad (7.3)$$

1660   Where  $\hat{e}_i$  is the spline estimator's value for  $x_i$ .  $x_i = E_{\nu_i}/m_\chi$ .  $\frac{dN_i}{dX_i}$  is the flux value from MC. I then  
 1661   take the RMS of the error distribution and the resulting value, err, is used to evaluate the fidelity of  
 1662   the spectral spline.

$$\text{err} = \sqrt{\frac{1}{x_{\max} - x_{\min}} \int_{x_{\min}}^{x_{\max}} e^2 dx} \quad (7.4)$$

1663    $x_{\min}$  and  $x_{\max}$  are the scope of the error evaluation and are provided in Tab. 7.1.

1664   Each SM channel had unique tolerances for 'err'. Channels with very hard cut-offs had looser  
 1665   tolerance for err because a significant error would be generated from single counts over/underes-  
 1666   timated at the cut-off. Soft channels do not share this issue, so the tolerance is much stricter. All  
 1667   annihilation channels from HDM are modeled well below IceCube's NST sensitivity which falls  
 1668   off substantially below 100 GeV [74]. We do not think it is necessary to evaluate the spline fits  
 1669   below 100 GeV and use this value as the default lower cut-off. Yet, HDM's model uncertainties  
 1670   at  $E_\nu < 10^{-6} \cdot m_\chi$  span an order of magnitude [67]. We also choose not to evaluate the splines  
 1671   below this critical value if it is within IceCube's sensitivity. Finally, the smoothing of the spectral  
 1672   lines in leptonic annihilation channels are ignored for evaluating the fit. We used the lower limit of

$\chi\chi \rightarrow$	GOOD	OK	FAIL	Limits of err calc [ $X_{min}, X_{max}$ ]
$Z^0 Z^0, W^+ W^-$	1.0E-3	1.0E-3, 1.0E-2	1.0E-2	MAX[100GeV/ $m_\chi$ , $10^{-6}$ ], 1.0
$t\bar{t}, hh$	1.0E-5	1.0E-5, 1.0E-4	1.0E-4	MAX[100GeV/ $m_\chi$ , $10^{-6}$ ], 1.0
$b\bar{b}, d\bar{d}, u\bar{u}$	9.0E-7	9.0E-7, 9.0E-6	9.0E-6	MAX[100GeV/ $m_\chi$ , $10^{-6}$ ], 1.0
$\nu\bar{\nu}_{e,\mu,\tau}$	1.0E-3	1.0E-3, 1.0E-2	1.0E-2	MAX[100GeV/ $m_\chi$ , $10^{-6}$ ], MIN[0.995, ( $E_n(\nu_{line}) - 4\sigma$ )/ $M_\chi$ ]
$e\bar{e}, \mu\bar{\mu}, \tau\bar{\tau}$	1.0E-3	1.0E-3, 1.0E-2	1.0E-2	MAX[100GeV/ $m_\chi$ , $10^{-6}$ ], MIN[0.995, ( $E_n(\nu_{line}) - 4\sigma$ )/ $M_\chi$ ]

Table 7.1 Spline err tolerances used for input in particle physics component to Eq. (5.1). Column 1 is the DM annihilation channel being fit. Columns 2, 3, and 4 are the tolerances for "GOOD" (pass), "OK" requires inspection, and "FAIL" (tune and refit) respectively. Column 5 has the X ranges over which the error is evaluated. MAX/MIN [ $\cdot, \cdot$ ] takes the maximum or minimum of the two enclosed values.

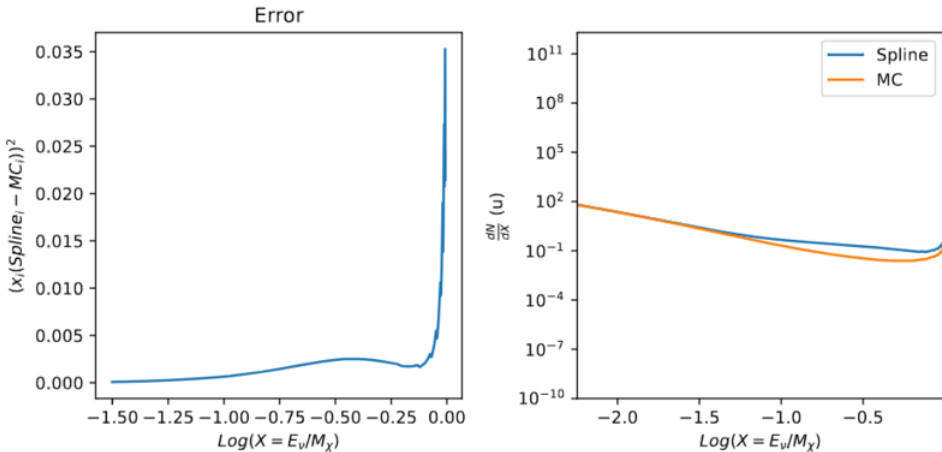


Figure 7.4 Example spline that failed the fit. Failed splined are corrected on a case by case basis unless the SM channel has a systematic problem fitting the splines. In this case, I made a bookkeeping error and loaded the incorrect spectral model

1673 the kernel mask as the upper limit of evaluation. Table 7.1 summarizes the tolerances for the DM  
 1674 annihilation channels used for this analysis.

1675 The errors are then assesed in two ways. First, FAIL and OK are directly plotted with  $e_i$  as a  
 1676 function of  $x$  with the full spline and MC. An example of a single failure is provided in Fig. 7.4.  
 1677 Second, a summary plot of all the splines is plotted and colors coded. Figure C.1 are the spline  
 1678 summaries as of writing this thesis. The goal broadly is to eliminate all red and inspect yellow  
 1679 statuses.

1680 The  $\nu_e$  spectra at Earth are not considered in this analysis, so no work was done to refine the

1681 spline fits for this flavor. Finally, I perform a visual inspection of the splines to verify that the spline  
 1682 fitting did not introduce spurious features that would corrupt the likelihood fitting.

### 1683 7.3.1.3 Composite Neutrino Spectra

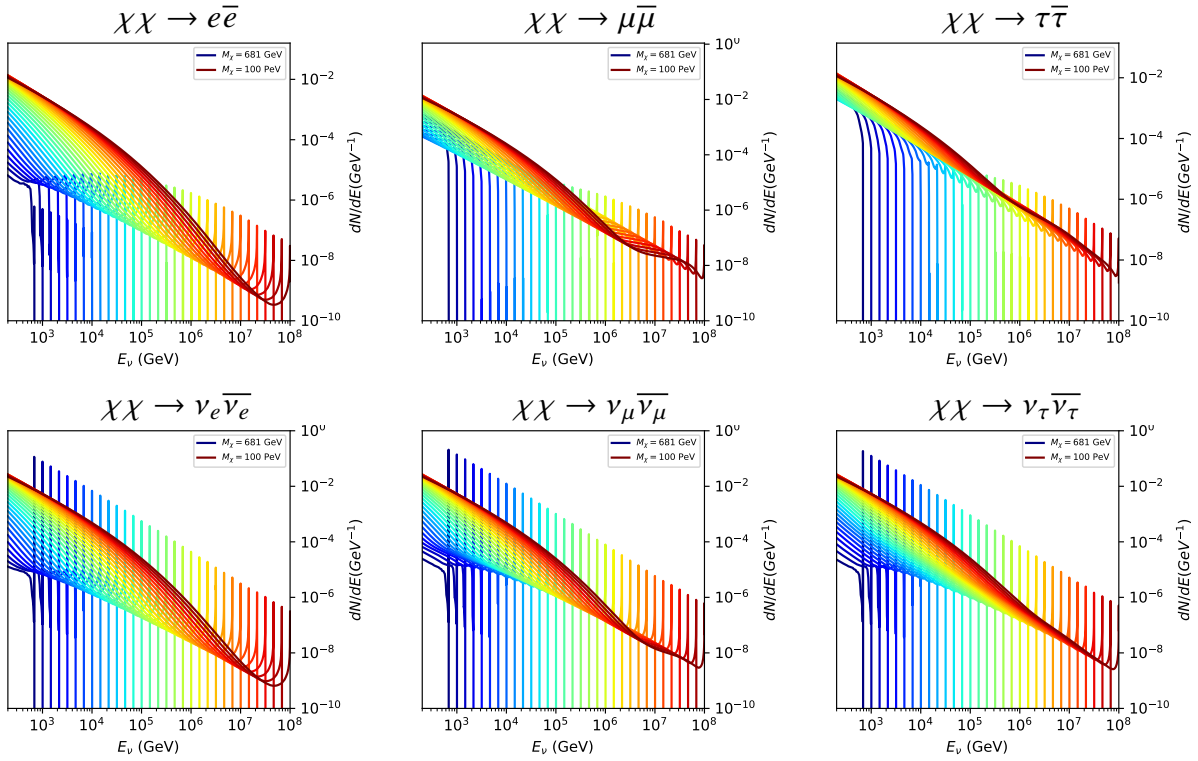


Figure 7.5 Summary of input spectral models that were smoothed with Gaussian kernels. Spectral models are for  $\chi\chi \rightarrow e\bar{e}$ ,  $\mu\bar{\mu}, \tau\bar{\tau}$ ,  $\nu_e\bar{\nu}_e$ ,  $\nu_\mu\bar{\nu}_\mu$ , and  $\nu_\tau\bar{\nu}_\tau$ . These spectra are the composite ( $\nu_\mu + \nu_\tau$ ) of neutrino flavors. Every spectral model used for this analysis is featured as a colored solid line. Bluer lines are for low  $m_\chi$  models.  $m_\chi$  ranges from 681 GeV to 100 PeV. HDM [67],  $\chi$ arov [73], and Photospline [77] are used to generate these spectra. Energy (x-axis) was chosen to roughly represent the energy sensitivity of NST.

1684 With all the previously mentioned pieces, we are ready to fully assemble a comprehensive  
 1685 description of the particle physics term  $dN/dE$  in Eq. (7.1).

$$\frac{dN_\nu}{dE_{\nu \oplus}} = \left( \frac{dN_{\nu_e}}{dE_{\nu_e}} + \frac{dN_{\nu_\mu}}{dE_{\nu_\mu}} + \frac{dN_{\nu_\tau}}{dE_{\nu_\tau}} \right)_{\text{src}} \cdot \mathbf{P}(\nu_\alpha \rightarrow \nu_\beta) \quad (7.5)$$

1686 Figure 7.5 shows the spectral models that required Gaussian smoothing, the leptonic annihilation  
 1687 channels. The remaining models where the only processing were spline fitting and neutrino  
 1688 oscillation are documented in Section C.3. Notice that the different neutrino flavors are unique,

1689 especially in their low energy tails. Therefore, this analysis will be sensitive to DM annihilating to  
1690 the distinct neutrino flavors.

### 1691 **7.3.2 J- Astrophysical Component**

1692 For this analysis, we re-adopt the  $\mathcal{GS}$  model [47] used in Sec. 5 for dSphs. These models  
1693 are based on a modified Navarro-Frenk-White (NFW) profile where the indices of the NFW  
1694 (traditionally 1,3,1) are allowed to float. The angular width of these sources is much smaller than  
1695 the angular resolution of IceCube NST [76]. We therefore treat these sources as point sources  
1696 in this analysis, and forgo generating maps. These sources and the  $\mathcal{GS}$  model have already been  
1697 discussed at length in Section 5.3.2 and is not repeated here. IceCube uses identical sources to  
1698 Tab. 5.1 except we analyze source with declinations above  $0.0^\circ$ .

### 1699 **7.3.3 Source Selection and Annihilation Channels**

1700 We use all the dSphs presented in IceCube’s previous dSph DM search [71] and expand beyond  
1701 it. IceCube’s sources for this analysis studies include Boötes I, Canes Venatici I, Canes Venatici II,  
1702 Coma Berenices, Draco, Hercules, Leo I, Leo II, Leo V, Leo T, Segue 1, Segue 2, Ursa Major I,  
1703 Ursa Major II, and Ursa Minor. A full description of all sources used is in Table 5.1. Sources with  
1704 declinations less than  $0.0$  are excluded from this analysis.

1705 This analysis improves on the previous IceCube dSph paper [71] in the following ways. Previ-  
1706 ously, the IceCube detector was not yet completed to the 86 string configuration. Many more dSphs  
1707 will be observed, from 4 to 15. Previously, the particle physics model used for neutrino spectra  
1708 from DM annihilation did not have EW corrections where they are now included [67]. The spectral  
1709 models also predict substantial differences between the neutrino flavors, so this analysis will be the  
1710 first DM dwarf analysis to discriminate between primary neutrino flavors. The study performed  
1711 here studies 10.4 years of data.

1712 The SM annihilation channels probed for this study include  $\chi\chi \rightarrow$

1713  $b\bar{b}, t\bar{t}, u\bar{u}, d\bar{d}, e\bar{e}, \mu\bar{\mu}, \tau\bar{\tau}, ZZ, W^+W^-, \nu_e\bar{\nu}_e, \nu_\mu\bar{\nu}_\mu$ , and  $\nu_\tau\bar{\nu}_\tau$

1714 **7.4 Likelihood Methods**

1715 I use the Point-Source search likelihood which is widely used in IceCube analyses. The  
1716 likelihood function is defined as the following:

$$L(n_s) = \prod_{i=1}^N \left[ \frac{n_s}{N} S_i + \left(1 - \frac{n_s}{N}\right) B_i \right] \quad (7.6)$$

1717 where  $i$  is an event index,  $S$  and  $B$  are the signal PDF and background PDF respectively. For a joint  
1718 analysis where the sources are stacked the likelihood is expanded in the simplified way:

$$L(n_s) = \prod_{i=1}^{N_{\text{sources}}} L_i(n_s) \quad (7.7)$$

1719 Where  $L_i$  is the likelihood from the  $i$ -th source in the stacked analysis. The Test Statistic (TS)  
1720 definition remains the same as Eq. (5.7)

1721 **7.5 Background Simulation**

1722 Before we look at data, we must first analyze background and signal injection to validate our  
1723 analysis. We set out to characterize the TS distributions for each source, annihilation channel, and  
1724  $m_\chi$ . Previous IceCube DM searches [75, 79] showed TS distributions that did not behave according  
1725 to a  $\chi^2$  distribution with 1 degree of freedom. TS distributions can also vary significantly between  
1726 DM mass and annihilation models. Therefore, Wilk's theorem may not be applicable to the analysis.  
1727 Instead, a critical value is defined from many background trials. We study the TS distributions  
1728 first for each source, then for the stacked analysis. The following sections show the results of the  
1729 likelihood fitting for a suite of background trials.

1730 I assume that TS values are physical:  $TS \geq 0$ .  $\epsilon[x]$  indicate the fraction of events where  $TS < x$ .  
1731 For TS plots shown here, the decimal values of  $x$  are 1.0e-2 and 1.0e-3. Each subplot represents  
1732 a simulation of 100,000 data-scrambled background trials. Section 7.5.1 show the background TS  
1733 distributions obtained from Segue 1, a source with little Earth attenuation and large  $J$ -factor, and  
1734 Ursa Major II, which has similarly large  $J$ -factor but significantly more Earth attenuation, assuming  
1735 DM annihilation into  $b\bar{b}$ ,  $\tau\bar{\tau}$ , and  $\nu_\mu\bar{\nu}_\mu$ . I show the TS distributions of a stacked study of 15 sources  
1736 for all DM annihilation channels.

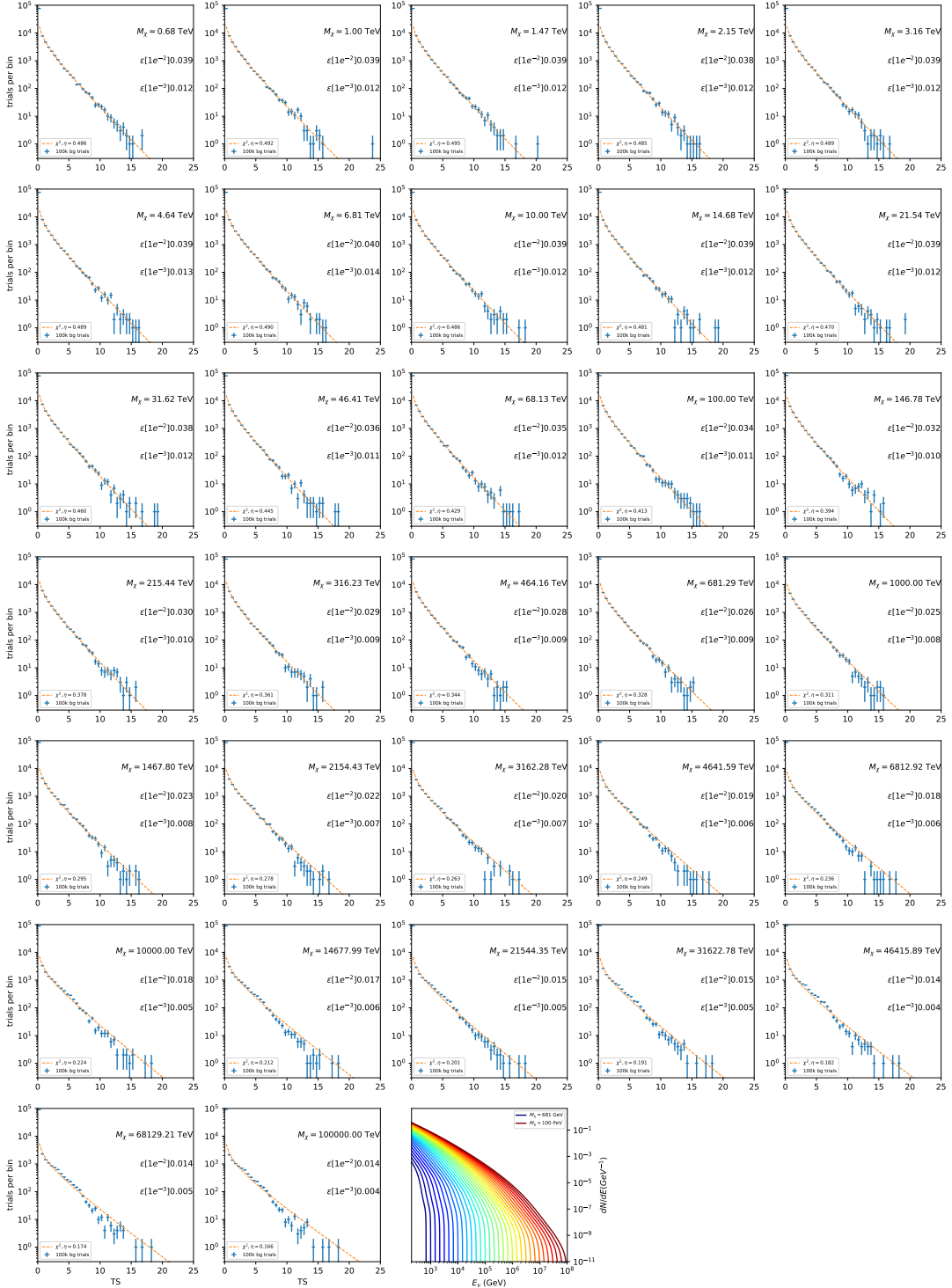


Figure 7.6 Test statistic (TS) distributions for Segue 1 and  $\chi\chi \rightarrow b\bar{b}$ . Each subplot, except the final, is the TS distribution for a specific DM mass listed in the subplot. Orange dashed lines are the traces for a  $\chi^2$  distribution with 1 degree of freedom.  $\epsilon[\cdot]$  is the fraction of trials smaller than the bracketed value. The final subplot features the all DM spectral models, similar to Fig. 7.5, used as input for the TS distributions.

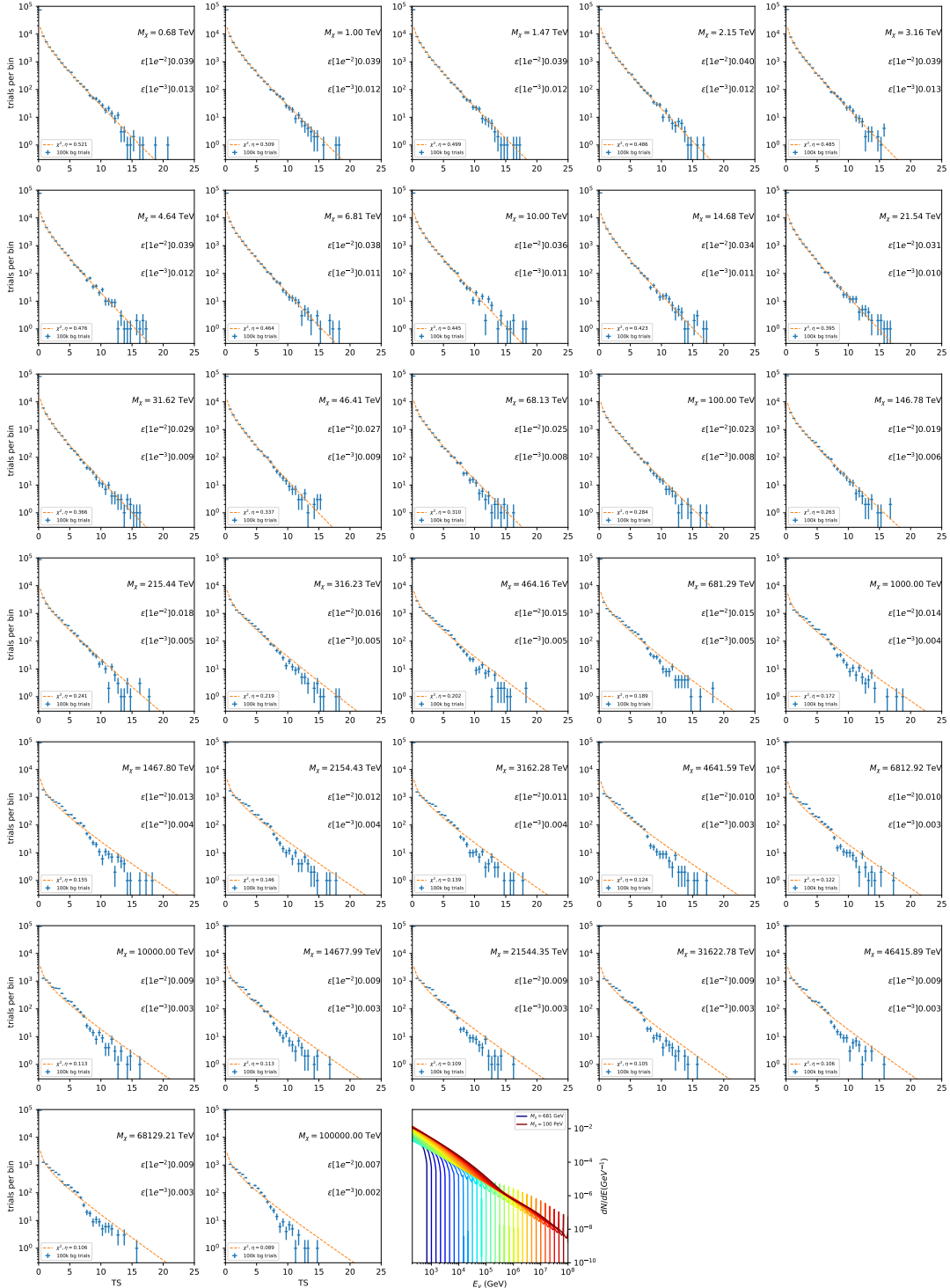


Figure 7.7 Same as Fig. 7.6 for Segue 1  $\chi\chi \rightarrow \tau\bar{\tau}$ .

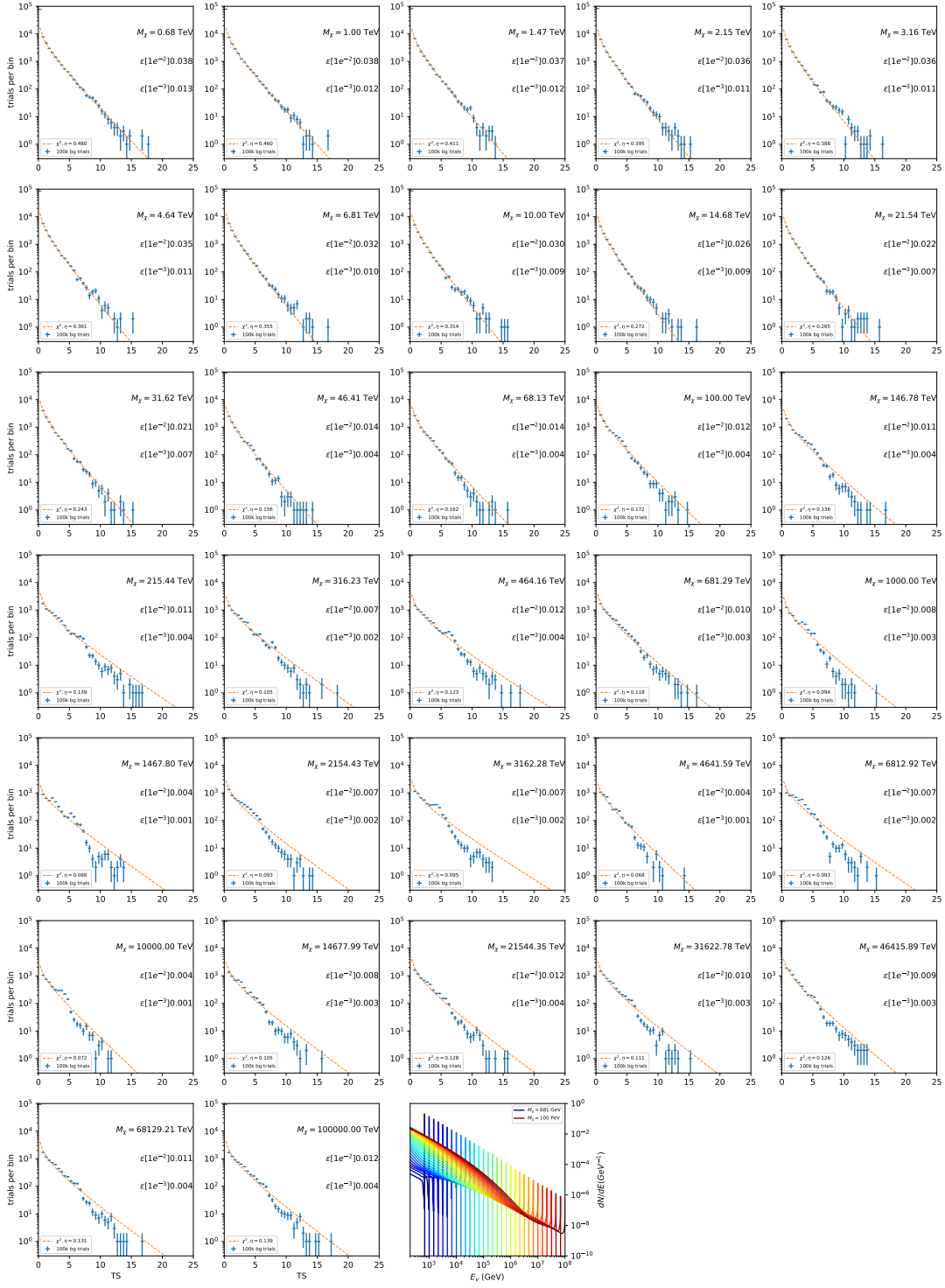


Figure 7.8 Same as Fig. 7.6 for Segue 1  $\chi\chi \rightarrow \nu_\mu\bar{\nu}_\mu$ .

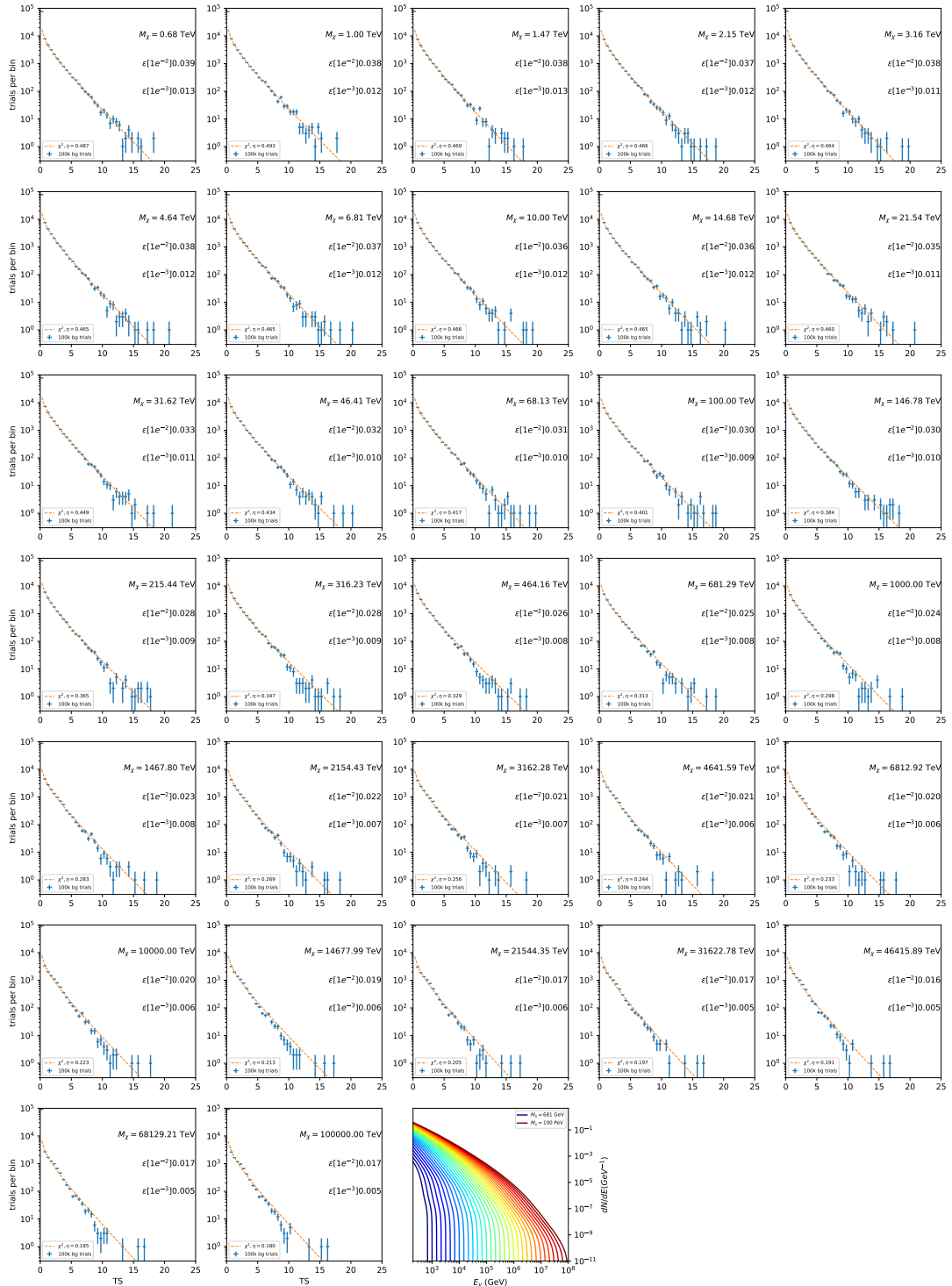


Figure 7.9 Same as Fig. 7.6 for Ursa Major II 1  $\chi\chi \rightarrow b\bar{b}$ .

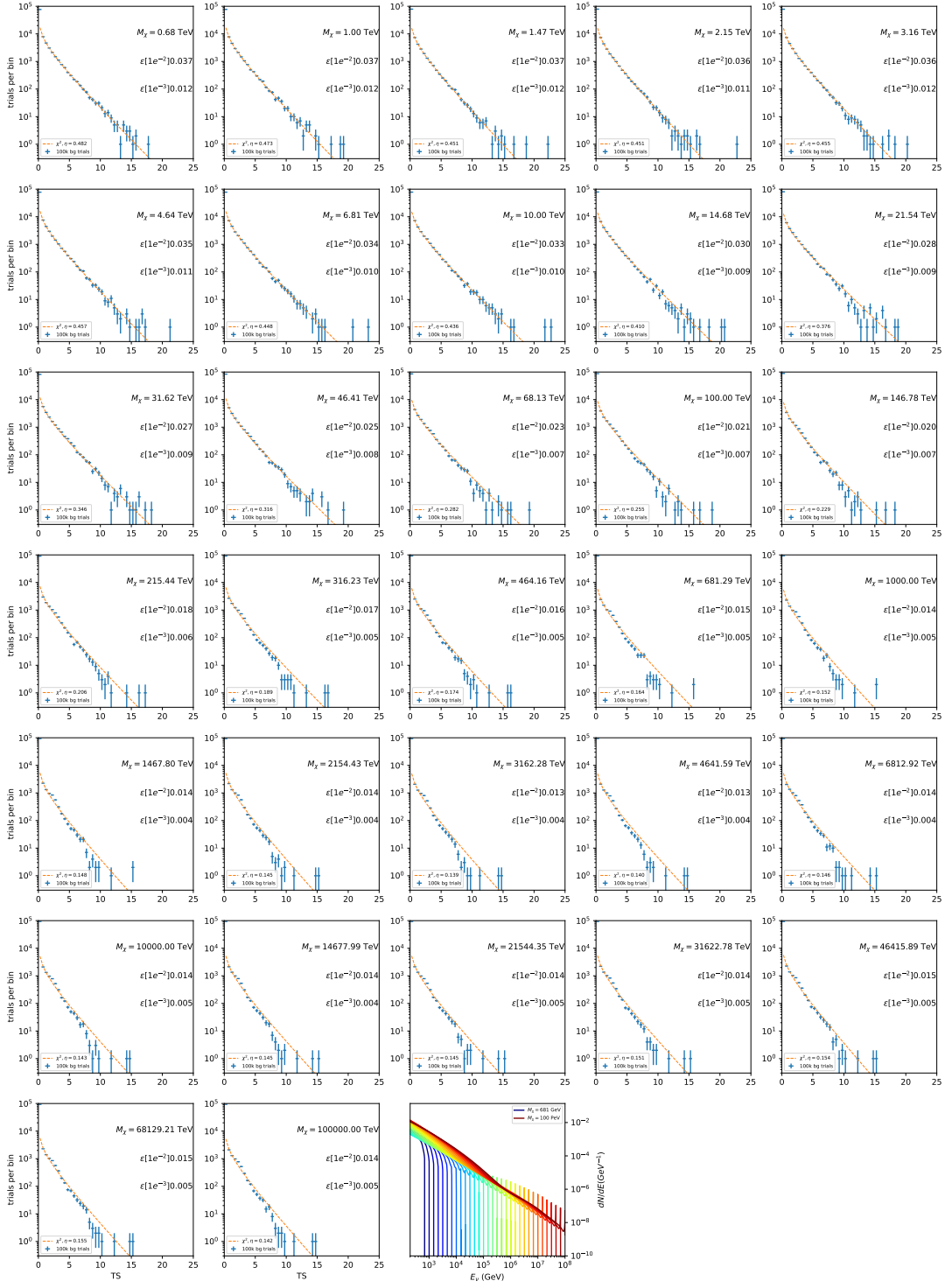


Figure 7.10 Same as Fig. 7.6 for Ursa Major II 1  $\chi\chi \rightarrow \tau\bar{\tau}$ .

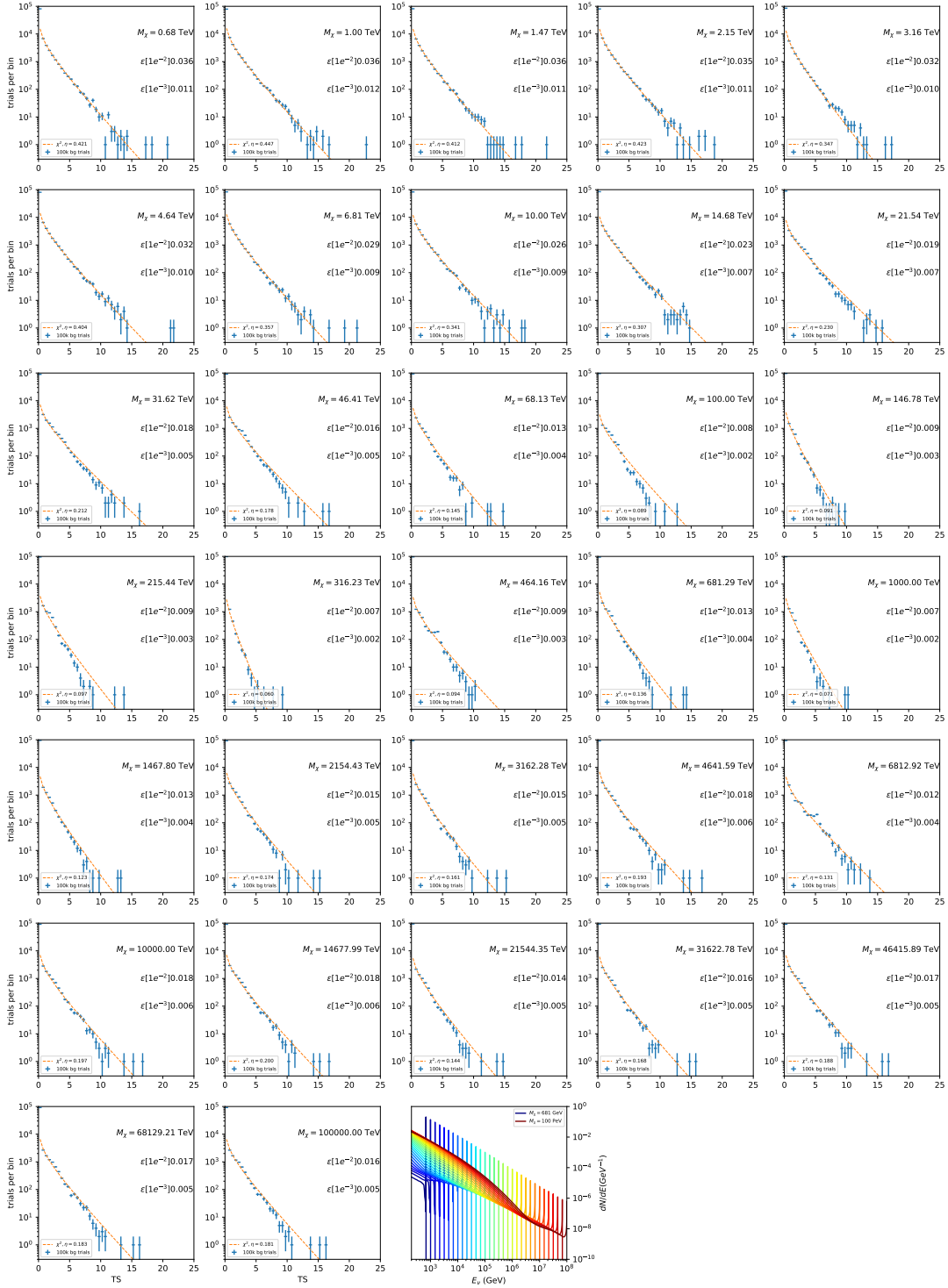


Figure 7.11 Same as Fig. 7.6 for Ursus Major II 1  $\chi\chi \rightarrow \nu_\mu \bar{\nu}_\mu$ .

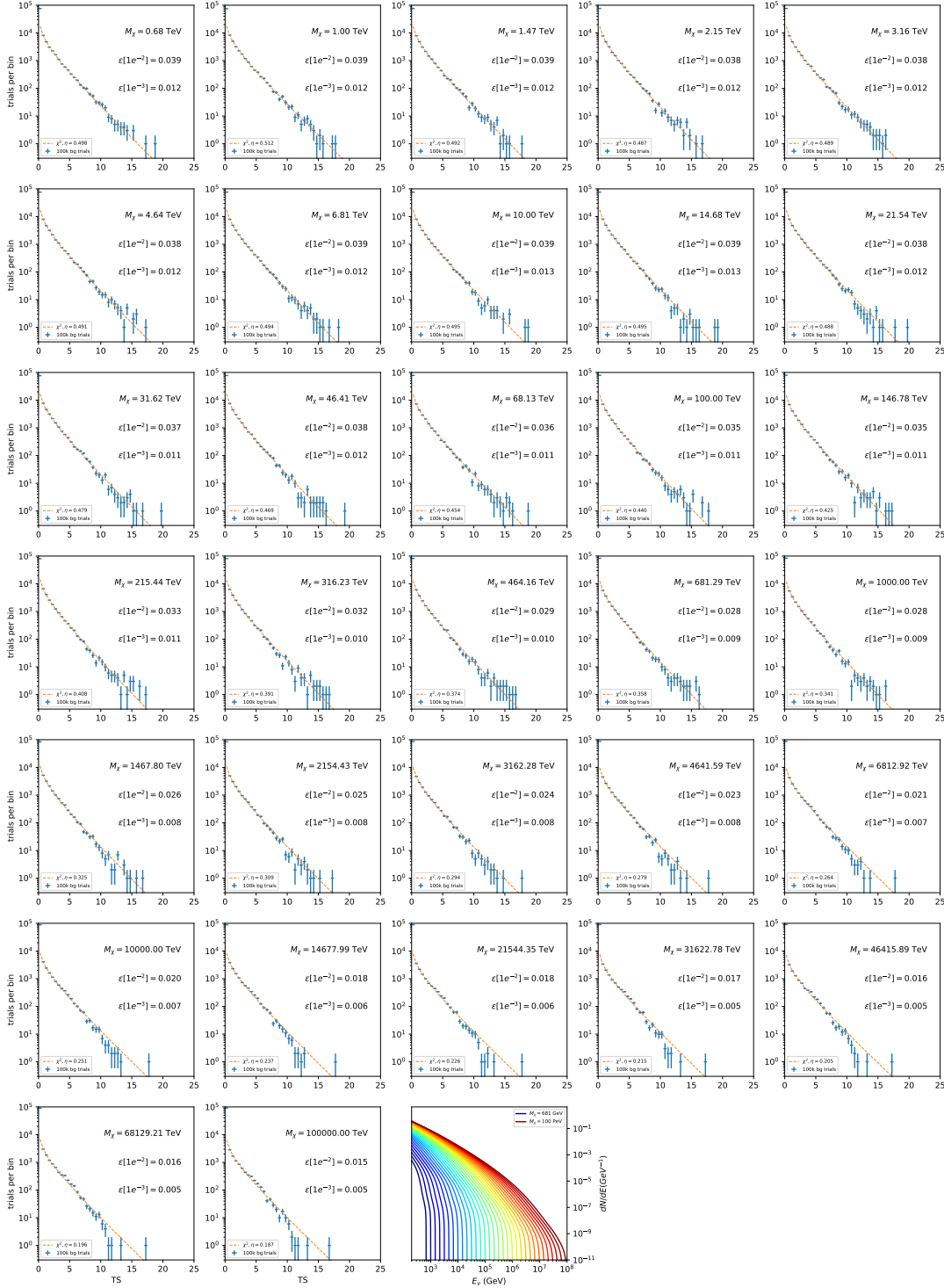


Figure 7.12 Same as Fig. 7.6 for 15,  $\mathcal{GS}$   $J$ -factor, stacked sources and  $\chi\chi \rightarrow b\bar{b}$ .

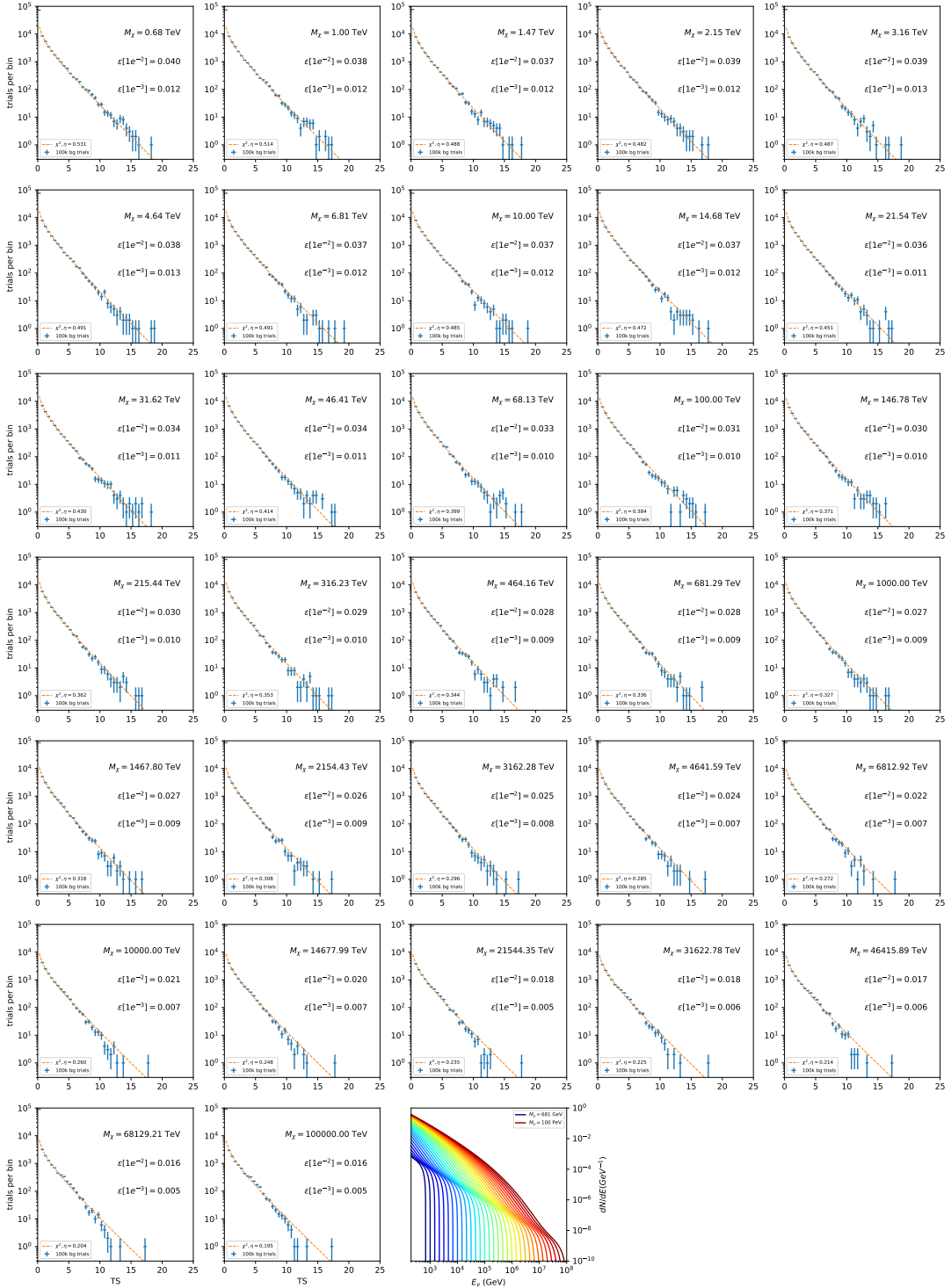


Figure 7.13 Same as Fig. 7.6 for 15, GS J-factor, stacked sources and  $\chi\chi \rightarrow t\bar{t}$ .

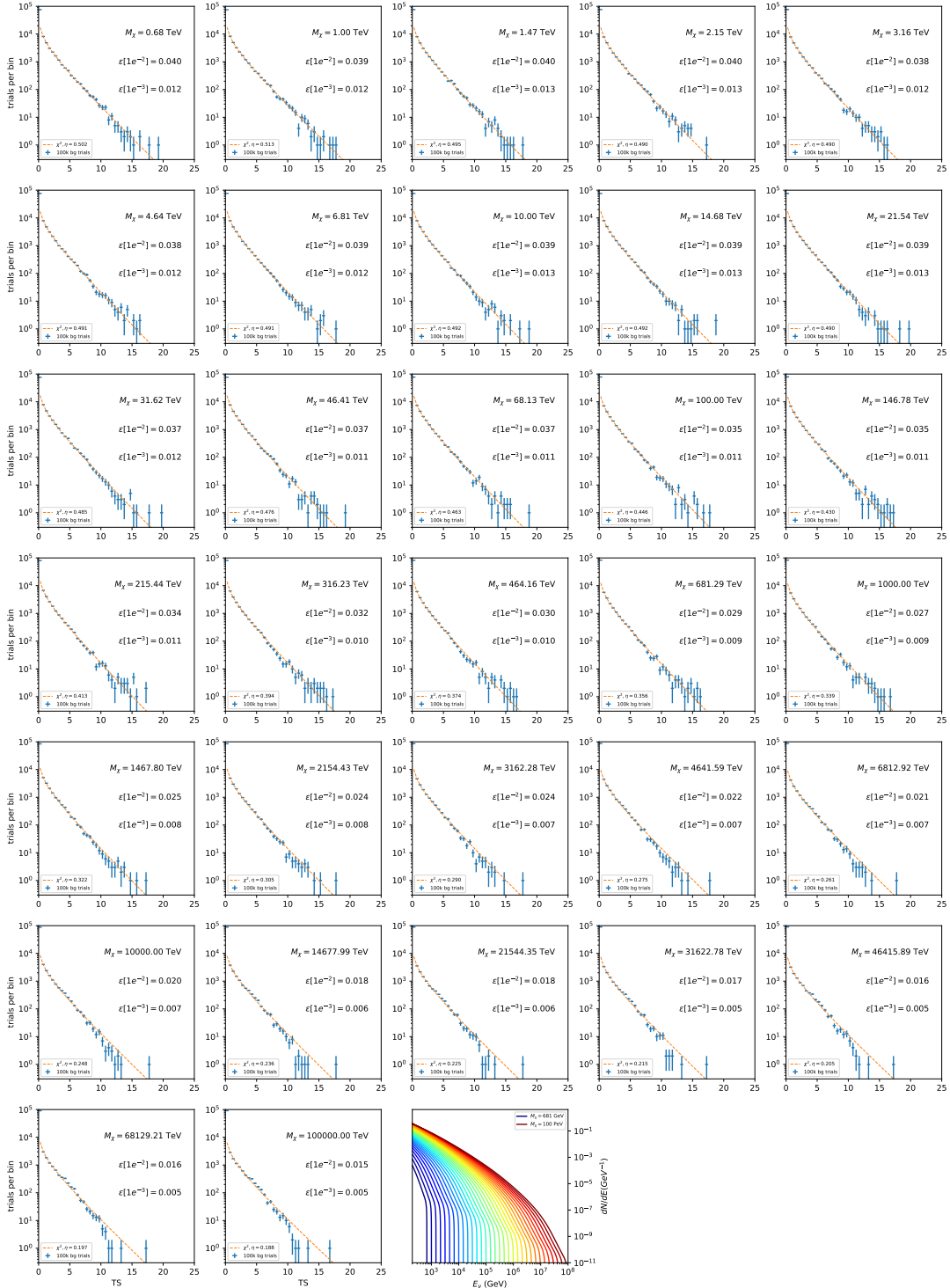


Figure 7.14 Same as Fig. 7.6 for 15,  $\mathcal{GS}$  J-factor, stacked sources and  $\chi\chi \rightarrow u\bar{u}$ .

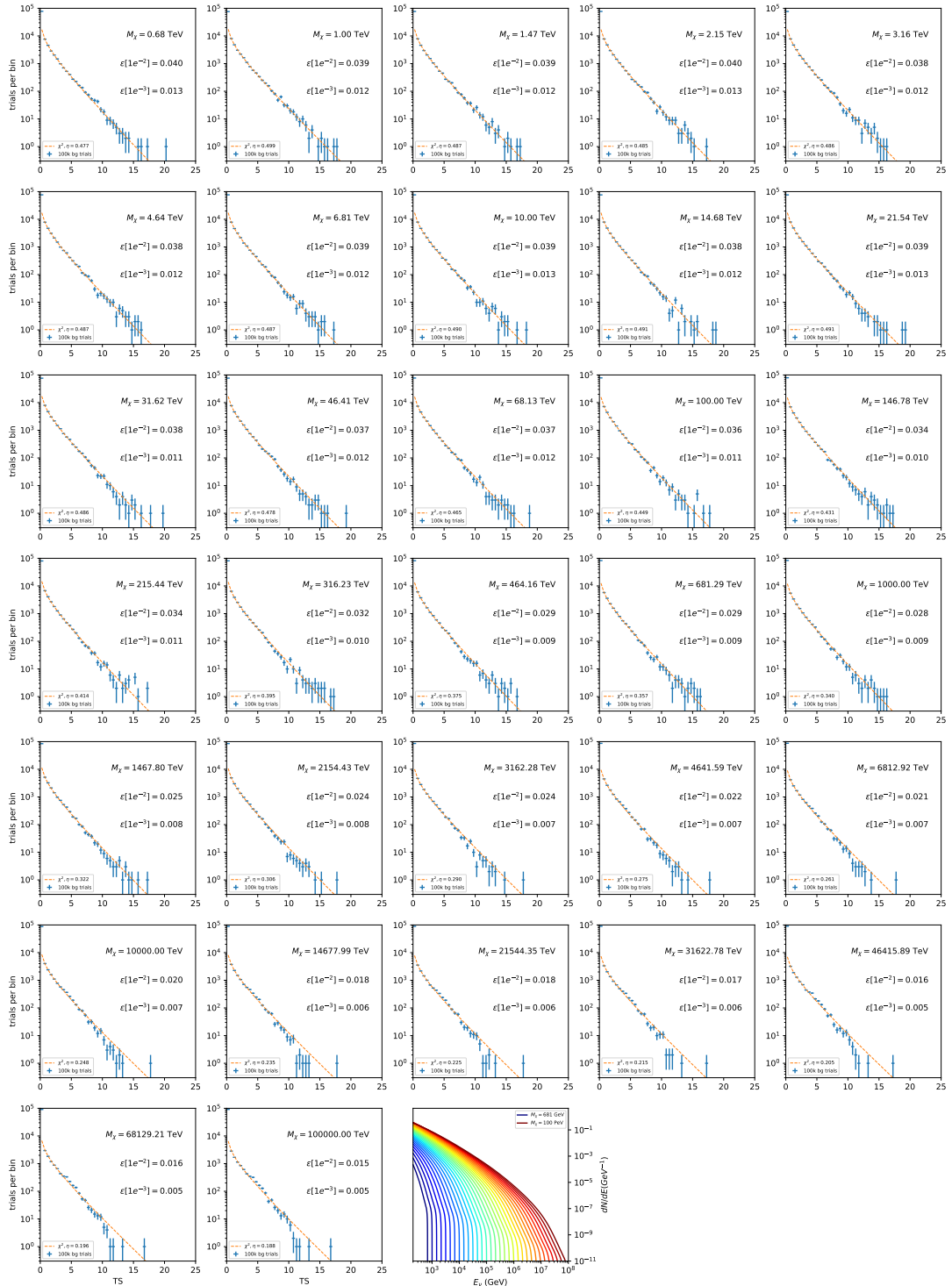


Figure 7.15 Same as Fig. 7.6 for 15,  $\mathcal{GS}$  J-factor, stacked sources and  $\chi\chi \rightarrow d\bar{d}$ .

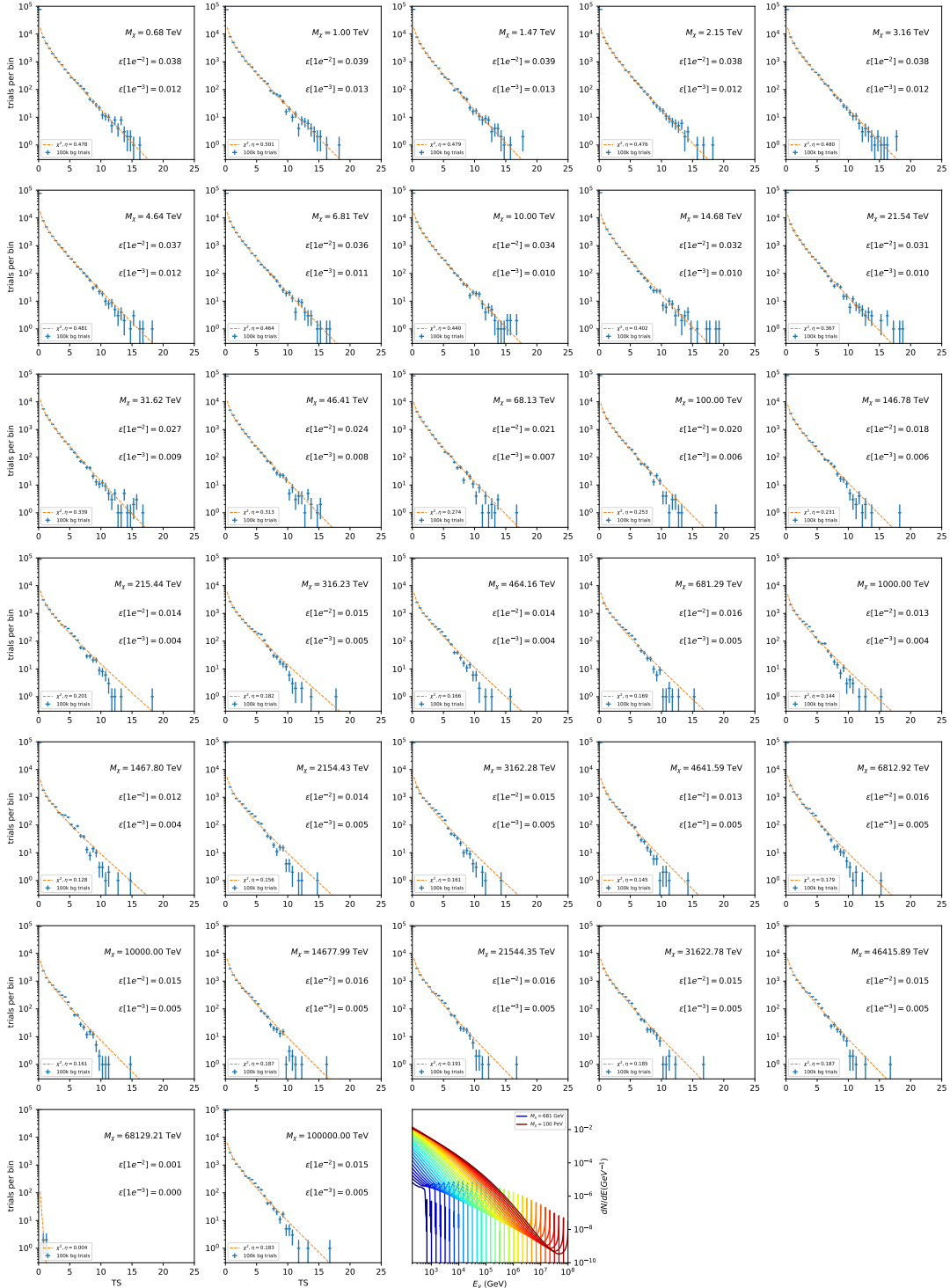


Figure 7.16 Same as Fig. 7.6 for 15,  $\mathcal{G}\mathcal{S}$  J-factor, stacked sources and  $\chi\chi \rightarrow e\bar{e}$ .

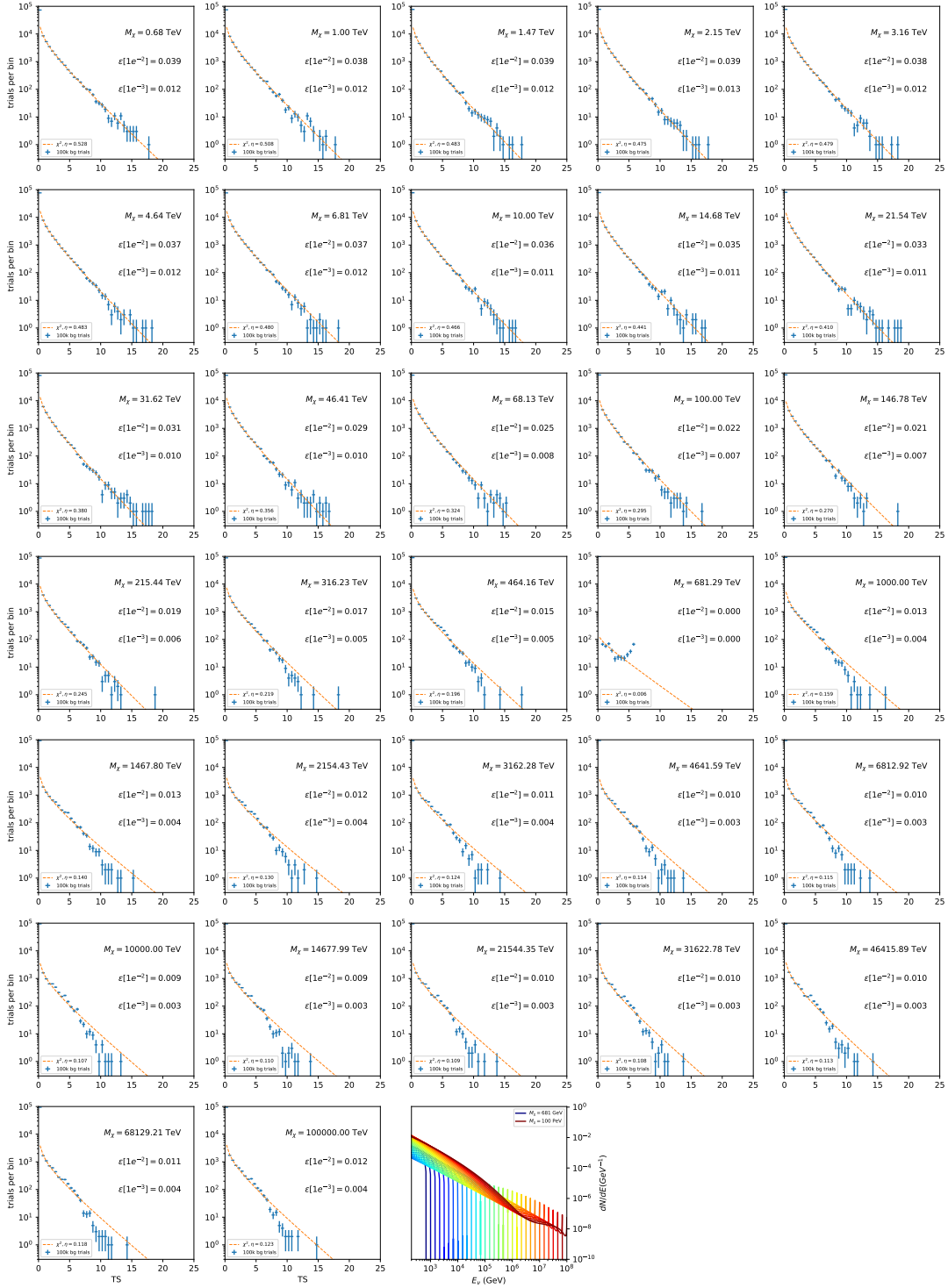


Figure 7.17 Same as Fig. 7.6 for 15,  $\mathcal{GS}$   $J$ -factor, stacked sources and  $\chi\chi \rightarrow \mu\bar{\mu}$ .

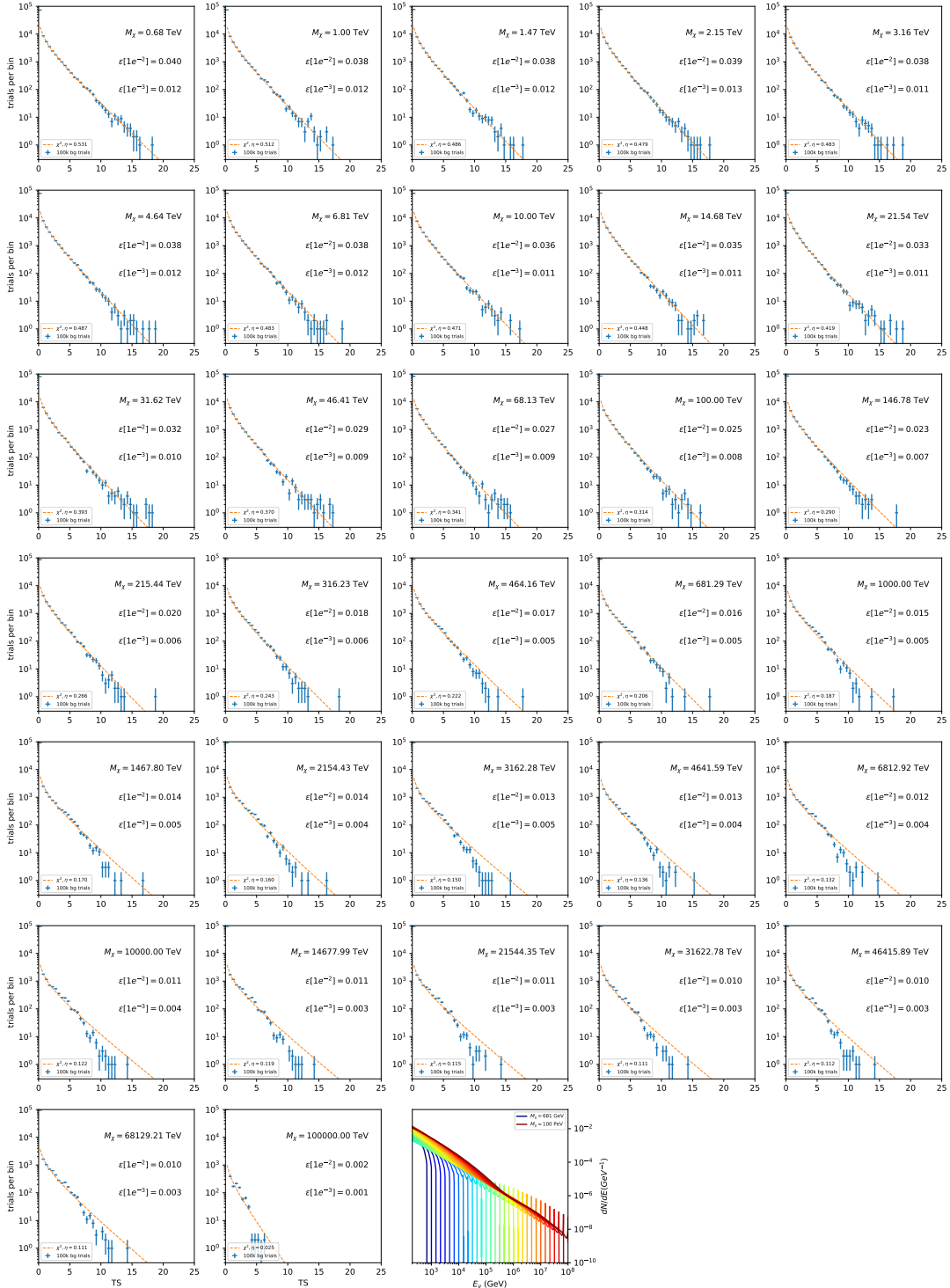


Figure 7.18 Same as Fig. 7.6 for 15,  $\mathcal{GS}$  J-factor, stacked sources and  $\chi\chi \rightarrow \tau\bar{\tau}$ .

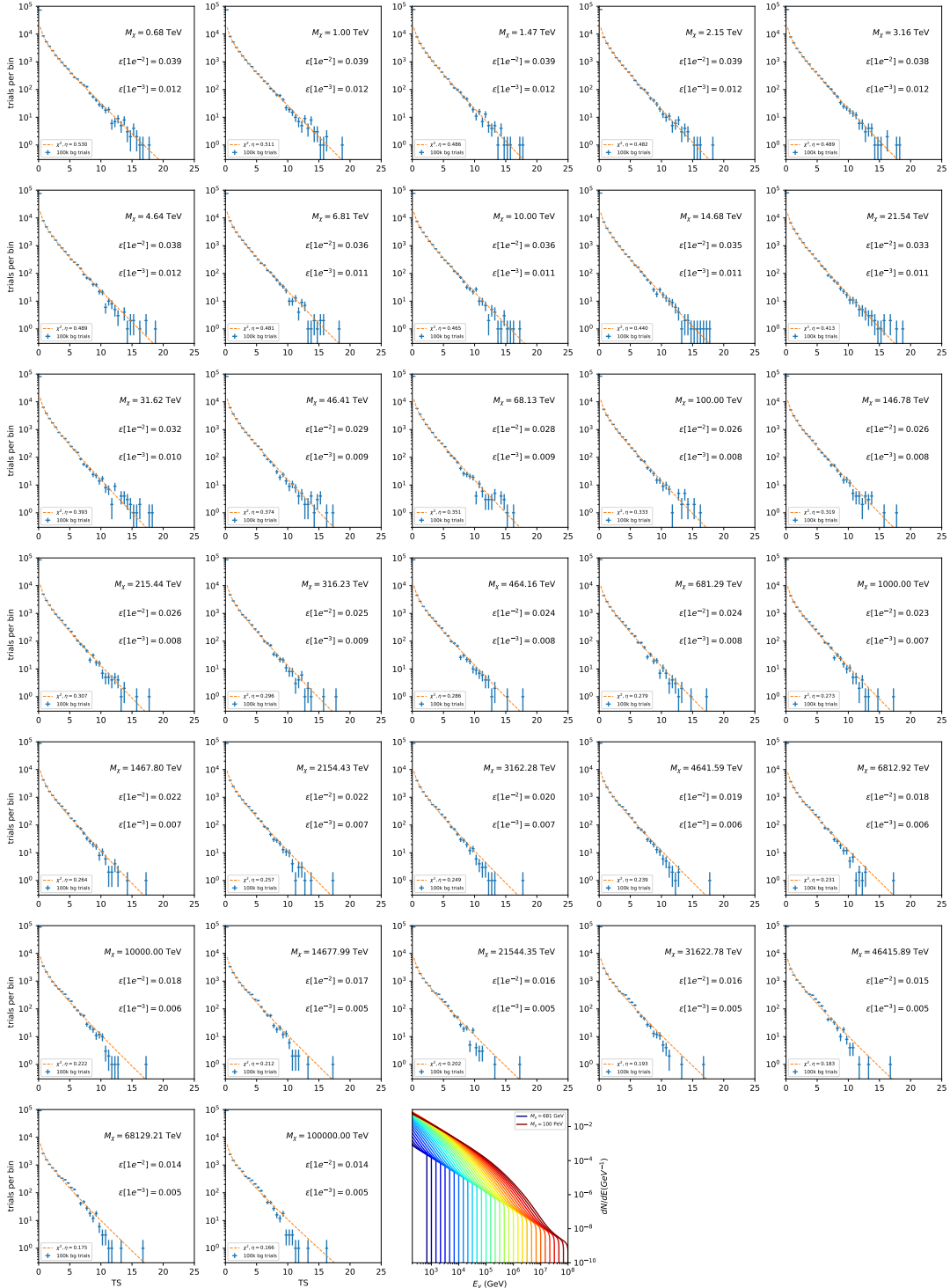


Figure 7.19 Same as Fig. 7.6 for 15,  $\mathcal{GS}$  J-factor, stacked sources and  $\chi\chi \rightarrow W^+W^-$ .

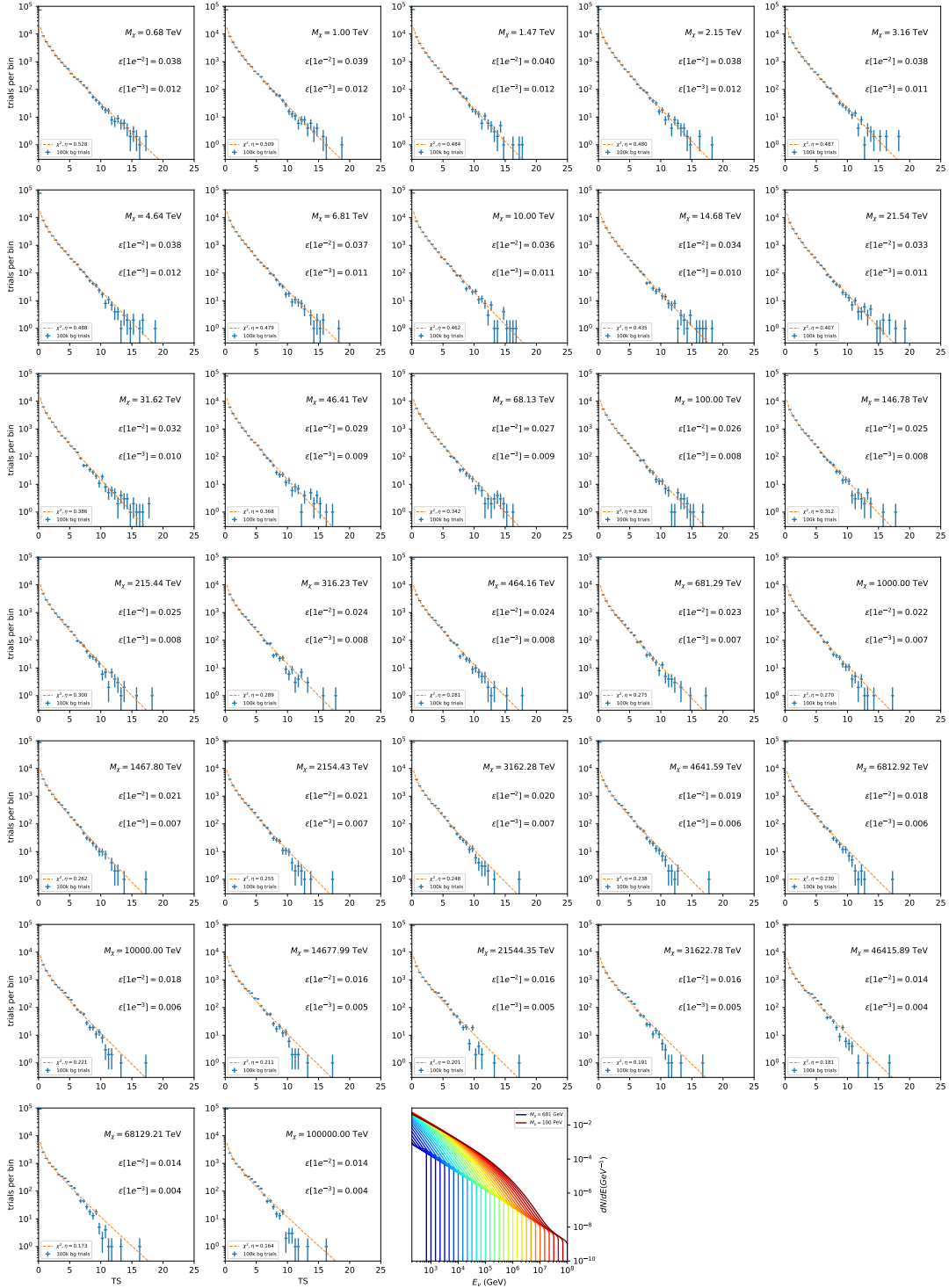


Figure 7.20 Same as Fig. 7.6 for 15,  $\mathcal{GS}$  J-factor, stacked sources and  $\chi\chi \rightarrow ZZ$ .

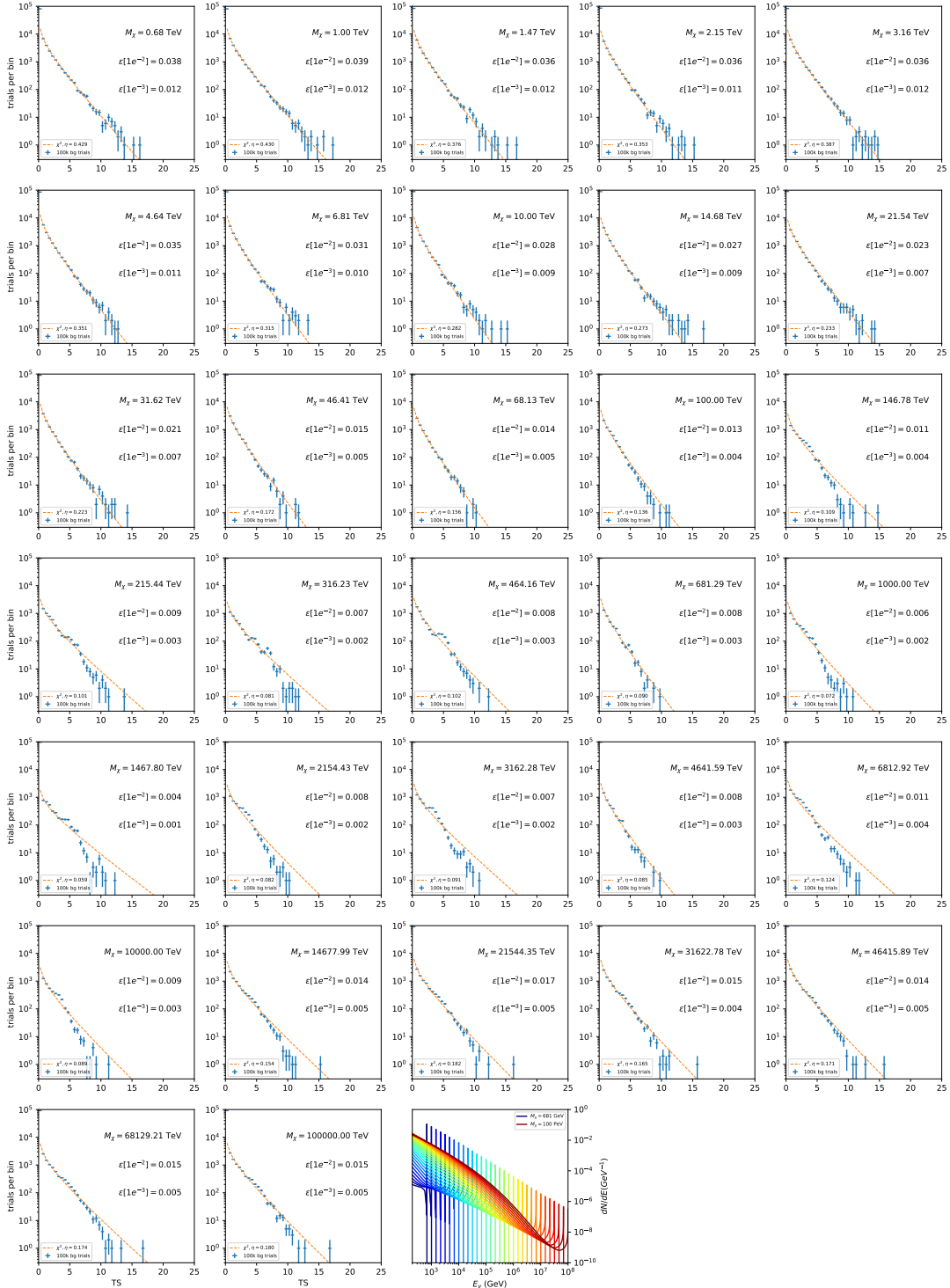


Figure 7.21 Same as Fig. 7.6 for 15,  $\mathcal{GS}$   $J$ -factor, stacked sources and  $\chi\chi \rightarrow \nu_e \bar{\nu}_e$ .

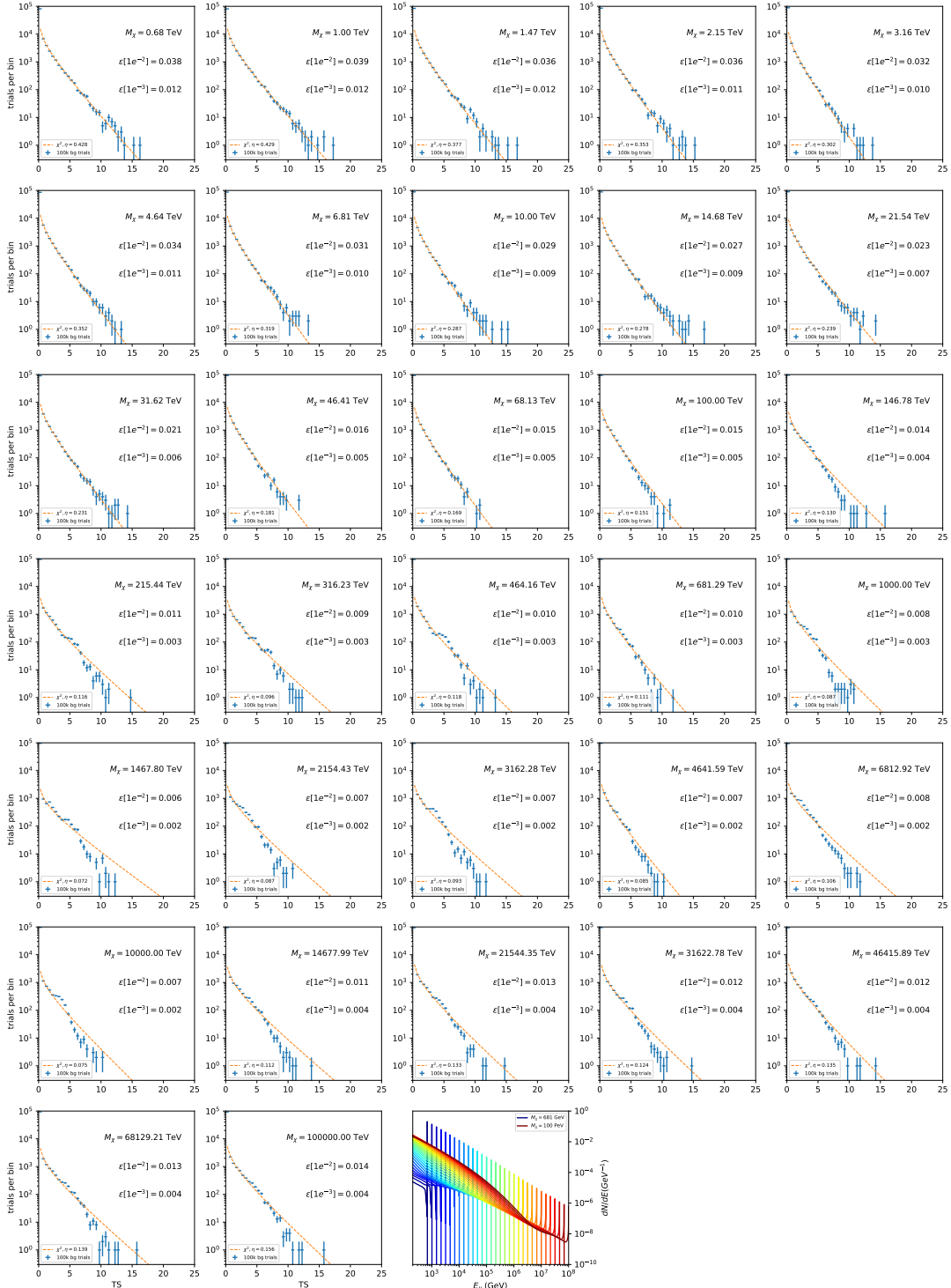


Figure 7.22 Same as Fig. 7.6 for 15, GS J-factor, stacked sources and  $\chi\chi \rightarrow \nu_\mu \bar{\nu}_\mu$ .

1737 **7.5.1 TS per Source**

1738 Figure 7.6 to Figure 7.11 present the TS distributions for Segue 1 and Ursa Major II for 100,000  
1739 trials. More studies for all annihilation channels and remaining 13 sources were also performed  
1740 and are documented in IceCube’s internal wiki.

1741 Almost every distribution produced follows a  $\chi^2$  distribution with 1 degree of freedom. This is  
1742 more true for low  $m_\chi$  than high  $m_\chi$  models. These observations are important for future assumptions  
1743 made in Sec. 8 and may justify statistical calculations assuming our test statistics follow a  $\chi^2$  with  
1744 1 degree of freedom.

1745 **7.5.2 Stacked TS**

1746 Figure 7.12 to Figure 7.22 present the TS distributions for a stacked study of 15 sources with  
1747  $\mathcal{GS}$   $J$ -factors on 100,000 trials. The presentation of these plots are identical to the single source  
1748 distributions in Section 7.5.1. We see similar behaviour in the stacked TS distributions compared  
1749 to the single source studies.

1750 **7.6 Signal Recovery**

1751 We also wish to understand how well the analysis is able to reconstruct signal neutrinos. In  
1752 order to test this, we inject neutrinos from our spectral models randomly then attempt to discern  
1753 the number of signal neutrinos in the simulated data. Figure 7.23 and Figure 7.24 show this study  
1754 for  $\chi\chi \rightarrow b\bar{b}$ ,  $t\bar{t}$ , and  $\nu_\mu\bar{\nu}_\mu$  for a stacked analysis of 15 sources. Figure C.3 to Figure C.8 show  
1755 identical studies for Segue 1 and Ursa Major II. We see that the analysis is conservative at smaller  
1756  $m_\chi$ , yet improves at larger  $m_\chi$ . We also see that the uncertainty is small for the neutrino annihilation  
1757 spectra, and the uncertainty is larger for softer channels like  $b\bar{b}$ .

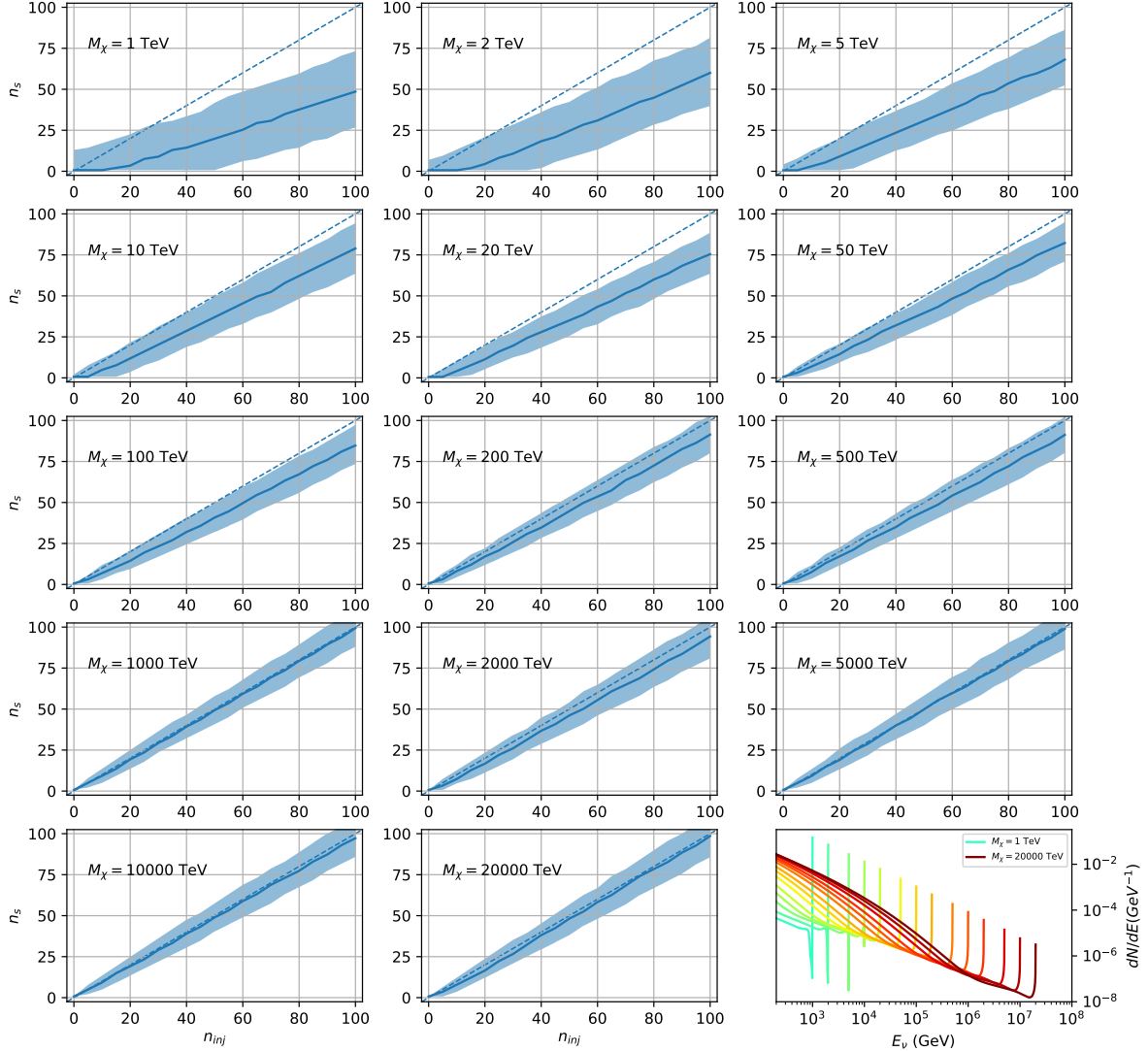


Figure 7.23 Signal Recovery study for an analysis with 15 stacked sources using the  $\mathcal{GS}$   $J$ -factors [47]. Above shows 14 studies for DM mass ranging between 1 TeV and 20 PeV for  $\chi\chi \rightarrow \mu_\mu\bar{\mu}_\mu$ . The bottom right subplot features every spectral model used as input for the remaining subplots. The remaining subplots show  $n_{inj}$  as the number of signal events injected into background simulation. Whereas,  $n_s$  is the number of signal events recovered from analyzing the injected simulation. Blue line represents the median values of 100 simulations. Light blue bands show the  $1\sigma$  statistical uncertainty around the median.

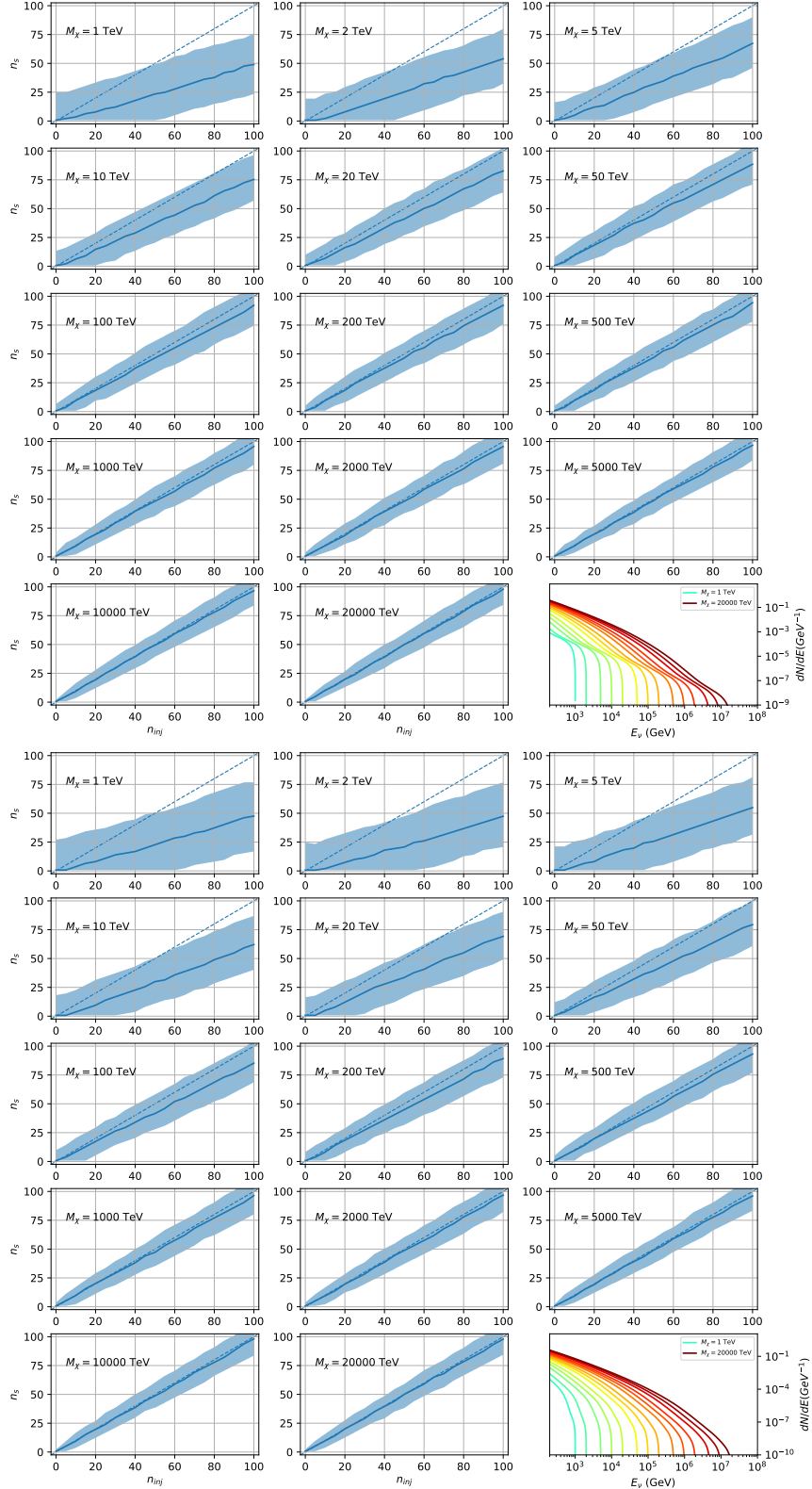


Figure 7.24 Same as Fig. 7.23 but for  $\chi\chi \rightarrow t\bar{t}$  (top) and  $b\bar{b}$  (bottom).

1758 **7.6.1 Sensitivities**

1759 In IceCube, we usually define the 90% confidence level (CL), as the minimum number of signal  
1760 events ( $n_s$ ) required to have a Type I error rate smaller than 0.5 and Type II error rate of 0.1. We  
1761 compute  $n_s$  from the following equation

$$n_s = T_{\text{live}} \int_0^{\Delta\Omega} d\Omega \int_{E_{\min}}^{E_{\max}} dE_\nu A_{\text{eff}}(\hat{n}, E_\nu) \frac{d\Phi_\nu}{d\Omega dE_\nu}(\hat{n}, E_\nu), \quad (7.8)$$

1762 to extract the sensitivity on the dark matter velocity-weighted annihilation cross-section,  $\langle\sigma v\rangle$ .  $T_{\text{live}}$   
1763 is the detector live time,  $A_{\text{eff}}$  is the effective area of the detector, and  $E_{\min}$ ,  $E_{\max}$  are the minimum,  
1764 maximum energies of the expected neutrinos, respectively.

1765 Sensitivities are calculated for each source individually as if they were the only source and as a  
1766 stack over 1000 trials. From Eq. (7.8) and Eq. (7.1) we can compute the  $\langle\sigma v\rangle$  at a 90% confidence  
1767 level. Figure 7.26 and Fig. 7.25 show the sensitivities for some DM annihilation channels. Not  
1768 all channels computed successfully in time for the writing of this dissertation. Among channels  
1769 missing include the charged leptons:  $e$  and  $\tau$ .

1770 **7.7 Systematics**

1771 The current analysis plan is to compare these sensitivities to another  $J$ -factor catalog such as  
1772  $\mathcal{LS}$  [68] although this was not completed in time for this dissertation. Additionally, we set out to  
1773 perform a standard suite of IceCube systematic studies which include: DOM efficiency, Hole ice,  
1774 ice absorption, and photon scattering. We do study Earth attenuation, and Section 7.7.1 enumerates  
1775 the impact of the Earth on our hardest neutrino spectra.

1776 **7.7.1 Earth Effects**

1777 We look to quantify the impact of the Earth on our sensitivity to  $\chi\chi \rightarrow \nu_\mu \bar{\nu}_\mu$ . This channel is  
1778 expected to be among the significantly impacted annihilation channels because it has a significant  
1779 contribution at PeV energies for  $m_\chi \geq 1\text{PeV}$ . The Earth is expected to attenuate these higher energy  
1780 neutrinos. However, these neutrino spectra have significant low energy contributions, so we do not  
1781 expect to entirely lose our sensitivity. This motivated a study examining our  $\langle\sigma v\rangle$  sensitivity over  
1782 all DM masses sampled for a selection of declinations.

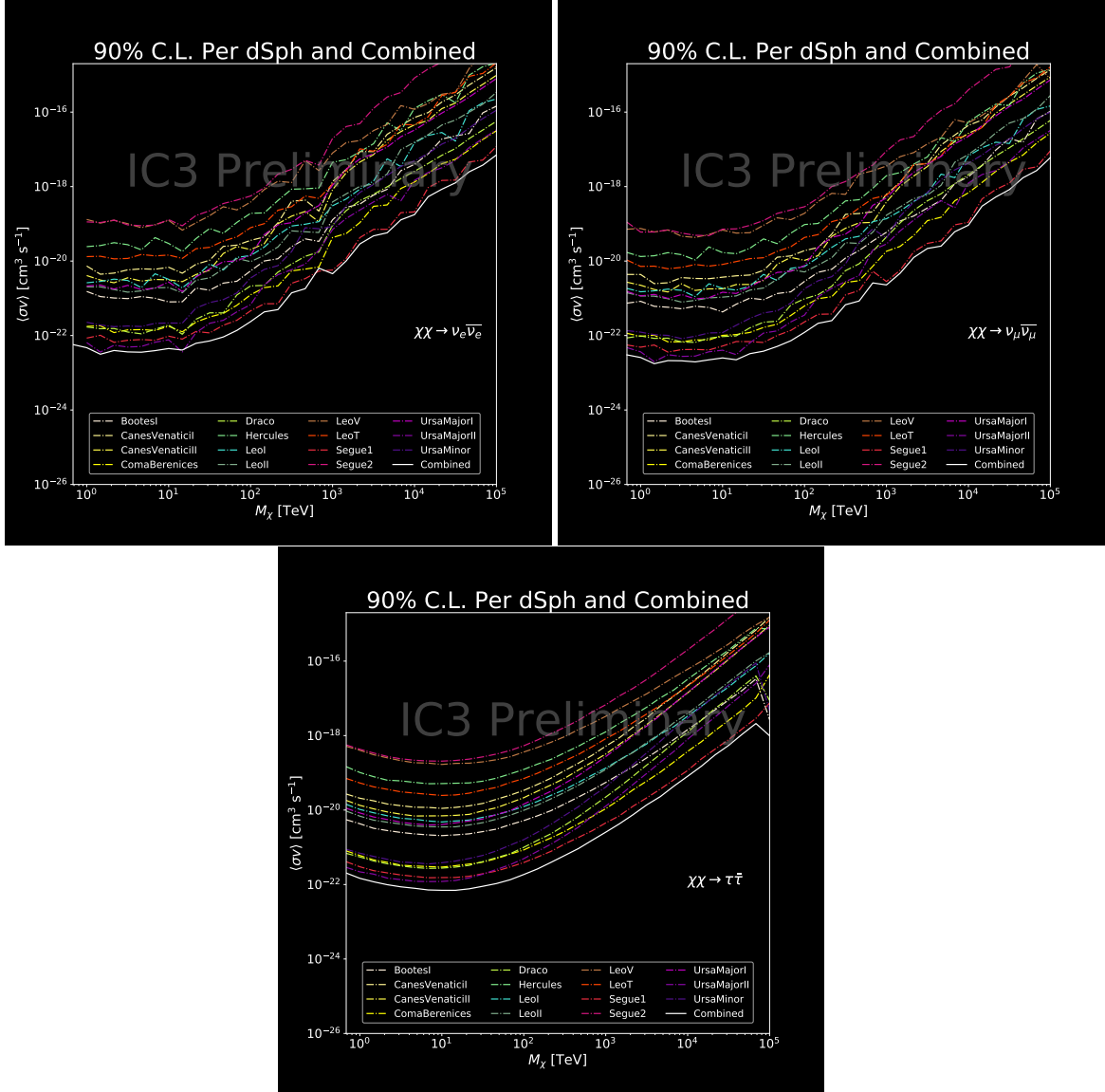


Figure 7.25 IceCube North Sky Track Sensitivities. Each panel shows sensitivity curves for various DM annihilation channels. Sensitivities are for the velocity-weighted cross-section  $\langle\sigma v\rangle$  versus  $m_\chi$ . Dotted, colored lines are sensitivities for individual sources. Solid white lines are for the combined sensitivity of all 15  $\mathcal{GS}$  sources used in this study.

1783 For this systematic study, I sample 6 DM masses per decade from 681 GeV to 100 PeV. I select  
 1784 declinations that are shared with sources in the  $\mathcal{GS}$  catalog: Boötes I, Canes Venatici II, Leo V,  
 1785 Ursa Major I, and Ursa Minor. I study a fake source who's  $J$ -factor is shared with Ursa Major II,  
 1786 but who's coordinates belong to the aforementioned list. The sensitivity studies performed for each  
 1787 source (Fig. 7.25 and Section C.5) provided  $n_s$  for 1000 trials which we extracted from Eq. (7.8).  
 1788 We derive  $\langle\sigma v\rangle$  using  $\log_{10} J = 19.42 \log_{10}(\text{GeV}^2 \text{cm}^{-5})$ . Figure 7.28 shows the results.

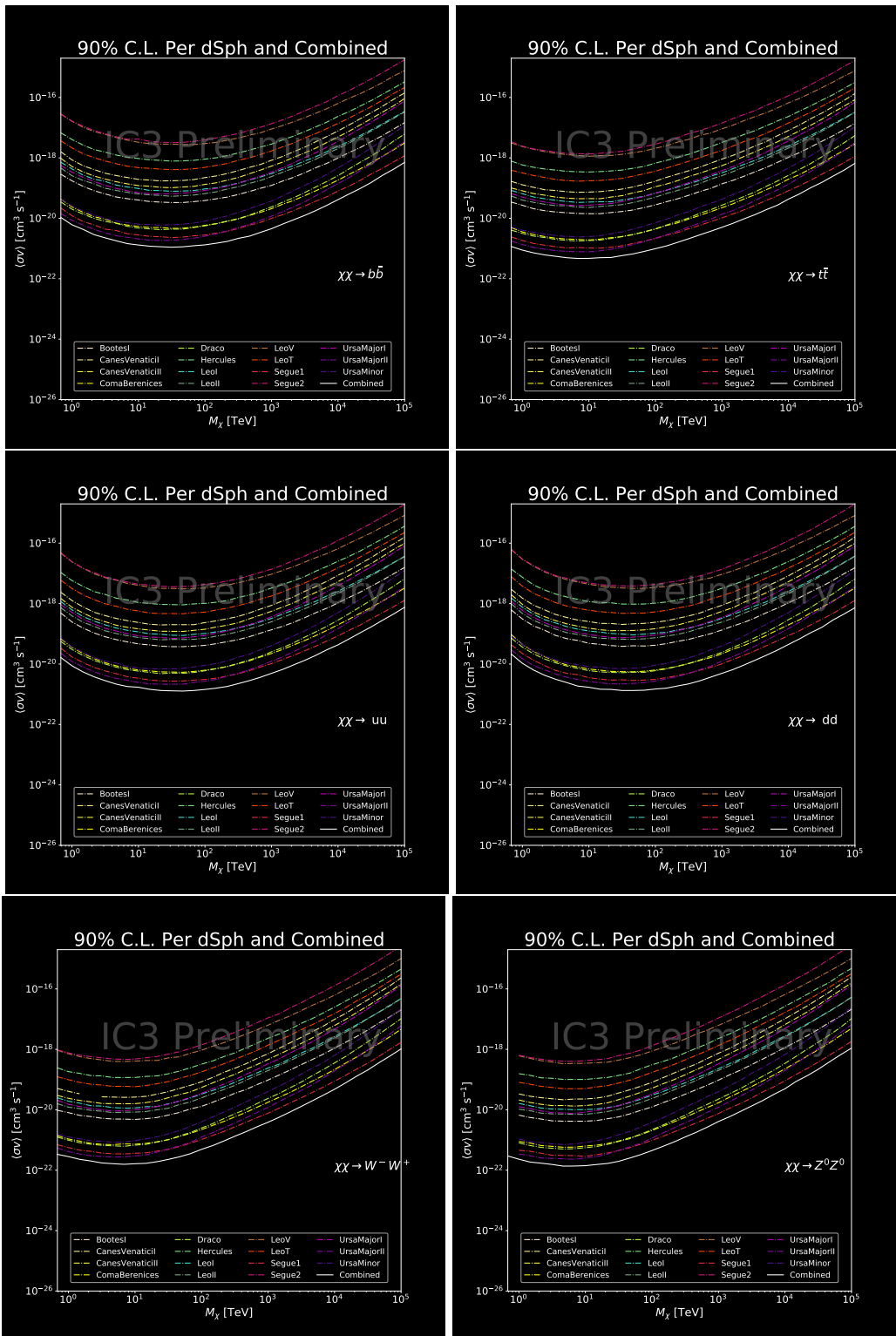


Figure 7.26 Same as Fig. 7.25 for three additional DM annihilation channels.

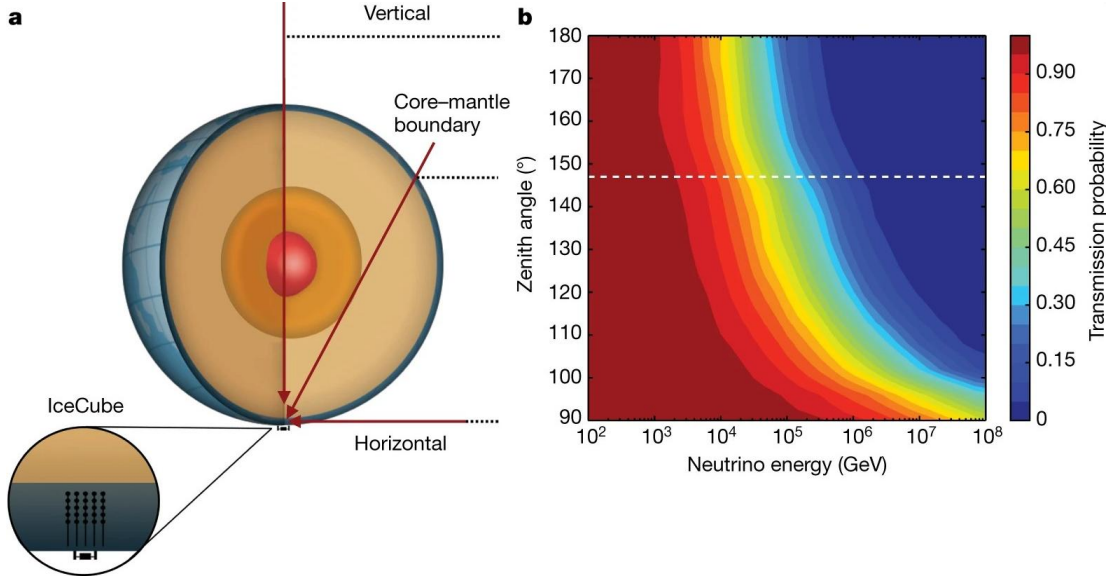


Figure 7.27 Panel A: Neutrino's from the Northern sky and incident on the IceCube detector will travel through the Earth. How much of the Earth these neutrinos travels is a function of zenith from the vertical axis. Panel B: SM prediction of neutrino transmission probabilities for neutrinos arriving at  $90^\circ - 180^\circ$  zenith and with 100 GeV to 100 PeV energies. High-energy neutrinos traversing the whole Earth are completely absorbed, whereas low-energy neutrinos pass through unimpeded. Neutrinos coming from above the horizon will arrive unimpeded for all neutrino energies. Figure pulled from [80].

1789     Figure 7.28 shows that we have significant but diminishing sensitivity to sources at high  
 1790     declination. We see in the worse case, the sensitivity at high declination is up to an order of  
 1791     magnitude worse than at low declination. However, for  $m_\chi < 1$  PeV, the sensitivities are very  
 1792     similar. The comparable sensitivities imply that a stacking analysis with IceCube is most powerful  
 1793     in the 500 GeV to 1 PeV region. Above 1 PeV, our limits and sensitivities are dominated by sources  
 1794     near the horizon. When we additionally consider the  $J$ -factors, we expect Segue 1 to dominate  
 1795     contributions to sensitivity and limits where  $m_\chi > 1$  PeV.

## 1796     7.8 Conclusions

1797     We utilized advanced computing techniques like parallel programming and spline fitting of  
 1798     particle physics Monte Carlo to greatly expand and refine IceCube's sensitivity to DM annihilation  
 1799     from dSphs. Furthermore, we imported updated astrophysical and particle physics models that  
 1800     better represent what we believe neutrino signals from DM annihilation should look like. We, for  
 1801     the first time, build an analysis that is sensitive to PeV DM annihilation.

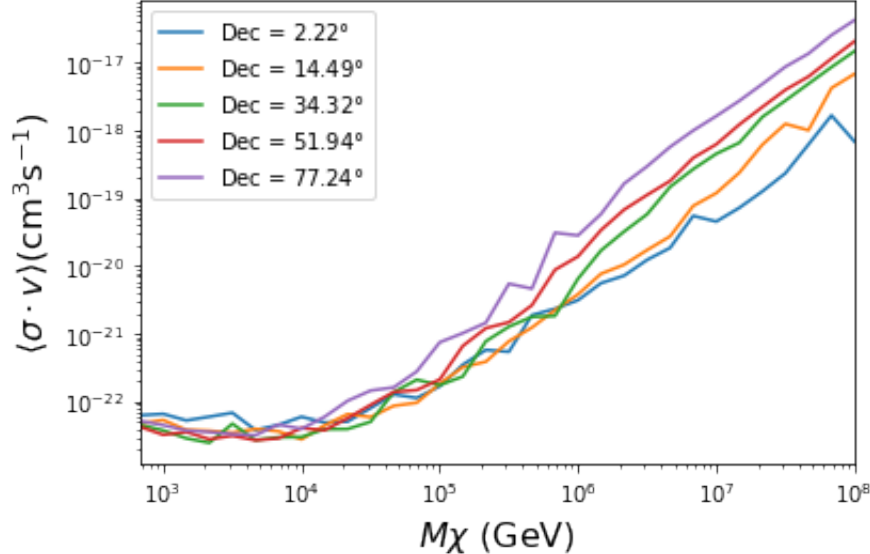


Figure 7.28  $\langle \sigma v \rangle$  sensitivities for 5 imaginary sources with  $\log_{10} J = 19.42$   $\log_{10}(\text{GeV}^2 \text{cm}^{-5})$ . Each imaginary source shares a declination with a source in Tab. 5.1

1802 When we compare to previous IceCube publications of dSphs [71], we see an order of magnitude

1803 improvement to our sensitivity. This analysis has been working group approved within IceCube

1804 and is currently under collaboration review before unblinding. These processes did not complete

1805 in time for this dissertation. Therefore we do not show data for this thesis and is the clear next step.

1806 The test statistic distributions in this analysis also demonstrate more characteristic behavior

1807 compared to previous DM analyses [75, 79]. With a 10-year dataset, we finally have enough

1808 statistics to almost trivially combine with other photon observatories, such as HAWC. The first

1809 groundwork for a multi-messenger DM search is provided with concluding remarks in chapter 8.

## CHAPTER 8

### 1810 NU DUCK: CONCLUSIONS AND FUTURE DIRECTIONS

#### 1811 8.1 Conclusions

1812 **TODO: Chat GPT the shit of everything below** In this work, three analyses were performed  
1813 with data from the HAWC and IceCube observatories in order to explore some of the fundamental  
1814 questions in particle astrophysics. The goal was to contribute to the understanding of the sources of  
1815 cosmic rays, their acceleration mechanisms, and the nature of dark matter. The detection techniques  
1816 and reconstruction methods for both observatories were described, along with the properties that  
1817 make them ideal instruments to perform such searches.

1818 This dissertation used data from the HAWC detector to probe cutting-edge physics beyond  
1819 the Standard Model. The techniques by which HAWC is able to detect cosmic gamma rays were  
1820 demonstrated and the many advantages of HAWC in probing ultra-high energy gamma-ray physics  
1821 were detailed. It was shown how HAWC data can be used to explore unanswered questions such as  
1822 the nature of dark matter and the limits of Lorentz invariance. In particular, a search for evidence of  
1823 WIMP dark matter in the Milky Way Galactic Halo was performed. To accomplish this, simulations  
1824 of the dark matter density profile were combined with estimates of the HAWC sensitivity to dark  
1825 matter-like energy spectra. This allowed strong constraints on dark matter annihilation and decay  
1826 from the Galactic Halo to be derived that are insensitive to the large uncertainties arising from  
1827 systematics in the dark matter spatial distribution. Multi-hundred TeV photon spectra were also  
1828 significantly detected from HAWC sources within the Galactic Plane. These results lead to the  
1829 strongest constraints on Lorentz invariance violation to be published at the time of writing.

1830 The work of this dissertation was made possible by the ongoing development of new algorithms  
1831 and reconstruction techniques within the HAWC collaboration. Probing the Galactic Halo required  
1832 the creation of a novel background estimation technique that relied on HAWC's wide field of view  
1833 and strong ability to discriminate between gamma rays and cosmic rays. Meanwhile, the constraints  
1834 on Lorentz invariance violation were enabled by the improved energy resolution from a machine  
1835 learning technique. HAWC has recently completed a reprocessing of all archival data using an

1836 updated set of algorithms that can lead to compelling follow-up work on these results. Combining  
 1837 the new background technique with the re-optimized energy estimators will allow for Galactic  
 1838 dark matter to be probed at even higher masses, as well as for analyses that require precise energy  
 1839 resolution such as gamma-ray line searches.

1840 **8.2 Future Directions**

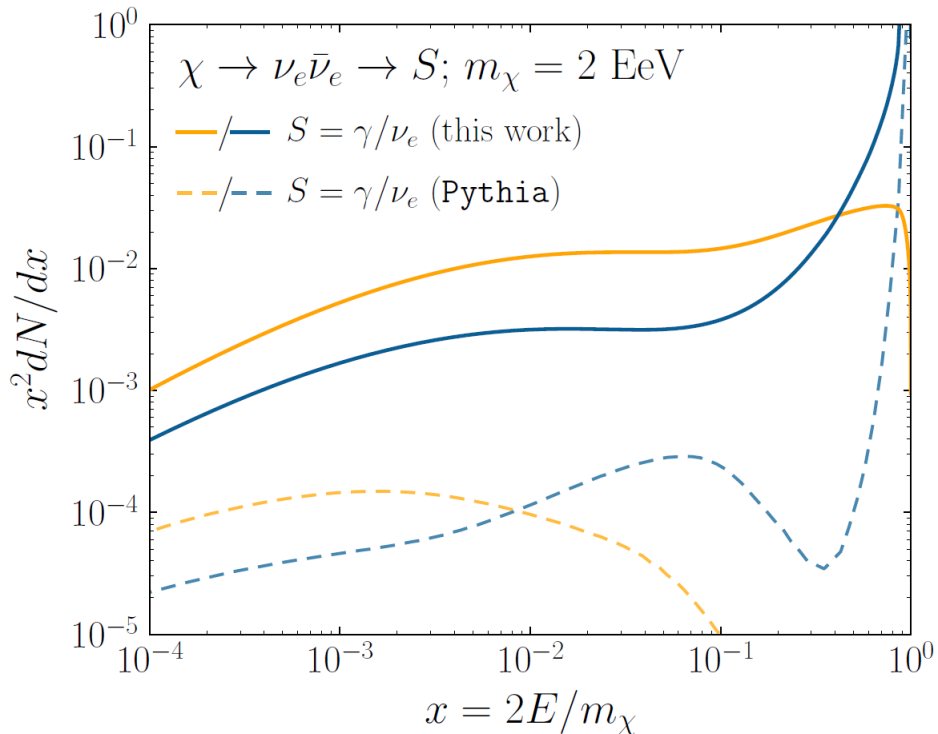


Figure 8.1 The prompt electron neutrino and photon spectrum resulting from the decay of a 2EeV DM particle to  $\nu_e\bar{\nu}_e$ , as currently being searched for at IceCube [5]. Solid curves represent the results of this work, and predict orders of magnitude more flux at certain energies than the dashed results of Pythia 8.2, one of the only existing methods to generate spectra at these masses. In both cases energy conservation is satisfied: there is a considerable contribution to a  $\delta$ -function at  $x = 1$ , associated with events where an initial W or Z was never emitted and thus no subsequent shower developed. Large disagreements are generically observed at these masses for electroweak dominated channels, while the agreement is better for colored initial SM states.

1841 As I have shown previously in Sec. 5 and Sec. 6, we can build a fast and robust analysis  
 1842 that shares tools with the field. The hope being that IceCube can eventually combine data with  
 1843 gamma-ray observatories.



Figure 8.2 TODO: neutrino and bb plot with nu Sensitivities[NEEDS A SOURCE][FACT CHECK THIS]

## MULTI-EXPERIMENT SUPPLEMENTARY FIGURES

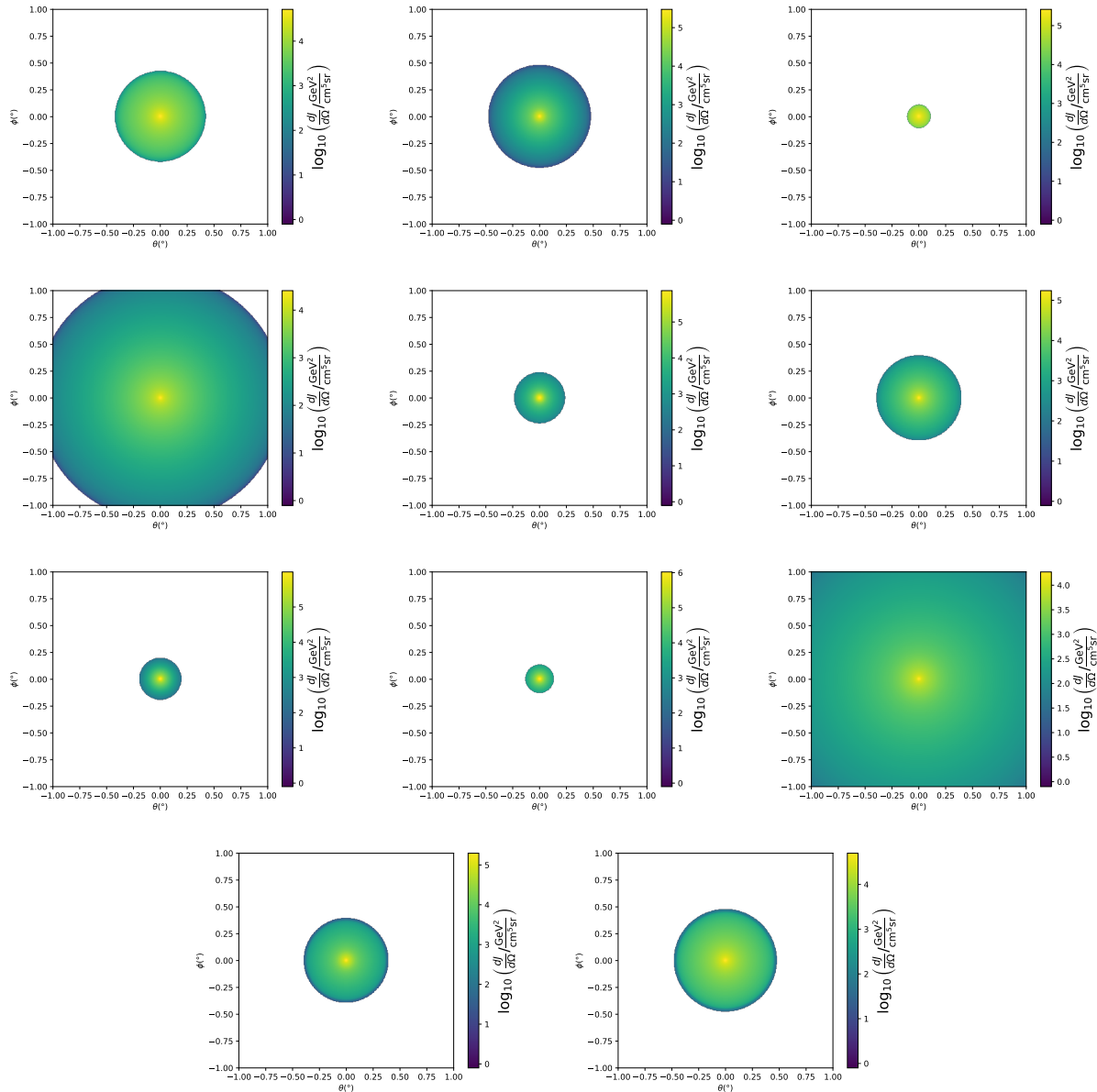


Figure A.1 Sister figure to Figure 5.3. Sources in the first row from left to right: Bootes I, Canes Venatici I, II. In second row: Draco, Hercules, Leo I. In the first row: Leo II, Leo IV, Sextans. In the final row: Ursa Major I, Ursa Major II.

## APPENDIX B

### 1845 MULTITHREADING DARK MATTER ANALYSES SUPPLEMENTARY MATERIAL

#### 1846 B.1 Remaining Spectral Models

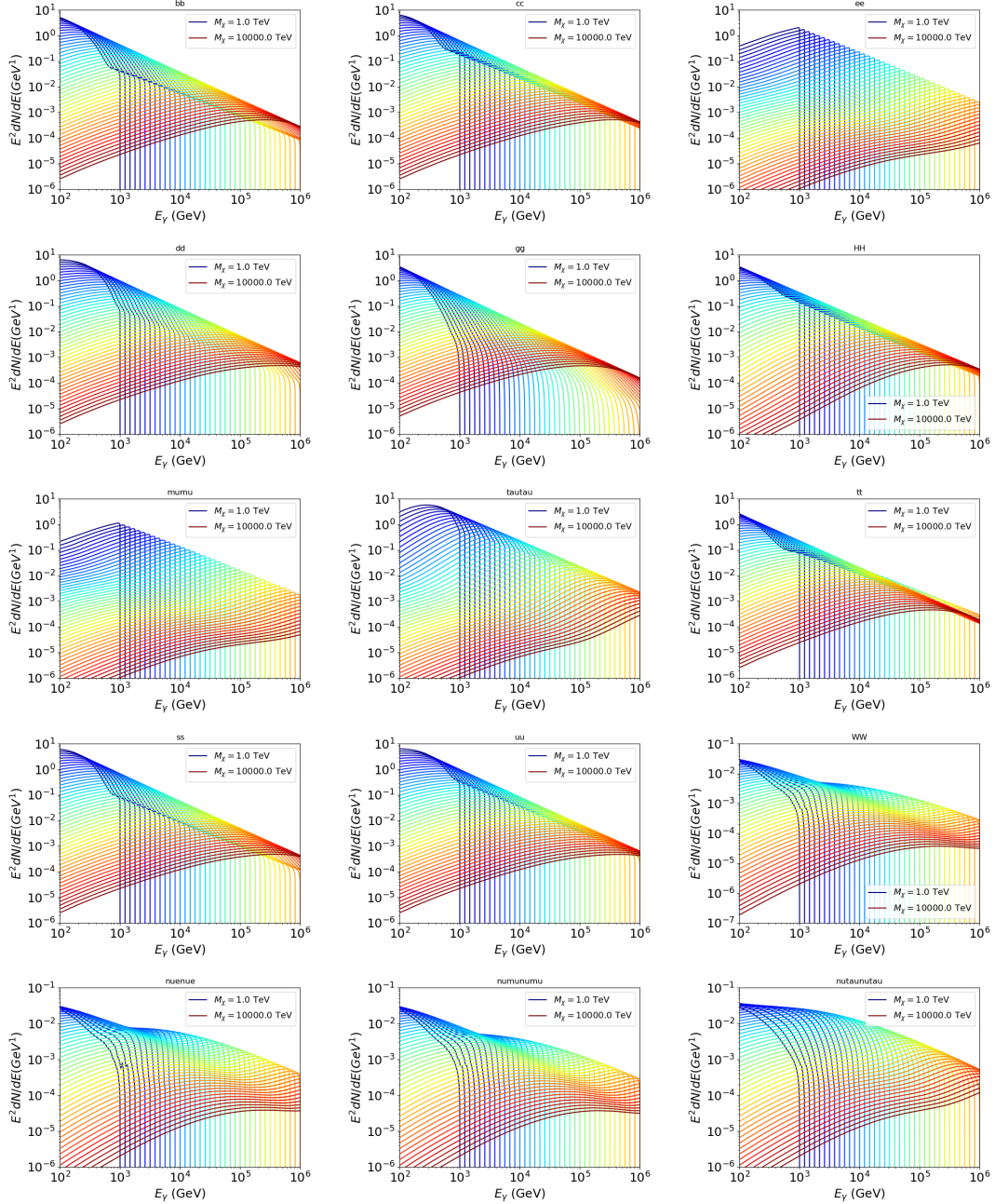


Figure B.1 Sister figure to Figure 6.2 for remaining SM primary annihilation channels studied for this thesis. These did not require any post generation smoothing and so are directly pulled from [67] with a binning scheme most helpful for a HAWC analysis.

1847 **B.2 mpu\_analysis.py**

```
18481 import warnings
18492 with warnings.catch_warnings():
18503     warnings.simplefilter("ignore")
18514 # Python base libraries
18525 import os
18536 import sys
18547 import time
18558 # Import general libraries with namespace
18569 import matplotlib
18570 # Necessary for computing on cluster
18581 matplotlib.use("agg")
18592 import numpy as np
18603 import multiprocessing as mp
18614 # Import HAWC software
18625 sys.path.insert(1, os.path.join(os.environ['HOME'], 'hawc_software', 'threeML-
1863     analysis-scripts', 'fitModel'))
18646 from analysis_modules import *
18657 from threeML import *
18668 from hawc_hal import HAL, HealpixConeROI
18679 from threeML.minimizer.minimization import FitFailed
18680 # Import Dark Matter HAWC Libraries
18691 import analysis_utils as au
18702 import spectra as spec
18713 import sources as srcs
18724
18735 #* READ ONLY PATHS This block will change eventually
18746 MASS_LIST = './plotting/studies/nd/masses.txt'
18757 CHAN_LIST = './plotting/studies/nd/chans.txt'
18768
18779 #* WRITE PATHS, default location is to scratch
18780 OUT_PATH = os.path.join(os.environ["SCRATCH"], os.environ["USER"], 'New_duck')
```

```

18791 print('Our out path is going to be {}'.format(OUT_PATH))
18802
18813 # Define parallel Function. Can also be run serially
18824 def some_mass_fit(sigVs, datalist, shape, dSph, jfactor, mass_chan,
18835                         progress=None, log_file='', queue=None, i_job=0):
18846
18857     if progress is None:
18868         progress = [0]
18879     else: # Create log files for each thread
18880         log_file = log_file.replace('.log', '_ThreadNo_')
18891         log_file = log_file + str(i_job) + ".log"
18902         sys.stdout = open(log_file, "w")
18913
18924     fits = []
18935
18946     try:
18957         for m_c in mass_chan:
18968             print(f'Mass chan tuple: {m_c}')
18979             mass = int(m_c[0])
18980             ch = m_c[1]
18991             # Build path to output files
19002             outPath = os.path.join(OUT_PATH, ch, dSph)
19013             au.ut.ensure_dir(outPath)
19024
19035             if progress[i_job] < 0:
19046                 # If the master gets a Keyboard interrupt, commit suicide.
19057                 break
19068
19079                 ### Start Model Building for DM mass and SM channel #####
19080                 spectrum = spec.DM_models.HDMSpectra()
19091                 spectrum.set_channel(ch)
19102
19113                 myDwarf = ExtendedSource(dSph, spatial_shape=shape,

```

```

19124                     spectral_shape=spectrum)
19135
19146             spectrum.J = jfactor * u.GeV**2 / u.cm**5
19157             spectrum.sigmav = 1e-24 * u.cm**3 / u.s
19168             spectrum.set_dm_mass(mass * u.GeV)
19179
19180             spectrum.sigmav.bounds = (1e-30, 1e-12)
19191             model = Model(myDwarf)
19202             ##### End model Building #####
19213
19224             jl = JointLikelihood(model, datalist, verbose=False)
19235
19246             try:
19257                 result, lhdf = jl.fit(compute_covariance=False)
19268                 ts = -2.* (jl.minus_log_like_profile(1e-30) - jl.
1927 _current_minimum)
19289                 # Also profile the LLH vs sv
19290                 ll = jl.get_contours(spectrum.sigmav, sigVs[0],
19301                                     sigVs[-1], len(sigVs),
19312                                     progress=False, log=['False'])
19323
19334                 sigv_ll = au.ut.calc_95_from_profile(ll[0], ll[2])
19345                 # Write results to file
19356                 outFileLL = outPath+f"/LL_{dSph}_{ch}_mass{int(mass)}_GD.txt"
19367                 np.savetxt(outFileLL, (sigVs, ll[2]),
19378                               delimiter='\t', header='sigV\tLL\n')
19389
19390                 with open(outPath+f"/results_{dSph}_{ch}_mass{int(mass)}_GD.
1940 txt", "w") as results_file:
19411                     results_file.write("mDM [GeV]\tsigV_95\tsigV_B.F.\n")
19422
19433                     results_file.write("%i\t%.5E\t%.5E\t%.5E"%(mass, sigv_ll,
19444                                         ts, result.value[0]))

```

```

1945      # End write to file
1946      except FitFailed: # Don't kill all threads if a fit fails
1947          print("Fit failed. Go back and calculate this spectral model
1948          later")
1949          fits.append((ch, mass, -1, -1))
1950          with open(log_file+'.fail', 'w') as f_file:
1951              f_file.write(f'{ch}, {mass}\n')
1952
1953          progress[i_job] += 1
1954          matplotlib.pyplot.close() # Prevent leaky memory
1955
1956          fits.append((ch, mass, result.value[0], ts))
1957          progress[i_job] += 1
1958          matplotlib.pyplot.close()
1959
1960      except KeyboardInterrupt:
1961          progress[i_job] = -1
1962
1963      fits = np.array(fits)
1964      if queue is None:
1965          return fits
1966      else:
1967          queue.put((i_job, fits))
1968
1969  def main(args):
1970      masses = np.loadtxt(MASS_LIST, dtype=int)
1971      chans = np.loadtxt(CHAN_LIST, delimiter=',', dtype=str)
1972      mass_chan = au.ut.permute_lists(chans, masses)
1973
1974      print(f"DM masses for this study are: {masses}")
1975      print(f"SM Channels for this study are XX -> {chans}")
1976      print(mass_chan)
1977
1978      # extract information from input argument

```

```

19787 dSph = args.dSph
19798 data_mngr = au.ut.Data_Selector('P5_NN_2D')
19809 dm_profile = srcts.Spatial_DM(args.catalog, dSph, args.sigma, args.decay)
19810
19821     ### Extract Source Information ####
19832 if dm_profile.get_dec() < -22.0 or dm_profile.get_dec() > 62.0:
19843     raise ValueError("HAWC can't see this source D: Exitting now...")
19854
19865 print(f'{dSph} information')
19876 print(f'jfac: {dm_profile.get_factor()}\tRA: {dm_profile.get_ra()}\tDec: {dm_profile.get_dec()}\n')
1988
19897
19908 shape = SpatialTemplate_2D(fits_file=dm_profile.get_src_fits())
19919     ### Finish Extract Source Information ####
19920
19931     ### LOAD HAWC DATA ####
19942 roi = HealpixConeROI(data_radius=2.0, model_radius=8.0,
19953                         ra=dm_profile.get_ra(), dec=dm_profile.get_dec())
19964 bins = choose_bins.analysis_bins(args, dec=dm_profile.get_dec())
19975
19986 hawc = HAL(dSph, data_mngr.get_datmap(), data_mngr.get_detres(), roi)
19997 hawc.set_active_measurements(bin_list=bins)
20008 datalist = DataList(hawc)
20019     ### FINISH LOAD HAWC DATA ####
20020
20031 # set up SigV sampling. This sample is somewhat standardized
20042 sigVs = np.logspace(-28,-18, 1001, endpoint=True) # NOTE This will change
2005 with HDM
20063
20074 if args.n_threads == 1:
20085     # No need to start || programming just iterate over the masses
20096     kw_arg = dict(sigVs=sigVs, datalist=datalist, shape=shape, dSph=dSph,
20107                     jfactor=dm_profile.get_factor(), mass_chan=mass_chan,

```

```

20158                 log_file=args.log)
20159         some_mass_fit(**kw_arg)
20160     else:
20161         # I Really want to suppress TQMD output
20162         from tqdm import tqdm
20163         from functools import partialmethod
20164         tqdm.__init__ = partialmethod(tqdm.__init__, disable=True)
20165
20166     x = np.array_split(mass_chan, args.n_threads)
20167     n_jobs = len(x)
20168
20169     print("Thread jobs summary by mass and SM channel")
20170     for xi in x:
20171         print(f'{xi}')
20172
20173     queue = mp.Queue()
20174     progress = mp.Array('i', np.zeros(n_jobs, dtype=int))
20175
20176     # Define task pool that will be split amongsts threads
20177     kw_args = [dict(sigVs=sigVs, datalist=datalist, shape=shape,
20178                     dSph=dSph, jfactor=dm_profile.get_factor(),
20179                     mass_chan=mass_chan, progress=progress,
20180                     queue=queue, i_job=i, log_file=args.log)
20181             for i, mass_chan in enumerate(x)]
20182
20183     # Define each process
20184     procs = [mp.Process(target=some_mass_fit, kwargs=kw_args[i]) \
20185             for i in range(n_jobs)]
20186
20187     ### Start MASTER Thread only code block ###
20188     # Begin running all child threads
20189     for proc in procs: proc.start()
20190

```

```

20441     try:
20452         # In this case, the master does nothing except monitor progress of
2046         the threads
20473         # In an ideal world, the master thread also does some computation.
20484         n_complete = np.sum(progress)
20495         while_count = 0
20506
20517         while n_complete < len(mass_chan):
20528
20539             if np.any(np.asarray(progress) < 0):
20540                 # This was no threads are stranded when killing the script
20551                 raise KeyboardInterrupt()
20562             if while_count%1000 == 0:
20573                 print(f"{np.sum(progress)} of {len(mass_chan)} finished")
20584
20595             n_complete = np.sum(progress)
20606             time.sleep(.25)
20617             while_count += 1
20628
20639         except KeyboardInterrupt:
20640             # signal to jobs that it's time to stop
20651             for i in range(n_jobs):
20662                 progress[i] = -2
20673                 print('\nKeyboardInterrupt: terminating early.')
20684             ### End MASTER Thread only code block ###
20695
20706             fitss = [queue.get() for proc in procs]
20717             print(fitss)
20728             print(f'Thread statuses: {progress[:]}')
20739
20740             # putting results in a file
20751
20762             print("QUACK! All Done!")

```

```

20773
20784
20795 if __name__ == '__main__':
20806     import argparse
20817
20828     p = argparse.ArgumentParser(description="Run a DM annihilation analysis on
2083         a dwarf spheroidal for a specific SM channel for DM masses [1 TeV to 10
2084         PeV]")
20859
20860     # Dwarf spatial modeling arguements
20871     p.add_argument("-ds", "--dSph", type=str,
20882                     help="dwarf spheroidal galaxy to be studied", required=
2089     True)
20903     p.add_argument("-cat", "--catalog", type=str, choices=['GS15', 'LS20'],
20914                     default='LS20', help="source catalog used")
20925     p.add_argument("-sig", "--sigma", type=int, choices=[-1, 0, 1], default=0,
20936                     help="Spatial model uncertainty. 0 corresponds to the
2094         median. +/-1 correspond to the +/-1sigma uncertainty respectively.")
20957
20968     # Arguements for the energy estimators
20979     p.add_argument("-e", "--estimator", type=str,
20980                     choices=['P5_NHIT', 'P5_NN_2D'],
20991                     default="P5_NN_2D", required=False,
21002                     help="The energy estimator choice. Options are: P5_NHIT,
2101         P5_NN_2D. GP not supported (yet).")
21023     p.add_argument("--use-bins", default=None, nargs="*",
21034                     help="Bins to use for the analysis", dest="use_bins")
21045     p.add_argument('--select_bins_by_energy', default=None, nargs="*",
21056                     help="Does nothing. May fill in later once better
2106         understood")
21077     p.add_argument('--select_bins_by_fhit', default=None, nargs="*",
21088                     help="Also does nothing see above")
21099     p.add_argument( '-ex', '--exclude', default=None, nargs="*",

```

```

21100         help="Exclude Bins", dest="exclude")

21151

21152     # Computing and logging arguements.

21153     p.add_argument('-nt', '--n_threads', type=int, default=1,
21154                         help='Maximum number of threads spawned by script. Default
21155                         is 4')

21156     p.add_argument('-log', '--log', type=str, required=True,
21157                         help='Name for log files. Especially needed for threads')

21158

21159     p.add_argument('--decay', action="store_true",
21160                         help='Set spectral DM hypothesis to decay')

21161

21162     args = p.parse_args()

21163     print(args.decay)

21164     if args.exclude is None: # default exclude bins 0 and 1
21165         args.exclude = ['B0C0Ea', 'B0C0Eb', 'B0C0Ec', 'B0C0Ed', 'B0C0Ee']

21166

21167     if args.decay: OUT_PATH += '_dec'
21168     else: OUT_PATH += '_ann'

21169

21170     OUT_PATH = OUT_PATH + '_' + args.catalog

21171     if args.sigma != 0: OUT_PATH += f'_{args.sigma}sig'

21172

21173     main(args)

```

2134 B.3 Comparison with Glory Duck

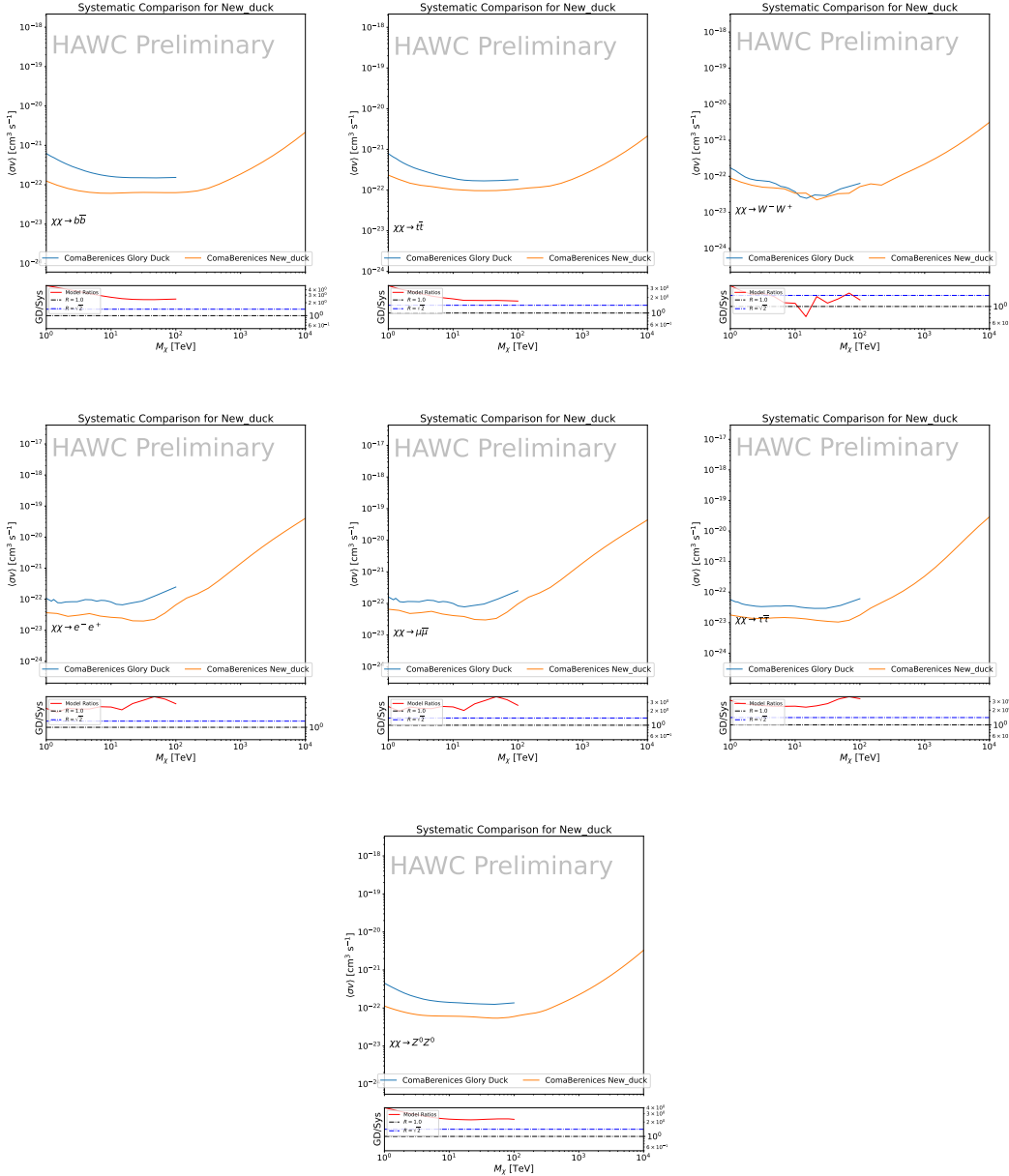


Figure B.2 Comparison of HAWC limits from this analysis to Glory Duck (Fig. 5.5) for Coma Berenices and 7 DM annihilation channels.

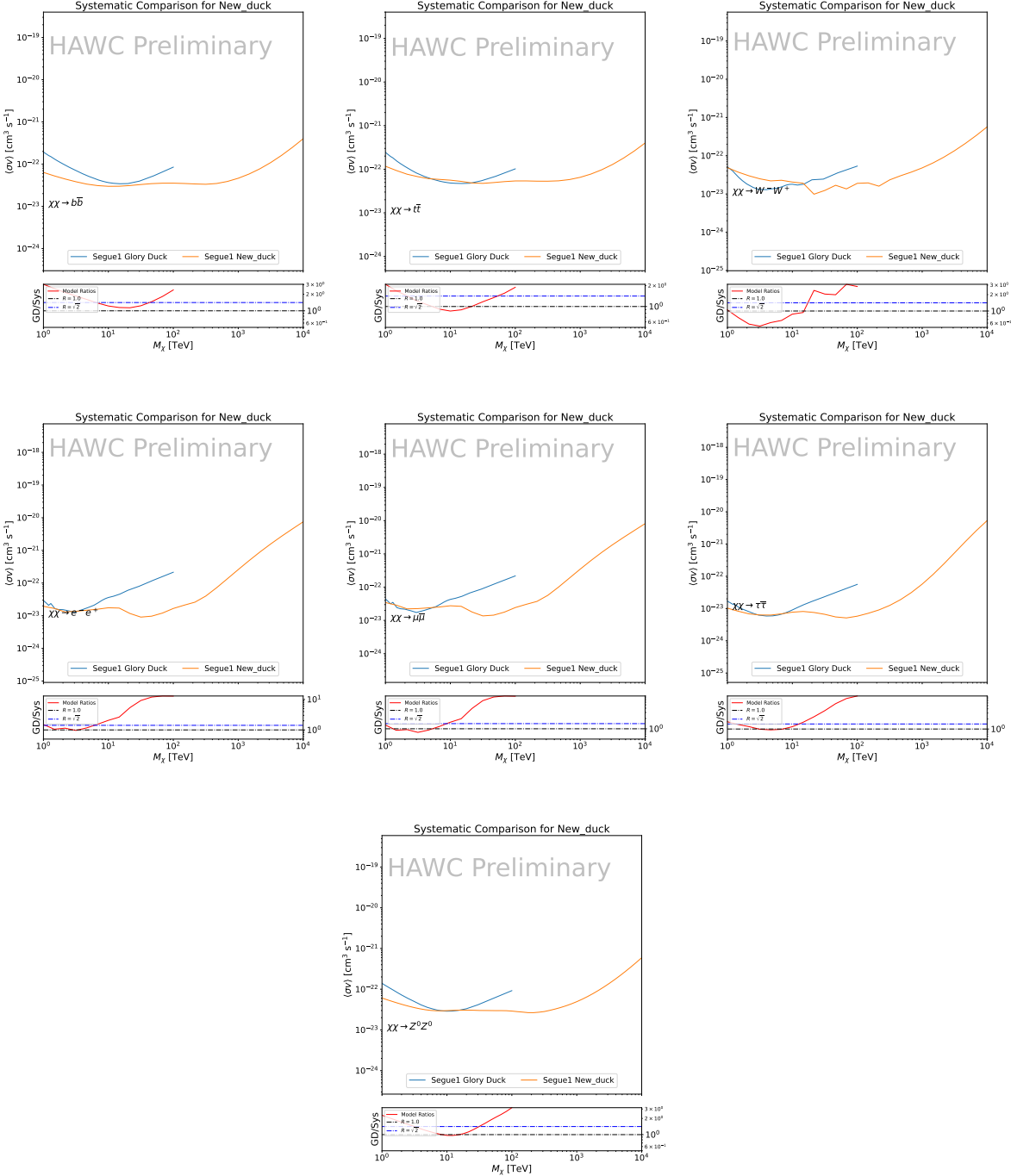


Figure B.3 Same as Fig. B.2 but for Segue 1.

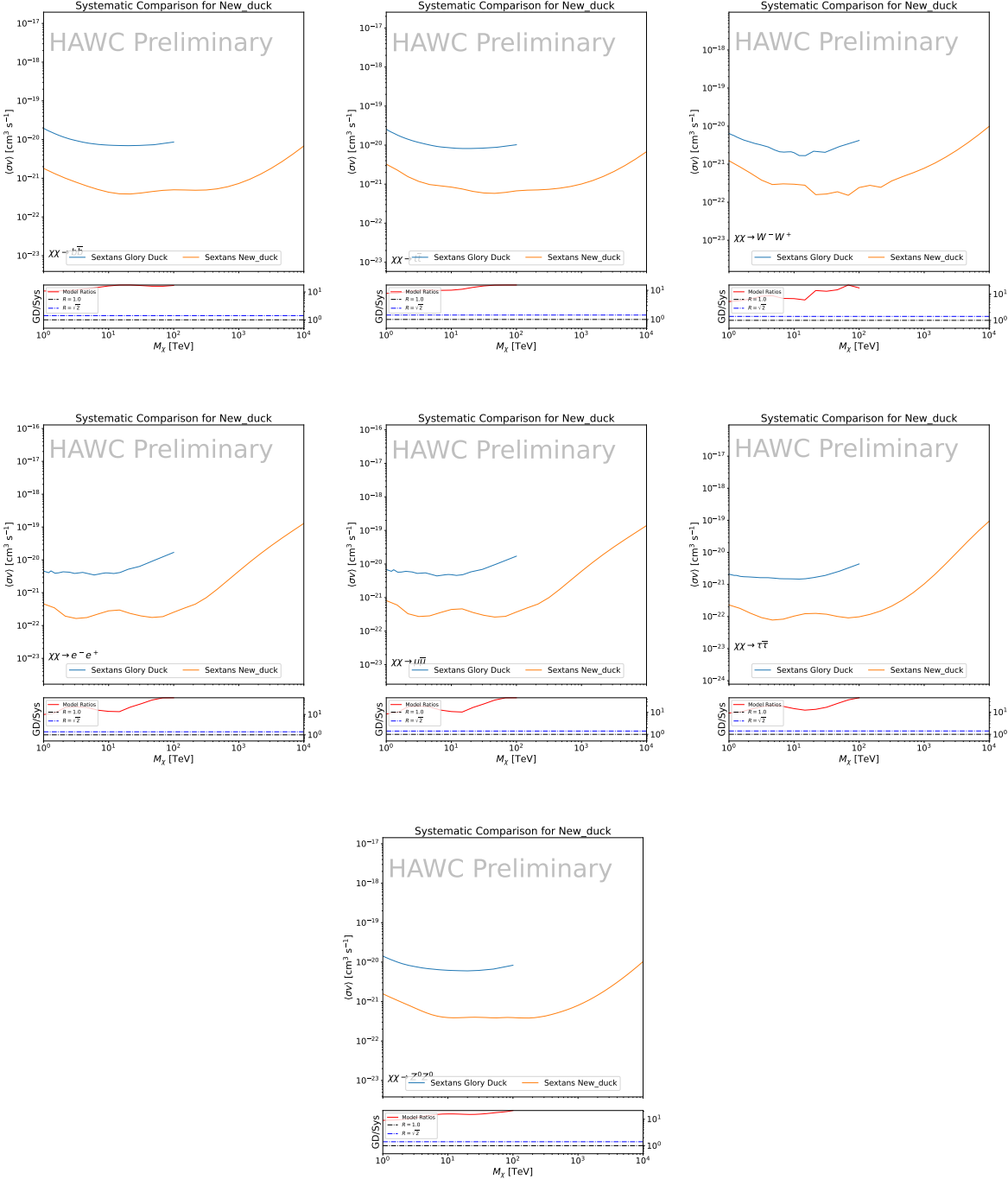


Figure B.4 Same as Fig. B.2 but for Sextans.

## APPENDIX C

### 2135 ICECUBE HEAVY DARK MATTER ANALYSIS SUPPLEMENTARY MATERIAL

#### 2136 C.1 Docker Image for Oscillating Neutrino Spectra

```
21371 FROM ubuntu:18.04
21382
21393 # Execute commands to install software packages
21404 RUN apt -y update
21415
21426 # Install utility programs
21437 RUN apt -y install vim wget git cmake
21448
21459 ARG DEBIAN_FRONTEND=noninteractive
21460
21471 # Install python
21482 RUN apt -y install python python-dev python-pip libjpeg-dev zlib1g-dev
21493
21504 # We need Python2 for installing Charon.
21515 RUN apt -y install python-numpy python-sympy python-matplotlib \
21526           python-sympy python-h5py python-astropy python-ipython
21537
21548 # Install dependencies of Charon : SQuIDS, NuSQuIDS
21559 RUN apt -y install libgsl-dev libgslcblas0 libgsl23 gsl-bin pkg-config
21560 # Install SQuIDS
21571 RUN mkdir /home/SQuIDS /home/SQuIDS_install
21582 WORKDIR /home/SQuIDS
21593 RUN git clone https://github.com/jsalvado/SQuIDS.git
21604 WORKDIR /home/SQuIDS/SQuIDS
21615 RUN git checkout 7ad9ba7c6ad06d1f0fa8418f937ebf1a403fef90
21626 # Before executing "make install" an environmental variable has to be set.
21637 ENV PKG_CONFIG_PATH=/home/SQuIDS/SQuIDS/lib
21648 RUN ./configure --prefix=../SQuIDS_install \
```

```

21659     && make
21660 RUN make install
21671
21682     # Set up an environmental variable that is required to install nuSQuIDS..
21693 ENV SQuIDS=/home/SQuIDS/SQuIDS
21704 ENV LD_LIBRARY_PATH=$SQuIDS/lib:$LD_LIBRARY_PATH
21715
21726     # Install NuSQuIDS
21737 RUN mkdir /home/nuSQuIDS
21748 WORKDIR /home/nuSQuIDS
21759 RUN git clone https://github.com/qrliu/nuSQuIDS.git
21760 WORKDIR /home/nuSQuIDS/nuSQuIDS
21771 RUN git checkout 072d8ef740e2fc7330f1fabaea94f0f4540c46f9
21782 RUN apt -y install libhdf5-dev hdf5-tools
21793 RUN apt -y install libboost1.65-all-dev
21804 RUN ./configure --with-squids=$SQuIDS --with-python-bindings --prefix=../
2181     nuSQuIDS_install \
21825     && make \
21836     && make install
21847
21858     # Set up an environmental variable for nuSQuIDS.
21869 ENV nuSQuIDS=/home/nuSQuIDS/nuSQuIDS
21870 ENV LD_LIBRARY_PATH=$nuSQuIDS/lib:$LD_LIBRARY_PATH
21881
21892     # Build the python bindings
21903 WORKDIR /home/nuSQuIDS/nuSQuIDS/resources/python/src
21914 RUN make
21925
21936     # Set up an environmental variable for the python bindings.
21947 ENV PYTHONPATH=$nuSQuIDS/resources/python/bindings/:$PYTHONPATH
21958
21969     # Install Charon in the /home/Charon/charon directory.
21970 RUN mkdir /home/Charon

```

```
21981 WORKDIR /home/Charon
21992 RUN git clone https://github.com/icecube/charon.git \
22003     && apt -y install unzip python-scipy
22014 WORKDIR charon
22025 RUN git checkout c531efe4e01dc364a60d1c83f950f04526ccd771
22036 RUN unzip ./charon/xsec/xsec.zip -d charon/xsec/ \
22047
22058 # Download neutrino spectra tables in the /home/Charon/charon/data directory
2206 .
22079 && mkdir ./charon/data
22080 WORKDIR ./charon/data
22091 RUN wget --no-check-certificate https://icecube.wisc.edu/~qliu/charon/
2210     SpectraEW.hdf5 \
22112 && wget --no-check-certificate https://icecube.wisc.edu/~qliu/charon/
2212     Spectra_PYTHIA.hdf5 \
22133 && wget --no-check-certificate https://icecube.wisc.edu/~qliu/charon/
2214     Spectra_noEW.hdf5
22154
22165 WORKDIR ../..
22176 RUN python setup.py install
22187 WORKDIR /home
```

2219 C.2 Spline Fitting Statuses

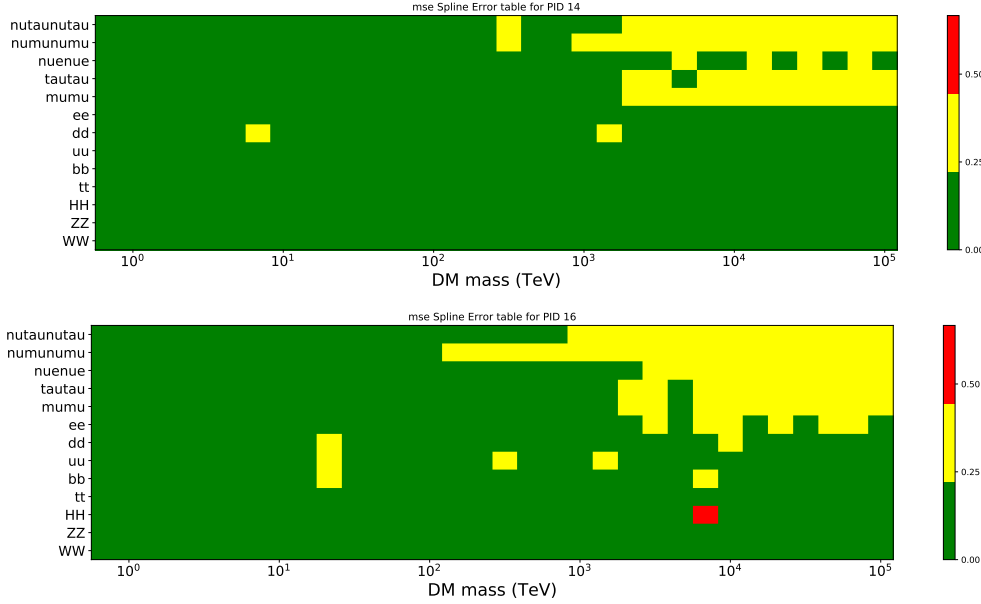


Figure C.1 Current status of spline tables according to constraints defined by Tab. 7.1. Green splines are splines that passed under the GOOD tolerance. Yellow are splines that are OK. Red are splines that FAIL. All yellow splines were inspected individually before running the analysis. Splines were made for the  $\mu$  (PID 14; top panel) flavor and  $\tau$  (PID 16; bottom panel) neutrino flavors.

2220 C.3 Neutrino Composite Spectra

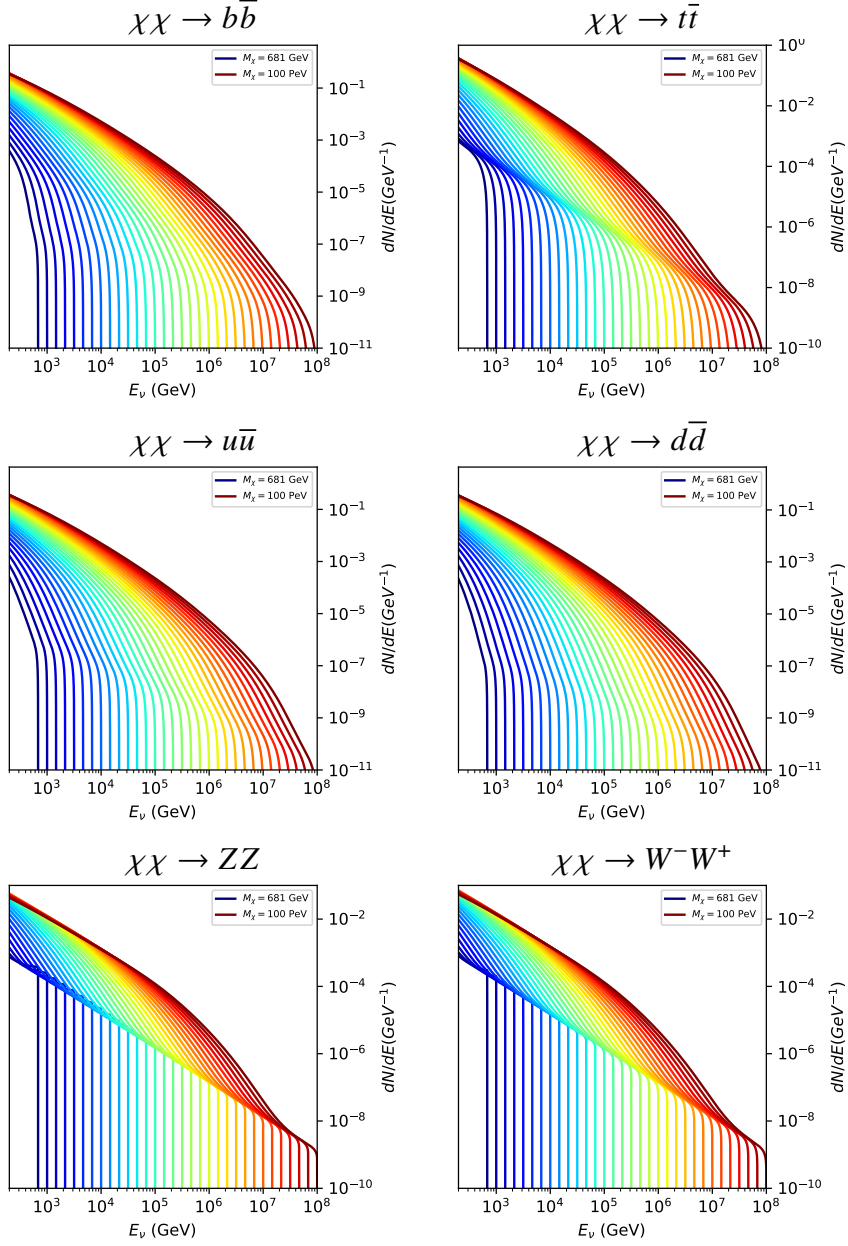


Figure C.2 Sister figure to Fig. 7.5 for annihilation channels that did not require kernel smoothing. These spectra are the composite ( $\nu_\mu + \nu_\tau$ ) of neutrino flavors. Every spectral model used for this analysis is featured as a colored solid line. Bluer lines are for lower DM mass spectral models. DM masses range from 681 GeV to 100 PeV.

2221 C.4 Segue 1 And Ursa Major II Signal Recovery

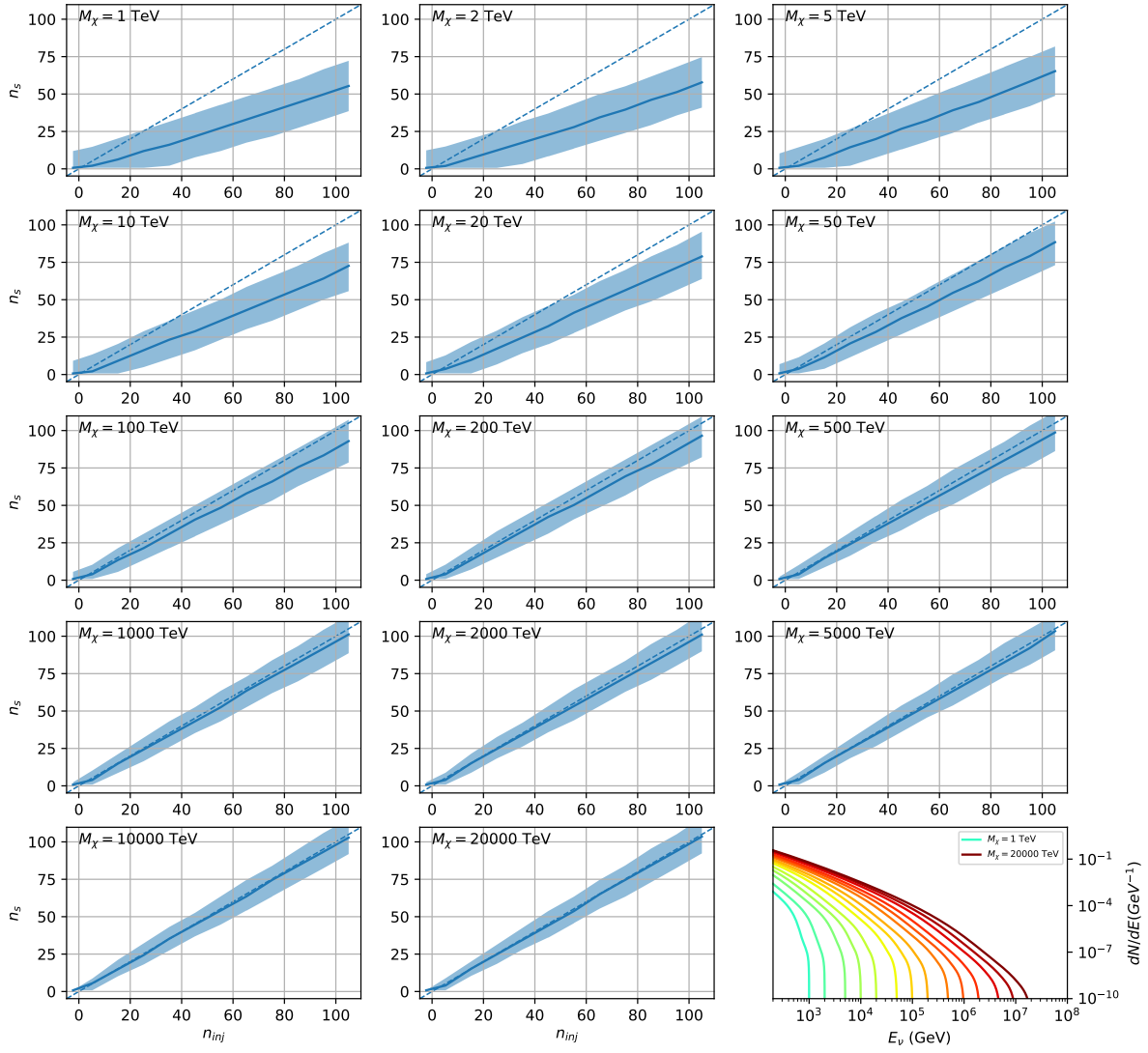


Figure C.3 Same as Fig. 7.23 but for Segue 1 and  $\chi\chi \rightarrow b\bar{b}$ .

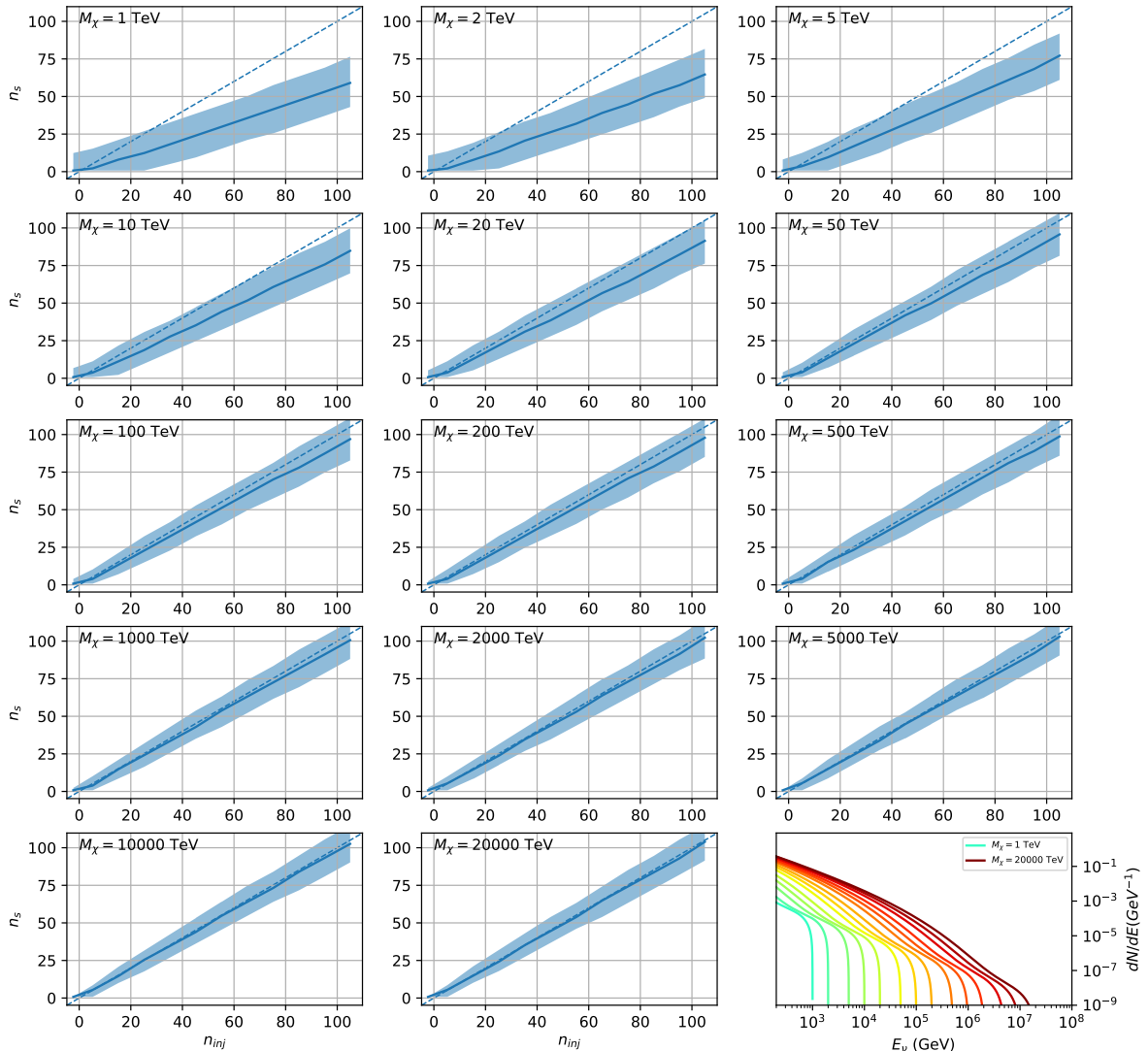


Figure C.4 Same as Fig. 7.23 but for Segue 1 and  $\chi\chi \rightarrow t\bar{t}$ .

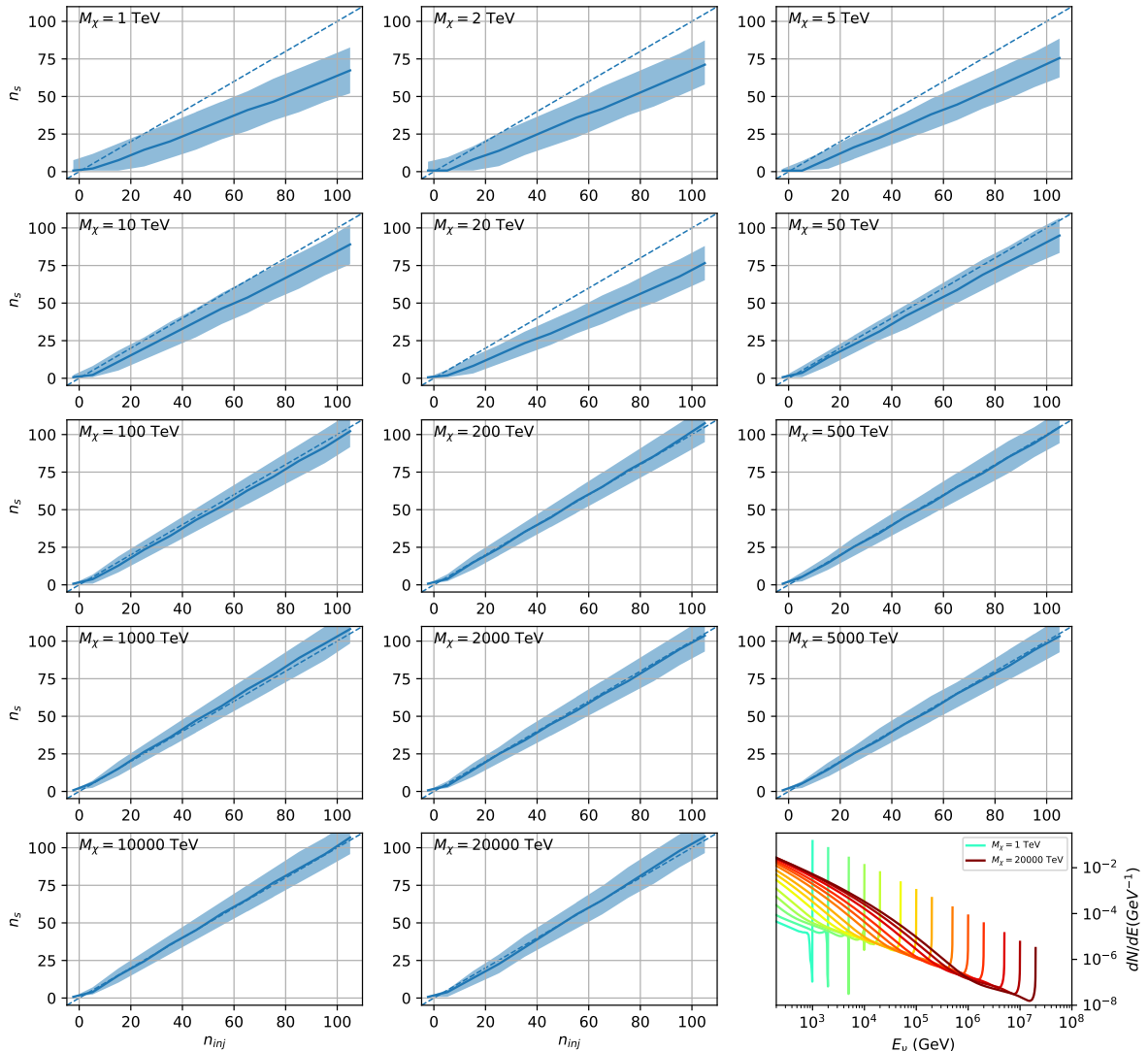


Figure C.5 Same as Fig. 7.23 but for Segue 1 and  $\chi\chi \rightarrow \nu_\mu \bar{\nu}_\mu$ .

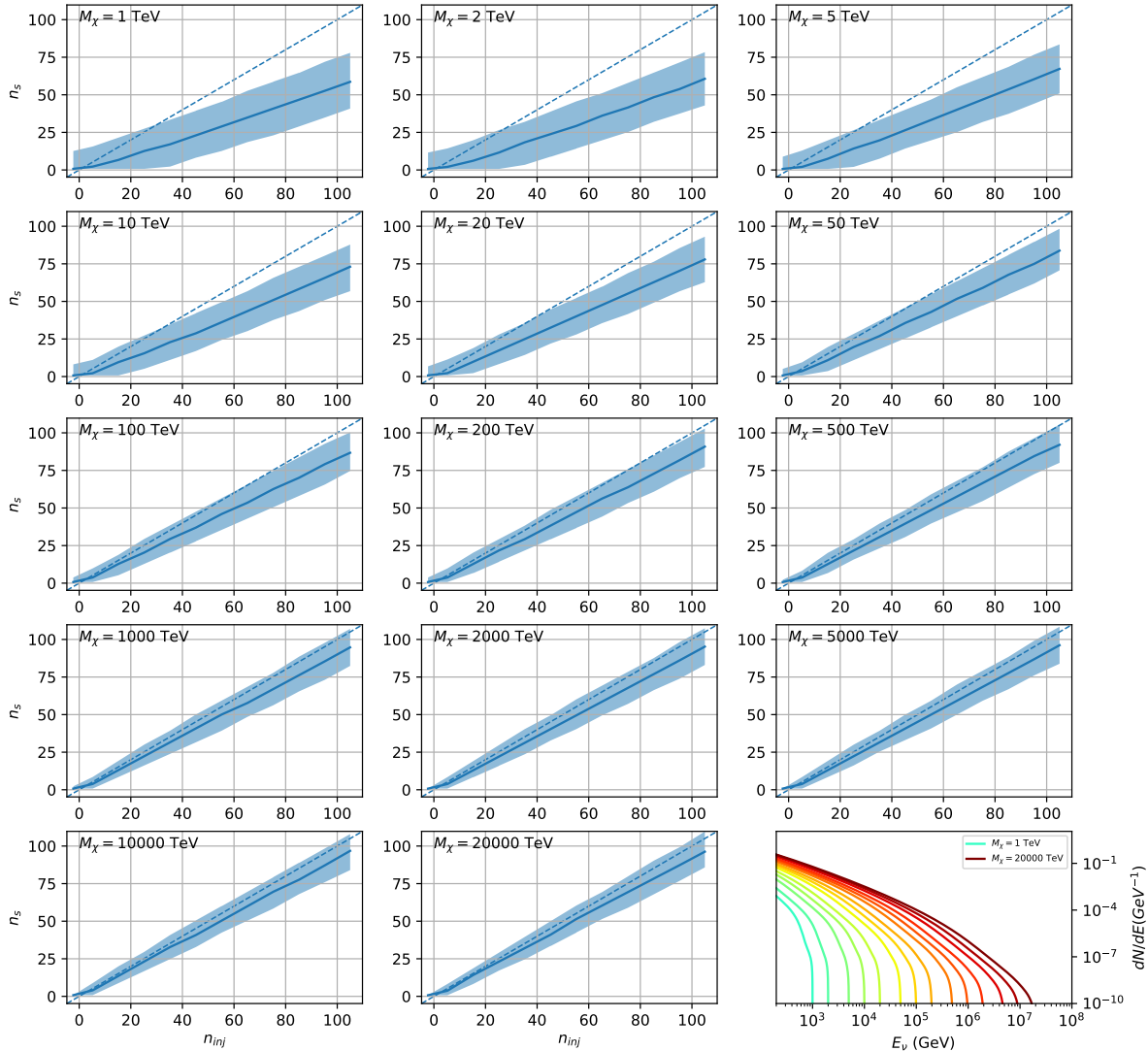


Figure C.6 Same as Fig. 7.23 but for Ursa Major II and  $\chi\chi \rightarrow b\bar{b}$ .

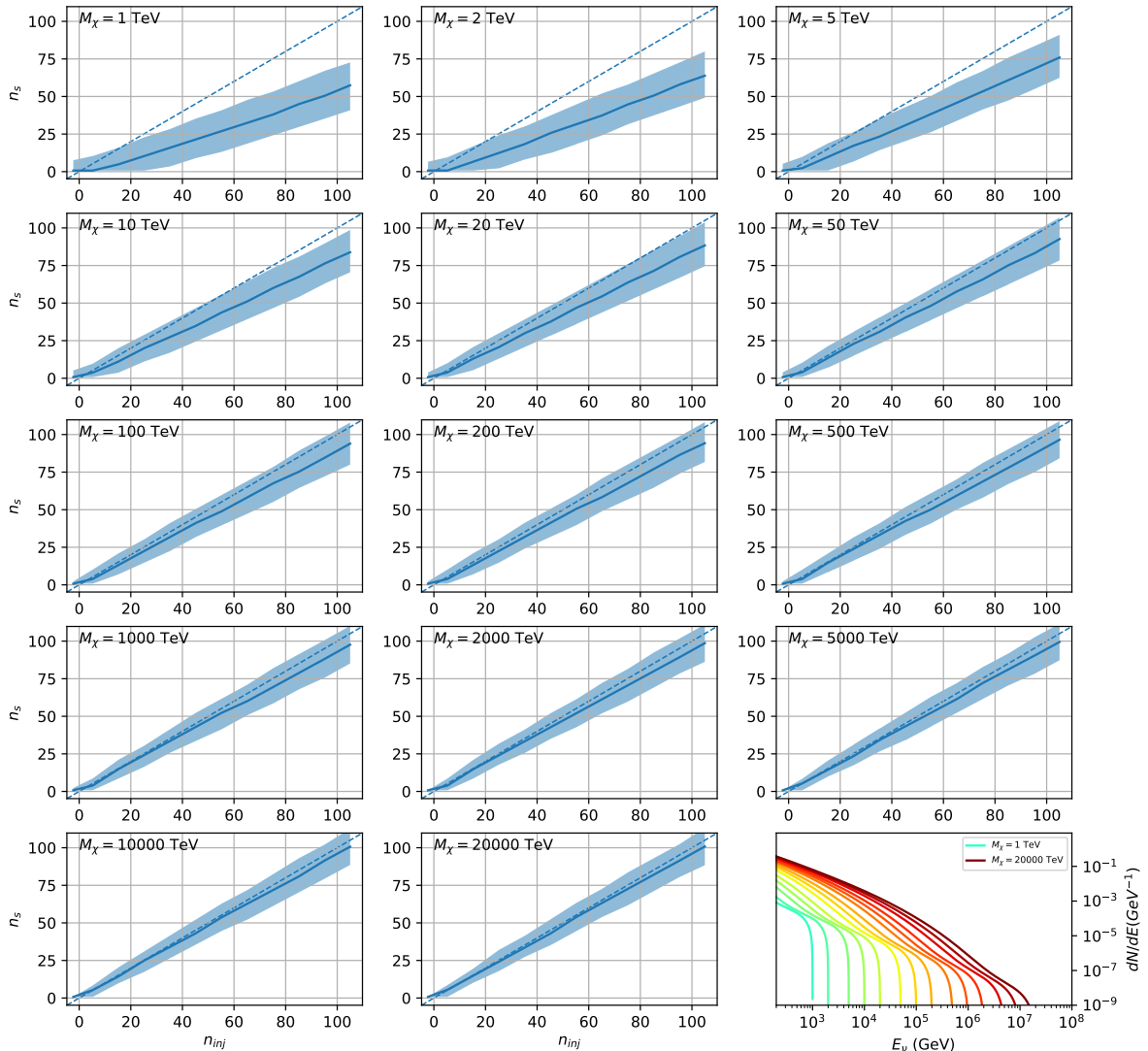


Figure C.7 Same as Fig. 7.23 but for Ursa Major II and  $\chi\chi \rightarrow t\bar{t}$ .

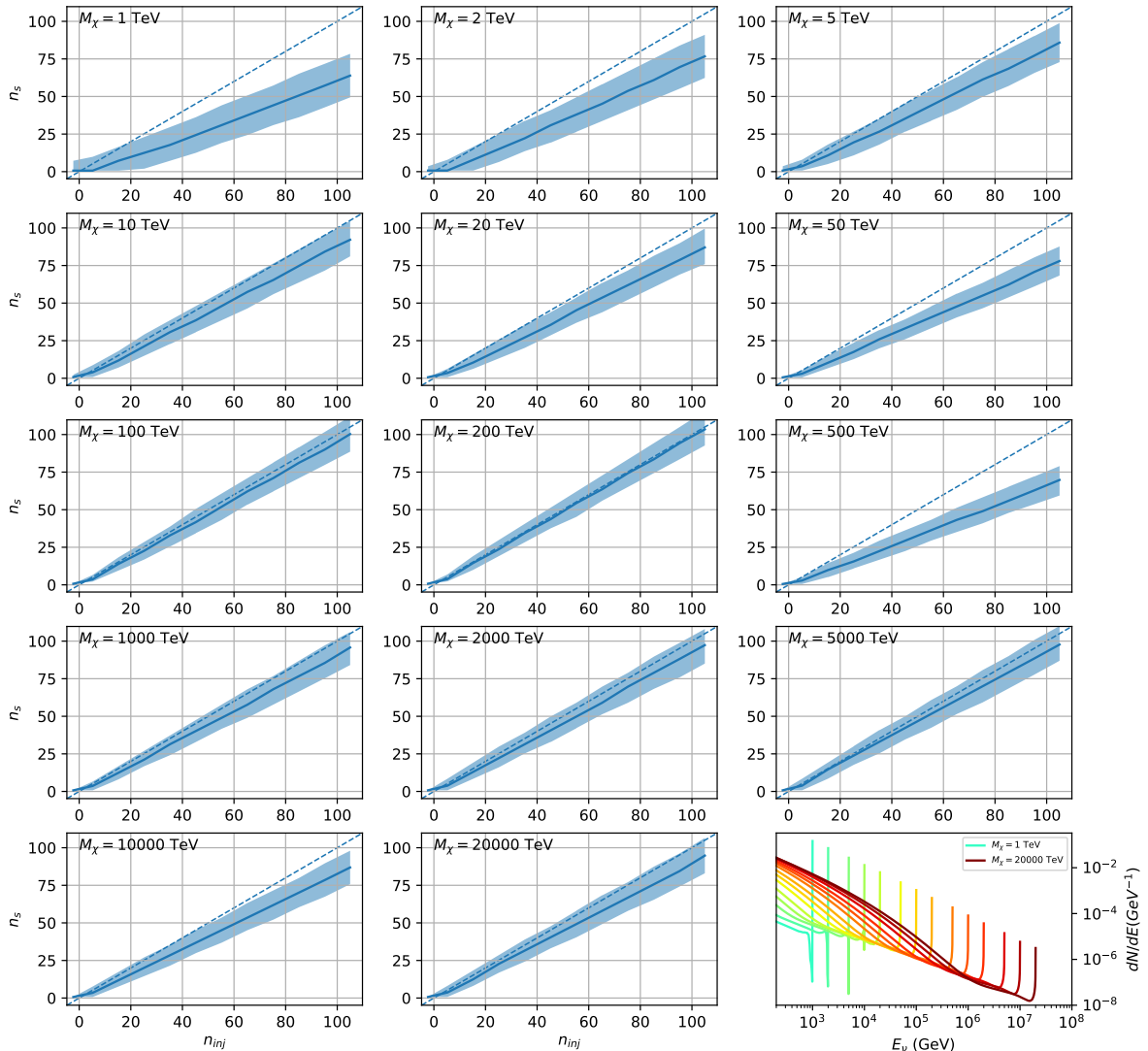


Figure C.8 Same as Fig. 7.23 but for Ursa Major II and  $\chi\chi \rightarrow \nu_\mu \bar{\nu}_\mu$ .

2222 C.5  $n_s$  Sensitivities

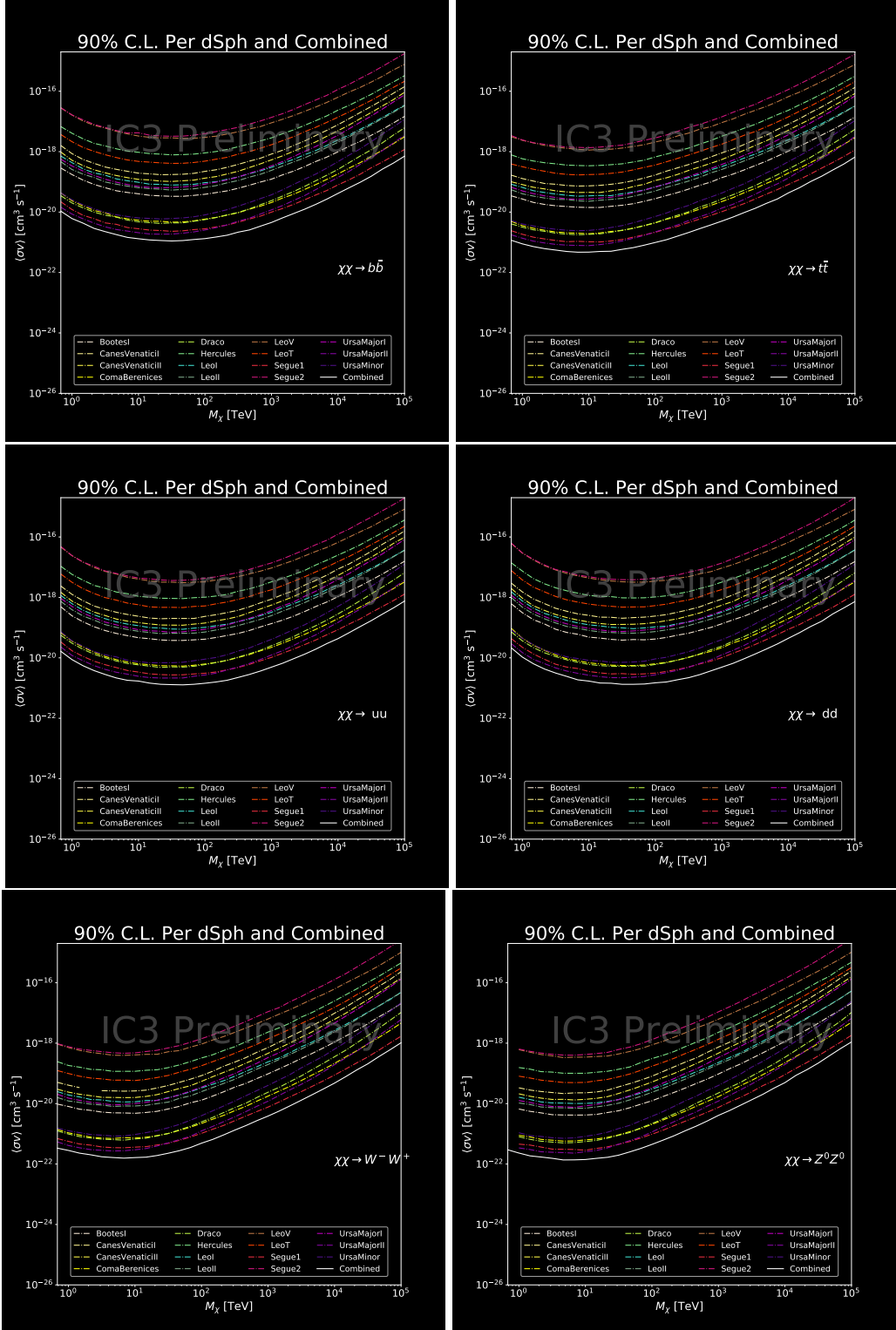


Figure C.9 IceCube North Sky Track Sensitivities for  $n_s/\langle N \rangle$ .  $n_s$  values are the counts fed into Eq. (7.8) to produce Fig. 7.26 and Fig. 7.25.

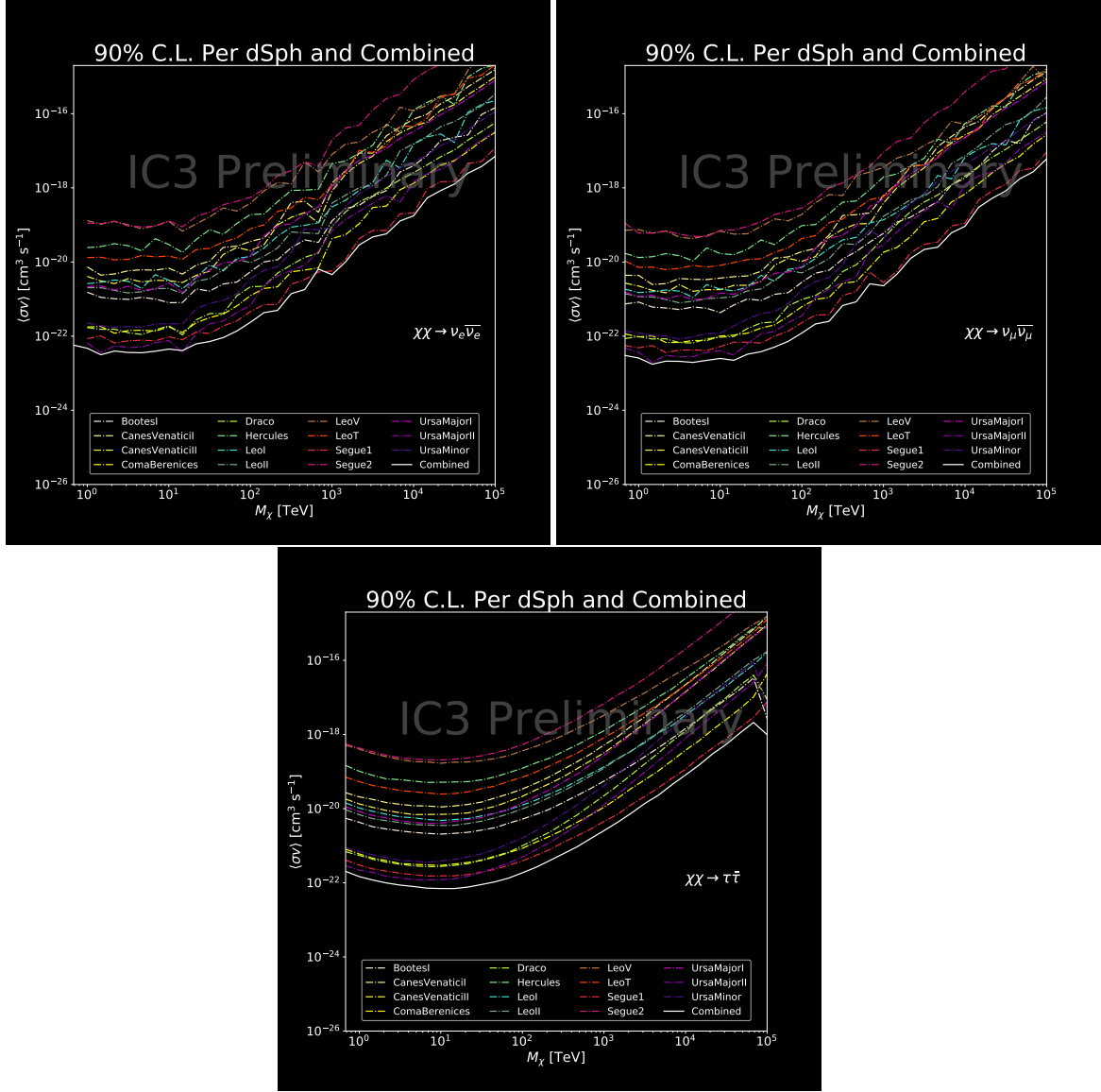


Figure C.10 Same as Fig. C.9 for three additional DM annihilation channels.

## BIBLIOGRAPHY

- 2224 [1] Anne M. Green. “Dark matter in astrophysics/cosmology”. In: *SciPost Phys. Lect.*  
 2225 *Notes* (2022), p. 37. doi: [10.21468/SciPostPhysLectNotes.37](https://doi.org/10.21468/SciPostPhysLectNotes.37). URL: <https://scipost.org/10.21468/SciPostPhysLectNotes.37>.
- 2226
- 2227 [2] Bing-Lin Young. “A survey of dark matter and related topics in cosmology”. In: *Frontiers*  
 2228 *of Physics* 12 (Oct. 2016). doi: <https://doi.org/10.1007/s11467-016-0583-4>.  
 2229 URL: <https://doi.org/10.1007/s11467-016-0583-4>.
- 2230 [3] Gianfranco Bertone, Dan Hooper, and Joseph Silk. “Particle dark matter: evidence,  
 2231 candidates and constraints”. In: *Physics Reports* 405.5 (2005), pp. 279–390. ISSN:  
 2232 0370-1573. doi: <https://doi.org/10.1016/j.physrep.2004.08.031>. URL:  
 2233 <https://www.sciencedirect.com/science/article/pii/S0370157304003515>.
- 2234 [4] Gianfranco Bertone and Dan Hooper. “History of dark matter”. In: *Rev. Mod. Phys.*  
 2235 90 (4 Aug. 2018), p. 045002. doi: [10.1103/RevModPhys.90.045002](https://doi.org/10.1103/RevModPhys.90.045002). URL: <https://link.aps.org/doi/10.1103/RevModPhys.90.045002>.
- 2236
- 2237 [5] Fritz Zwicky. “The Redshift of Extragalactic Nebulae”. In: *Helvetica Physica Acta* 6.  
 2238 (1933), pp. 110–127. doi: [10.5169/seals-110267](https://doi.org/10.5169/seals-110267).
- 2239 [6] Vera C. Rubin and Jr. Ford W. Kent. “Rotation of the Andromeda Nebula from a  
 2240 Spectroscopic Survey of Emission Regions”. In: *ApJ* 159 (Feb. 1970), p. 379. doi:  
 2241 [10.1086/150317](https://doi.org/10.1086/150317).
- 2242 [7] K. G. Begeman, A. H. Broeils, and R. H. Sanders. “Extended rotation curves of spiral galax-  
 2243 ies: dark haloes and modified dynamics”. In: *Monthly Notices of the Royal Astronomical So-*  
 2244 *ciet* 249.3 (Apr. 1991), pp. 523–537. ISSN: 0035-8711. doi: [10.1093/mnras/249.3.523](https://doi.org/10.1093/mnras/249.3.523).  
 2245 eprint: <https://academic.oup.com/mnras/article-pdf/249/3/523/18160929/mnras249-0523.pdf>. URL: <https://doi.org/10.1093/mnras/249.3.523>.
- 2246
- 2247 [8] *Different types of gravitational lenses*. website. Feb. 2004. URL: <https://esahubble.org/images/heic0404b/>.
- 2248
- 2249 [9] Douglas Clowe et al. “A Direct Empirical Proof of the Existence of Dark Matter”. In: *apjl*  
 2250 648.2 (Sept. 2006), pp. L109–L113. doi: [10.1086/508162](https://doi.org/10.1086/508162). arXiv: [astro-ph/0608407](https://arxiv.org/abs/astro-ph/0608407)  
 2251 [*astro-ph*].
- 2252 [10] Planck Collaboration and N. et. al. Aghanim. “Planck 2018 results I. Overview and the  
 2253 cosmological legacy of Planck”. In: *A&A* 641 (2020). doi: [10.1051/0004-6361/201833880](https://doi.org/10.1051/0004-6361/201833880). URL: <https://doi.org/10.1051/0004-6361/201833880>.
- 2254
- 2255 [11] Wayne Hu. *Matter Density Animation*. web. 2024. URL: <http://background.uchicago.edu/~whu/animbut/anim2.html>.
- 2256

- 2257 [12] Wenlong Yuan et al. “A First Look at Cepheids in a Type Ia Supernova Host with JWST”. in:  
2258 *The Astrophysical Journal Letters* 940.1 (Nov. 2022). doi: [10.3847/2041-8213/ac9b27](https://doi.org/10.3847/2041-8213/ac9b27).  
2259 URL: <https://dx.doi.org/10.3847/2041-8213/ac9b27>.
- 2260 [13] Wendy L. Freedman. “Measurements of the Hubble Constant: Tensions in Perspective”. In:  
2261 *The Astrophysical Journal* 919.1 (Sept. 2021), p. 16. doi: [10.3847/1538-4357/ac0e95](https://doi.org/10.3847/1538-4357/ac0e95).  
2262 URL: <https://dx.doi.org/10.3847/1538-4357/ac0e95>.
- 2263 [14] Jodi Cooley. “Dark Matter direct detection of classical WIMPs”. In: *SciPost Phys. Lect.  
2264 Notes* (2022), p. 55. doi: [10.21468/SciPostPhysLectNotes.55](https://doi.org/10.21468/SciPostPhysLectNotes.55). URL: <https://scipost.org/10.21468/SciPostPhysLectNotes.55>.
- 2266 [15] “Search for new phenomena in events with an energetic jet and missing transverse momentum  
2267 in  $pp$  collisions at  $\sqrt{s} = 13$  TeV with the ATLAS detector”. In: *Phys. Rev. D* 103  
2268 (11 July 2021), p. 112006. doi: [10.1103/PhysRevD.103.112006](https://doi.org/10.1103/PhysRevD.103.112006). URL: <https://link.aps.org/doi/10.1103/PhysRevD.103.112006>.
- 2270 [16] *Jetting into the dark side: a precision search for dark matter*. website. July 2020. URL:  
2271 <https://atlas.cern/updates/briefing/precision-search-dark-matter>.
- 2272 [17] Celine Armand et. al. “Combined dark matter searches towards dwarf spheroidal galaxies  
2273 with Fermi-LAT, HAWC, H.E.S.S., MAGIC, and VERITAS”. in: *Proceedings of Science*.  
2274 Vol. 395. Mar. 2022. doi: <https://doi.org/10.22323/1.395.0528>.
- 2275 [18] Tracy R. Slatyer. “Les Houches Lectures on Indirect Detection of Dark Matter”. In: *SciPost  
2276 Phys. Lect. Notes* (2022), p. 53. doi: [10.21468/SciPostPhysLectNotes.53](https://doi.org/10.21468/SciPostPhysLectNotes.53). URL:  
2277 <https://scipost.org/10.21468/SciPostPhysLectNotes.53>.
- 2278 [19] Christian W Bauer, Nicholas L. Rodd, and Bryan R. Webber. “Dark matter spectra from  
2279 the electroweak to the Planck scale”. In: *Journal of High Energy Physics* 2021.1029-8479  
2280 (June 2021). doi: [https://doi.org/10.1007/JHEP06\(2021\)121](https://doi.org/10.1007/JHEP06(2021)121).
- 2281 [20] Riccardo Catena and Piero Ullio. “A novel determination of the local dark matter density”.  
2282 In: *Journal of Cosmology and Astroparticle Physics* 2010.08 (Aug. 2010), p. 004. doi:  
2283 [10.1088/1475-7516/2010/08/004](https://doi.org/10.1088/1475-7516/2010/08/004). URL: <https://dx.doi.org/10.1088/1475-7516/2010/08/004>.
- 2285 [21] B. P. Abbott et al. “Observation of Gravitational Waves from a Binary Black Hole Merger”.  
2286 In: *Phys. Rev. Lett.* 116 (6 Feb. 2016), p. 061102. doi: [10.1103/PhysRevLett.116.061102](https://doi.org/10.1103/PhysRevLett.116.061102). URL: <https://link.aps.org/doi/10.1103/PhysRevLett.116.061102>.
- 2288 [22] R. Abbasi et. al. “Observation of high-energy neutrinos from the Galactic plane”. In: *Science*  
2289 380.6652 (June 2023), pp. 1338–1343.
- 2290 [23] NASA Goddard Space Flight Center. *Fermi’s 12-year view of the gamma-ray sky*. website.

- 2291 2022. URL: <https://svs.gsfc.nasa.gov/14090>.
- 2292 [24] Marco Cirelli et al. “PPPC 4 DM ID: a poor particle physicist cookbook for dark matter  
2293 indirect detection”. In: *Journal of Cosmology and Astroparticle Physics* 2011.03 (Mar.  
2294 2011), p. 051. doi: [10.1088/1475-7516/2011/03/051](https://doi.org/10.1088/1475-7516/2011/03/051). URL: <https://dx.doi.org/10.1088/1475-7516/2011/03/051>.
- 2296 [25] The HAWC Collaboration. “The High-Altitude Water Cherenkov (HAWC) observatory in  
2297 México: The primary detector”. In: *Nuclear Instruments and Methods in Physics Research*  
2298 *Section A: Accelerators, Spectrometers, Detectors and Associated Equipment* 1052 (2023),  
2299 p. 168253. ISSN: 0168-9002. doi: <https://doi.org/10.1016/j.nima.2023.168253>.  
2300 URL: <https://www.sciencedirect.com/science/article/pii/S0168900223002437>.
- 2302 [26] Alicia Lopez Oramas. “Multi-year Campaign of the Gamma-Ray Binary LS I +61° 303  
2303 and Search for VHE Emission from Gamma-Ray Binary Candidates with the MAGIC Tele-  
2304 scopes”. In: *Institut de Fisica d’Altes Energies* (2014). doi: <http://dx.doi.org/10.13140/RG.2.1.4140.4969>.
- 2306 [27] Javier Rico. “Gamma-Ray Dark Matter Searches in Milky Way Satellites—A Comparative  
2307 Review of Data Analysis Methods and Current Results”. In: *Galaxies* 8.1 (Mar. 2020), p. 25.  
2308 doi: [10.3390/galaxies8010025](https://doi.org/10.3390/galaxies8010025). arXiv: [2003.13482 \[astro-ph.HE\]](https://arxiv.org/abs/2003.13482).
- 2309 [28] W. B. Atwood et al. “The Large Area Telescope on the Fermi Gamma-Ray Space Telescope  
2310 Mission”. In: *apj* 697.2 (June 2009), pp. 1071–1102. doi: [10.1088/0004-637X/697/2/1071](https://doi.org/10.1088/0004-637X/697/2/1071). arXiv: [0902.1089 \[astro-ph.IM\]](https://arxiv.org/abs/0902.1089).
- 2312 [29] M. Ackermann et al. “Searching for Dark Matter Annihilation from Milky Way Dwarf  
2313 Spheroidal Galaxies with Six Years of Fermi Large Area Telescope Data”. In: *prl* 115.23,  
2314 231301 (Dec. 2015), p. 231301. doi: [10.1103/PhysRevLett.115.231301](https://doi.org/10.1103/PhysRevLett.115.231301). arXiv:  
2315 [1503.02641 \[astro-ph.HE\]](https://arxiv.org/abs/1503.02641).
- 2316 [30] Mattia Di Mauro, Martin Stref, and Francesca Calore. “Investigating the effect of Milky  
2317 Way dwarf spheroidal galaxies extension on dark matter searches with Fermi-LAT data”.  
2318 In: *Phys. Rev. D* 106 (12 Dec. 2022), p. 123032. doi: [10.1103/PhysRevD.106.123032](https://doi.org/10.1103/PhysRevD.106.123032).  
2319 URL: <https://link.aps.org/doi/10.1103/PhysRevD.106.123032>.
- 2320 [31] F. et al. Aharonian. “Observations of the Crab Nebula with H.E.S.S.”. In: *Astron. Astrophys.*  
2321 457 (2006), pp. 899–915. doi: [10.1051/0004-6361:20065351](https://doi.org/10.1051/0004-6361:20065351). arXiv: [astro-ph/0607333](https://arxiv.org/abs/astro-ph/0607333).
- 2323 [32] J. Albert et al. “VHE  $\gamma$ -Ray Observation of the Crab Nebula and its Pulsar with the MAGIC  
2324 Telescope”. In: *The Astrophysical Journal* 674.2 (Feb. 2008), p. 1037. doi: [10.1086/525270](https://doi.org/10.1086/525270). URL: <https://dx.doi.org/10.1086/525270>.

- 2326 [33] N. Park. “Performance of the VERITAS experiment”. In: *Proceedings, 34th International*  
2327 *Cosmic Ray Conference (ICRC2015): The Hague, The Netherlands, July, 30th July - 6th*  
2328 *August.* Vol. 34. 2015, p. 771. arXiv: [1508.07070](https://arxiv.org/abs/1508.07070) [[astro-ph.IM](#)].
- 2329 [34] A. Abramowski et al. “H.E.S.S. constraints on Dark Matter annihilations towards the Sculptor  
2330 and Carina Dwarf Galaxies”. In: *Astropart. Phys.* 34 (2011), pp. 608–616. doi: [10.1016/j.astropartphys.2010.12.006](https://doi.org/10.1016/j.astropartphys.2010.12.006). arXiv: [1012.5602](https://arxiv.org/abs/1012.5602) [[astro-ph.HE](#)].
- 2332 [35] A. Abramowski et al. “Search for dark matter annihilation signatures in H.E.S.S. observations  
2333 of Dwarf Spheroidal Galaxies”. In: *Phys. Rev. D* 90 (2014), p. 112012. doi: [10.1103/PhysRevD.90.112012](https://doi.org/10.1103/PhysRevD.90.112012). arXiv: [1410.2589](https://arxiv.org/abs/1410.2589) [[astro-ph.HE](#)].
- 2335 [36] H. Abdalla et al. “Searches for gamma-ray lines and ‘pure WIMP’ spectra from Dark  
2336 Matter annihilations in dwarf galaxies with H.E.S.S”. in: *JCAP* 11 (2018), p. 037. doi:  
2337 [10.1088/1475-7516/2018/11/037](https://doi.org/10.1088/1475-7516/2018/11/037). arXiv: [1810.00995](https://arxiv.org/abs/1810.00995) [[astro-ph.HE](#)].
- 2338 [37] J. Aleksić et al. “Optimized dark matter searches in deep observations of Segue 1 with  
2339 MAGIC”. in: *JCAP* 1402 (2014), p. 008. doi: [10.1088/1475-7516/2014/02/008](https://doi.org/10.1088/1475-7516/2014/02/008).  
2340 arXiv: [1312.1535](https://arxiv.org/abs/1312.1535) [[hep-ph](#)].
- 2341 [38] V.A. Acciari et al. “Combined searches for dark matter in dwarf spheroidal galaxies observed  
2342 with the MAGIC telescopes, including new data from Coma Berenices and Draco”. In: *Physics of the Dark Universe* (2021), p. 100912. issn: 2212-6864. doi: <https://doi.org/10.1016/j.dark.2021.100912>. URL: <https://www.sciencedirect.com/science/article/pii/S2212686421001370>.
- 2346 [39] M. L. Ahnen et al. “Indirect dark matter searches in the dwarf satellite galaxy Ursa Major II  
2347 with the MAGIC Telescopes”. In: *JCAP* 1803.03 (2018), p. 009. doi: [10.1088/1475-7516/2018/03/009](https://doi.org/10.1088/1475-7516/2018/03/009). arXiv: [1712.03095](https://arxiv.org/abs/1712.03095) [[astro-ph.HE](#)].
- 2349 [40] S. et al. Archambault. “Dark matter constraints from a joint analysis of dwarf Spheroidal  
2350 galaxy observations with VERITAS”. in: *prd* 95.8 (Apr. 2017). doi: [10.1103/PhysRevD.95.082001](https://doi.org/10.1103/PhysRevD.95.082001). arXiv: [1703.04937](https://arxiv.org/abs/1703.04937) [[astro-ph.HE](#)].
- 2352 [41] Louise Oakes et al. “Combined Dark Matter searches towards dwarf spheroidal galaxies with  
2353 Fermi-LAT, HAWC, HESS, MAGIC and VERITAS”. in: *Proceedings of Science*. 2019.
- 2354 [42] Celine Armand et al. on behalf of the Fermi-LAT, HAWC, HESS, MAGIC, VERITAS.  
2355 “Combined Dark Matter searches towards dwarf spheroidal galaxies with Fermi-LAT,  
2356 HAWC, HESS, MAGIC and VERITAS”. in: *Proceedings of Science*. 2021.
- 2357 [43] Daniel Kerszberg et al. on behalf of the Fermi-LAT, HAWC, HESS, MAGIC, and VER-  
2358 TIAS collaborations. “Search for dark matter annihilation with a combined analysis of  
2359 dwarf spheroidal galaxies from Fermi-LAT, HAWC, H.E.S.S., MAGIC and VERITAS”. in:  
2360 *Proceedings of Science*. 2023.

- 2361 [44] A. U. Abeysekara et al. “Observation of the Crab Nebula with the HAWC Gamma-Ray  
2362 Observatory”. In: *The Astrophysical Journal* 843.1 (June 2017), p. 39. doi: [10.3847/1538-4357/aa7555](https://doi.org/10.3847/1538-4357/aa7555). URL: <https://doi.org/10.3847/1538-4357/aa7555>.
- 2364 [45] Giacomo Vianello et al. *The Multi-Mission Maximum Likelihood framework (3ML)*. 2015.  
2365 arXiv: [1507.08343 \[astro-ph.HE\]](https://arxiv.org/abs/1507.08343).
- 2366 [46] Marco Cirelli et al. “PPPC 4 DM ID: a poor particle physicist cookbook for dark matter  
2367 indirect detection”. In: *Journal of Cosmology and Astroparticle Physics* 2011.03 (Mar.  
2368 2011). ISSN: 1475-7516. doi: [10.1088/1475-7516/2011/03/051](https://doi.org/10.1088/1475-7516/2011/03/051). URL: <http://dx.doi.org/10.1088/1475-7516/2011/03/051>.
- 2370 [47] Alex Geringer-Sameth, Savvas M. Koushiappas, and Matthew Walker. “DWARF GALAXY  
2371 ANNIHILATION AND DECAY EMISSION PROFILES FOR DARK MATTER EXPERI-  
2372 MENTS”. in: *The Astrophysical Journal* 801.2 (Mar. 2015), p. 74. ISSN: 1538-4357. doi:  
2373 [10.1088/0004-637X/801/2/74](https://doi.org/10.1088/0004-637X/801/2/74). URL: <http://dx.doi.org/10.1088/0004-637X/801/2/74>.
- 2375 [48] A. Albert et al. “Dark Matter Limits from Dwarf Spheroidal Galaxies with the HAWC  
2376 Gamma-Ray Observatory”. In: *The Astrophysical Journal* 853.2 (Feb. 2018), p. 154. ISSN:  
2377 1538-4357. doi: [10.3847/1538-4357/aaa6d8](https://doi.org/10.3847/1538-4357/aaa6d8). URL: <http://dx.doi.org/10.3847/1538-4357/aaa6d8>.
- 2379 [49] HongSheng Zhao. “Analytical models for galactic nuclei”. In: *Mon. Not. Roy. Astron. Soc.*  
2380 278 (1996), pp. 488–496. doi: [10.1093/mnras/278.2.488](https://doi.org/10.1093/mnras/278.2.488). arXiv: [astro-ph/9509122](https://arxiv.org/abs/astro-ph/9509122)  
2381 [astro-ph].
- 2382 [50] Julio F. Navarro, Carlos S. Frenk, and Simon D. M. White. “The Structure of Cold Dark  
2383 Matter Halos”. In: *ApJ* 462 (May 1996), p. 563. doi: [10.1086/177173](https://doi.org/10.1086/177173). eprint:  
2384 [astro-ph/9508025](https://arxiv.org/abs/astro-ph/9508025) (astro-ph).
- 2385 [51] V. Bonnivard et al. “Spherical Jeans analysis for dark matter indirect detection in dwarf  
2386 spheroidal galaxies - Impact of physical parameters and triaxiality”. In: *Mon. Not. Roy.  
2387 Astron. Soc.* 446 (2015), pp. 3002–3021. doi: [10.1093/mnras/stu2296](https://doi.org/10.1093/mnras/stu2296). arXiv:  
2388 [1407.7822 \[astro-ph.HE\]](https://arxiv.org/abs/1407.7822).
- 2389 [52] M. Ackermann et al. “Searching for Dark Matter Annihilation from Milky Way Dwarf  
2390 Spheroidal Galaxies with Six Years of Fermi Large Area Telescope Data”. In: *prl* 115.23,  
2391 231301 (Dec. 2015), p. 231301. doi: [10.1103/PhysRevLett.115.231301](https://doi.org/10.1103/PhysRevLett.115.231301). arXiv:  
2392 [1503.02641 \[astro-ph.HE\]](https://arxiv.org/abs/1503.02641).
- 2393 [53] M. L. Ahnen et al. “Limits to Dark Matter Annihilation Cross-Section from a Combined  
2394 Analysis of MAGIC and Fermi-LAT Observations of Dwarf Satellite Galaxies”. In: *JCAP*  
2395 1602.02 (2016), p. 039. doi: [10.1088/1475-7516/2016/02/039](https://doi.org/10.1088/1475-7516/2016/02/039). arXiv: [1601.06590](https://arxiv.org/abs/1601.06590)  
2396 [astro-ph.HE].

- 2397 [54] Javier Rico et al. *gLike: numerical maximization of heterogeneous joint*  
2398 *likelihood functions of a common free parameter plus nuisance parameters.*  
2399 <https://doi.org/10.5281/zenodo.4601451>. Version v00.09.03. Mar. 2021. doi: [10.5281/zenodo.4601451](https://doi.org/10.5281/zenodo.4601451). URL: <https://doi.org/10.5281/zenodo.4601451>.
- 2401 [55] Tjark Miener and Daniel Nieto. *LklCom: Combining likelihoods from different experiments.*  
2402 <https://doi.org/10.5281/zenodo.4597500>. Version v0.5.3. Mar. 2021. doi: [10.5281/zenodo.4597500](https://doi.org/10.5281/zenodo.4597500). URL: <https://doi.org/10.5281/zenodo.4597500>.
- 2404 [56] T. Miener et al. “Open-source Analysis Tools for Multi-instrument Dark Matter Searches”.  
2405 In: *arXiv e-prints*, arXiv:2112.01818 (Dec. 2021), arXiv:2112.01818. arXiv: [2112.01818](https://arxiv.org/abs/2112.01818)  
2406 [[astro-ph.IM](#)].
- 2407 [57] Alex Geringer-Sameth and Matthew Koushiappas Savvas M. and Walker. “Dwarf galaxy  
2408 annihilation and decay emission profiles for dark matter experiments”. In: *Astrophys.*  
2409 *J.* 801.2 (2015), p. 74. doi: [10.1088/0004-637X/801/2/74](https://doi.org/10.1088/0004-637X/801/2/74). arXiv: [1408.0002](https://arxiv.org/abs/1408.0002)  
2410 [[astro-ph.CO](#)].
- 2411 [58] Gianfranco Bertone, Dan Hooper, and Joseph Silk. “Particle dark matter: evidence, can-  
2412 didates and constraints”. In: *Physics Reports* 405.5-6 (Jan. 2005), pp. 279–390. ISSN:  
2413 0370-1573. doi: [10.1016/j.physrep.2004.08.031](https://doi.org/10.1016/j.physrep.2004.08.031). URL: <http://dx.doi.org/10.1016/j.physrep.2004.08.031>.
- 2415 [59] V. Bonnivard et al. “Dark matter annihilation and decay in dwarf spheroidal galaxies: The  
2416 classical and ultrafaint dSphs”. In: *Mon. Not. Roy. Astron. Soc.* 453.1 (2015), pp. 849–867.  
2417 doi: [10.1093/mnras/stv1601](https://doi.org/10.1093/mnras/stv1601). arXiv: [1504.02048](https://arxiv.org/abs/1504.02048) [[astro-ph.HE](#)].
- 2418 [60] A. et al. Albert. “Searching for Dark Matter Annihilation in Recently Discovered Milky Way  
2419 Satellites with Fermi-LAT”. in: *Astrophys. J.* 834.2 (2017), p. 110. doi: [10.3847/1538-4357/834/2/110](https://doi.org/10.3847/1538-4357/834/2/110). arXiv: [1611.03184](https://arxiv.org/abs/1611.03184) [[astro-ph.HE](#)].
- 2421 [61] Mattia Di Mauro and Martin Wolfgang Winkler. “Multimessenger constraints on the dark  
2422 matter interpretation of the Fermi-LAT Galactic Center excess”. In: *prd* 103.12, 123005  
2423 (June 2021), p. 123005. doi: [10.1103/PhysRevD.103.123005](https://doi.org/10.1103/PhysRevD.103.123005). arXiv: [2101.11027](https://arxiv.org/abs/2101.11027)  
2424 [[astro-ph.HE](#)].
- 2425 [62] H. C. Plummer. “On the Problem of Distribution in Globular Star Clusters: (Plate 8.)”  
2426 In: *Monthly Notices of the Royal Astronomical Society* 71.5 (Mar. 1911), pp. 460–470.  
2427 ISSN: 0035-8711. doi: [10.1093/mnras/71.5.460](https://doi.org/10.1093/mnras/71.5.460). eprint: <https://academic.oup.com/mnras/article-pdf/71/5/460/2937497/mnras71-0460.pdf>. URL:  
2429 <https://doi.org/10.1093/mnras/71.5.460>.
- 2430 [63] Daniel R. Hunter. “Derivation of the anisotropy profile, constraints on the local velocity  
2431 dispersion, and implications for direct detection”. In: *JCAP* 02 (2014), p. 023. doi:  
2432 [10.1088/1475-7516/2014/02/023](https://doi.org/10.1088/1475-7516/2014/02/023). arXiv: [1311.0256](https://arxiv.org/abs/1311.0256) [[astro-ph.CO](#)].

- 2433 [64] Barun Kumar Dhar and Liliya L. R. Williams. “Surface mass density of the Einasto family  
2434 of dark matter haloes: are they Sersic-like?” In: *Mon. Not. Roy. Astron. Soc.* (2010). doi:  
2435 [10.1111/j.1365-2966.2010.16446.x](https://doi.org/10.1111/j.1365-2966.2010.16446.x).
- 2436 [65] M. Baes and E. Van Hese. “Dynamical models with a general anisotropy profile”. In: *Astron. Astrophys.* 471 (2007), p. 419. doi: [10.1051/0004-6361:20077672](https://doi.org/10.1051/0004-6361:20077672). arXiv: [0705.4109 \[astro-ph\]](https://arxiv.org/abs/0705.4109).
- 2439 [66] Matthew G. Walker, Edward W. Olszewski, and Mario Mateo. “Bayesian analysis of re-  
2440 solved stellar spectra: application to MMT/Hectochelle observations of the Draco dwarf  
2441 spheroidal”. In: *mnras* 448.3 (Apr. 2015), pp. 2717–2732. doi: [10.1093/mnras/stv099](https://doi.org/10.1093/mnras/stv099).  
2442 arXiv: [1503.02589 \[astro-ph.GA\]](https://arxiv.org/abs/1503.02589).
- 2443 [67] Nicholas L. Rodd et al. “Dark matter spectra from the electroweak to the Planck scale”. In:  
2444 *J. High Energy Physics* 121.10.1007 (June 2021).
- 2445 [68] Pace, Andrew B and Strigari, Louis E. “Scaling relations for dark matter annihilation and  
2446 decay profiles in dwarf spheroidal galaxies”. In: *Monthly Notices of the Royal Astronomical  
2447 Society* 482.3 (Oct. 2018), pp. 3480–3496. issn: 0035-8711. doi: [10.1093/mnras/sty2839](https://doi.org/10.1093/mnras/sty2839).
- 2449 [69] Albert, A. et al. “Search for gamma-ray spectral lines from dark matter annihilation in  
2450 dwarf galaxies with the High-Altitude Water Cherenkov observatory”. In: *Phys. Rev. D* 101 (10 May 2020), p. 103001. doi: [10.1103/PhysRevD.101.103001](https://doi.org/10.1103/PhysRevD.101.103001). URL:  
2451 <https://link.aps.org/doi/10.1103/PhysRevD.101.103001>.
- 2453 [70] Victor Eijkhout and Edmund Show and Robert van de Geijn. *The Science of Computing.  
2454 The Art of High Performance Computing*. Vol. 3. Open Copy published under CC-BY 4.0  
2455 license, 2023, pp. 63–66.
- 2456 [71] Aartsen, M. et al. “IceCube search for dark matter annihilation in nearby galaxies and galaxy  
2457 clusters”. In: *Phys. Rev. D* 88 (12 Dec. 2013), p. 122001. doi: [10.1103/PhysRevD.88.122001](https://doi.org/10.1103/PhysRevD.88.122001). URL: <https://link.aps.org/doi/10.1103/PhysRevD.88.122001>.
- 2459 [72] Pearl Sandick et al. “Sensitivity of the IceCube neutrino detector to dark matter annihilating  
2460 in dwarf galaxies”. In: *Phys. Rev. D* 81 (8 Apr. 2010), p. 083506. doi: [10.1103/PhysRevD.81.083506](https://doi.org/10.1103/PhysRevD.81.083506). URL: <https://link.aps.org/doi/10.1103/PhysRevD.81.083506>.
- 2462 [73] Qinrui Liu and Jeffrey Lazar and Carlos A. Argüelles and Ali Kheirandish. “χaro: a tool  
2463 for neutrino flux generation from WIMPs”. In: *Journal of Cosmology and Astroparticle  
2464 Physics* 2020.10 (Oct. 2020), p. 043. doi: [10.1088/1475-7516/2020/10/043](https://doi.org/10.1088/1475-7516/2020/10/043). URL:  
2465 <https://dx.doi.org/10.1088/1475-7516/2020/10/043>.
- 2466 [74] Tessa Cerver. “Time Integrated searches for Astrophysical Neutrino Sources using the  
2467 IceCube Detector and Gender in Physics studies for the Genera Project”. In: *UNIVERSITE*

- 2468 DE GEN `EVE (2019), pp. 57–64.
- 2469 [75] Minjin Jeong on behalf of the IceCube Collaboration. “Search for Dark Matter Decay in  
2470 Nearby Galaxy Clusters and Galaxies with IceCube”. In: *Proceedings of Science* 444.38  
2471 (2023).
- 2472 [76] IceCube Collaboration. “Evidence for neutrino emission from the nearby active galaxy NGC  
2473 1068”. In: *Science* 378.6619 (2022).
- 2474 [77] Nathan Whitehorn and Jakob van Santen. *Photospline*. IceCube: GitHub.
- 2475 [78] Paul H. C. Eilers and Brian D. Marx. “Flexible smoothing with B-splines and penalties”.  
2476 In: *Statistical Science* 11.2 (1996), pp. 89–121. doi: [10.1214/ss/1038425655](https://doi.org/10.1214/ss/1038425655). URL:  
2477 <https://doi.org/10.1214/ss/1038425655>.
- 2478 [79] The IceCube Collaboration. *Search for neutrino lines from dark matter annihilation and*  
2479 *decay with IceCube*. 2023. arXiv: [2303.13663 \[astro-ph.HE\]](https://arxiv.org/abs/2303.13663).
- 2480 [80] The IceCube Collaboration. “Measurement of the multi-TeV neutrino interaction cross-  
2481 section with IceCube using Earth absorption”. In: *Nature* 551 (2017).